**UAB**

Universitat Autònoma de Barcelona

# Conjugated Materials for Thermoelectrics and Photovoltaics

PhD Thesis of

## Bernhard Dörling

Supervisors:

Mariano Campoy Quiles

Miquel Garriga Bacardi

Tutor:

F. Xavier Àlvarez Calafell

Departament de Física
Facultat de Ciències

**Universitat Autònoma de Barcelona**

ICMAB
INSTITUT DE CIÈNCIA DE MATERIALS DE BARCELONA

EXCELENCIA SEVERO OCHOA

CSIC
Consejo Superior de Investigaciones Científicas

April 2017

# Abstract

In times of global warming and rising energy prices, the need for renewable energy is quite clear to most people. The best way to accelerate their widespread adoption, is to continue pushing the limits in terms of efficiency, reliability and price. One way that could allow for a cost-effective generation of renewable energy, is by using cheap organic materials and solution-based coating processes.

This thesis explores ways of how interactions between organic materials can be exploited to obtain additional functionality in a simple manner, without the need for complex processing. The obtained results have applications in the field of organic photovoltaics and thermoelectrics.

PART I: INTRODUCTION

1 - MOTIVATION

In the first part of this work, I start by motivating why organic materials can be a potential solution to the problem of distributed renewable energy generation, briefly going over the unique combination of advantages these materials possess.

2 - CONJUGATED MATERIALS

Then I will summarize the basics of conjugated polymers and carbon nanotubes—the materials used in this work—as well as how their properties can be influenced by doping or by preferentially orienting them along one direction.

3 - ORGANIC THERMOELECTRICS

Furthermore, thermoelectricity—the direct conversion of heat to electricity—will be introduced. Special emphasis will be placed on doping and its effect on the highly correlated thermoelectric properties.

4 - ORGANIC PHOTOVOLTAICS

The other area of interest is photovoltaics—the generation of electricity from sunlight—particularly as it applies to organic materials.

PART II: RESULTS

5 - ELLIPSOMETRY

[VFM+16] Michelle S. Vezie et al. *Nat. Mater.* **15**, 746 (2016)

[GDR+13] Antonio Guerrero et al. *ACS Nano*, **7**, 4637 (2013)

The first presented results report on the ellipsometric characterization of the optical properties of conjugated polymers and their blends with fullerenes or dopants. During the course of this thesis, the optical constants of several conjugated polymers were characterized by variable angle spectroscopic ellipsometry, leading to the observation that some of them exhibit an unexpectedly high absorption [VFM+16]. Another study investigates the influence of solvent additives on the vertical phase segregation of conjugated polymer:fullerene blends and their effect on solar cell efficiency [GDR+13].

6 - CARBON NANOTUBE COMPOSITES

[DRC+16] Bernhard Dörling et al. *Adv. Mater.* **28**, 2782 (2016)

After that I will detail the work on a promising class of thermoelectric materials—nanocomposites of conjugated polymers and carbon nanotubes. The interaction between conjugated polymers such as polythiophenes and carbon nanotubes allows for the efficient debundling of tubes. These nanocomposites of polymer coated nanotubes exhibit good electrical conductivity and low thermal conductivity, and thus are promising organic thermoelectric materials. Composites of polythiophene and nitrogen-doped multi-walled carbon nanotubes were prepared and characterized, with the goal of obtaining air-stable n-type materials [DRC+16]. The developed simple fabrication methods, which make use of UV-light to induce an irreversible conversion from a p-type to an n-type composite or vice versa, have

been patented [CGD+15]. Subsequently, investigations were directed towards doped composites of single-walled carbon nanotubes, which are expected to reach higher efficiency [DSK+17].

[CGD+15] Mariano Campoy Quiles et al. Patent pending ES1641.1145, PCT/EP2016/078459. 2015
[DSK+17] Bernhard Dörling et al. *Synth. Met.* **225**, 70 (2017)

**7 - ORIENTED POLYMER LAYERS**

The following chapters focus on simple fabrication techniques for organic photovoltaic devices, with the particular objective of obtaining oriented layers of conjugated polymers. To that end, the directional epitaxial crystallization of polythiophene on the crystalline solvent additive 1,3,5-trichlorobenzene was adapted to allow the one-step deposition of oriented films during blade coating.

By controlling solvent evaporation, the nucleation of the additive can be confined to the one-dimensional contact line during blade-coating. This way, uniaxially oriented layers of conjugated polymers could be deposited directly from solution [DVT+14]. Further development of this method enabled the controlled nucleation at directed points, enabling the deposition of circular crystalline superstructures known as spherulites at desired locations [DSA+17].

[DVT+14] Bernhard Dörling et al. *J. Mater. Chem. C*, **2**, 3303 (2014)
[DSA+17] Bernhard Dörling et al. *submitted*, (2017)

The organic photovoltaic devices that were prepared from these oriented films, are documented in the last experimental chapter. Particular focus is given to potential applications as detectors of the polarization state of light.

**8 - ORIENTED PHOTOVOLTAICS**

Additionally, it was observed that small amounts of the additive can increase the device efficiency of organic bilayer solar cells due to an improved vertical composition gradient [VDH+16].

[VDH+16] Varun Vohra et al. *Appl. Phys. Express*, **9**, 012301 (2016)

The results are wrapped up in a few brief conclusions which also try to give an indication of the direction of future work.

**PART III: CONCLUSIONS & OUTLOOK**

The appendix contains additional information on two setups which were designed and built during this thesis. To characterize the prepared polymer:CNT composites, a simple setup for the automatic measurement of the average Seebeck coefficient close to room temperature, based on a Raspberry Pi, was built. In order to be able to prepare blade-coated layers with a controlled thickness gradient, an Arduino-based programmable voltage source was built, which allowed to control the velocity of the blade-coater.

**PART IV: APPENDIX**

**A - EXPERIMENTAL SETUPS**

Furthermore, the appendix contains a chapter detailing sample preparation as well as characterization, and a reproduction of the scripts that are used to control the custom-made setups.

**B - EXPERIMENTAL METHODS**

**C - SCRIPTS**

The thesis ends with an extensive bibliography, as well as a list of figures, a list of tables and a glossary of technical terms and symbols.

**BIBLIOGRAPHY**

**LISTS**

The last pages contain a list of the publications, conference presentations and posters that have been written and presented during this thesis, as well as of the patent and prize which were obtained.

**SCIENTIFIC CONTRIBUTIONS**

iv

# Acknowledgements

First of all, I would like to thank Mariano and Miquel, whom I am very grateful for having given me the chance to work at ICMAB and for supervising and guiding me during all this time. Whenever I had a problem, I could depend on Miquel to find a solution. And I will certainly remember the Friday afternoon experiments with Mariano, which more often than not, lead to some curious new finding. I will strive to keep the tradition going!

I also want to express my gratitude to Alejandro for finding a way to keep employing me, after the initial project ran out. And also to Trini, Pietat, Maria and Vicente, for helping me navigate the intricacies of Spanish bureaucracy.

I of course have to mention my fellow students, with whom I shared so much time. I am thankful to Ignasi and Malte for helping me out and showing me around when I was still starting out. Thanks to Damià and to Laura, for the continued reminder that we work in the best of all offices, and thanks to Xabier, whose sheer presence is enough inspiration to go to the gym more often. I am particularly indebted to Ana, who single-handedly taught me Spanish.

Thanks to the motley crew of people I shared lunch with all these years. To Blai, my untiring Catalan teacher, and to my namesakes, Bernat and Bernat; to Ashley, citizen of the world and to Ela, who by now has stashed enough four-leaf clovers to last a lifetime. Thanks to the always good-humored Federico, to Roque and to Laura; to James, Alex and Gustau, who are always planning the next climbing excursion; and of course to Jaume, the hands-down most inventive person I ever met.

I would also like to thank Murata Sensei, who kindly offered me to stay at his group at JAIST. The group dinner at Yuu Yuu's was quite an experience, as was the rest of my stay. I would also like to thank Dao-san who helped me with the experiments, irrespective of hour or day. Varun-san I thank for showing me around town, even after he witnessed my ghastly interpretation of Nena at the Karaoke place.

Furthermore, I am thankful to Christian Müller for inviting me to spend some time at Chalmers in January—really the best time to get some work done. Thanks also to Amaia and Camilla, who showed me around and helped me get my bearings.

Lastly, I would like to thank my family. My parents, Walter and Inge, who always provided for everything I needed, yet thank god never for everything I wanted. I did not visit them as much as I should have during this time, but my sister Adelheid and my brother Wolfgang took it upon themselves to visit me regularly and to keep me updated. They assure me that was indeed the reason, and that this beautiful city and its welcoming people were purely secondary.

Finally, I would like to thank Kaddi, who accompanied me throughout all of this adventure. Hopefully there will be many more to come.

# Contents

# I

# INTRODUCTION

# MOTIVATION

## 1.1. Organic Conjugated Materials

Organic conjugated materials consist mostly of carbon and hydrogen and depending on the specific material, of small quantities of for example sulfur, oxygen or nitrogen. They combine characteristics commonly attributed to "plastics", such as flexibility and simple processing, with those of semiconductors or metals. They can conduct electricity and have a band gap absorbing and emitting light in the visible spectral range.

These organic conjugated materials and their potential applications for thermoelectricity and organic photovoltaics are the topic of this thesis. In particular, the main materials of interest are conjugated polymers like P3HT, and carbon allotropes such as carbon nanotubes and fullerenes.

**Thermoelectricity** Conversion of heat directly into electricity, and vice versa.

**OPV Organic photovoltaic** Generation of electricity from sunlight, using carbon-based materials.

**P3HT**
Poly(3-hexylthiophene-2,5-diyl)

**CNT**
Carbon nanotube

## 1.2. Energy

An average human being subsists on a diet of 2500 kcal or about 10 kJ per day. This amounts to an average power of about 120 W, a number that is remarkably low, compared to the additional energy needs of that same human, given in Table 1.1.

In 2014, humanity used about $1.1 \times 10^{17}$ W h globally [Int16], which corresponds to an average continuous consumption of 2000 W per person. Only about 20 % of this energy was provided in the form of electricity, the rest was used for transportation, heating and in industrial processes, among other things. Most of this primary energy still comes from limited sources such as fossil fuels, with renewable sources only accounting for a few percent.

SOLAR ENERGY Compared to those numbers, the amount of energy that we receive from the sun is gigantic. The Earth continuously receives $1.2 \times 10^{17}$ W from the Sun [KAB+08], which means that if all of that energy would be usable, the global demand could be covered in a single hour. The irradiation of course strongly depends on the location, with an annual average of 1000 kW h m$^{-2}$ in Central Europe and 2200 kW h m$^{-2}$ in the Sahara [SJI+16].

WASTE HEAT Similarly, the amount of energy that is lost as heat to the environment without doing any useful work is estimated between 40–60 % of the total primary energy use. While the quantity of this wasted heat is enormous, most of it is low quality heat. For example, less than 6 % of the waste heat of thermal power plants is discharged at temperatures above 50 °C [GM15].
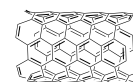
Table 1.1: Average power used per person.

|  | [W] |
| --- | --- |
| Biological needs | 120 |
| Electricity | 400 |
| Global primary energy use | 2000 |
| in USA | 12000 |
| in Europe | 6000 |
| in India | 1000 |

[Int16] International Energy Agency. *Key World Energy Statistics* (2016)

[KAB+08] Frederik C. Krebs et al. *Polymer Photovoltaics: A Practical Approach* (2008)

[SJI+16] Arno H. M. Smets et al. *Solar Energy: The Physics and Engineering of Photovoltaic Conversion, Technologies and Systems* (2016)

[GM15] Daniel B. Gingerich et al. *Environ. Sci. Technol.* **49**, 8297 (2015)

What is needed then is cheap and scalable technology that can be applied in a profitable manner to make use of these untapped reserves of distributed energy.

## 1.3. Advantages of Organic Materials

Organic semiconductors have demonstrated that they can be used in a wide variety of applications, such as organic light emitting diodes [GBI+97], organic photovoltaic cells [KEH+14], thermoelectric generators [BC12], transistors [KJP+15] and even complementary circuits [BSD+16]. They also enable new applications, such as a thermally gated transistors [ZFB+17], and emerging forms of neuromorphic computing. There, organic semiconductors act as artificial neurons with a switching energy that is potentially lower than that of biological synapses, which would allow for highly efficient implementations of neural nets [BLF+17].

Compared to their inorganic counterparts, organic (semi-)conductors have a number of advantages that make them particularly well suited for certain applications.

ABUNDANCE  Organic semiconductors are composed mostly of carbon and hydrogen atoms, with small quantities of heteroatoms such as sulfur, oxygen and nitrogen. These elements are more abundant than inorganic semiconductors, except for silicon. Furthermore, they are not toxic unlike for example lead, bismuth, indium, arsenic or cadmium, which allows for easier recycling or disposal of all-organic based devices.

FLEXIBILITY  While organic semiconductors are less flexible than non-conductive "plastics", they still allow even for intrinsic stretchability, which is required for future applications such as electronic skin [XWW+17]. Because of the low required active layer thicknesses, they are comparatively lightweight, a similarly important attribute for wearable applications.

SOLUTION PROCESSABILITY  Because of their flexibility and solubility, organic semiconductors can be deposited by roll-to-roll processing [Kre09] [ADH+14], using a variety of large-scale solution-based coating and additive printing techniques [BSL+14], without the need for high temperature processes.

LOW ENERGY INVESTMENT  Because commodity polymers used for substrates can be produced in large quantities in scalable processes, and because the more expensive organic semiconductors are used in very small quantities, comparatively little energy has to be expended for the manufacture of complete devices. Consequently, organic photovoltaic cells have demonstrated an energy payback time on the order of a few months [KEH+14], a number which is predicted to drop down to a single day [EHA+12]. This is a significant improvement over traditional silicon based technology, which has an EPBT of up to several years. A similar indicator is what is called the energy return on investment. For devices prepared from easily synthesized small molecule acceptor materials, it has been estimated, that the energy

[GBI+97] Martin Grell et al. *Adv. Mater.* **9**, 798 (1997)

[KEH+14] Frederik C. Krebs et al. *Adv. Mater.* **26**, 29 (2014)

[BC12] Olga Bubnova et al. *Energy Environ. Sci.* **5**, 9345 (2012)

[KJP+15] Nam-Koo Kim et al. *Chem. Mater.* **27**, 8345 (2015)

[BSD+16] Sadir Gabriele Bucella et al. *Adv. Electron. Mater.* **2**, 1600094 (2016)

[ZFB+17] Dan Zhao et al. *Nat. Commun.* **8**, 14214 (2017)

[BLF+17] Yoeri van de Burgt et al. *Nat. Mater.* **16**, 414 (2017)

[XWW+17] Jie Xu et al. *Science*, **355**, 59 (2017)

[Kre09] Frederik C. Krebs. *Sol. Energy Mater. Sol. Cells*, **93**, 465 (2009)

[ADH+14] Thomas R. Andersen et al. *Energy Environ. Sci.* **7**, 2925 (2014)

[BSL+14] Ignasi Burgués-Ceballos et al. *J. Mater. Chem. A*, **2**, 17711 (2014)

EPBT Energy payback time  The time it takes a device to generate as much energy as is needed for its own manufacture, installation and disposal.

[KEH+14] Frederik C. Krebs et al. *Adv. Mater.* **26**, 29 (2014)

[EHA+12] Nieves Espinosa et al. *Energy Environ. Sci.* **5**, 5117 (2012)

EROI Energy return on investment Ratio of energy produced during the lifetime of a device, relative to the energy invested during its fabrication.

returned during their nine year lifetime could be more than 100 times higher than the energy that was required for their manufacture. This would equate to an improvement of more than an order of magnitude, compared to other photovoltaic technologies [BAH+16].

[BAH+16] Derya Baran et al. *Nat. Mater.* **16**, 363 (2016)

COST OF ENERGY GENERATION  In the past, one of the main selling points of organic materials was their low-cost potential, as quantified by the levelized cost of energy.

$$\text{LCOE} = \frac{\text{total monetary life cycle cost}}{\text{total energy produced}} \tag{1.1}$$

The calculation includes all costs from the cradle to the grave, such as production, installation, operation, maintenance, disassembly and recycling costs. This number is compared to the total energy produced during the lifetime of the device.

An optimistic study estimated cost-parity with traditional coal-based electricity generation for OPV devices with 5 % efficiency and a 5 year lifetime [MBZ+15]. Using more conservative estimates, it was found that if a lifetime of 10 years is reached, OPV can compete with traditional photovoltaic technology [GSN16].

[MBZ+15] Cara J. Mulligan et al. *Sol. Energy Mater. Sol. Cells*, **133**, 26 (2015)

[GSN16] Ajay Gambhir et al. *Sol. Energy Mater. Sol. Cells*, **156**, 49 (2016)

TRANSPARENCY  Organic materials are (semi-)transparent, unlike most inorganic (semi-)conductors. This feature alone makes them promising candidates for building integrated OPV and display applications.

TUNABILITY  The properties of organic semiconductors can be varied by minor changes in the chemical structure. For example, their color can be tuned by changing the band gap, or their crystallinity by changing the side chains.

## 1.4. Disadvantages of Organic Materials

STABILITY  The main disadvantage of organic conjugated materials can be summed up under the topic of stability.

For example, the range of permissible temperatures for organic materials spans a comparatively narrow window around room temperature. However, if it is possible to continue narrowing the performance gap between organic materials and established technology, then this restriction will become nearly insignificant. As we saw, most energy is available in the form of distributed sources close to room temperature.

Another issue is the stability of organic materials towards exposure to humidity, oxygen or UV radiation, which may result in rapid degradation. Particularly, doped n-type materials are prone to oxidation, which makes intrinsically stable organic materials particularly sought-after, and which is why part of the work of this thesis is concerned with this topic.

# CONJUGATED MATERIALS

This chapter briefly introduces some of the basics of electrically conductive organic materials. A selection of the materials used for this thesis are depicted in Figure 2.1.
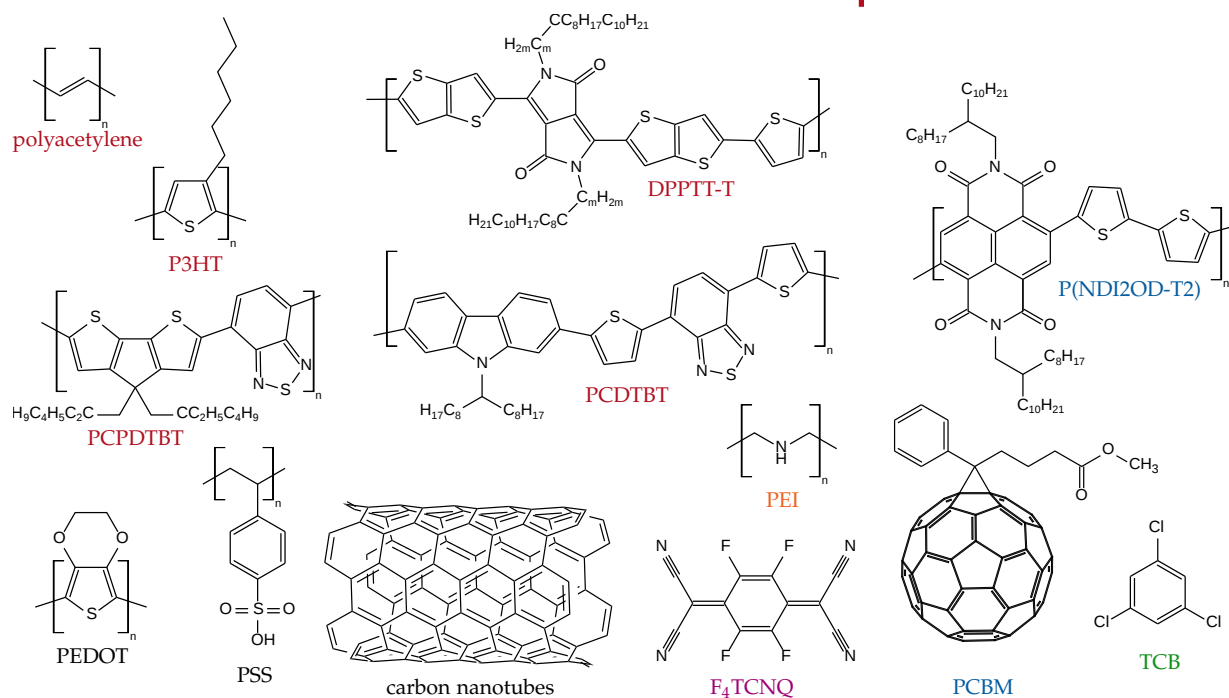
Figure 2.1: Materials used in this thesis. Materials are separated by color according to their typical usage into groups of donors, acceptors, n-type dopants, p-type dopants and solvent additives.

## 2.1. Conjugation

BONDING   If it is energetically advantageous, atoms will bond together to form molecules. The atomic orbitals overlap, sharing their electron density, forming bonds and as a consequence decreasing the inter-atomic distance. Depending on the molecule formed, there are different types of molecular bonds.

$\sigma$ bonds are rotation symmetric with respect to the axis between the two participating atoms. They are bonding orbitals, stabilizing the molecule, with the shared electron density being concentrated at the center between both atoms. The electron density for the corresponding antibonding $\sigma^*$ orbitals with the same rotational symmetry is concentrated on opposite sides, far away from the center between the two atoms. If one were to excite an electron from a $\sigma$ orbital to a $\sigma^*$ orbital, the bond between atoms would be cut, since the energy of the $\sigma^*$ orbital lies above the ionization energy.

$\pi$ bonds are weaker than $\sigma$ bonds, since there is less overlap of the electron densities of the participating atomic orbitals. The binding energy of a C=C double bond, which is composed of one $\sigma$ and one $\pi$ bond, is less than twice that of two $\sigma$ bonds. This means, that an electron can be excited from a filled $\pi$ to an empty $\pi^*$ orbital without cutting the molecular bond.

Since $\pi$-conjugation is formed between the overlap of out-of-plane p-orbitals, this requires the molecule to be planar. The molecule is rigid and cannot arbitrarily bend, or rotate along the bond axis without breaking the $\pi$ bonds.

Conjugation  Alternation of single and multiple bonds, resulting in delocalized electrons.
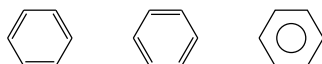[GH13] Mark Geoghegan et al. *Polymer Electronics* (2013)



Figure 2.2: The benzene resonance structure.

CONJUGATION  The benzene molecule sketched in Figure 2.2 is an instructive example of the emergent effects of conjugation [GH13]. Benzene has alternating single and double bonds, which can theoretically be arranged in two equivalent ways. From experiments, it is known that all the bonds are in fact the same length, which means that the real structure is more akin to the one shown on the right in Figure 2.2. The electrons comprising the $\pi$ bonds are delocalized. If an external magnetic field is applied to the benzene molecule, the electrons will move freely around the ring, in an aromatic ring current. But since the interactions between neighboring benzene molecules is very weak, the delocalization is restricted to a single molecule and benzene is not macroscopically conductive.

BAND STRUCTURE  For macroscopically conductive organic materials, more extended molecules, or materials with a strong interaction between molecules are needed. However, in most conjugated materials, $\pi$ electrons are not perfectly delocalized like in benzene. Imagine two carbon atoms bound by a single double bond, an ethylene molecule. It has a single pair of $\pi$–$\pi^*$-orbitals. The length of the molecule can be increased by joining it with another ethylene molecule. The resulting 1-3-butadiene now has two $\pi$–$\pi^*$ orbital pairs, which initially are degenerate—being two identical copies of the ethylene levels. This degeneracy is lifted, and the two levels are instead split into four. The lowest energy $\pi$ level corresponds to an electronic wave function with zero nodes, while the number incrementally increases for the higher energy states, as shown in Figure 2.3.
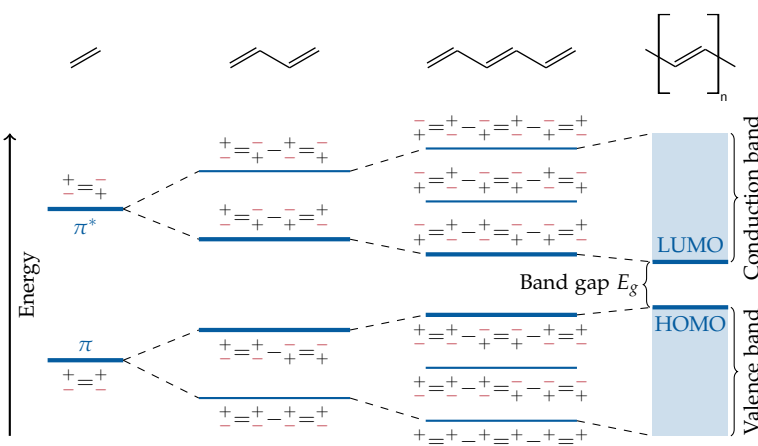


Figure 2.3: Band gap, $\pi$ and $\pi^*$ levels, polarity of the electron wave functions and HOMO and LUMO levels for an increasing degree of polymerization.

By increasing the length further, more $\pi$ and $\pi^*$ levels are added, all the while decreasing the gap between the highest $\pi$ and the lowest $\pi^*$ level. In the limit of an infinite chain—for polyacetylene—the large number of levels form quasi continuous bands of states, separated by a band gap, where no allowed states exist. The top of the $\pi$ orbital is called the highest occupied molecular orbital, while the bottom of the $\pi^*$ orbital is the lowest unoccupied molecular orbital. These frontier orbitals correspond to the valence and conduction band edges in inorganic semiconductors.

If the band gap were to dissappear with increasing chain length, then the $\pi$ electrons in polyacetylene would be delocalized all along the chain, exhibiting metallic conductivity, which is not the case for pristine polyacetylene. It was shown that an equal spacing of a one-dimensional chain with one electron per ion is unstable [Pei79]. Instead, polyacetylene has two degenerate ground states, which are separated by an energy barrier of the order of the band gap as sketched in Figure 2.4.

The band gap typically lies in the visible for conjugated materials, with values of about 1–2 eV, which means that thermal activation alone is not enough to go from one state to the other. An overview over $\pi$-conjugation is given in [MG12].

SOLITONS    A real chain is not perfect however. It has defects in the form of bends or rotations, which disrupt the rigid $\pi$ bonds, and delimit the conjugation length. A double bond that is broken in this manner leaves two unpaired electrons. Once created, these defects of the bond-length alternation can move freely along the chain by exchanging single and double bonds, which is why they are called solitons. However, solitons are not perfectly localized, like they are sketched in Figure 2.5. Instead, they are extended over several repeat units. When moving along the chain and passing over a soliton, the bond-length alternation does not instantly switch, but changes gradually.

QUINOID STRUCTURE    Unlike the symmetric polyacetylene, which does not differ in length when single and double bonds are exchanged with each other, most conjugated materials do not have a degenerate ground state, but instead two dissimilar resonance structures. For example, by replacing every double bond of polyacetylene by a phenyl group, we obtain polyparaphenylene, which has an aromatic ground state, and a quinoid state which is higher in energy. Both are depicted in Figure 2.6.

## 2.2. Doping

POLARONS    When doping, charges are added or removed from the $\pi$-conjugated system. It may then be energetically favorable to localize these charges by relaxing the backbone on several neighboring repeat units. This localized charge and its induced distortion is called a polaron or bipolaron. They have a locally quinoid structure, and lead to the appearance of new absorption features below the absorption edge because of the newly created states in the band gap. For a positive polaron, an electron is removed from these states in the

Band gap    The minimum amount of energy required to raise an electron from a localized state to a conducting state.

HOMO Highest occupied molecular orbital

LUMO Lowest unoccupied molecular orbital

[Pei79] Rudolf Ernst Peierls. *Surprises in Theoretical Physics* (1979)
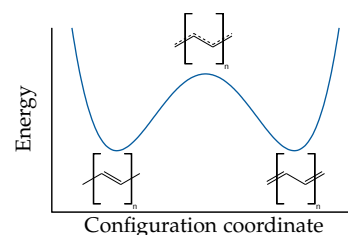


Figure 2.4: Energy of an infinite polyacetylene molecule as a function of the bond-length alternation.

[MG12] Begoña Milián-Medina et al. *Wiley Interdiscip. Rev. Comput. Mol. Sci.* **2**, 513 (2012)

Conjugation length    Chain length over which transport is coherent and band-like.
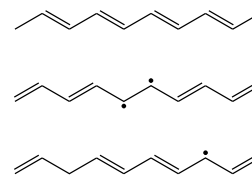


Figure 2.5: Soliton pair on a polyacetylene chain segment.
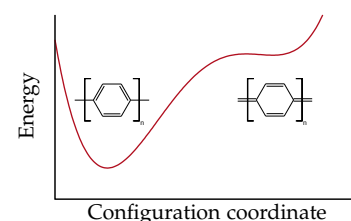


Figure 2.6: Aromatic and quinoid form of polyparaphenylene.

Polaron    A quasiparticle composed of a charge which is screened by the surrounding atoms. Because of this, the surrounding atoms are no longer at their equilibrium positions—the polymer backbone is distorted.

Bipolaron    Two polarons sharing the same geometric distortion.

Figure 2.7: Schematic of the formation of polarons and bipolarons on a P3HT chain upon doping.
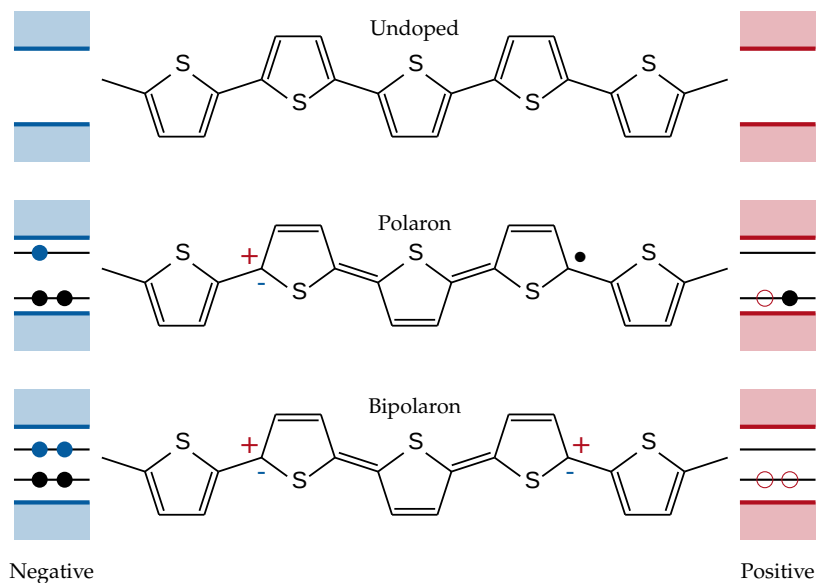


band gap, as illustrated on the right side in Figure 2.7, while for a negative polaron, there will be a surplus electron on the chain. The completely empty or filled bipolaron states lie further into the band gap, because two charges can share the same geometric defect. Like solitons, (bi)polarons are delocalized over several repeat units, with the associated gradual change of bond-length alternation. Polarons are formed if the residence time of the charge carrier is larger than the typical time for vibrational relaxation. Only then the polymer chain has time to adapt to the new electronic density that is due to the doped charge. This charge carrier then has trapped itself in the local defect it created.

Charge transport then takes place by hopping between these localized polaronic states [BC12]. Because the highest occupied molecular orbital and the lowest unoccupied molecular orbital are still completely filled and empty respectively, transport behavior is not metallic. Only for very high doping levels—due to broadening—the bipolaron states form bands, which may overlap with the HOMO and LUMO, resulting in a half filled band that exhibits metallic conduction.

The amount of dopant used can then be as high as tens of mol% per polymer repeat unit, which is of a completely different scale than in the case of doping in inorganic semiconductors. Still, because the effect—an increase of the electrical conductivity—is the same, both processes are referred to as doping, even though the details differ considerably. A good introduction to polarons and bipolarons can be found in [BS85].

TYPES OF DOPING   Conjugated materials are not conductive by themselves, but they can be doped in a variety of ways, increasing their conductivity from the level of insulators to near metallic levels. The discovery of doped polyacetylene—the first of these "synthetic metals"—in the late 1970s, was awarded the Nobel prize in chemistry in 2000 [Shi01] [Mac01] [Hee01].

[BC12] Olga Bubnova et al.
*Energy Environ. Sci.* **5**, 9345 (2012)

[BS85] Jean Luc Bredas et al.
*Acc. Chem. Res.* **18**, 309 (1985)

[Shi01] Hideki Shirakawa.
*Angew. Chemie Int. Ed.* **40**, 2574 (2001)

[Mac01] Alan G. MacDiarmid.
*Angew. Chemie Int. Ed.* **40**, 2581 (2001)

[Hee01] Alan J. Heeger.
*Rev. Mod. Phys.* **73**, 681 (2001)

Several methods exist, that allow to increase the charge carrier density and which may be referred to as doping:

- Chemical doping
  - Redox doping
  - Acid–base doping
- Electrochemical doping
- Charge injection from contacts
- Photogeneration of charges
- Field effect doping

REDOX DOPING  Doping can proceed by way of a redox reaction, where an electron is completely or partly exchanged between dopant and the doped material, forming an ion pair or a charge transfer complex respectively. Classic oxidants are for example iodine or iron chloride which accept electrons and p-dope, leaving a delocalized hole on the conjugated material. There are fewer effective n-type dopants, since the donated electrons in the LUMO are very reactive and prone to oxidation. One traditional example is lithium.  For redox doping to be effective, it has to be energetically favorable, which necessitates a certain offset between the respective HOMO and LUMO levels, as sketched in Figure 2.8 Atmospheric oxygen may act as p-type dopant, which is why most organic semiconductors exhibit dominant p-type conductivity if exposed to air.



Figure 2.8: Illustration of p- and n-type doping.

ACID–BASE DOPING  Another way to chemically dope is in an acid–base reaction, where an ion is exchanged instead of only an electron.

In both cases, the charges in the doped material are stabilized by oppositely charged counterions, which maintain charge neutrality. Because these counterions have to be incorporated in the material, a change in crystalline structure can be observed, as is the case for $F_4TCNQ$ and P3HT [DWA+13].  However, this incorporation may negatively affect the mechanical properties of conjugated polymers, making them brittle, due to a more rigid backbone, as is the case for P3HT doped with $FeCl_3$ [BDC+13].  Another possible issue may be the formation of insoluble polymer–dopant complexes, that hinder processing [DWA+13].

[DWA+13] Duc T. Duong et al. *Org. Electron.* **14**, 1330 (2013)

[BDC+13] Celine Bounioux et al. *Energy Environ. Sci.* **6**, 918 (2013)

ELECTROCHEMICAL DOPING  When immersed in an electrolyte, and by applying a voltage between the conjugated material and a counter electrode, ions diffuse into the material, to balance the extra charge due to the applied voltage. This way, the doping level can be controlled with great precision, however, doping may not be stable once the voltage is removed.

CHARGE INJECTION FROM CONTACTS  In organic light emitting diodes, charges are injected at the contacts by applying a sufficiently high voltage to overcome the Schottky barrier.

PHOTOGENERATION OF CHARGES  In solar cells and photodetectors [BBN+13], free electron–hole pairs are created by exciting carriers to the conduction band, using light of a sufficient wavelength.
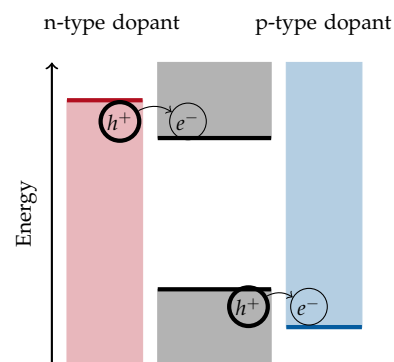
[BBN+13] Kang Jun Baeg et al. *Adv. Mater.* **25**, 4267 (2013)

**Secondary doping** Increase of $\sigma$ due to changes in morphology or crystallinity and not due to an increase in $n$. This increase remains even after the removal of the secondary dopant.

[KSM+11] Yong Hyun Kim et al. *Adv. Funct. Mater.* **21**, 1076 (2011)

[TMF+12] Takumi Takano et al. *Macromolecules*, **45**, 3859 (2012)

[WMN+13] Qingshuo Wei et al. *Adv. Mater.* **25**, 2831 (2013)

[LWL+15] Jun Liu et al. *Macromolecules*, **48**, 585 (2015)

[ME94] Alan G. MacDiarmid et al. *Synth. Met.* **65**, 103 (1994)

[ME95] Alan G. MacDiarmid et al. *Macromol. Symp.* **98**, 835 (1995)

**DP Degree of polymerization** Number of monomers in a polymer chain.

$M_\mathrm{n}$ **Number average molecular weight** For a given molecular weight distribution, the *number* of molecules above and below $M_\mathrm{n}$ are equal.

$M_\mathrm{w}$ **Weight average molecular weight** For a given molecular weight distribution, the *weight* of molecules above and below $M_\mathrm{w}$ is equal.

FIELD EFFECT DOPING   In field effect transistors, the distribution of charges in a channel can be controlled locally by a gate voltage.

SECONDARY DOPING   Another way to increase the electrical conductivity is by increasing the charge carrier mobility instead of increasing the charge carrier density. This can be achieved by changing the nanostructure of the material, by for example influencing molecular ordering, or the number of grain boundaries by post-treatments with solvents in the case of PEDOT:PSS [KSM+11] [TMF+12] [WMN+13] [LWL+15]. This effect has been termed secondary doping [ME94] [ME95]. Importantly, because it is morphological in nature, it persists even after the removal of secondary dopant.

## 2.3. Conjugated Polymers

Besides $\pi$-conjugation, the polymers used in this thesis have other important characteristics, that influence the final film properties, and which will be mentioned here briefly.

MOLECULAR WEIGHT   Polymers are not monodisperse, which means that not all molecules are identical. Instead the degree of polymerization of the backbone varies significantly around an average value. There are different ways to quantify the molecular weight, used in different circumstances.

The number average molecular weight is the adequate parameter when the physical properties only depend on the number of molecules in the sample, as may be the case for chemical reactions that only take place at the end of polymer chains. It is defined as

$$M_\mathrm{n} = \frac{\sum_i N_i M_i}{\sum_i N_i} \tag{2.1}$$

where $N_i$ is the number of polymers with an exact molecular weight $M_i$. To understand the name, this can be written slightly differently, using the number fraction (or mole fraction),

$$x_i = \frac{N_i}{\sum_i N_i} \tag{2.2}$$

which is just the fraction of the number of molecules with a particular weight divided by the total number of molecules. With this (2.1) becomes

$$M_\mathrm{n} = \sum_i x_i M_i \tag{2.3}$$

The weight average molecular weight, defined in (2.4), is important for properties that depend on the molecular size, such as light scattering.

$$M_\mathrm{w} = \frac{\sum_i N_i M_i^2}{\sum_i N_i M_i} \tag{2.4}$$

Similarly, it can be rewritten using the weight fraction of polymer $i$, which is just the weight of polymer $i$ divided by the total weight.

$$w_i = \frac{N_i M_i}{\sum_i N_i M_i} \tag{2.5}$$

Using this, (2.4) can be rewritten just like (2.1).

$$M_\text{w} = \sum_i w_i M_i \tag{2.6}$$

Comparing (2.6) to (2.3), the names should become clear. Both of them are sums of the constituent molecular weights. But whereas in the first case, the weight of each summand is the number fraction, in the second case it is the weight fraction.

The dispersity is defined as

$$Đ = \frac{M_\text{w}}{M_\text{n}} \tag{2.7}$$

By definition Đ is always larger than 1, with Đ = 1 corresponding to a completely monodisperse material.

Đ Dispersity   Measure of the spread of a molecular weight distribution.

|          | $M_\text{w}$ | Đ   | $l$ | DP |
|----------|--------------|-----|------------|-----------------|
| PE       | 6 MDa        |     | 60 µm      | $2 \times 10^5$ |
| PS       |              | 1.1 |            |                 |
| P3HT     | 50 kDa       | 2   | 120 nm     | 300             |
| PFO      | 100 kDa      | 3   |            | 250             |
| PCPDTBT  | 20 kDa       |     |            | 40              |
| PCDTBT   | 30 kDa       | 2   |            | 40              |
| PEDOT    | 2 kDa        |     |            | 14              |

Table 2.1: Molecular weight $M_\text{w}$, dispersity Đ, extended chain length $l$ and degree of polymerization DP for some example polymers.

For illustrative purposes, some examples are given in Table 2.1. Typical conjugated polymers have a lower degree of polymerization and a larger dispersity than nonconductive polymers. At the same time, their monomers are significantly larger. Molecular weight has a strong effect on the charge transport properties of conjugated polymers [KRF+13].

[KRF+13] Felix Peter Vinzenz Koch et al.
*Prog. Polym. Sci.* **38**, 1978 (2013)

PERSISTENCE LENGTH   The concept of persistence length is used to quantify the mechanical flexibility of polymer chains.

$$\langle \cos\theta \rangle = \text{e}^{-\frac{L}{P}} \tag{2.8}$$

$P$ Persistence length   Measure of the stiffness of a polymer chain, below which a single polymer molecule can be treated as an elastic rod.

Here $\theta$ is the change in direction between two points on the chain that are separated by a distance $L$, and $\langle \ldots \rangle$ denotes the average over all pairs of points. For example, for a large persistence length $P \gg L$ the chain behaves as a rigid rod, and $\theta$ will barely change along the length of the chain.

SIDE CHAINS   To make conjugated polymers sufficiently soluble, they are functionalized with alkyl side-chains. These side-chains are insulating and have a strong effect on polymer crystallinity due to their bulkiness. Furthermore, the glass transition and melting temperatures of the polymer decreases with increasing alkyl side-chain length.



Figure 2.9: Illustration of the different ways to couple asymmetric monomers.

RR Regioregularity   Measure for the degree of order along a polymer chain that is composed of asymmetric monomers.

REGIOREGULARITY   In asymmetric polymers like P3HT, the relative arrangement of the side-chains is also important.Two monomers of a polymer chain, can be coupled in a head-to-head or a head-to-tail manner, as sketched in Figure 2.9. A polymer with the highest regioregularity of 1 has all the side-chains pointing in the same direction. A regiorandom polymer on the other hand has an equal number

[KCT+06] Youngkyoo Kim et al. *Nat. Mater.* **5**, 197 (2006)

**$\pi$–$\pi$-stacking**   Attractive interaction due to $\pi$-orbital overlap between adjacent aromatic rings.

[ÖAJ+00] Ronald Österbacka et al. *Science*, **287**, 839 (2000)

[Bri11] Martin Brinkmann. *J. Polym. Sci. Part B Polym. Phys.* **49**, 1218 (2011)

of head-to-head and head-to-tail links, that are randomly distributed. Regioregularity has been shown to strongly influence OPV device performance in P3HT:PCBM bulk heterojunctions [KCT+06]. Higher RR was shown to result in better $\pi$–$\pi$-stacking, which in turn improves both charge transport and absorption. Similarly, electronic excitations in regiorandom P3HT were found to only extend along the one-dimensional backbone. In regioregular P3HT however, the polarons show two-dimensional delocalization, with the additional direction along $\pi$–$\pi$-stacked monomers [ÖAJ+00].

SEMI-CRYSTALLINITY   While regiorandom polymers tend to be amorphous due to their intrinsic disorder, there are comparably crystalline polymers. Above a certain length, polymer chains may fold back upon themselves, forming lamellar crystallites. These are not perfect crystals however, mainly due to entangled chains and the dispersity of the polymer. Even in the best, most crystalline case therefore, these crystalline nanofibrils are embedded in a matrix of their own amorphous chain ends and entangled chains [Bri11]. In these polymers, the amount of crystallinity can be tuned from completely amorphous to a semi-crystalline state. For example, by decreasing the amount of time available for crystallization, by rapidly quenching from the melt or by quickly evaporating the solvent, a more amorphous state of an otherwise crystalline material can be obtained.

Figure 2.10 shows the three crystallographic unit vectors using the example of P3HT.



Figure 2.10: Crystallographic unit vectors of a P3HT crystallite.

- The inter-chain distance $a$ or [100] points along the alkyl side-chains.
- The inter-plane distance $b$ or [010] points along the $\pi$–$\pi$-stacking direction.
- And the inter-lamellar distance $c$ or [001] points along the polymer backbone.

In thin films, the texture of crystallites, that is their preferential orientation with respect to the substrate, is mostly either face-on or edge-on, as sketched in Figure 2.11. The third possibility is observed less commonly, for example for very low molecular weight polymers. In the literature, it is known both as end-on and flat-on.

Figure 2.11: Sketch of possible crystalline textures.
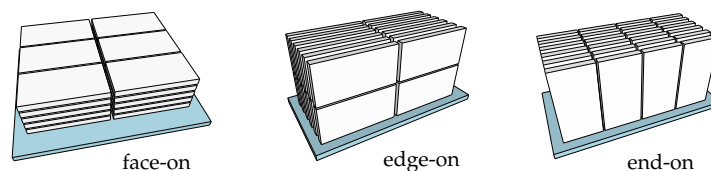


face-on          edge-on          end-on

**Spherulite**   A semicrystalline region of material with spherical, or in two dimensions circular shape.

SPHERULITES   Nanoscopic fibrillar polymer crystallites can organize into larger, even macroscopic superstructures. A particular type of polycrystalline superstructure, observed in semicrystalline polymers, are spherulites. Figure 2.12 shows an example micrograph of such a spherulite. The crystallization starts from an initial random seed, and proceeds in radial direction, all the while branching out and filling the available space. Spherulites are an ubiquitous phenomenon, that can be observed in a wide range of materials. For an extensive review of the phase-field models used to phenomenologically

describe their formation, see [GRS+14]. During the nonequilibrium growth process, single crystal growth is disturbed by "secondary nucleation" or "growth front nucleation" [GPB+04]. Three different types of disturbances can all lead to the same polycrystalline spherulites [GPT+05]:

1. Static heterogeneities, or disorder in the form of impurities. For polymeric materials, the dispersity has a similar effect. Because of the impurity, a new crystal grain forms, that takes its orientation from the impurity, rather than the original crystal.
2. Dynamic heterogeneities, such as those that occur in molecularly pure, heavily supercooled liquids. In this situation, the rotational diffusion coefficient may be orders of magnitude smaller than the translational diffusion coefficient. Then, the reorientation of molecules is slow, compared to the speed of the growth front, and consequently, the molecules will have difficulties aligning with the original crystal.
3. Noncrystallographic branching with a preferred misorientation angle, which can explain many of the morphologies observed in polymers.

In the absence of any of these disturbances, one would expect the growth of perfect crystals, or if far from equilibrium, of symmetric dendrites, such as snowflakes.

Two types of spherulites can be distinguished:

*Category I*  These spherulites grow radially, while branching out to fill the available space.
*Category II*  These spherulites start growing anisotropically, as elongated needles that splay and branch at their tips until covering all of the available space as well. This type may develop two "eyes" that are not crystalline, one on each side of the initial nucleation site.

Regardless of the underlying symmetry of the crystal, spherulites form if the disorder and the driving force are sufficiently large. Because of their circular shape, which contains all possible fiber orientations in the plane, spherulites are an attractive system to probe orientation-dependent electrical and optical properties. Conventional deposition techniques such as spin- and blade-coating usually result in isotropic layers with a random orientation of the crystalline lamellae down to the microscopic scale. This is caused by the immense density of nucleation sites and the resulting uncontrolled growth. Using solvent vapor annealing, this density can be tuned [SL17]. By a judicious control of solvent partial pressure, the nucleation density in P3HT films can be controlled accurately by nearly completely dissolving and then regrowing the film [CRR+11]. This allowed to probe the charge transport along and across of P3HT fibrils [CTF+12]. Spherulites are not limited to polymers though, and exist in many different materials. For example, by changing the surface energy of part of the substrate, it was demonstrated that the growth of small-molecule spherulites can be controlled, in effect guiding the direction of crystallization—and the molecular orientation—around corners [LTS+12].

[GRS+14] László Gránásy et al. *Metall. Mater. Trans. A*, **45**, 1694 (2014)

[GPB+04] László Gránásy et al. *Nat. Mater.* **3**, 645 (2004)

[GPT+05] László Gránásy et al. *Phys. Rev. E*, **72**, 011605 (2005)

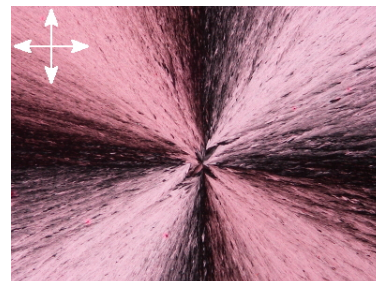Figure 2.12: Transmission micrograph of a P3HT spherulite displaying the characteristic Maltese cross pattern between crossed polarizers.

[SL17] Gisela L. Schulz et al. *Adv. Funct. Mater.* **27**, 1603083 (2017)

[CRR+11] Edward Crossland et al. *Adv. Funct. Mater.* **21**, 518 (2011)

[CTF+12] Edward Crossland et al. *Adv. Mater.* **24**, 839 (2012)

[LTS+12] Stephanie S. Lee et al. *Adv. Mater.* **24**, 2692 (2012)

## 2.4. Carbon Allotropes

Besides conjugated polymers, there are other electrically conductive organic materials, which are based on graphene and its extended system of delocalized $\pi$-electrons.
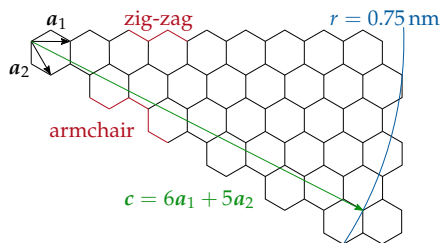


Figure 2.13: Example CNT chiral vector for a $(6, 5)$ tube.

CARBON NANOTUBES    The structure of carbon nanotubes is that of a rolled up sheet of graphene. Depending on the chiral vector $c$, along which the CNTs are rolled up, they have different properties. Using the unit vectors of the hexagonal lattice defined in Figure 2.13, the chiral vector is written as

$$c = na_1 + ma_2 \tag{2.9}$$

The length of the chiral vector $|c|$ then is the circumference of the rolled up nanotube. If $n = m$, the resulting nanotube is called an "armchair" nanotube, and if $m = 0$, it is referred to as a "zig-zag" tube, named for the shape of the visible edge at the open ends of the tube. Both of these classes of nanotubes are achiral. All other possible combinations $(n, m)$ are chiral. It should be noted that Figure 2.13, which is the typical way to represent $c$, only maps one chiral type, and is not including tubes with the opposite handedness.

SWCNT Single-walled carbon nanotube

ELECTRICAL CONDUCTIVITY    One third of single-walled carbon nanotubes exhibit metallic electrical conductivity, while the rest are semiconductors.

- All armchair tubes $(m = n)$ do not have a band gap and show metallic behavior.
- Tubes are semi-metallic for $m - n = 3i$ for $i \in \mathbb{N}$.
- All other tubes are semiconductors with a significant band gap, the size of which is inversely proportional to the diameter of the tube [KKM+99].

[KKM+99] Hiromichi Kataura et al. *Synth. Met.* **103**, 2555 (1999)

There are expected to be deviations from this general rule for small diameter nanotubes, such as $c \leq (5, 0)$.

[CHT+13] Qing Cao et al. *Nat. Nanotechnol.* **8**, 180 (2013)

[KFZ+00] Jing Kong et al. *Science*, **287**, 622 (2000)

A single metallic CNT has a resistance of about $270\,\mathrm{k\Omega}$ per micrometer length [CHT+13], while values between $300\,\mathrm{k\Omega}$ and $5\,\mathrm{M\Omega}$ were observed for semiconducting single-walled carbon nanotubes [KFZ+00].

Because CNTs are quasi one-dimensional conductors, their density of states has sharp Van Hove singularities as sketched in Figure 2.14.

As their name implies, multi-walled carbon nanotubes consist of several layers. They generally have a larger diameter than SWCNTs and are mostly metallic, since a single metallic layer will dominate the behavior of the whole tube.
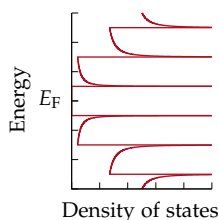


Figure 2.14: van Hove Singularities in the 1D density of states of SWCNTs

MWCNT Multi-walled carbon nanotube

[LWG+17] Bilu Liu et al. *ACS Nano*, **11**, 31 (2017)

PROCESSING    While there have been significant improvements in the past [LWG+17], CNTs still cannot be synthesized chirally pure. Instead, a wide range of methods exists to separate metallic from semiconducting tubes, or even to select tubes of a distinct chirality.

Semiconducting single-walled carbon nanotubes can be extracted from an as-synthesized mixture, by selectively dispersing only semi-

conducting tubes with the help of conjugated polymers like poly-thiophenes or polyfluorenes [NHD+07], using bad solvents in which CNTs would not disperse otherwise, like toluene or xylene [SFS+14]. Besides the type of polymer, the efficiency and selectivity to particular CNT chiralities depends on a variety of factors, such as the molecular weight of the polymer [JSM+12], the length and type of side chains [LYP+11] [GCC+13], or the processing temperature [GSD+15]. Density functional theory calculations have shown that the diameter selectivity is due to a competition between bundling of CNTs and adsorption of polymer onto the CNT surface [YBK+15].

Another separation method uses the fact that metallic CNTs oxidize more readily. By properly adjusting the pH of a CNT dispersion, it is possible to separate metallic from semiconducting tubes due to their opposite surface charge [WNC+16]

A potentially scalable approach to selectively disperse nanotubes employs the successive use of chirally selective and diameter selective surfactants [YTZ+16]. Another approach uses an H-bonded supramolecular polymer based on a fluorene unit with long side chains [PWF+15]. The fluorene unit selectively wraps semiconducting CNTs, allowing to disperse them in solvents, while metallic tubes remain undissolved. The degree of polymerization can be tuned by disrupting the hydrogen bonds, allowing to turn the interaction on and off on demand. This allows to obtain pure semiconducting single-walled carbon nanotubes without any metallic CNTs as well as without any remaining polymer. On the other hand, the monomers can be reused. A similar approach uses a fluorene based polymer built from imine-bonds, which can be easily depolymerized [LCP+16].

If one wants to disperse and debundle CNTs without the use of surfactants, then the CNTs have to be functionalized with solu-bilizing groups, which negatively affects their electronic properties. The only solvents, which can truly dissolve CNTs, are su-peracids like >100 % sulfuric acid, or chlorosulfonic acid, which works best [RED+04] [DPG+09].

FULLERENES Besides carbon nanotubes, which correspond to a one dimensional form of the hexagonal graphene lattice, there exists a zero dimensional class, the fullerenes. Composed of six- and five-membered rings arranged like the white and black patches on a football, $C_{60}$ is the most well-known one. This basic unit can be modified by adding solubilizing groups, like in the case of [6,6]-phenyl $C_{61}$ butyric acid methyl ester [HKL+95], allowing for simple solution processing. Fullerenes with a larger number of carbon atoms also exist, like $PC_{70}BM$, which due to its asymmetric shape, has more allowed optical transitions and an absorption that is redshifted with respect to PCBM, which is useful for increasing light absorption in OPV devices.

Fullerene-based materials make up the great majority of acceptor materials used in organic photovoltaics, due to their favorable energy-level alignment and good electron conductivity. However, in recent times, new classes of small-molecule acceptors with higher morpho-logical stability are being developed [BAH+16].

[NHD+07] Adrian Nish et al.
*Nat. Nanotechnol.* **2**, 640 (2007)

[SFS+14] Suman Kalyan Samanta et al.
*Acc. Chem. Res.* **47**, 2446 (2014)

[JSM+12] Florian Jakubka et al.
*ACS Macro Lett.* **1**, 815 (2012)

[LYP+11] Hang Woo Lee et al.
*Nat. Commun.* **2**, 541 (2011)

[GCC+13] Widianta Gomulya et al.
*Adv. Mater.* **25**, 2948 (2013)

[GSD+15] Widianta Gomulya et al.
*Carbon*, **84**, 66 (2015)

[YBK+15] Hongliu Yang et al.
*ACS Nano*, **9**, 9012 (2015)

[WNC+16] Jing Wang et al.
*ACS Nano*, **10**, 3222 (2016)

[YTZ+16] Yohei Yomogida et al.
*Nat. Commun.* **7**, 12056 (2016)

[PWF+15] Igor Pochorovski et al.
*J. Am. Chem. Soc.* **137**, 4328 (2015)

sc-SWCNT Semiconducting single-walled carbon nanotube

[LCP+16] Ting Lei et al.
*J. Am. Chem. Soc.* **138**, 802 (2016)

[RED+04] Sivarajan Ramesh et al.
*J. Phys. Chem. B*, **108**, 8794 (2004)

[DPG+09] Virginia A. Davis et al.
*Nat. Nanotechnol.* **4**, 830 (2009)
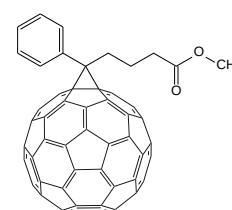
PCBM
[6,6]-phenyl $C_{61}$ butyric acid methyl ester A soluble fullerene, widely used as acceptor material.

[HKL+95] Jan C. Hummelen et al.
*J. Org. Chem.* **60**, 532 (1995)

[BAH+16] Derya Baran et al.
*Nat. Mater.* **16**, 363 (2016)

[SWF+00] Henning Sirringhaus et al.
*Appl. Phys. Lett.* **77**, 406 (2000)

[KPT+06] Theo Kreouzis et al.
*Phys. Rev. B*, **73**, 235201 (2006)

[SHT+10] Sheng Shen et al.
*Nat. Nanotechnol.* **5**, 251 (2010)

[JTM+09] Leslie H. Jimison et al.
*Adv. Mater.* **21**, 1568 (2009)

[LCD+13] Alessandro Luzio et al.
*Sci. Rep.* **3**, 3425 (2013)

[KJP+15] Nam-Koo Kim et al.
*Chem. Mater.* **27**, 8345 (2015)

[MFS+14] Nicola Martino et al.
*ACS Nano*, **8**, 5968 (2014)

[TMF+12] Takumi Takano et al.
*Macromolecules*, **45**, 3859 (2012)

[KKL+14] Nara Kim et al.
*Adv. Mater.* **26**, 2268 (2014)

[GB99] Martin Grell et al.
*Adv. Mater.* **11**, 895 (1999)

[ZKY11] Rui Zhu et al.
*Adv. Mater.* **23**, 4193 (2011)

[RAS+16] S. Gupta Roy et al.
*Opt. Express*, **24**, 14737 (2016)

[MGC12] Christian Müller et al.
*Appl. Phys. Lett.* **101**, 171907 (2012)

[BHB+14] Martin Brinkmann et al.
*Macromol. Rapid Commun.* **35**, 9 (2014)

[DG92] Peter Dyreklev et al.
*Solid State Commun.* **82**, 317 (1992)

[OKC+11] Brendan T. O'Connor et al.
*Adv. Funct. Mater.* **21**, 3697 (2011)

[HY95] Maki Hamaguchi et al.
*Appl. Phys. Lett.* **67**, 3381 (1995)

[VAB+12] Varun Vohra et al.
*J. Phys. Chem. Lett.* **3**, 1820 (2012)

[SHD+16] Leo Shaw et al.
*ACS Appl. Mater. Interfaces*, **8**, 9285 (2016)

[PPG+15] Steve Park et al.
*Adv. Mater.* **27**, 2656 (2015)

[DTG+13] Ying Diao et al.
*Nat. Mater.* **12**, 665 (2013)

[SSH+12] Robert Steyrleuthner et al.
*J. Am. Chem. Soc.* **134**, 18303 (2012)

[BLG+15] Sadir Gabriele Bucella et al.
*Nat. Commun.* **6**, 8394 (2015)

[DMN+12] Arnaud Dauendorffer et al.
*Appl. Phys. Express*, **5**, 092101 (2012)

[CHT+13] Qing Cao et al.
*Nat. Nanotechnol.* **8**, 180 (2013)

[SMO+14] Junshi Soeda et al.
*Adv. Mater.* **26**, 6430 (2014)

## 2.5. Orientation

Alignment along one direction has been employed to understand inter- and intra-chain transport in conjugated polymers [SWF+00] [KPT+06]. Alignment affects properties like the thermal conductivity [SHT+10], the charge carrier mobility [JTM+09] [LCD+13] [KJP+15] [MFS+14] and the electrical conductivity [TMF+12] [KKL+14]

On the other hand, novel types of devices can be created from oriented films, that exhibit polarized emission [GB99] or absorption [ZKY11] [RAS+16] and hidden security features only visible with polarized illumination [MGC12].

As a consequence, a variety of methods have been developed to manipulate and control the microstructure and the orientation of conjugated polymers [BHB+14].

STRETCHING   By stretching films of polymers, their backbones take on a more extended conformation, aligning in the stretching direction [DG92] [OKC+11] [MGC12].

RUBBING   Similarly, by repeatedly rubbing a polymer film above the glass transition temperature, the chains align in the rubbing direction [HY95] [ZKY11] [VAB+12].

COATING   Using solution shearing, a deposition process at speeds below $1 \, \text{mm} \, \text{s}^{-1}$ that is similar to blade coating, allowed to align polymers [SHD+16]. By further engineering the wettability of the substrate, it was possible to align CNTs [PPG+15] or even deposit single-crystalline films of small-molecule materials [DTG+13].

The commercially available n-type polymer P(NDI2OD-T2) is known to aggregate in solution [SSH+12]. However, it was shown that this is not necessarily bad, and instead can be used to orient the polymer chains during deposition by bar-coating, when depositing from a solvent that favors aggregation [BLG+15]. In this case, a large anisotropy in charge carrier mobility was measured, far surpassing the level of optical anisotropy. This shows that even small amounts of oriented material can result in big changes in charge carrier mobility.

LIQUID SUBSTRATES   Aligned films of conjugated polymers or CNTs can be prepared using an intermediate step. The solution is deposited onto a high surface tension liquid such as water or an ionic liquid, which serves as a temporary substrate. The liquid crystalline PFO was shown to align itself simply due to the high mobility of the solvent on the liquid substrate [DMN+12]. The film may also be compressed after evaporation of the solvent, introducing alignment by the application of an external force in the case of CNTs [CHT+13], or polymers [SMO+14]. Afterwards, the films are transferred to a regular substrate in one of two ways. By immersing a rigid substrate vertically in the high surface tension liquid, the film is transferred gradually from one to the other—the Langmuir-Blodgett method. If the rigid substrate is placed horizontally, and all of the film is transferred at once, then the method is known as Langmuir-Schaefer.

SPINNING   The simplest way to align CNTs takes advantage of the strong van der Waals forces between tubes. Simply by pulling on CNT "forests", long CNT yarns can be spun [ZAB04].

CNTs have been oriented into threads of any desired length by wet spinning of ribbons, that are washed and dried afterwards [VPC+00]. This method has been improved upon, by forgoing the use of surfactants, and instead using superacids like chlorosulfonic acid as the solvent [EFP+04]. Additionally, the fibers are stretched as they are spun, resulting in higher orientation and density, which in turn gives rise to large values for both the electrical and thermal conductivity, as well as the tensile strength [BYT+13].

Direct spinning during chemical vapor deposition synthesis is another way to orient CNTs [LKW04], resulting in extraordinary toughness [KVM+07]. Hereby, the aerogel of entangled CNTs that is formed in the reactor during synthesis is gradually pulled out. Kilometer-long fibers made up of bundles of $\approx 1\,\text{mm}$ long CNTs can be prepared this way. The particular type of CNTs, ranging from single-walled to collapsed double-walled, to multi-walled, can be controlled by the ratio of sulphur to carbon in the feedstock [RAM+14]. By drawing these fibers as they exit the reactor, the CNTs are uniaxially aligned due to frictional shear forces at the interface with the surrounding gas [ARM+15]. Further densifying these fibers by capillary forces does not prove efficient, as no significant influence on the electrical and mechanical properties of these fibers was observed.

The method adopted in this thesis to orient films of conjugated polymers directly from solution, is based on directional epitaxial crystallization [BW06]. It will be presented in detail in Chapter 7: Oriented Polymer Layers.

[ZAB04] Mei Zhang et al.
*Science*, **306**, 1358 (2004)

Wet spinning   Extrusion of a solution through a pinhole into a high viscosity, laminar flowing second liquid, in which the solvent is soluble, but the dissolved material is not. The dissolved material aligns itself to the flow, and coagulates due to the new environment.
[VPC+00] Brigitte Vigolo et al.
*Science*, **290**, 1331 (2000)

[EFP+04] Lars M. Ericson et al.
*Science*, **305**, 1447 (2004)

[BYT+13] Natnael Behabtu et al.
*Science*, **339**, 182 (2013)

CVD Chemical vapor deposition   A process that uses volatile precursors in the gas phase, that react to form a product.
[LKW04] Ya-Li Li et al.
*Science*, **304**, 276 (2004)

[KVM+07] Krzysztof Koziol et al.
*Science*, **318**, 1892 (2007)

[RAM+14] Víctor Reguero et al.
*Chem. Mater.* **26**, 3550 (2014)

[ARM+15] Belén Alemán et al.
*ACS Nano*, **9**, 7392 (2015)

[BW06] Martin Brinkmann et al.
*Adv. Mater.* **18**, 860 (2006)

# ORGANIC THERMOELECTRICS

<span style="float:right">3</span>

This chapter will present an emerging area of interest for the application of organic materials—the field of organic thermoelectricity.

## 3.1. Thermoelectricity

An intuitive understanding of thermoelectricity can be gained by thinking of the free charge carriers as a gas that is being heated. Particles on the hot side, diffuse farther than those on the cold side, due to their higher kinetic energy or their longer mean free path—comparable to a difference in "pressure". This leads to a buildup of particles at the cold side, which in turn results in increased diffusion in the opposite direction, this time caused by the difference in density. Naturally, in the steady state both effects balance out, as sketched in Figure 3.1. Since the particles are charged, a resulting voltage can be measured. The sign of the voltage at the cold side with respect to the hot side will depend on the sign of the majority charge carriers—positive for holes, and negative for electrons.

Introductions to thermoelectricity of organic materials can be found in [KMK+16] and [RGU+16]. In a nutshell, a good thermoelectric material needs to have a high Seebeck coefficient and a high electrical conductivity, while maintaining a low (lattice) thermal conductivity. This has been succinctly put as "phonon-glass and electron-crystal" [BMN15], emphasizing the role that molecular order plays in determining these properties.

**Thermoelectricity** Conversion of heat directly into electricity, and vice versa.



Figure 3.1: Sketch illustrating the thermoelectric effect.

[KMK+16] Renee Kroon et al.
*Chem. Soc. Rev.* **45**, 6147 (2016)

[RGU+16] Boris Russ et al.
*Nat. Rev. Mater.* **1**, 16050 (2016)

[BMN15] Matt Beekman et al.
*Nat. Mater.* **14**, 1182 (2015)

## 3.2. Important Parameters

SEEBECK COEFFICIENT  The Seebeck coefficient, defined in (3.1), relates a temperature difference $\Delta T = T_{\text{hot}} - T_{\text{cold}}$ across a slab of material with the gradient of electric potential—the voltage $\Delta V$—across the slab.

$$S = \frac{\Delta V}{\Delta T} \tag{3.1}$$

For $\Delta V > 0$, which implies a positive $S$, one talks about a p-type material, since the majority of moving charges are holes. In the opposite case, the material is called n-type. Historically, this effect has been described in two distinct ways. Either as the Seebeck effect according to (3.1), where an applied temperature gradient causes the voltage; or as the Peltier effect, where the current $I$ flowing across a junction of dissimilar materials, reversibly transports heat $Q$.

$$\Pi = \left. \frac{\frac{\partial Q}{\partial t}}{I} \right|_{\Delta T = 0} \tag{3.2}$$

$S$ Seebeck coefficient  The average amount of entropy transported per charge carrier. Also called the thermopower $\alpha$.

Π Peltier coefficient   The amount of energy, relative to the Fermi energy, that is transported per unit charge.

Table 3.1: Some typical values for the Seebeck coefficient.

| | $S$ [$\mu$V K$^{-1}$] |
|---|---|
| $\frac{k_B}{e}$ | 86.17 |
| Bi$_2$Te$_3$ | $\pm$200 |
| PEDOT | 200 |
| sc-SWCNT | 100 |
| m-SWCNT | 10 |
| Copper, Silver | 1.5 |
| Constantan | $-40$ |

[Fri71] Hellmut Fritzsche.
*Solid State Commun.* **9**, 1813 (1971)

σ Electrical conductivity

Table 3.2: Electrical conductivity for some materials of interest.

| | $\sigma$ [$\Omega^{-1}$ cm$^{-1}$] |
|---|---|
| Silver | $6.2 \times 10^5$ |
| Copper | $5.9 \times 10^5$ |
| Gold | $4.4 \times 10^5$ |
| CNTs | $<1 \times 10^5$ |
| Constantan | $2 \times 10^4$ |
| Bi$_2$Te$_3$ | $1 \times 10^3$ |
| PEDOT | 100 |
| DI water | $5.5 \times 10^{-8}$ |
| Air | $5 \times 10^{-13}$ |
| PE | $1 \times 10^{-14}$ |

μ Charge carrier mobility   Proportionality factor between an applied electric field, and the resulting drift velocity of a charged particle.

[DJ16] Stephen Dongmin Kang et al.
*Nat. Mater.* **16**, 252 (2016)

where the Peltier coefficient can be written as $\Pi = TS$.

A measurement of the Seebeck voltage is always a relative measurement. In a—closed—electric circuit needed for a measurement, the total accumulated heat gradient along the connectors is always zero—for every increase in temperature there will be a corresponding decrease. If the circuit consists of a single material, then the Seebeck voltages along the conductor cancel out exactly. A typical measurement therefore combines a known reference material with the material under test into a junction. Temperature differences are then restricted to this junction, such that the external circuitry cannot contribute with spurious voltages. To get a feeling for the orders of magnitude, a few typical Seebeck coefficients are provided in Table 3.1.

The Seebeck coefficient can be understood as the entropy per unit charge, weighed by the contribution of that charge to the total conductivity [Fri71].

$$S = \frac{k_B}{e} \int \frac{E - E_F}{k_B T} \frac{\sigma(E)}{\sigma} \, dE \qquad (3.3)$$

with $\sigma(E)$, called the conductivity density of states, or differential conductivity, and the conductivity $\sigma = \int \sigma(E) \, dE$. From (3.3) follows that $S$ and $\sigma$ are correlated, with a change in one generally producing a change in the other.

ELECTRICAL CONDUCTIVITY   Consequently, the electrical conductivity is another important parameter. Not only because of its effect on $S$ but also because a useful thermoelectric circuit element should have a low internal resistance. The electrical conductivity is defined as the proportionality constant in Ohm's law, given in (3.4).

$$\boldsymbol{j} = \sigma \boldsymbol{E} \qquad (3.4)$$

It relates an electric field $\boldsymbol{E}$ to the resulting current density $\boldsymbol{j}$. For a rectangular slab of material, it can directly be calculated from its resistance $R$ and its length $l$, width $w$ and height $h$ as given in (3.5).

$$\sigma = \frac{l}{wh} \frac{1}{R} \qquad (3.5)$$

For metallic conduction, the electrical conductivity decreases with increasing temperature due to increased scattering. In semiconductors on the other hand, it increases with temperature, indicating the thermal activation of carriers, or even transport through hopping between localized states. Typical values of $\sigma$ for a few different materials are given in Table 3.2.

CHARGE CARRIER MOBILITY   The commonly used definition of the charge carrier mobility, given in (3.6), relates it to the electrical conductivity and the free carrier concentration $n$.

$$\sigma = |e| n \mu \qquad (3.6)$$

For most organic semiconductors, this definition is not satisfactory, since the number of free charges is hard to define properly. Due to the hopping-type transport between localized or even trapped states, other models may be better suited to describe the charge transport in partly disordered materials [DJ16]. The limiting factor to reach high

$\mu$ in organic materials is the inherent disorder which results in a large number of grain boundaries. For a high $\mu$, a high crystallinity is not sufficient, instead, distinct domains of high charge carrier mobility have to be connected. One way to increase $\sigma$ is then to increase molecular order, facilitating long range charge transport at a high charge carrier mobility. Increasing $\sigma$ this way is termed secondary doping [ME94] [ME95].

[ME94] Alan G. MacDiarmid et al. *Synth. Met.* **65**, 103 (1994)

[ME95] Alan G. MacDiarmid et al. *Macromol. Symp.* **98**, 835 (1995)

CHARGE CARRIER DENSITY   TraditionaI doping increases $\sigma$ by directly increasing the free charge carrier density. While increasing the charge carrier mobility will always result in better thermoelectric performance, this is not the case for the charge carrier density. Because of (3.3), there is an often inverse correlation of $S$ and $\sigma$. Consequently, a trade-off between $S$ and $\sigma$ has to be found, which is achieved for a unique, optimal amount of charge carriers—an optimal amount of doping.

$n$ Charge carrier density   The number of free charge carriers per unit volume.

POWER FACTOR   This optimum is determined by maximizing the power factor $S^2\sigma$. It is used to benchmark the effectiveness—as opposed to the efficiency—of thermoelectric materials. When looking for the largest obtained effect, irrespective of the cost in terms of input, then the power factor is the correct parameter to consider. For example, for a fixed temperature difference—that is for infinite heat reservoirs—a thermoelectric generator with twice the power factor will provide twice the output power. In the case of a peltier cooler, a higher power factor will allow to reach higher temperature differences between the hot and the cold sides of the device if sufficient current is supplied. Table 3.3 lists some typical values for the power factor of thermoelectric materials.

$S^2\sigma$ Power factor

Table 3.3: Thermoelectric power factors for some typical materials.

| | $S^2\sigma$ [$\mu\mathrm{W\,m^{-1}\,K^2}$] |
|---|---|
| $Bi_2Te_3$ | 4770 |
| Constantan | 3200 |
| sc-SWCNT | 340 |
| PEDOT-Tos | 300 |
| Copper | 134 |

To understand why this particular combination of $S$ and $\sigma$ delivers the largest effect, consider the power $P$, that is transferred from a source with resistance $R_{source}$ to a load with resistance $R_{load}$, where the thermoelectric generator can be either one. Assuming a fixed amount of power generated by a source with finite resistance $R_{source}$, the maximum power is transferred to the load if $R \equiv R_{load} = R_{source}$. Then

$$P = VI = \frac{V^2}{4R} \propto S^2\sigma, \qquad (3.7)$$

since $V \propto S$ and $R \propto \frac{1}{\sigma}$.

THERMAL CONDUCTIVITY   The description of thermoelectricity cannot be complete by only considering infinite thermal reservoirs. Instead, the thermal conductivity of the thermoelectric element connecting finite reservoirs has to be considered. $\kappa$ appears as a constant in Fourier's law of heat conduction given in (3.8), which relates the heat flux density $\boldsymbol{q}$ to a gradient in temperature.

$\kappa$ Thermal conductivity

$$\boldsymbol{q} = -\kappa \boldsymbol{\nabla} T \qquad (3.8)$$

This flux of heat has to be minimized, since it will decrease the temperature difference between the reservoirs. Heat is transported by moving electric charges as well as by vibrations of the lattice—phonons. The thermal conductivity therefore has both an electronic and a lattice contribution.

$$\kappa = \kappa_{ph} + \kappa_{el} \qquad (3.9)$$

[LHY+17] Sangwook Lee et al. *Science*, **355**, 371 (2017)

Although exceptions have been reported [LHY+17], in inorganic semi-conductors and metals, the electronic contribution $\kappa_{\mathrm{el}}$ is generally related to $\sigma$ according to the Wiedemann-Franz law, given in (3.10).

$$\frac{\kappa_{\mathrm{el}}}{\sigma} = LT \tag{3.10}$$

Table 3.4: $\kappa_{\mathrm{el}}$ according to the Wiedemann-Franz law at 300 K.

| $\sigma$ [$\Omega^{-1}\,\mathrm{cm}^{-1}$] | $\kappa_{\mathrm{el}}$ [$\mathrm{W\,m^{-1}\,K^{-1}}$] |
|---|---|
| 1 | $\approx 1 \times 10^{-3}$ |
| 1000 | $\approx 1$ |

The proportionality constant $L = \frac{\pi^2}{3}\left(\frac{k_{\mathrm{B}}}{e}\right)^2 = 2.44 \times 10^{-8}\,\mathrm{W\,\Omega\,K^{-2}}$ is called the Lorenz number. (3.10) can be useful to estimate the relative contribution of $\kappa_{\mathrm{ph}}$ and $\kappa_{\mathrm{el}}$ to $\kappa$. As can be learned by comparing the estimates from Table 3.4 to Table 3.5, the contribution to total thermal conductivity due to moving electrons, starts to become significant only at high electrical conductivities of about $1000\,\Omega^{-1}\,\mathrm{cm}^{-1}$.

Table 3.5: Thermal conductivity for different materials.

| | $\kappa$ [$\mathrm{W\,m^{-1}\,K^{-1}}$] |
|---|---|
| Air | 0.023 |
| $C_{60}$ | 0.1 |
| Polymers | $\gtrsim 0.3$ |
| Cellulose | $\approx 0.4$ |
| Water | 0.6 |
| Glass | 1 |
| $Bi_2Te_3$ | 1.2 |
| PEDOT:PSS | $< 1.8$ |
| Oriented PE | $< 10$ |
| Constantan | 23 |
| SWCNT film | $\approx 30$ |
| Copper | 390 |
| Silver | 420 |
| Single SWCNT | $> 1000$ |

For orientation, Table 3.5 gives $\kappa$ for some reference materials. In general, polymers have quite low thermal conductivity, if they are amorphous, isotropic and undoped. If however, high levels of crystallinity and orientation are induced by stretching them for example, then the thermal conductivity can be as high as that of some metals [SHT+10].

[SHT+10] Sheng Shen et al. *Nat. Nanotechnol.* **5**, 251 (2010)

Due to restrictions in sample preparation, and measurement, $\kappa$ and $\sigma$ are often measured on different, dissimilar samples. This is problematic for two reasons.

[MLE+16] Cheng-Kang Mai et al. *Macromolecules*, **49**, 4957 (2016)

[LWL+15] Jun Liu et al. *Macromolecules*, **48**, 585 (2015)

- Both values should be measured in the same molecular direction, to minimize any influence due to an intrinsic anisotropy of the thermal conductivity in organic materials. For example, $\kappa$ of CNT composites was found to be one order of magnitude higher in plane, than out of plane [MLE+16], due to a preferential alignment of the tubes in the substrate plane. A qualitatively similar behavior has also been observed for PEDOT:PSS [LWL+15]. Nonetheless, $\sigma$ is generally measured in-plane, while $\kappa$ is most easily measured out-of-plane.

- It is often assumed that doping does not influence $\kappa$, i.e. $\kappa \not\propto \sigma$ or $L_{\mathrm{Polymer}} = 0$. But measuring $\sigma$ on doped samples, while using undoped ones for $\kappa$ should not be done, because it was observed that for films of PEDOT-Tos and PEDOT:PSS, $\kappa$ does in fact increase together with $\sigma$ in doped films. It was rationalized that this could not be due to an increase in lattice thermal conductivity $\kappa_{\mathrm{ph}}$, but was instead due to an increase of $\kappa_{\mathrm{el}}$ that is larger than would be predicted by (3.10) [WKB+15]. Another report observed a similar increase of $\kappa$ with $\sigma$, but in line with what was expected according to (3.10) [LWL+15].

[WKB+15] Annie Weathers et al. *Adv. Mater.* **27**, 2101 (2015)

[LWL+15] Jun Liu et al. *Macromolecules*, **48**, 585 (2015)

$\alpha$ Thermal diffusivity A measure of how fast temperature spreads inside a material, comparable to an inverse inertia.

THERMAL DIFFUSIVITY The thermal conductivity is often only measured indirectly, through measurements of the thermal diffusivity. The latter appears as a constant in the heat equation, the equation that describes the temperature distribution of a given region over time.

$$\frac{\partial T}{\partial t} - \alpha \boldsymbol{\nabla}^2 T \tag{3.11}$$

Using (3.12), $\kappa$ can be calculated from $\alpha$, the (mass) density $\rho$ and the specific heat $C_{\mathrm{P}}$.

$$\alpha = \kappa \rho C_{\mathrm{P}} \tag{3.12}$$

DIMENSIONLESS FIGURE OF MERIT  All these correlated effects are combined into a single parameter, the dimensionless figure of merit.

$$ZT = \frac{S^2 \sigma}{\kappa} T \tag{3.13}$$

Where $T = \frac{1}{2}\left(T_{\text{hot}} + T_{\text{cold}}\right)$ is the average temperature. $ZT$ is used when comparing the relative efficiency of different thermoelectric materials, and some typical values are given in Table 3.6.

EFFICIENCY  The power conversion efficiency of a thermoelectric generator is proportional to $ZT$, as well as to the average temperature $T$. Due to the mutual interdependence of $\Delta T$ and the current $I$, in the general case, the generated power will in fact not be maximal for $R_{\text{load}} = R_{\text{source}}$, but instead for [YS12][Lin13][YS13]:

$$\frac{R_{\text{load}}}{R_{\text{source}}} = \sqrt{1 + ZT} \neq 1 \tag{3.14}$$

Under this conditions, $\eta$ is given in (3.15) and plotted in Figure 3.2 versus $\Delta T$.

$$\eta = \frac{P_{\text{out}}}{\frac{\partial Q_{\text{in}}}{\partial t}} = \underbrace{\frac{T_{\text{hot}} - T_{\text{cold}}}{T_{\text{hot}}}}_{\eta_{\text{Carnot}}} \underbrace{\frac{\sqrt{ZT+1}-1}{\sqrt{ZT+1}+\frac{T_{\text{cold}}}{T_{\text{hot}}}}}_{(0 < \cdots < 1)} \tag{3.15}$$

It goes without saying, that $\eta$ is bounded by the efficiency of the Carnot cycle, since $\eta \to \eta_{\text{Carnot}} = 1 - \frac{T_{\text{cold}}}{T_{\text{hot}}}$ for $ZT \to \infty$.

## 3.3. Parameter Correlations

To understand why there has been so little progress towards higher performing thermoelectric materials in the recent decades, one has to understand the strong correlation between $S$, $\sigma$ and $\kappa$. The schematic dependence of the thermoelectric parameters on the charge carrier density is sketched in Figure 3.3. If only states close to the Fermi level contribute to the conduction, such as in a metal, then (3.3) can be written as [Fri71]:

$$S = -\frac{\pi^2}{3} \frac{k_{\text{B}}}{e} k_{\text{B}} T \left[ \frac{\text{d}\ln\left(D(E)\mu(E)\right)}{\text{d}E} \right]_{E=E_{\text{F}}} \tag{3.16}$$

 where $D(E)$ is the density of states and $n(E) = D(E)f(E)$ is the carrier distribution. In metals, the derivative $\frac{\partial f}{\partial E}$ of the Fermi distribution function $f(E)$ is $\delta$-shaped, and so (3.16) can also be written as

$$S = \frac{\pi^2}{3} \frac{k_{\text{B}}}{e} k_{\text{B}} T \left[ \frac{\text{d}\ln\sigma(E)}{\text{d}E} \right]_{E=E_{\text{F}}} \tag{3.17}$$

which is is known as one of the Mott relations [CM69] [JM80].

Or using $\sigma$ written in terms of the energy dependent carrier distribution and mobility,

$$\sigma(E) = |e| n(E) \mu(E) \tag{3.18}$$

(3.16) can be rewritten in yet another equivalent form, given in [KP16]

$ZT$ Dimensionless figure of merit
The ratio between the reversible and the irreversible contributions to the flow of heat.

Table 3.6: $ZT$ for some thermoelectric materials at $T = 300\,\text{K}$.

|  | $ZT$ |
| --- | --- |
| $Bi_2Te_3$ | 1 |
| PEDOT:PSS | 0.42 |
| PEDOT-Tos | 0.25 |
| SWCNTs | $\approx 0.1$ |
| Constantan | 0.04 |
| Copper | $1 \times 10^{-4}$ |

$\eta$ Power conversion efficiency

[YS12] Kazuaki Yazawa et al. *J. Appl. Phys.* **111**, 024509 (2012)

[Lin13] Bihong Lin. *J. Appl. Phys.* **114**, 176101 (2013)

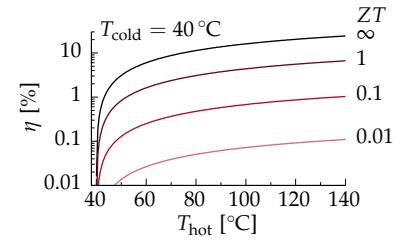[YS13] Kazuaki Yazawa et al. *J. Appl. Phys.* **114**, 176102 (2013)



Figure 3.2: Thermoelectric efficiency $\eta$ versus temperature difference for different $ZT$.

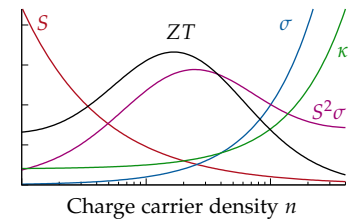[Fri71] Hellmut Fritzsche. *Solid State Commun.* **9**, 1813 (1971)



Figure 3.3: Thermoelectric parameters versus charge carrier density.

[CM69] Melvin Cutler et al. *Phys. Rev.* **181**, 1336 (1969)

[JM80] Mats Jonson et al. *Phys. Rev. B*, **21**, 4223 (1980)

[KP16] *Innovative Thermoelectric Materials* (2016)

$$S = \frac{\pi^2}{3} \frac{k_B}{e} k_B T \left[ \frac{1}{n(E)} \frac{dn(E)}{dE} + \frac{1}{\mu(E)} \frac{d\mu(E)}{dE} \right]_{E=E_F} \tag{3.19}$$

From these equations it can be learned that a large asymmetry in the density of states, like that present in CNTs close to the band edges, can lead to a large $S$, without necessarily affecting $\sigma$. Similarly, an energy-dependent mobility, could allow to increase Seebeck coefficient. This so-called energy filtering is predicted to take place at appropriately engineered interfaces in a composite, by selectively scattering low-energy carriers. Yet few experimental realizations are reported [HGL+12].

[HGL+12] Ming He et al.
*Energy Environ. Sci.* **5**, 8351 (2012)

## 3.4. Equivalent Derivation

$S^*$ Entropy   "Quantity of heat".
Carrier of thermal energy.

ENTROPY   In classical derivations of the thermoelectric phenomenon, entropy does not play a central role. Yet a derivation in terms of entropy yields some interesting insights, and allows for a more intuitive understanding of thermoelectricity. Entropy can be treated as a substance-like quantity, much like the one that is commonly referred to as "heat". Entropy obeys half a conservation law—it can be created, but not destroyed [Fal85]. Instead of the flow of thermal energy, we now consider the flow of entropy [Fuc14]. That way, the simple tensor equation shown in (3.20) can be derived. The charge flux $\boldsymbol{j}_q$ and the entropy flux $\boldsymbol{j}_{S^*}$ depend on their conjugate potentials, the electrochemical potential $\tilde{\mu}$ and temperature $T$, as well as on a thermoelectric material dependent tensor, that does not explicitly depend on temperature [Fel15] [GSZ+11].

[Fal85] Gottfried Falk.
*Eur. J. Phys.* **6**, 108 (1985)

[Fuc14] Hans U. Fuchs.
*Energy Harvest. Syst.* **1**, 1 (2014)

[Fel15] Armin Feldhoff.
*Energy Harvest. Syst.* **2**, 5 (2015)

[GSZ+11] Christophe Goupil et al.
*Entropy*, **13**, 1481 (2011)

$$\begin{pmatrix} \boldsymbol{j}_q \\ \boldsymbol{j}_{S^*} \end{pmatrix} = \begin{pmatrix} \sigma_T & \sigma_T S \\ \sigma_T S & \sigma_T S^2 + \Lambda_{j_q=0} \end{pmatrix} \cdot \begin{pmatrix} -\nabla\left(\frac{\tilde{\mu}}{q}\right) \\ -\nabla T \end{pmatrix} \tag{3.20}$$

Equation (3.20) has the simple form of fluxes = thermoelectric material tensor · potentials. It can be written as a sum of a reversible and an irreversible component as follows.

$$\begin{pmatrix} \boldsymbol{j}_q \\ \boldsymbol{j}_{S^*} \end{pmatrix} = \left. \begin{pmatrix} \sigma_T & \Lambda_{cc} \cdot \frac{1}{S} \\ \sigma_T S & \Lambda_{cc} \end{pmatrix} \cdot \begin{pmatrix} -\nabla\left(\frac{\tilde{\mu}}{q}\right) \\ -\nabla T \end{pmatrix} \right\} \text{reversible}$$
$$+ \left. \begin{pmatrix} 0 & 0 \\ 0 & \Lambda_{j_q=0} \end{pmatrix} \cdot \begin{pmatrix} -\nabla\left(\frac{\tilde{\mu}}{q}\right) \\ -\nabla T \end{pmatrix} \right\} \text{irreversible} \tag{3.21}$$

$\Lambda$ Entropy conductivity   The thermal conductivity normalized by temperature $\Lambda = \frac{\kappa}{T}$.

Like the thermal conductivity in the traditional derivation, the specific entropy conductivity has two contributions. The power factor $\Lambda_{cc} \equiv \sigma_T S^2$ appears as the charge-coupled specific entropy conductivity, which describes reversible energy transfer between electrical current and entropy current. While $\Lambda_{j_q=0}$ includes the irreversible contributions not due to the movement of charges. The dimensionless figure of merit $ZT = \frac{\Lambda_{cc}}{\Lambda_{j_q=0}}$ appears naturally as quotient of the reversible and irreversible specific entropy conductivities. Intuitively, it is the ratio of entropy transported reversibly by charge carriers, to that generated irreversibly by phonons. Particularly satisfying is that

the dimensionless figure of merit no longer explicitly depends on temperature.

## 3.5. Doping of Organic Thermoelectrics

As we have seen, the charge carrier density plays a crucial role, since it controls $S$, $\sigma$ as well as $\kappa_{\mathrm{el}}$. That is why an optimized level of doping is central to a good thermoelectric material. This section contains a non-exhaustive review of the literature on doping of different organic materials.

DEPENDENCE OF $S$ ON $\sigma$  Determining the charge carrier density experimentally is problematic, especially in organic materials which have low mobility compared to inorganic semiconductors. In these materials, unlike in metals, the clear cut distinction between completely free charges in the conduction band and completely localized charges in the valence band cannot be made. Instead, due to a large number of energetically and spatially disperse trap states, the charge carrier density may not be well defined. This was proposed to manifest as a transport edge, below which charges are localized and do not contribute to conduction. Above the transport edge, charges are not free, but instead electrical conductivity is thermally activated [DJ16]. This agrees well with with the experimentally observed disorder in conjugated polymers, where nanometrically crystalline regions are often separated by amorphous regions.

[DJ16] Stephen Dongmin Kang et al. *Nat. Mater.* **16**, 252 (2016)

By instead using $\sigma$ as a proxy for $n$, general trends were reported in $S$ versus $\sigma$ for doped polyacetylene samples [Kai89] [Kai01]. This observation has since been shown to be quite universal for many conjugated polymers [GCP+15] [RGU+16]. An empirical power law of the form

$$S(\sigma) = \frac{k_{\mathrm{B}}}{e} \left( \frac{\sigma}{\sigma_S} \right)^{-\frac{1}{4}} \tag{3.22}$$

seems to be the observed upper limit for most of the studied materials, notable exceptions being PEDOT-based materials and CNT composites. Here $\frac{k_{\mathrm{B}}}{e} = 86.17\,\mu\mathrm{V\,K^{-1}}$ is the natural unit of the Seebeck coefficient and $\sigma_S \approx 1\,\mathrm{S\,cm^{-1}}$ is a fitting constant.

[Kai89] Alan B. Kaiser. *Phys. Rev. B*, **40**, 2806 (1989)

[Kai01] Alan B. Kaiser. *Reports Prog. Phys.* **64**, 1 (2001)

[GCP+15] Anne M. Glaudell et al. *Adv. Energy Mater.* **5**, 1401072 (2015)

[RGU+16] Boris Russ et al. *Nat. Rev. Mater.* **1**, 16050 (2016)

SEMICONDUCTING POLYMERS  Doping ordered polymers like P3HT with $F_4$TCNQ may affect the crystal packing, forming polymer:dopant co-crystals [DWA+13]. While this increases doping efficiency, it also affects charge transport through the crystalline domains. By instead locating the dopant in the amorphous parts of a semi-crystalline film—away from the charge transport pathways—mobility remains unaffected. This was achieved by diffusion of $F_4$TCNQ in the solid state [KWB+16], allowing for free-electron like coherent charge transport.



$F_4$TCNQ
2,3,5,6-tetrafluoro-7,7,8,8-tetracyanoquinodimethane  Strong p-type dopant.

[DWA+13] Duc T. Duong et al. *Org. Electron.* **14**, 1330 (2013)

[KWB+16] Keehoon Kang et al. *Nat. Mater.* **15**, 896 (2016)

PEDOT  The monomer ratio of electrically conducting EDOT to electrically insulating sulfonate in as synthesized PEDOT:PSS is about 1:4 [WAG+15]. This high amount of sulfonate is necessary to stabilize the PEDOT:PSS emulsion in water during synthesis. While the PSS counterion serves to p-dope the PEDOT, it does so inefficiently, with only about every third sulfonate monomer accepting an electron.
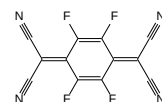
[WAG+15] Hui Wang et al. *Adv. Energy Mater.* **5**, 1500044 (2015)

[TMF+12] Takumi Takano et al.
*Macromolecules*, **45**, 3859 (2012)

[WMN+13] Qingshuo Wei et al.
*Adv. Mater.* **25**, 2831 (2013)

[KSZ+13] Gun-Ho Kim et al.
*Nat. Mater.* **12**, 719 (2013)

[RK14] Stephan Van Reenen et al.
*Org. Electron.* **15**, 2250 (2014)

[KKP16] Gun-Ho Kim et al.
*Appl. Phys. Lett.* **108**, 093301 (2016)

[BKM+11] Olga Bubnova et al.
*Nat. Mater.* **10**, 429 (2011)

[BBC12] Olga Bubnova et al.
*J. Am. Chem. Soc.* **134**, 16456 (2012)

[WAG+15] Hui Wang et al.
*Adv. Energy Mater.* **5**, 1500044 (2015)

[AJW+16] Ujwala Ail et al.
*Adv. Funct. Mater.* **26**, 6288 (2016)

[ZWK+16] Dan Zhao et al.
*Energy Environ. Sci.* (2016)

[CFL+16] William B. Chang et al.
*ACS Macro Lett.* **5**, 455 (2016)

[HD93a] L. D. Hicks et al.
*Phys. Rev. B*, **47**, 727 (1993)

[HD93b] L. D. Hicks et al.
*Phys. Rev. B*, **47**, 16631 (1993)

[KFZ+00] Jing Kong et al.
*Science*, **287**, 622 (2000)

[CFK+01] Robert J. Chen et al.
*Appl. Phys. Lett.* **79**, 2258 (2001)

[SS03] Moonsub Shim et al.
*Appl. Phys. Lett.* **83**, 3564 (2003)

Removing inactive dopant then should result in higher $\sigma$ simply by increasing the amount of active material, as well as improving the charge carrier mobility due to secondary doping. And indeed, the amount of PSS can be reduced by selectively washing it away with hydrophilic ethylene glycol [TMF+12] [WMN+13], leading to reported values of $ZT = 0.42$ [KSZ+13]. However, concerns have been raised regarding the device geometry used in the latter report [RK14]. A follow up report justifies the high value of $ZT = 0.42$ with the increased performance of PEDOT:PSS at high humidity conditions, while rejecting any influence of the device geometry [KKP16].

An alternative to the bulky PSS counterion is tosylate. Controlled de-doping of PEDOT-Tos allowed to reach an ideal oxidation level, which resulted in a value of $ZT = 0.25$ [BKM+11], with an EDOT:sulfonate molar ratio of 2.7:1.

A particularly instructive example is the electrochemical doping of bulk PEDOT:PSS in an electrochemical transistor [BBC12]. It was found that $S$ can turn negative for an oxidation level above 50 % and that $S$ and $\sigma$ are inversely correlated with the oxidation level. This nicely illustrates that just like in inorganic materials, the power factor has a maximum at an optimum doping level, again emphasizing the necessity for secondary doping as an independent method to reach higher power factors.

IONIC THERMOELECTRICITY   Not only electrons or holes contribute to the Seebeck voltage. Mobile ions also diffuse due to a temperature gradient, just as electrons do. This is called the Soret effect. Mixed electronic and ionic contributions have been observed for PEDOT:PSS, as well as purely ionic contributions from small, mobile ions like Na$^+$, in PSSNa [WAG+15] [AJW+16]. These ions cannot leave the sample though, and the current flowing in a closed circuit decays down to the electronic contribution once the ions accumulate at the electrode. Still, some envisioned applications, like hybrids of thermoelectric generators and supercapacitors that generate electricity from intermittent heat sources, may be feasible. After all, the voltages that can be achieved with ions rather than electrons are several orders of magnitude larger [ZWK+16]. Another approach tries to harness these large voltages for extended periods, by allowing electrochemical reactions of silver ions at silver electrodes [CFL+16]. That way current can flow in these thermogalvanic cells until one electrode is depleted, upon which the temperature gradient has to be reversed.

CARBON NANOTUBES   Carbon nanotubes, like all low-dimensional conductors, were predicted to have an elevated Seebeck coefficient compared to bulk materials, due to the dimensional confinement of charges, which leads to a strongly peaked density of states [HD93a] [HD93b].

While CNTs are ambipolar in the absence of atmospheric oxygen, their properties are strongly influenced by the adsorption of gas molecules onto the surface [KFZ+00], which has uses for detectors. These molecules can then be photodesorbed by UV-light [CFK+01] [SS03].

It was demonstrated that the Seebeck coefficient of CNTs depends on their electronic type. The Seebeck coefficient of undoped networks

of CNTs varies linearly with their composition between the values of $13\,\mu V\,K^{-1}$ for metallic tubes to $88\,\mu V\,K^{-1}$ for pure semiconducting tubes respectively [PJN+14]. This value is about twice that of a single semiconducting tube, which was found to be $42\,\mu V\,K^{-1}$ [YSY+05]. This suggests an important contribution of the inter-tube junctions to the Seebeck coefficient, emphasizing the potential of composites.

The Fermi level of semiconducting single-walled carbon nanotubes can be tuned in an OFET architecture by tuning the gate voltage. Since the Seebeck coefficient is proportional to the derivative of the density of states at the Fermi level, as seen from (3.16), this allows to directly influence $S$ [YKO+14]. In a similar transistor geometry, large oscillations of $S$ have been observed in single CNTs by varying the gate voltage [SPK03] [LFJ+04], which is a particular instructive way to show that carbon nanotubes can be both p-type and n-type conductors [OKM+15]. For example, theoretical estimates place the Seebeck coefficient of pure semiconducting SWCNT with (7,5) chirality at approximately $\pm 1300\,\mu V\,K^{-1}$, if the Fermi energy is shifted by only $\mp 60\,meV$ [AZL+16]. While chirally pure films of CNTs are still quite expensive, a giant Seebeck coefficient for pure semiconducting SWCNTs has been independently reported [NHY+14].

To achieve the highest electrical conductivities, carbon nanotubes should be as dispersed as possible, resulting in very small bundle diameters. Furthermore, they should not be covered with any remaining materials which were used to disperse them. It was reported, that this can only be optimally achieved, if the dispersant is removed after—not before—deposition, to prevent reaggregation in solution [NIG+16].

In composites of polyaniline and double-walled CNTs doped with camphorsulfonic acid, both the electrical conductivity and the Seebeck coefficient can be improved at the same time [WYP+15]. This is commonly rationalized with an increase in the charge carrier mobility due to a better molecular ordering or chain extension of the polymer in the composites. Multilayer composites of CNTs with PANI and graphene have demonstrated a power factor of $1825\,\mu W\,m^{-1}\,K^{-2}$ [CSH+15], while CNT-mats infiltrated with PANI and doped with gold nanoparticles have reached $S^2\sigma = 3548\,\mu W\,m^{-1}\,K^{-2}$ and $ZT = 0.2$ [AKL+16].

Using conjugated polyelectrolytes—conjugated polymers with ionic functionalities attached to their side-chains—allows to disperse and dope CNTs in much the same way as with regular conjugated polymers. Crucially, the type of doping depends on the selected ions, and therefore allows for a degree of tunability without having to change the conjugated backbone [MRF+15] [MLE+16]. This way, both p- and n-type SWCNTs composites were demonstrated.

n-Type Thermoelectricity   Both n-type and p-type materials are needed for modern electronics. For example, using complementary materials provides a number of advantages for logic circuits [CDL+00], such as lower current draw, and greater resilience towards small fluctuations in transistor performance.

The same is true for thermoelectricity, where two complementary materials with $S_{+/-} = \pm S$ allow to double the performance of a thermoelectric generator, compared to one that relies on two materials

[PJN+14] Mingxing Piao et al. *J. Phys. Chem. C*, **118**, 26454 (2014)

[YSY+05] Choongho Yu et al. *Nano Lett.* **5**, 1842 (2005)

[YKO+14] Kazuhiro Yanagi et al. *Nano Lett.* **14**, 6437 (2014)

[SPK03] Joshua P. Small et al. *Phys. Rev. Lett.* **91**, 256801 (2003)

[LFJ+04] Mark C. Llaguno et al. *Nano Lett.* **4**, 45 (2004)

[OKM+15] Yuki Oshima et al. *Appl. Phys. Lett.* **107**, 043106 (2015)

[AZL+16] Azure D. Avery et al. *Nat. Energy*, **1**, 16033 (2016)

[NHY+14] Yusuke Nakai et al. *Appl. Phys. Express*, **7**, 025103 (2014)

[NIG+16] Brenna Norton-Baker et al. *ACS Energy Lett.* **1**, 1212 (2016)

[WYP+15] Hong Wang et al. *ACS Appl. Mater. Interfaces*, **7**, 9589 (2015)

[CSH+15] Chungyeon Cho et al. *Adv. Mater.* **27**, 2996 (2015)

[AKL+16] Cheng Jin An et al. *ACS Appl. Mater. Interfaces*, **8**, 22142 (2016)

[MRF+15] Cheng-Kang Mai et al. *Energy Environ. Sci.* **8**, 2341 (2015)

[MLE+16] Cheng-Kang Mai et al. *Macromolecules*, **49**, 4957 (2016)

[CDL+00] B. Crone et al. *Nature*, **403**, 521 (2000)

PEI
Polyethylenimine

[SJS+01] Moonsub Shim et al.
*J. Am. Chem. Soc.* **123**, 11512 (2001)

[HMB+14] Corey A. Hewitt et al.
*J. Appl. Phys.* **115**, 184502 (2014)

[YMC+12] Choongho Yu et al.
*Energy Environ. Sci.* **5**, 9481 (2012)

[MHB+16] David S. Montgomery et al.
*Carbon*, **96**, 778 (2016)

[KCT+14] Suk Lae Kim et al.
*ACS Nano*, **8**, 2377 (2014)

[TTS+03] Taishi Takenobu et al.
*Nat. Mater.* **2**, 683 (2003)

[FFN15b] Takahiro Fukumaru et al.
*Sci. Rep.* **5**, 7951 (2015)

[NOK+13] Yoshiyuki Nonoguchi et al.
*Sci. Rep.* **3**, 3344 (2013)

[NNM+16] Yoshiyuki Nonoguchi et al.
*Adv. Funct. Mater.* **26**, 3021 (2016)

[NTI+17] Yoshiyuki Nonoguchi et al.
*Small*, **13**, 1603420 (2017)

[WHY+15] Hong Wang et al.
*Adv. Mater.* **27**, 6855 (2015)

[SBG+14] Ruth A. Schlitz et al.
*Adv. Mater.* **26**, 2825 (2014)

[RRB+14] Boris Russ et al.
*Adv. Mater.* **26**, 3473 (2014)

with $S_+ = S$ and $S_- = 0\,\mu V\,K^{-1}$. In particular, n-type organic thermoelectric materials are important because so far, there are fewer of them. They are generally not air-stable due to the tendency of the molecular dopants to oxidize in atmosphere.

A well known n-type dopant for CNTs is PEI [SJS+01], which can be used to manufacture flexible TEGs [HMB+14]. When encapsulated, stability over one month was reported [YMC+12]. PEI can also be used to spray-dope CNT mats [MHB+16], allowing for a simple fabrication. In the quest for higher power factors, even complex concoctions of CNTs, PEI and two additional dopants have been reported [KCT+14].

Air stable doping of CNTs have been demonstrated by encapsulating different small molecules in their interior [TTS+03] [FFN15b]. A multitude of potential n-type dopants for CNTs with varying levels of air stability are being investigated [NOK+13] [NNM+16]. N-type air-stable CNTs have been demonstrated by doping them with nanoparticles of a triarylmethane derivative in a basic solution. The delocalized nature of the positive charges on the dopant stabilizes the delocalized charges on the CNTs, which is given as one reason for the observed stability [NTI+17].

Composites of CNTs and in situ polymerized PEDOT have been dedoped with TDAE [WHY+15], reporting an n-type composite with $ZT \approx 0.5$.

While there are reports on thermoelectric n-type polymers suchs as P(NDI2OD-T2) [SBG+14] or small molecules [RRB+14], little is known about their stability in air.

## 3.6. Organic Thermoelectric Generators

TEG Thermoelectric generator

[BPL+17] Davide Beretta et al.
*Sustain. Energy Fuels*, **1**, 174 (2017)

[BML+17] Davide Beretta et al.
*Rev. Sci. Instrum.* **88**, 015103 (2017)

[HHF16] R. Haight et al.
*Science*, **353**, 124 (2016)

By connecting a large number of thermocouples electrically in series and thermally in parallel, an organic thermoelectric generator can be constructed. These devices could supply sufficient power for real applications [BPL+17], such as micro-TEGs powering sensor applications for the internet of things [BML+17]. For these applications, the power consumption is estimated at $100\,\mu W$ for processing, $1\,mW$ for sensing and $5\,mW$ for wireless data transmission [HHF16].

$R^{thermal}$ Thermal contact resistance

THERMAL CONTACT RESISTANCE The generated power of a TEG of course depends on the available temperature gradient. But until now, important losses in temperature difference due to finite thermal contact resistance have been neglected. Just like an electrical resistance brings about a drop in voltage across said resistance, a drop in temperature is observed across a thermal contact resistance. Thermal contact resistances are simply due to the imperfect mechanical contact of rough surfaces with little contact pressure. The largest thermal contact resistances are typically at the interfaces between the generator and the hot and cold reservoirs. Assuming identical $R^{thermal}$ at the hot and cold sides, then for maximum power output, the real temperature gradient across the generator will only be half of the available maximum temperature gradient of the reservoirs.

In any TEG, the generated voltage is proportional to the total number of thermocouples, while the power output depends on the area, that is covered by the generator. Because of that, utilizing the available area in the best way possible, by selecting a suitable generator geometry is important as well.

OUT-OF-PLANE GEOMETRY Traditionally, TEGs made from inorganic materials are built in an out-of-plane geometry, where heat and current flow through the active material in a direction perpendicular to the substrate, as pictured in Figure 3.4. The dimensions of a single thermoelectric leg in such an architecture are of the order of a few millimeters. This allows to easily maintain the necessary temperature gradient across the thickness or height of the device. At the same time, the large cross section of each leg guarantees a low internal resistance of the device. The optimal leg length for symmetric thermal contacts is given by



Figure 3.4: Sketch of a TEG with out-of-plane geometry normal geometry.

$$d_{\text{optimal}} = 2R^{\text{thermal}}\kappa\frac{R_{\text{load}}}{R_{\text{source}}} \qquad (3.23)$$

The main advantage of this geometry is that it allows to integrate a very high density of thermocouples per area. Because the output voltage is directly proportional to the number of thermocouples, the required voltages to cold-start and drive electronic components, which are typically $\gtrsim 300\,\mu\text{V}$, are most easily reached in this architecture. Examples of organic out-of-plane TEGs do exist, but fabrication is often complex and involves the printing of multiple layers [SHK13] [BKM+11].

[SHK13] Kouji Suemori et al. *Appl. Phys. Lett.* **103**, 2011 (2013)

[BKM+11] Olga Bubnova et al. *Nat. Mater.* **10**, 429 (2011)

IN-PLANE GEOMETRY Because of the difficulties associated with the deposition of thick layers from solution, the out-of-plane geometry is seldom used for organic materials. While stacks of thin films, have been tried [SHE+13], the results were rather sobering for two very instructive reasons. First, for a stack of $N$ layers, the temperature gradient $\Delta T$ across a single thermocouple is only a fraction $\frac{\Delta T}{N}$ of the total, making this design practically unfeasible. Second, even in the case of a single layer $N = 1$, part of the temperature gradient is lost in the substrate. In the case of thin films, with active layers that may be even thinner than the substrate, this constitutes a significant problem. While it is conceivable to use thick films of polymer aerogels [GZZ+17], no devices have been demonstrated so far.



Figure 3.5: Sketch of an in-plane TEG geometry suitable for thin films.

[SHE+13] Roar R. Søndergaard et al. *Energy Sci. Eng.* **1**, 81 (2013)

[GZZ+17] Madeleine P. Gordon et al. *J. Appl. Polym. Sci.* **134**, 44070 (2017)

So instead, an in-plane geometry sketched in Figure 3.5 can be chosen, where current and heat flow parallel to the substrate. While this necessitates thin substrates with a low thermal conductivity, it does alleviate most problems related to manufacturing. A high integration density can be achieved by folding or rolling up the layer of thermocouples to form thick modules, similar in appearance to regular out-of-plane devices [FPT+17]. Furthermore, the thickness of the deposited layer now no longer coincides with the direction of heat flow, but instead determines the resistance of a leg. Because of that, a large resistance due to a limited layer thickness is no longer a problem, as it can be counteracted with an increase in the width of the thermocouple [MHB+16].
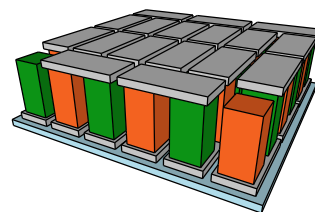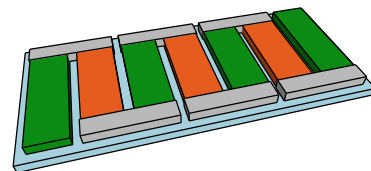
[FPT+17] Haiyu Fang et al. *J. Appl. Polym. Sci.* **134**, 44208 (2017)

[MHB+16] David S. Montgomery et al. *Carbon*, **96**, 778 (2016)

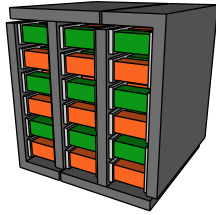[Bel08] Lon E. Bell. *Science*, **321**, 1457 (2008)



Figure 3.6: Sketch of a stack geometry for TEGs.

STACK GEOMETRY   Another, entirely different approach is the stack geometry. Here heat and current flow are not parallel throughout all of the device [Bel08]. Instead, the generator consists of stacks of regular out-of-plane generators, which are supplied with heat and cooled along in-plane heat spreaders. An example is sketched in Figure 3.6.

The experimental results that have been obtained on thermoelectric carbon nanotube composites during the course of this thesis, will be presented in Chapter 6: Carbon Nanotube Composites.

# ORGANIC PHOTOVOLTAICS

<span style="float:right; font-size:3em;">4</span>

Another already well established area of application for organic materials is that of organic photovoltaics, which will be introduced in this chapter.

## 4.1. Sunlight

Since solar cells are mostly used to generate power from the light of our sun, let us start by first having a closer look at what sunlight is. In Figure 4.1, the spectral irradiance of the sun is plotted depending on where it is measured—for different air mass coefficients. AM0 is defined at the top of the atmosphere, before any light is absorbed by ozone, oxygen, water and carbon dioxide, with a measured incident power or irradiance of $1366.1\,\mathrm{W\,m^{-2}}$. For an angle $\delta = \sin^{-1}\frac{1}{1.5} \approx 42°$ between the horizon and the sun, light traverses 1.5 times the normal thickness of Earth's atmosphere, as is typical in Europe. The combined irradiance of both direct, and diffusely scattered sunlight in this case is reasonably close to $1\,\mathrm{sun} \equiv 1000\,\mathrm{W\,m^{-2}}$, and so AM1.5G (G as in "global") has been standardized to this value.

BLACK BODY RADIATION   The spectral irradiance of a black body at its surface is given by Planck's law.

$$F(\lambda) = \frac{2\pi h c^2}{\lambda^5 e^{\frac{hc}{k_B T \lambda}}} \tag{4.1}$$

For photovoltaic applications, we are interested in the spectral irradiance not at the surface of the sun, but on Earth. In the former case, the black body covers a whole hemisphere, while in the latter case, the angle subtended by the sun as seen from Earth is $\alpha = 0.53°$. By introducing a factor of $\sin^2(\frac{\alpha}{2}) \approx 2.16 \times 10^{-5}$, (4.1) is modified accordingly [Nel03].

EFFECTIVE TEMPERATURE OF THE SUN   Integrating the spectral irradiance over all wavelengths results in the irradiance of a black body

$$F \equiv \int F(\lambda)\,\mathrm{d}\lambda = \sigma T^4 \equiv \frac{2\pi^5 k_B^4}{15 h^3 c^2}, \tag{4.2}$$

where $\sigma$ is the Stefan-Boltzmann constant. Using the accepted value of $F = 1366.1\,\mathrm{W\,m^{-2}}$ set forth in the AM0 standard, one can calculate the effective temperature of the sun as an ideal black body. This black body spectrum at 5779 K is plotted in Figure 4.1 together with the reference spectra.

EMISSION PEAK   The wavelength at which the spectral irradiance of a black body peaks, moves to lower wavelengths with higher temperatures. This is known as Wien's displacement law,

$$\lambda_{\max} = \frac{b}{T} \tag{4.3}$$

OPV Organic photovoltaic   Generation of electricity from sunlight, using carbon-based materials.

$F(\lambda)$ Spectral irradiance   Power arriving at a surface at a given wavelength.

AM Air mass coefficient   The length of the path traversed within the atmosphere, relative to the length of the shortest path—that in radial direction.
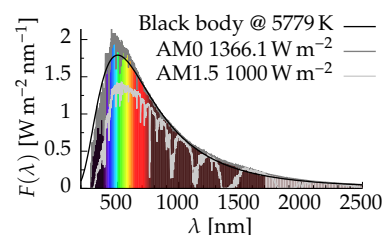


Figure 4.1: Spectral irradiance $F(\lambda)$ for sunlight at the top of the atmosphere (AM0), at mid-latitudes (AM1.5) and for an equivalent black body as a function of wavelength $\lambda$.

[Nel03] Jenny Nelson. *The Physics of Solar Cells* (2003)

where $b$ is Wien's displacement constant, which can be derived from (4.1) and which is approximately $b \approx 2900 \, \mu m \, K$.

THEORETICAL MAXIMUM EFFICIENCY   The maximum power conversion efficiency of a single-junction solar cell is inherently limited. This limit is due to the spectral distribution of sunlight and does not exist in the same form for a monochromatic light source. For any monochromatic light source, it is possible to select the band gap of a solar cell in such a way that all incoming photons have enough energy to excite charges to the conduction band, while minimizing losses due to the thermalization of the excited charges. These thermalization losses are due to the relaxation of exited charge carriers back down to the LUMO, giving of as heat any excess energy that was imparted by photons with energy above the band gap.

In the non-monochromatic case, it is no longer desirable to maximize absorption for all wavelengths. While it is possible to absorb all low energy photons with a low band gap material, this at the same time means increased thermalization losses for higher energy photons. Instead, a trade-off has to be found between the losses due to an incomplete absorption, and those due to the thermalization of charges.

[SQ61] William Shockley et al. *J. Appl. Phys.* **32**, 510 (1961)

Using the available AM1.5 sunlight here on Earth, the optimal band gap was found to be 1.34 eV. The corresponding maximum power conversion efficiency of a single-junction solar cell is 33.7 %, which was originally derived by Shockley and Queisser [SQ61].

POLARIZATION OF THE SKY   While direct sunlight is not polarized, our sky—like all reflected and scattered light—is, depending on the angle. Because light is a transverse wave, according to Brewster's law, light scattered at an angle of 90° is completely polarized. In this case the angle of polarization of the scattered light has to be perpendicular to the direction of propagation of both the incident and the scattered light. Any other polarization is forbidden, because it would suppose a polarization component in propagation direction. For example, with the sun directly overhead, light scattered at the horizon will be polarized horizontally. This is a simple way to determine the orientation of a polarizer, if no second, known polarizer is at hand.

## 4.2.  The Charge Generation Process

Exciton   Quasiparticle consisting of an electron–hole pair in an excited state, bound by the Coulomb interaction.

[KB15] Anna Köhler et al. *Electronic Processes in Organic Semiconductors* (2015)

When sunlight is incident on an organic photovoltaic cell, charges are made available at the electrodes to do useful work. This charge generation process in OPV can be decomposed into four distinct steps, which we will now describe in more detail [KB15].

1.  Absorption of light and generation of excitons.
2.  Exciton diffusion towards a heterojunction.
3.  Separation of the exciton into free charges at the heterojunction.
4.  Drift towards the electrodes, where free charges are collected.

The steps are sketched in Figures 4.2 to 4.5 for light absorption in the polymer donor, which is typically the case in polymer:fullerene cells.

LIGHT ABSORPTION   Light that is incident onto a solar cell, will be absorbed, if its energy is larger than the energy band gap of the semiconductor in question. In this case, electrons can be excited from the HOMO to the LUMO, generating excitons. In inorganic semiconductors like silicon, free charges are generated directly, since the attractive force due to the electric field between electron and hole is strongly screened by the comparatively large relative permittivity. Table 4.1 compares the typical binding energy $E_{\text{binding}}$ to that of excitons in organic semiconductors, which are so strongly bound that both charges may even be located on the same molecule.

Loss mechanisms which reduce the efficiency at this stage are of two types. There are the inevitable losses due to a trade-off between absorption of low energy photons, and thermalization of high energy photons, which were already mentioned. And then there are losses due to light that is not absorbed, even when it could be. These losses can be minimized by increasing the absorption of light in the active layer. For example by increasing the absorption of the used semiconductor, or by increasing the time light spends inside the active layer. This can be achieved in a simple way by increasing the thickness of the active layer, or in more elaborate ways by scattering light, or using interference effects.

EXCITON DIFFUSION   Because of its large binding energy, the exciton cannot dissociate in an organic photovoltaic cell composed of a single, pure material. Because of this limitation, a second semiconductor is needed, forming a heterojunction. In these structures, excitons diffuse along a gradient in chemical potential towards an interface with the second semiconductor. It should be emphasized that this is a diffusive process, because the exciton carries no net charge, and therefore cannot drift along a gradient in electrical potential.

Due to its finite lifetime, the exciton will decay if it does not reach such a donor–acceptor interface in time. This effectively wastes the absorbed photon, unless it is reabsorbed upon exciton decay, potentially allowing for efficient photon recycling, like in perovskite solar cells [PSL+16]. Losses at this stage can be reduced by ensuring that excitons can reach an interface. In OPV, which have a typical exciton diffusion length below 10 nm, this is done by using bulk heterojunctions, which have a massively increased interfacial area compared to a simple bilayer.

EXCITON DISSOCIATION   Once it reaches a heterojunction interface, the exciton can dissociate into a less strongly bound charge transfer state, if the energy level alignment at the donor–acceptor interface is favorable. The energy required to dissociate, is provided by the difference in donor and acceptor LUMO if an electron crosses the interface, or by the difference in acceptor and donor HOMO for the opposite case of hole transfer.

This geminate pair can either recombine by geminate recombination, or dissociate into a charge separated state, which is nothing more than a pair of free charges.

DRIFT TOWARDS THE ELECTRODES   Before being collected at the electrodes, charges have to reach them by drifting along the

$\varepsilon_r$ Relative permittivity   Factor by which the electric field between two charges is decreased compared to vacuum. Also called dielectric constant.
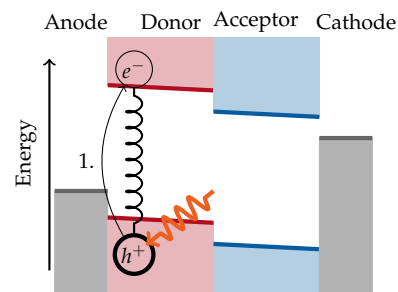


Figure 4.2: Exciton generation.

Table 4.1: Typical exciton binding energy $E_{\text{Binding}}$.

|  | $E_{\text{Binding}}$ |
| --- | --- |
| Organics | 0.3–0.5 eV |
| Inorganics | 10 meV |
| $k_{\text{B}}T\vert_{T=300\,\text{K}}$ | 26 meV |

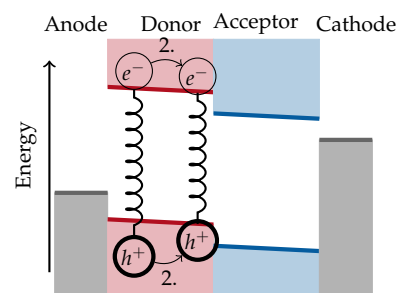Heterojunction   Interface between two semiconductors with unequal band gap.



Figure 4.3: Exciton diffusion.

[PSL+16] Luis M. Pazos-Outón et al. *Science*, **351**, 1430 (2016)

Charge transfer state   Weakly bound, energetically favorable state across a donor–acceptor interface.

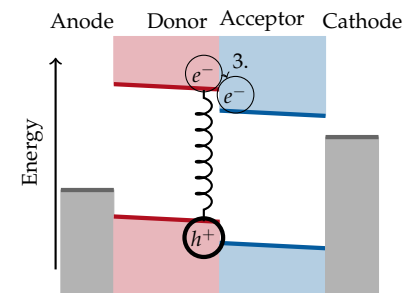Geminate pair   An electron–hole pair originating from the same exciton.



Figure 4.4: Exciton dissociation.

**Bimolecular recombination**  The recombination of electrons and holes originating from different excitons.
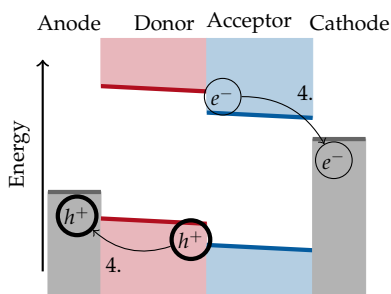


Figure 4.5: Charge extraction.

[SSH+92] Niyazi Serdar Sariciftci et al. *Science*, **258**, 1474 (1992)

[BZC+01] Christoph J. Brabec et al. *Chem. Phys. Lett.* **340**, 232 (2001)

[ML15] Katherine A. Mazzio et al. *Chem. Soc. Rev.* **44**, 78 (2015)

[SRM11] Jonathan D. Servaites et al. *Energy Environ. Sci.* **4**, 4410 (2011)

[CD10] Tracey M. Clarke et al. *Chem. Rev.* **110**, 6736 (2010)

[FFN15a] Sheridan Few et al. *Phys. Chem. Chem. Phys.* **17**, 2311 (2015)
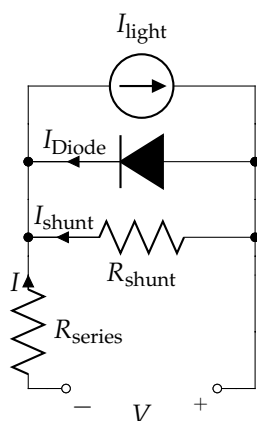
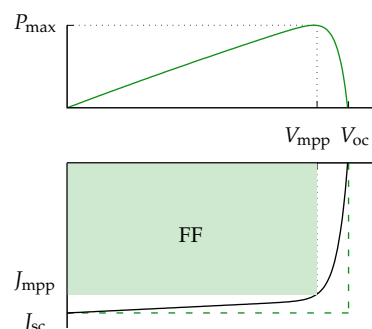Figure 4.6: Equivalent circuit of a photovoltaic device.



Figure 4.7: Current density and generated power of a solar cell versus voltage.

gradient in electric potential, that is inbuilt into the device due to the nonidentical work functions of the electrodes.

On their way to the electrodes, charges can be lost due to bimolecular recombination. This is particularly pronounced when charges accumulate due to low charge carrier mobility or a tortuous and long pathway to the electrodes. Bimolecular recombination can be decreased by reducing the distance to the electrodes in thinner active layers for example, or by isolating separated electrons from holes, like they are in the pure domains of a bilayer architecture.

Photoinduced charge transfer from a conjugated polymer to a fullerene was first demonstrated in [SSH+92]. The observed charge transfer is a very effective process that happens below the picosecond timescale [BZC+01] and which is the basis for these excitonic solar cells that rely on interfaces to dissociate charges. A quick yet complete introduction suitable as a first reading on OPV is [ML15], while more details on the photogeneration of charges are available in [SRM11] [CD10] [FFN15a].

## 4.3. Equivalent Circuit Model

The behavior of any solar cell can be more or less approximated by the equivalent circuit model sketched in Figure 4.6. In its simplest form, it consists of a current source—the photogenerated current generated upon illumination—connected in parallel with a diode. Because no electrical component is perfect, two resistances have to be included to account for losses. The current $I$ that can be extracted from the circuit can be read directly from Figure 4.6

$$I = I_{\text{light}} - I_{\text{Diode}} - I_{\text{shunt}} \tag{4.4}$$

The same is possible for the voltages in the circuit.

$$V_{\text{Diode}} = V_{\text{shunt}} = V + IR_{\text{series}} \tag{4.5}$$

The current through the diode is described by the Shockley diode equation.

$$I_{\text{Diode}} = I_0 \left( e^{\frac{eV_{\text{Diode}}}{nk_{\text{B}}T}} - 1 \right) \tag{4.6}$$

Here $n$ is the diode ideality factor. This empirical fitting factor has a value of 1 for an ideal diode, and in most cases takes values of $1 \leq n \leq 2$. $I_0$ is the device specific reverse saturation current. By definition, a positive applied voltage $V_{\text{Diode}} > 0$ across the diode results in an exponential increase in current—the diode is said to be in forward bias. Substituting these in (4.4) gives the characteristic equation of a solar cell plotted in Figure 4.7, which relates the measurable current and voltage in the circuit to the solar cell parameters.

$$I = I_{\text{light}} \quad -I_0 \left( e^{\frac{e(V+IR_{\text{series}})}{nk_{\text{B}}T}} - 1 \right) \quad -\frac{V + IR_{\text{series}}}{R_{\text{shunt}}} \tag{4.7}$$

This model does not capture all the intricacies of organic solar cells. For example, the photogenerated current appears as a simple offset, such that an IV-curve measured in the dark and another measured

under light will never cross, which is not what is observed experimentally. Extensions to this basic model exist, for example including a second diode with a different ideality factor.

## 4.4. Important Parameters

Most parameters in this theoretical derivation cannot be measured directly. Instead, the parameters of interest indicated in Figure 4.7 are used to gauge the performance of photovoltaic cells. Some typical values are given in Table 4.2.

DENSITIES  Because parameters like the current $I$ and the resistances $R$ depend on the size of the solar cell in question, it is customary to normalize by the device active area. When comparing different devices, current densities and resistances per unit area are compared.

OPEN CIRCUIT VOLTAGE  As is obvious from its name, the open circuit voltage is the voltage that builds up across an illuminated solar cell, if no current is allowed to flow. A first approximation for $V_{oc}$ can be obtained from the difference between the HOMO of the donor and the LUMO of the acceptor. While this energy level difference does not exactly translate to $V_{oc}$, a strong correlation has been observed and explained [VTG+09].

SHORT CIRCUIT CURRENT DENSITY  Analogously, the short circuit current density is measured without an applied voltage bias. The sign of this current can vary with convention. Here we will use a negative sign of the current for a positive applied voltage, to indicate that energy is generated in the solar cell.

SERIES RESISTANCE  The series resistance accounts for the resistance of the contacts, and of the bulk and interface resistances of all the constituent layers of the solar cell. It can be estimated from the inverse of the slope of the I-V curve at $V = V_{oc}$.

SHUNT RESISTANCE  A finite shunt resistance is caused by leakage currents in the device, normally due to trap states, edge effects or pinholes in layers. All of these undesired effects lead to a decrease of $R_{shunt}$, affecting the JV-curve as sketched in Figure 4.8. $R_{shunt}$ can be estimated from the inverse of the slope of the I-V curve at $V = 0$

FILL FACTOR  The contributions of the resistances and other non-idealties to the shape of the JV-curve are subsumed into a single parameter, the fill factor. It is defined using the voltage $V_{mpp}$ and current density $J_{mpp}$ at the point of maximum power generation.

$$FF = \frac{J_{mpp} V_{mpp}}{J_{sc} V_{oc}} \qquad (4.8)$$

POWER CONVERSION EFFICIENCY  The final power conversion efficiency is then given by

$$\eta = \frac{P_{out}}{P_{in}} = \frac{V_{oc} J_{sc} FF}{\frac{P_{in}}{A}}, \qquad (4.9)$$

Table 4.2: Typical parameters of a P3HT:PCBM solar cell.

| | |
|---|---|
| $J_{sc}$ | $10\,\mathrm{mA\,cm^{-2}}$ |
| $V_{oc}$ | $0.6\,\mathrm{V}$ |
| FF | $60\,\%$ |
| $R_{series}/A$ | $10\,\mathrm{k\Omega\,cm^{-2}}$ |
| $R_{shunt}/A$ | $600\,\mathrm{k\Omega\,cm^{-2}}$ |
| $\eta$ | $3.6\,\%$ |

$A$ Device active area

$V_{oc}$ Open circuit voltage

[VTG+09] Koen Vandewal et al. *Nat. Mater.* **8**, 904 (2009)

$J_{sc}$ Short circuit current density

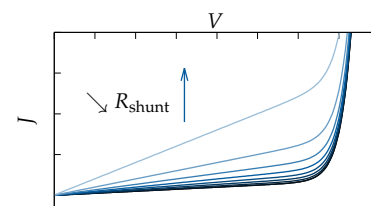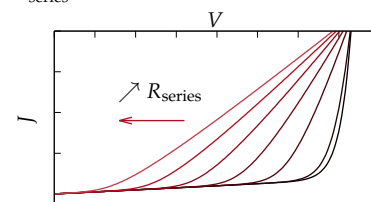$R_{series}$ Series resistance





Figure 4.8: Effect of $R_{series}$ and $R_{shunt}$ on the JV-curve.

$R_{shunt}$ Shunt resistance

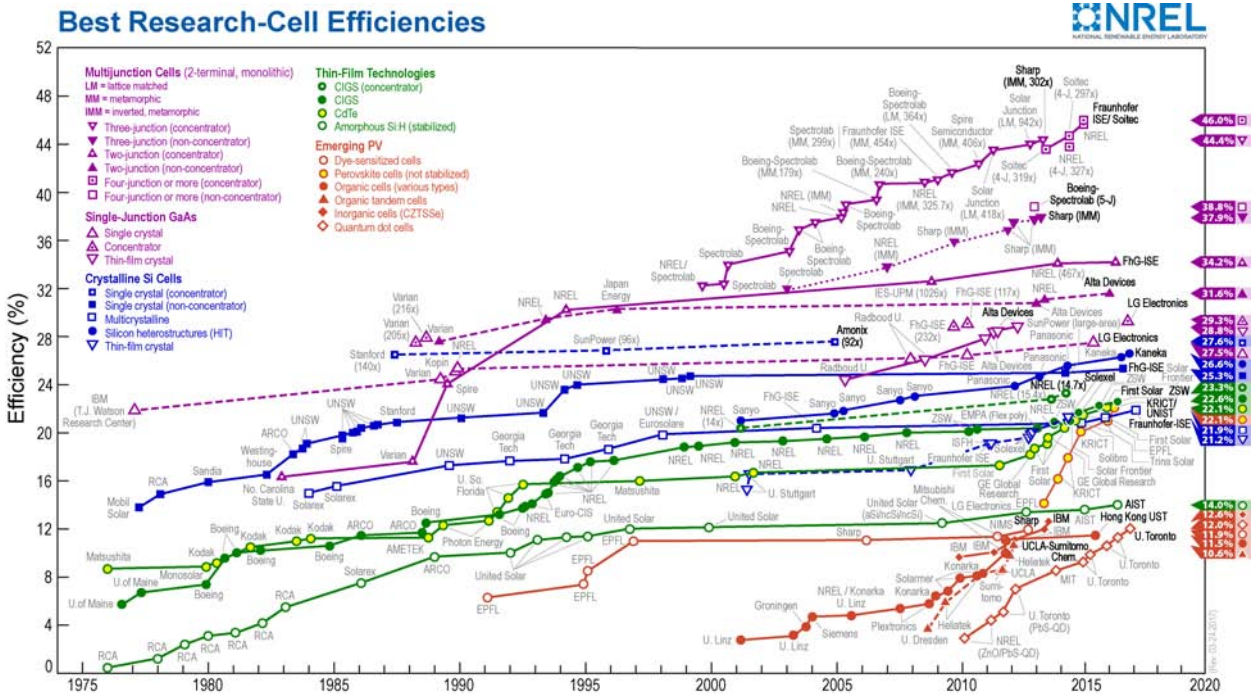FF Fill factor  A measure of the "squareness" of the JV-curve.

Figure 4.9: Certified record efficiencies for different photovoltaic technologies over time. The version shown is from March 2017. An up-to-date version of the chart is maintained at http://www.nrel.gov/pv/.

with the device active area $A$ and $\frac{P_{in}}{A} = 1000\,\text{W}\,\text{m}^{-2}$ under standardized test conditions.

The state of the art power conversion efficiencies of a wide variety of solar cell technologies are summarised regularly by NREL in the chart shown in Figure 4.9. For a succinct review of the different technologies and the challenges they face, see [PKG+16].

[PKG+16] Albert Polman et al. *Science*, **352**, aad4424 (2016)

EQE External quantum efficiency
The number of generated charges per incoming photon.

EXTERNAL QUANTUM EFFICIENCY  The external quantum efficiency is the efficiency of charge generation at a particular wavelength. It can be represented as a product of four probabilities, corresponding to the four main processes involved in charge generation, as given in (4.10) and already described in detail.

$$\text{EQE}(\lambda) = \eta_{\text{abs}}(\lambda)\eta_{\text{diff}}(\lambda)\eta_{\text{diss}}(\lambda)\eta_{\text{coll}}(\lambda) \tag{4.10}$$

Here $\eta_{\text{abs}}$ is the probability of an incident photon to be absorbed in the active layer, $\eta_{\text{diff}}$ is the probability that an exciton reaches a donor–acceptor interface, $\eta_{\text{diss}}$ is the probability that an exciton successfully dissociates into free charges at the interface, and $\eta_{\text{coll}}$ is the probability that these free charges successfully drift to the electrodes, where they can be collected.

When measuring the EQE, what one really measures is the dependence of the photocurrent on wavelength. The EQE can then be calculated from.

$$\text{EQE} = \frac{J_{\text{sc}}(\lambda)}{F(\lambda)}\frac{hc}{e\lambda} \tag{4.11}$$

The EQE can not only be used to determine wavelengths for which a particular device perfoms well, but it also serves as a cross-check for $J_{\text{sc}}$, since both values are normally measured using different

equipment [ZEP+14]. To calculate $J_{sc}$ from the EQE, (4.12) can be used.

$$J_{sc}^{calc} = e \int \text{EQE}(\lambda) N_p(\lambda) \, d\lambda \qquad (4.12)$$

where $e$ is the elementary charge, and $N_p$ is the number of incident photons per second per unit area. Based on the evaluation of reported values for $J_{sc}$ and EQE, a recent survey showed that 37 % of publications overestimate efficiency [ZEP+14]. Similarly, a round-robin study showed that differences between laboratories can be as large as $\Delta \eta = 15\,\%$ for OPV, and 7 % for silicon reference cells [GZS+14].

INTERNAL QUANTUM EFFICIENCY    Another related parameter is the internal quantum efficiency, which can be obtained from the EQE if $\eta_{abs}$ is known.

$$\text{IQE} = \frac{\text{EQE}}{1 - T - R} \qquad (4.13)$$

Here $T$ is the transmission coefficient, $R$ is the reflection coefficient, and therefore $1 - T - R$ is the fraction of light that is absorbed. It is important to have in mind, that only the light absorbed in the active layer should be considered, since only that part actually generates charges. For this reason, calculating the IQE is not as trivial as (4.13) may lead to believe, and care has to be taken when combining measurements done on different samples [AVW+14], since the presence of a reflective electrode for example, not only increases parasitic absorption, but also changes the intensity distribution due to interference.

## 4.5.  Active Layer Morphology

A SINGLE MATERIAL    Organic materials do not perform well as photovoltaic devices if only a single material is used, because the binding energy of excitons is so high, that they cannot dissociate on their own at room temperature. When they do dissociate however, the charges drift apart because of the inbuilt electric field that is due to the work function difference of the dissimilar electrode materials [GMF+74].

NANOMETRICALLY MIXED BLEND    In order to ensure that most of the photogenerated excitons can be dissociated, an interface with favorable energy level alignment has to be close enough, so that the exciton can reach it during its lifetime. While the energy level alignment is important for the maximum achievable efficiency [SMK+06], in practice, morphology is the dominant limiting factor [JSM+15]. In a typical organic semiconductor, the average distance from any point in the bulk to an interface has to be of the order of 1–10 nm [HPF+96] [SSS+14]. If this were the only constraint, then an ideal active layer morphology that maximizes $\eta_{diff}$, would be a completely intermixed one, which could look something like Figure 4.10.

BILAYER    In an active layer like Figure 4.10, $\eta_{coll}$ is minimal. No charges are collected, since there are no unbroken pathways connecting to the electrodes. A morphology that optimizes $\eta_{coll}$, sketched in Figure 4.11, is a simple bilayer that optimizes the pathways towards the electrodes [Tan86]. It is immediately apparent that for such a

[ZEP+14] Eugen Zimmermann et al. *Nat. Photonics*, **8**, 669 (2014)

[GZS+14] Suren A. Gevorgyan et al. *Renew. Energy*, **63**, 376 (2014)

IQE Internal quantum efficiency    The number of generated charges per photon absorbed in the active layer.

[AVW+14] Ardalan Armin et al. *ACS Photonics*, **1**, 173 (2014)

[GMF+74] Amal K. Ghosh et al. *J. Appl. Phys.* **45**, 230 (1974)

[SMK+06] Markus C. Scharber et al. *Adv. Mater.* **18**, 789 (2006)

Morphology    The microscale organization and ordering of polymer chains.

[JSM+15] Nicholas E. Jackson et al. *J. Phys. Chem. Lett.* **6**, 77 (2015)

[HPF+96] Jonathan J M Halls et al. *Appl. Phys. Lett.* **68**, 3120 (1996)

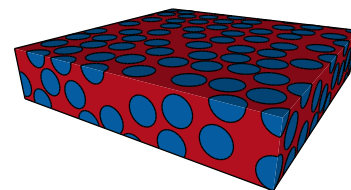[SSS+14] Myungsun Sim et al. *J. Phys. Chem. C*, **118**, 760 (2014)

Figure 4.10: Active layer morphology that optimizes exciton dissociation.

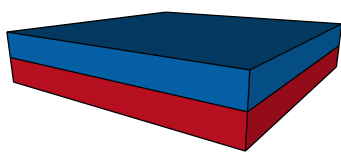[Tan86] C. W. Tang. *Appl. Phys. Lett.* **48**, 183 (1986)

Figure 4.11: Bilayer morphology, which optimizes charge collection.
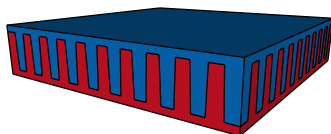


Figure 4.12: Optimal active layer morphology.

BHJ Bulk heterojunction   Hetero-junction with a large interfacial area between two unbroken phases.

[YH95] G. Yu et al.
*J. Appl. Phys.* **78**, 4510 (1995)

[HWG+95] J. J. M. Halls et al.
*Nature*, **376**, 498 (1995)

[YGH+95] G. Yu et al.
*Science*, **270**, 1789 (1995)

[SWB02] Pavel Schilinsky et al.
*Appl. Phys. Lett.* **81**, 3885 (2002)

[LZL+14] Yuhang Liu et al.
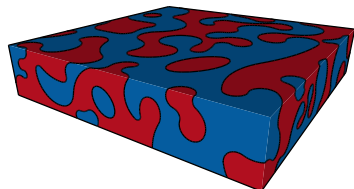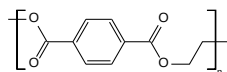*Nat. Commun.* **5**, 5293 (2014)



Figure 4.13: Bulk heterojunction morphology.



PET
Polyethylene terephthalate

ITO Indium tin oxide   Transparent conductor.

morphology, the interfacial area between donor and acceptor components is orders of magnitude smaller, and consequently the number of excitons that can actually dissociate at the interface is tiny compared to a nanometric blend.

OPTIMAL MORPHOLOGY   Thus, a trade-off between exciton diffusion to an interface $\eta_{\mathrm{diff}}$ and charge collection at the electrodes $\eta_{\mathrm{coll}}$ has to be found. The morphology shown in Figure 4.12 could be regarded as optimal. It maximizes surface area, while allowing for direct paths to the connecting electrodes. Wetting layers of donor on the anode and acceptor on the cathode side of the device additionally bar charges from reaching the wrong electrode, thereby further increasing current. The drawback of this optimal morphology, is that it is prohibitively complicated and thus expensive to fabricate.

BULK HETEROJUNCTION   An astonishingly simple way to prepare a morphology that is quite similar to the optimal one, is by directly processing two or more materials from the same solution [YH95] [HWG+95] [YGH+95]. The resulting morphology, shown in Figure 4.13, is known as a bulk heterojunction. Ideally, a morphology that is sufficiently fine grained, yet still has pure and connected domains, can be prepared. The first promising results of a BHJ using P3HT and PCBM reported an EQE of 76 %, and an IQE close to unity [SWB02].

The process of forming the desired morphology is very sensitive to a range of parameters, most importantly the drying kinetics and the solubility of the semiconductors in the solvent as well as in each other. Furthermore, it is possible to trap metastable morphologies, for example for polymers that require elevated temperatures to fully dissolve [LZL+14]. During deposition, the solution cools down and the polymer aggregates. While these elaborate processing protocols have allowed to reach record efficiencies, they are also a disadvantage. Device performance eventually degrades, because the resulting morphologies are not in a thermodynamic ground state.

## 4.6. Device Geometry

Every organic solar cell consists of several layers, the order of which depends on the particular device geometry.

*Substrate*  Serves as a support. For devices prepared in the lab, substrates are typically made of glass, or PET if flexibility is required, for example during roll-to-roll coating.

*Active layer*  Consists typically of a bulk heterojunction or a bilayer of a donor polymer like P3HT and a fullerene acceptor like PCBM.

*Electrodes*  Charges are extracted at the electrodes.

  *Anode*  Holes are extracted at the anode. Typical anode materials are sputter-deposited indium tin oxide or evaporated silver.

  *Cathode*  Electrons are extracted at the cathode, which is typically made from evaporated aluminium or ITO.

*Charge blocking layers*  To maximize efficiency, one has to ensure to only collect a single type of charge at each electrode. Because this cannot be guaranteed with the limited number of viable electrode materials, an additional charge selective layer may be necessary.

*Hole blocking layer*  To stop holes from reaching an aluminium cathode, a layer of $< 1\,\mathrm{nm}$ of LiF or $20\,\mathrm{nm}$ of Ca can be evaporated, beforehand. On an ITO cathode, typically ZnO is used.

*Electron blocking layer*  On an ITO anode on the other hand, solution-deposited PEDOT:PSS allows only holes to pass. Together with a silver anode, $MoO_3$ is typically used.

NORMAL GEOMETRY  The standard device geometry used for OPV devices is pictured in Figure 4.14. In the most basic case, the layer stack consists of ITO, PEDOT:PSS, the active layer and an evaporated Al cathode.

INVERTED GEOMETRY  The normal geometry has several problems related to device stability. Among them are the acidity and hydrophilicity of PEDOT:PSS, which may degrade devices from within. In fact, it has been shown that due to its acidic, as well as hygroscopic nature, PEDOT:PSS etches ITO during deposition and when exposed to a humid atmosphere [JIV00]. Another problem is that the low work function metal electrode—the one that is more susceptible to oxidation—is exposed to air and humidity. The inverted geometry, where to order of layers is reversed, increases stability, though the use of PEDOT:PSS remains problematic [LPG+11].

TANDEM CELLS  A meta-geometry if you will, is that of tandem cells, which are basically several cells stacked on top of each other, separated by aptly named charge recombination layers. While this increases complexity, tandem cells do have tangible benefits, which are related to light absorption, and the Shockley-Queisser limit. This limit only holds for a single junction device. It can be circumvented by stacking materials with different, ideally non-overlapping, absorption spectra. If sunlight first traverses the subcell that absorbs at higher energy—the one with the largest band gap—then high energy photons are absorbed with less thermalization losses than would occur in the second subcell. Low energy photons are not absorbed, yet they are not wasted either, since they pass on to the second, lower bad gap subcell.

While this sounds simple, and in principle would allow the subdivision into infinitely many subcells with increasingly narrow, successive absorption profiles, there are practical limitations. In most cases, subcells are connected electrically in series, which requires the same amount of current to pass through all of them. Because the generated current depends on the thickness and absorption profile of each subcell, this places stringent requirements on potential materials. If currents are not matched, charges will accumulate in the device, resulting in increased recombination. Furthermore, we assumed that light passes unhindered from one subcell to the next. However, that presupposes that the layers connecting the subcells are perfectly transparent, which of course, they are not.

For example, when starting the preparation of this manuscript, the record efficiency of a single cell was $\eta = 10.5\,\%$ [LZL+14], while that of tandem cells was of a similar value [YDY+13]. Triple junction cells were reported with $\eta = 11.5\,\%$ [CCY+14]. In the meantime, single junction cells have caught up, achieving $\eta = 11.7\,\%$ [ZLY+16].
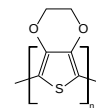
PEDOT
Poly(3,4-ethylenedioxythiophene)
Transparent conducting polymer.
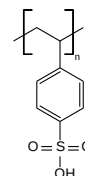
PSS
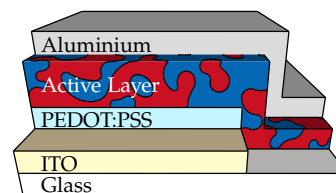Poly(styrenesulfonate)  Water-soluble polymer, used to disperse and dope PEDOT.



Figure 4.14: Normal OPV cell geometry, where the anode is deposited first, and light enters from the anode side.

[JIV00] M. P. de Jong et al.
*App. Phys. Lett.* **77**, 2255 (2000)

[LPG+11] Matthew T. Lloyd et al.
*Sol. Energy Mater. Sol. Cells*, **95**, 1382 (2011)

[LZL+14] Yuhang Liu et al.
*Nat. Commun.* **5**, 5293 (2014)

[YDY+13] Jingbi You et al.
*Nat. Commun.* **4**, 1446 (2013)

[CCY+14] Chun-Chao Chen et al.
*Adv. Mater.* **26**, 5670 (2014)

[ZLY+16] Jingbo Zhao et al.
*Nat. Energy*, **1**, 15027 (2016)

A method to deposit films of oriented polymers is presented in Chapter 7: Oriented Polymer Layers, which will be followed by the results on organic photovoltaic devices that incorporate these oriented films, summarized in Chapter 8: Oriented Photovoltaics.

# II

# RESULTS



● to live
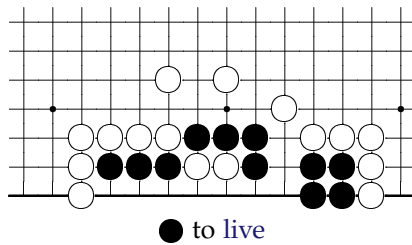
# ELLIPSOMETRY

<div style="text-align: right; font-size: 3em;">5</div>

Ellipsometry is a non-invasive optical characterization method [AB77]. Traditionally, it has been used to accurately determine the optical properties and thickness of thin films of inorganic semiconductors, though more recently, ellipsometry is increasingly used to characterize organic semiconducting materials as well [CAB+14].

The determined optical constants allow to accurately model OPV device structures using transfer matrix models. In blends, they allow to gain an understanding of the morphology and vertical phase segregation, which are important factors affecting device efficiency. In doped polymers, ellipsometry may provide information regarding the efficiency and the degree of doping, which is important information for thermoelectric applications.

For this thesis, a variety of conjugated polymers, and their blends with fullerenes have been characterized by variable angle spectroscopic ellipsometry. This chapter briefly summarizes the obtained results.

Ellipsometry   Coherent measurement of the change in polarization state of light reflected from materials.

[AB77] R.M.A. Azzam et al. *Ellipsometry and Polarized Light* (1977)

[CAB+14] Mariano Campoy-Quiles et al.
*Adv. Funct. Mater.* **24**, 2116 (2014)

## 5.1. Theory

POLARIZATION OF LIGHT   Any ray of light can be written as a superposition of orthogonally polarized plane waves [HZ02]. A particularly useful convention for light incident on a surface, is to consider polarizations parallel and perpendicular to the plane of incidence—the plane that is spanned by the incident ray and the surface normal.  Depending on the amplitude change and phase shift between the two components, the resulting superposition can be linearly, circularly or in the general case, elliptically polarized—giving the method its name.

[HZ02] Eugene Hecht et al. *Optics* (2002)

$$E = E_0 \exp[\mathrm{i}(kx - \omega t + \delta)] \tag{5.1}$$

The propagation of light inside a medium is characterized by the complex index of refraction.

$$n + \mathrm{i}k \tag{5.2}$$

where the real part $n = \frac{c}{v}$, which is responsible for refraction, is the ratio of the speed of light in vacuum and the phase velocity $v$ of light in the medium. The extinction coefficient $k$ quantifies the absorption of light. These material properties can also be given in the form of the dielectric function.

$$\varepsilon_\mathrm{r} + \mathrm{i}\varepsilon_\mathrm{i} = (n + \mathrm{i}k)^2 \tag{5.3}$$

At the interface with the medium, light may be reflected, as sketched in Figure 5.1. The Fresnel reflection coefficients $r_\mathrm{s/p} = \left(\frac{E_\mathrm{r}}{E_\mathrm{i}}\right)_\mathrm{s/p}$ are defined as the ratio of the reflected electric field $E_\mathrm{r}$ to the incoming field

$c$ Speed of light   Defined as $299\,792\,458\,\mathrm{m\,s^{-1}}$ in vacuum.
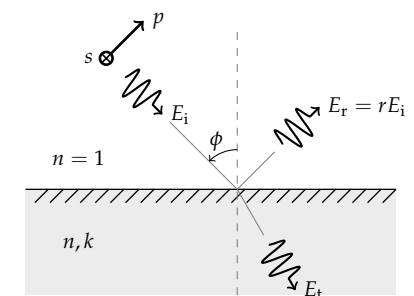


Figure 5.1: Ray of light incident at an interface.

$\phi$ Angle of incidence

Table 5.1: Average refractive index $n$ in the visible spectral range for some common materials.

| | $n$ |
|---|---|
| Vacuum | 1 |
| Water | 1.33 |
| Fused quartz | 1.46 |
| PMMA | 1.49 |
| Glasses | $1.5 - 1.6$ |
| Diamond | 2.45 |
| Crystalline Silicon | $4 - 7$ |

**Dichroism** Selective absorption of one polarization direction of light, $k = k(\varphi)$. When this absorption is wavelength dependent, this results in two colors, hence the name.

**Birefringence** Both refraction and absorption depend on the polarization of light, $n + \mathrm{i}k = n(\varphi) + \mathrm{i}k(\varphi)$. This may lead to double refraction, a single beam of light splitting up in two, explaining the name.

[TI05] Harland G. Tompkins et al. *Handbook of Ellipsometry* (2005)

$E_\mathrm{i}$, for a given polarization p or s. The indices refer to polarization parallel or perpendicular to the plane of incidence respectively, named for their German expressions "parallel" and "senkrecht". Apart from the material, the Fresnel reflection coefficients strongly depend on the angle of incidence of the incoming light ray relative to the surface normal. Some average values for $n$ are given in Table 5.1. Importantly, both $n$ and $k$ depend on the wavelength, as well as on the polarization, giving rise to dichroism or more generally, birefringence.

While reflectometry just measures the amplitude of the reflected light $I_\mathrm{r} \propto |E_\mathrm{r}|^2 \propto |r|^2$ for both polarizations, ellipsometry measures both the amplitude as well as the phase information in the form of the complex reflectance ratio [TI05].

$$\rho = \frac{r_\mathrm{p}}{r_\mathrm{s}} = \tan(\Psi)\mathrm{e}^{\mathrm{i}\Delta} \tag{5.4}$$

As given in (5.4), $\rho$ can be written in terms of the ellipsometric angles $\Psi$ and $\Delta$, emphasizing that upon reflection, the light undergoes a relative phase shift $\Delta$ between the two polarizations, as well as a change in the amplitude ratio $\tan(\Psi)$. Because ellipsometry also measures the phase of the light, results strongly depend on wavelength dependent interference effects in thin films. For accurate results, the ellipsometric angles should be measured for several angles of incidence, centered around the effective Brewster angle, since there the relative variation of polarization is largest.

## 5.2. Modeling the Dielectric Function

To obtain the complex refractive index from the measured values of $\tan(\Psi)$ and $\cos(\Delta)$, the sample is modeled as a stack of discrete, homogeneous layers. The simplest case being a single interface between a semi-infinite substrate and the semi-infinite surrounding vacuum. With each additional thin film that is placed on top of the substrate, the calculations become more complex due to the interference of incident and multiply reflected rays of light.

[Fuj07] Hiroyuki Fujiwara. *Spectroscopic Ellipsometry: Principles and Applications* (2007)

Since only the simplest geometries can be solved analytically, the optical constants are instead obtained by numerical minimization of the error between the experiment and the modeled values obtained from transfer-matrix calculations of the light reflected by the stack [Fuj07].

In this work three different models to parametrize the complex refractive index have been used. The modified Cauchy law and the Tauc-Lorentz model have been used for glass substrates, which are nearly transparent in the visible spectral range. Thin films of organic materials have been parametrized using the standard critical point model.

[Cau30] Louis Cauchy. *Bull. des Sci. Mathématiques*, **14**, 9 (1830)

CAUCHY LAW The Cauchy law is the first empirical dispersion relation [Cau30]. It works best for materials that are not absorbing. In this case materials exhibit normal dispersion—the refractive index $n$ monotonously decreases with increasing wavelength, which can be approximated by the simple relation in (5.5). The Cauchy law may

be used to model small extinction coefficients $k$, approximating the remaining tail of absorption at higher energies.

$$n = A + \frac{B}{\lambda^2} + \frac{C}{\lambda^4} + \dots$$
$$k = \frac{D}{\lambda} + \frac{E}{\lambda^3} + \frac{F}{\lambda^5} + \dots$$

(5.5)

$A$ through $F$ are fitting parameters. It is also possible, and indeed may be preferable in some situations to fit the complex dielectric function $\varepsilon_r$ and $\varepsilon_i$ instead of $n$ and $k$ with an identical relation.

MODIFIED CAUCHY LAW   When including small levels of absorption, a modified Cauchy law on $n$ and $k$ may be better suited to fit the refractive index of glass substrates in some situations.

$$n = A + \frac{B}{\lambda^2} + \frac{C}{\lambda^4}$$
$$k = D + \frac{E}{\lambda^2} + \frac{F}{\lambda^4}$$

(5.6)

TAUC LORENTZ MODEL   When it is necessary to include the strong absorption of glass in the UV-range, then the Tauc-Lorentz model is better suited. It allows to include a rapidly increasing absorption above a certain band gap for $E \geq E_g$. The model is an extension of the Tauc joint density of states, incorporating Lorentz oscillators [JM96b] [JM96a]. The imaginary part $\varepsilon_i$ of the dielectric function is modeled as

[JM96b] Gerald E. Jellison et al. *Appl. Phys. Lett.* **69**, 371 (1996)

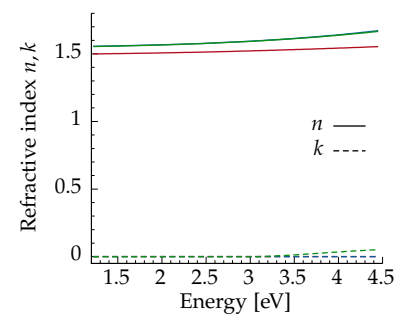[JM96a] Gerald E. Jellison et al. *Appl. Phys. Lett.* **69**, 2137 (1996)

$$\varepsilon_i(E) = \begin{cases} \dfrac{1}{E} \displaystyle\sum_{n=1}^{N} \dfrac{A_n E_n C_n \left(E - E_g\right)^2}{\left(E^2 - E_n^2\right)^2 + C_n^2 E^2} & \text{for } E > E_g \\ 0 & \text{for } E \leq E_g \end{cases}$$

(5.7)

where the fitting parameters are the peak transition energy $E_n$ of the $n$th Lorentzian peak, the broadening term $C_n$, $A_n$ which is proportional to the transition probability matrix element, and the optical band gap $E_g$. The real part $\varepsilon_r$ of the dielectric function is derived from $\varepsilon_i$ using the Kramers-Kronig relation.

$$\varepsilon_r(E) = \varepsilon_r(\infty) + \frac{2}{\pi} \fint_{-\infty}^{\infty} \frac{\varepsilon_i(\xi)}{\xi - E} \, d\xi$$

(5.8)

where $\fint$ denotes the Cauchy principal value. The high frequency dielectric constant $\varepsilon_r(\infty)$ is the last fitting parameter.



Figure 5.2: Complex refractive index of two different glass substrates. The first ● and second ● substrate were fit using a Cauchy law, neglecting absorption. The second substrate was also fit using a Tauc-Lorentz law, giving effectively the same $n$, but nonzero $k$ ●.

GLASS SUBSTRATES   Figure 5.2 shows results of the complex refractive index obtained for substrates made from two different types of glass. Measurements were fit using a Cauchy law without absorption, as well as a Tauc-Lorentz model with 2 peaks and a fixed band gap energy of $E_g = 3\,\text{eV}$. The results are presented mainly to demonstrate the small wavelength dependence of $n$, and the negligible $k$ of glass substrates, compared to conjugated polymers presented in the following sections..

STANDARD CRITICAL POINT MODEL   To model the optical constants of semiconductors, the standard critical point model has been

[LGV+87] P. Lautenschlager et al.
*Phys. Rev. B*, **36**, 4821 (1987)

[Gar90] Miquel Garriga Bacardi. PhD thesis. 1990

[ZGH+91] Stefan Zollner et al.
*Phys. Rev. B*, **43**, 4349 (1991)

[ZGK+93] Stefan Zollner et al.
*Thin Solid Films*, **233**, 185 (1993)

[Cam05] Mariano Campoy-Quiles. PhD thesis. 2005

[CHX+05] Mariano Campoy-Quiles et al.
*Adv. Funct. Mater.* **15**, 925 (2005)

[CEB05] Mariano Campoy-Quiles et al.
*Synth. Met.* **155**, 279 (2005)

[CNB+07] Mariano Campoy-Quiles et al.
*Phys. Rev. B*, **76**, 235206 (2007)

All of the refractive indices presented in this section have been published in [GDR+13] Antonio Guerrero et al. *ACS Nano*, **7**, 4637 (2013).



PCPDTBT
Poly[2,6-(4,4-bis-(2-ethylhexyl)-4H-cyclopenta [2,1-b;3,4-b']dithiophene)-alt-4,7(2,1,3-benzothiadiazole)]
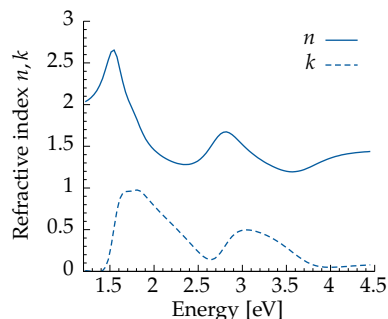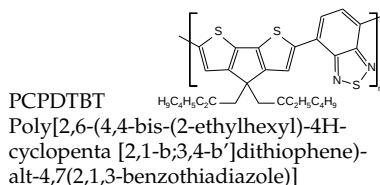


Figure 5.3: Complex refractive index of PCPDTBT.

Table 5.2: Fit parameters of the standard critical point model used to model the complex refractive index of PCPDTBT.

| $n$ | $A_n$ | $E_{c,n}$ | $\Gamma_n$ | $\phi_n$ |
|---|---|---|---|---|
| 1 | 0.445 | 1.549 | 0.110 | -1.211 |
| 2 | 1.333 | 1.525 | 0.775 | -0.331 |
| 3 | 0.080 | 1.793 | 0.124 | -0.369 |
| 4 | 0.342 | 2.771 | 0.227 | -1.768 |
| 5 | 0.355 | 3.705 | 0.495 | 2.528 |
| UV term | 2.2941 | $t_{\text{fixed}}$ | 29 nm | |

Figure 5.4: Comparison between the measured ellipsometric angles and the modeled values for PCPDTBT. The standard deviation $\sigma$ of the fit was $2.2 \times 10^{-4}$.

used [LGV+87] [Gar90] [ZGH+91] [ZGK+93], which has been shown to give good results for organic materials [Cam05] [CHX+05] [CEB05] [CNB+07]. As given in (5.9), the complex-valued dielectric function $\varepsilon(E)$ is modeled as the sum of the contributions from several critical points or van Hove singularities.

$$\varepsilon(E) = \sum_{n=1}^{N} \left[ C_n - A_n e^{i\phi_n} \left( E - E_{c,n} + i\Gamma_n \right)^{\left(\frac{d}{2}-1\right)} \right] \quad (5.9)$$

Here each of the $N$ critical points is described by the following fit parameters. The amplitude $A_n$, the energy $E_{c,n}$, the peak broadening $\Gamma_n$ and the phase angle $\phi_n$. Depending on the dimensionality of the critical point, $d$ takes on integer values between 0 and 3. The last parameter is the UV term $\sum_n^N C_n$.

The following sections summarize results obtained for the complex refractive indices of several neat polymers, as well as for systems composed of more than one material, such as polymer:fullerene blends, or doped polymers.

## 5.3. Vertical Phase Segregation

PCPDTBT    Unlike for many other conjugated polymer:fullerene blends, thermal annealing of PCPDTBT:PCBM bulk heterojunctions does not improve the power conversion efficiency of solar cells. Instead, it was found that solvent additives have a beneficial effect on performance.

To investigate this further, spin coated films of neat polymers as well as blends with $PC_{70}BM$ on glass substrates were provided by Antonio Guerrero from Universitat Jaume I.

The samples were measured at five distinct angles of incidence $\phi \in \{55°, 60°, 65°, 70°, 75°\}$. Measurements of the ellipsometric angles were fit between 1.22–4.45 eV using a standard critical point model with an increasing number of zero-dimensional critical points. Film thickness $t$ always converged to about 29 nm, in agreement with profilometry. To maintain a positive $k$ throughout the fitted range, film thickness was subsequently fixed to $t = 29$ nm. The obtained complex
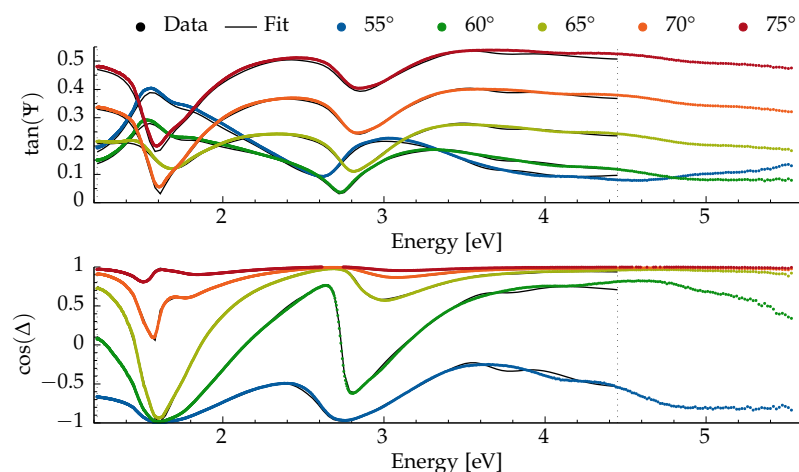
refractive index for a model comprised of five 0D critical points is plotted in Figure 5.3. The fit parameters needed to reproduce the plot are provided for reference in Table 5.2. The measured ellipsometric angles are compared to their corresponding fits in Figure 5.4.

PCDTBT  Another polymer that was provided by Antonio Guerrero is the donor–acceptor polymer PCDTBT, which has an improved environmental stability and power conversion efficiency compared to earlier generations of conjugated polymers.

An identical study was performed, using the received thin film samples on glass. Measurements were fit between 1.22–4.45 eV using a standard critical point model with four 0D critical points with a fixed film thickness of $t = 37$ nm. The obtained complex refractive index for a model comprised of four critical points is plotted in Figure 5.5. The measured ellipsometric angles are compared to their corresponding fits in Figure 5.6. The fit parameters are reproduced for reference in Table 5.3.





PCDTBT
Poly[N-9'-heptadecanyl-2,7-carbazole-alt-5,5-(4',7'-di-2-thienyl-2',1',3'-benzothiadiazole)]
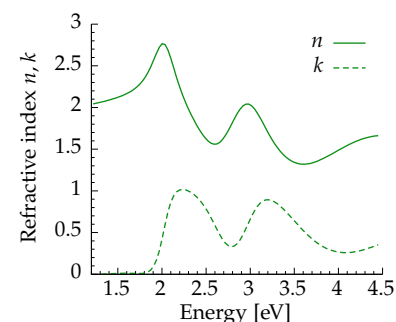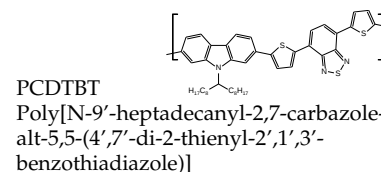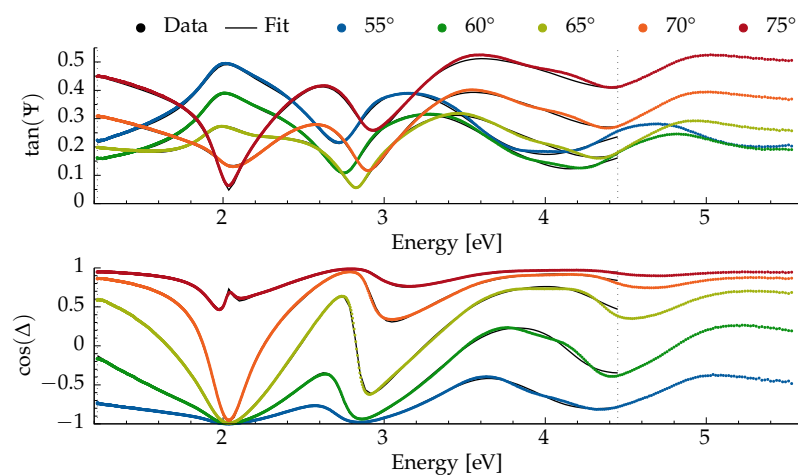


Figure 5.5: Complex refractive index of PCDTBT.

Figure 5.6: Comparison between the measured ellipsometric angles and the modeled values for PCDTBT. The standard deviation $\sigma$ of the fit was $1.6 \times 10^{-4}$.

Table 5.3: Fit parameters of the standard critical point model used to model the complex refractive index of PCDTBT.

| $n$ | $A_n$ | $E_{c,n}$ | $\Gamma_n$ | $\phi_n$ |
|---|---|---|---|---|
| 1 | 0.613 | 2.024 | 0.152 | -1.339 |
| 2 | 2.618 | 2.406 | 0.639 | 0.507 |
| 3 | 1.197 | 2.973 | 0.288 | -1.212 |
| 4 | 1.430 | 4.420 | 0.816 | -1.382 |
| UV term | 2.3037 | $t_{fixed}$ | 37 nm | |

PC$_{70}$BM  The complex refractive index of PC$_{70}$BM plotted in Figure 5.7 is required for the further characterization of blends, and was modeled by Mariano Campoy Quiles.

EFFECTIVE MEDIUM APPROXIMATION  Vertical phase segregation between the donor polymer and the acceptor fullerene component in bulk heterojunctions has a strong effect on OPV performance. In particular, an increased accumulation of acceptor at the cathode—the electron extracting contact—improves the charge selectivity by suppressing the undesired extraction of holes at the cathode.

In order to estimate the degree of vertical phase segregation in PCPDTBT:PC$_{70}$BM bulk heterojunctions, the refractive indices of the pure materials, determined above, were used. Four types of samples were provided by Antonio Guerrero. The samples were spin-coated from a solution without any solvent additive, or from solutions that contained small amounts of either hexanedithiol, octanethiol or octanedithiol.



Figure 5.7: Complex refractive index of PC$_{70}$BM.

To relate the measurements of the ellipsometric angles to the degree of phase segregation, the thin BHJ films were modeled as a stack

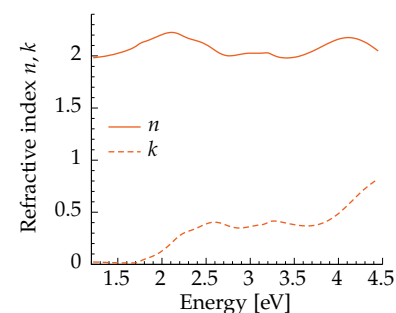composed of three homogeneous sublayers. Of these, the bottom-most layer was required to only contain polymer, while the two layers above were allowed to contain both polymer and fullerene as well as empty space, to account for potential surface roughness. This three-layer model was chosen because it was the simplest one that gave consistently good results for all four types of samples. The optical constants of the mixed sublayers were calculated according to the Bruggeman effective medium approximation [Bru35]. The fitting parameters of the model were the three sublayer thicknesses, as well as the relative composition of the two top-most layers.

The results are summarized in Figure 5.8. Several observations can be made, when considering the sequence 1. no additive, 2. hexanedithiol, 3. octanethiol, 4. octanedithiol. First, the thickness of the neat polymer layer near the substrate slightly increases. And second, at the same time, the amount of $PC_{70}BM$ close to the surface—on the cathode side—significantly increases. Both effects lead to an increased charge carrier selectivity at the respective contacts for OPV devices in a normal geometry, as was confirmed by a significant in-sequence increase of the short circuit current density [GDR+13]. Additionally, these ellipsometric measurements served to back up measurements of the $PC_{70}BM$ surface coverage determined by capacitance–voltage measurements [GDR+13].

[Bru35] Dirk A. G. Bruggeman.
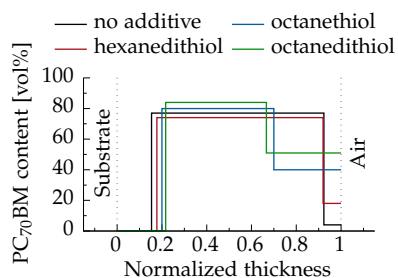*Ann. Phys.* **416**, 636 (1935)



Figure 5.8: Vertical segregation in PCPDTBT:$PC_{70}BM$ films as a function of solvent additive.

[GDR+13] Antonio Guerrero et al.
*ACS Nano*, **7**, 4637 (2013)

## 5.4. Doped Polymers

Effective medium theories like the Bruggeman approximation can only be used if the interaction between components is negligible. However, for doped polymers, this is not the case. The absorption spectrum of a blend of polymer and dopant shows additional features, that are due to new polaron states in the band gap of the polymer.

Additionally, even the addition of inert materials may have an effect beside a simple decrease in absorption proportional to the volume change. For example, it is well known that pure, highly crystalline P3HT shows a characteristic redshift in absorption, compared to amorphous P3HT. When disrupting the crystalline order by introducing an inert material, a blueshift is observed, which cannot be accounted for by a simple mixture of non-interacting particles.

Instead, in the general case, the blend has to be modeled as a new material, with its own optical constants.
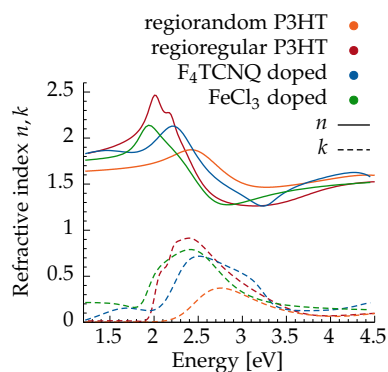
DOPED P3HT  Initial experiments to characterize P3HT p-type doped with $F_4TCNQ$ and $FeCl_3$ have been undertaken, to determine if it is possible to extract information on the doping level from measurements of the optical constants. Information of this type could prove useful in studying the efficiency of doping in organic thermoelectric materials.

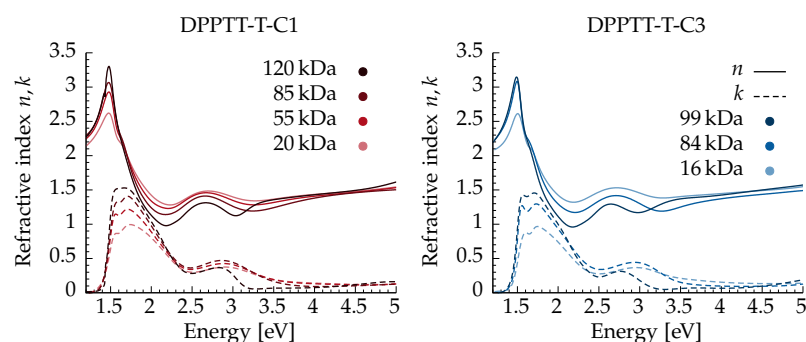A summary is presented in Figure 5.9. It shows the complex refractive index for two samples of neat P3HT of different crystallinity, determined by Mariano Campoy Quiles. The highly crystalline film of regioregular P3HT shows a strong redshift compared to amorphous



Figure 5.9: Complex refractive index of undoped regiorandom and regioregular P3HT, as well as regioregular P3HT doped with $F_4TCNQ$ and $FeCl_3$.

regiorandom P3HT. Compared to these, both of the doped samples exhibit significantly increased absorption below 2 eV, which is attributed to the formation of polaron states in the band gap. Additionally, the $F_4$TCNQ-doped sample shows a blueshift of the absorption, both due to the absorption of $F_4$TCNQ as well as the change in crystal order of the P3HT [DWA+13]. The FeCl$_3$-doped sample shows the opposite trend, a slight redshift. This was somewhat unexpected, as simple absorption measurements did not show anything of this magnitude. Instead, further investigation is required.

[DWA+13] Duc T. Duong et al. *Org. Electron.* **14**, 1330 (2013)

## 5.5. Molecular Weight Dependence

Another promising material with good photovoltaic performance and a high field effect mobility is the low band gap polymer DPPTT-T. Its photovoltaic performance in particular has been observed to depend on the position of the alkyl side-chain branching point [MAM+13] and on the molecular weight [MAN+14].

To understand the origin of this effect, we determined the complex refractive index of a series of spin coated thin film samples, provided by Michelle Vezie from Imperial College London. Fractions with different number average molecular weight of two types of DPPTT-T with different side-chain branching points were characterized. For DPPTT-T-C1, the branching point of the side-chains is located closer to the backbone than for DPPTT-T-C3. The results are summed up in Figure 5.10.
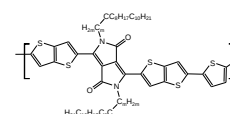
**DPPTT-T**
Thieno[3,2-b]thiophene-diketopyrrolopyrrole   The branched side-chains may be attached to the polymer backbone across $m = 1$ or 3 intermediate carbon atoms, referred to as C1 and C3 respectively.

[MAM+13] Iain Meager et al. *J. Am. Chem. Soc.* **135**, 11537 (2013)

[MAN+14] Iain Meager et al. *J. Mater. Chem. C*, **2**, 8593 (2014)



Figure 5.10: Dependence of the complex refractive index of DPPTT-T on $M_\mathrm{n}$ and the side-chain branching point.

While there is little difference of the complex refractive index between the two variants, the extinction coefficient $k$ is strongly dependent on the number average molecular weight, with the highest $k$ obtained for the highest molecular weight fraction.

Most importantly, $k$ reaches values as high as 1.5, compared to $k \lessgtr 1$ for most organic conjugated materials characterized in the past. In fact, it was found that this—for organic materials extraordinarily large—extinction coefficient can be explained by the large persistence length of the polymer, and the consequently more linear, extended chains in the high $M_\mathrm{n}$ samples [VFM+16]. The reported dependence on the side-chain branching point can also be ascribed to the effect of the molecular weight, which was not considered as a possible explanation in the original report [MAM+13].

[VFM+16] Michelle S. Vezie et al. *Nat. Mater.* **15**, 746 (2016)

[MAM+13] Iain Meager et al. *J. Am. Chem. Soc.* **135**, 11537 (2013)

# CARBON NANOTUBE COMPOSITES 6

## 6.1. Motivation

GENERAL TRENDS IN ELECTRICAL CHARACTERISTICS Figure 6.1 shows a summary of the Seebeck coefficients and power factors of thermoelectric CNTs and CNT-composites plotted as a function of their electrical conductivity. The plotted data is taken from [AZL+16] and [BDC+13] (empty symbols) as well as from work conducted during the course of this thesis (filled symbols). The type of CNT is differentiated by color, with multi-walled carbon nanotubes in red, single-walled carbon nanotubes in blue, and semiconducting single-walled carbon nanotubes in green. The plot includes data on CNT composites prepared with polythiophenes and polyethylenimine, as well as results on nitrogen-doped multi-walled carbon nanotubes, which exhibit a negative Seebeck coefficient.

Figure 6.1 allows us to observe general trends in the thermoelectric characteristics of CNTs and their composites with conjugated polymers. The black dashed line represents the empirical relation observed in doped semiconducting polymers, which was given in (3.22) [GCP+15], while the colored dashed lines correspond to similar power law fits to the corresponding groups.

As can be seen, carbon nanotubes and their composites follow this trend to a varying degree. MWCNTs follow it quite closely, yet stay consistently below the level of doped polymers. SWCNTs on the other hand exhibit an increased Seebeck coefficient compared to MWCNTs, which is attributed to the more semiconducting character of SWCNTs. At high $\sigma$, this allows SWCNTs to surpass doped polymers. The largest $S$ across most of the conductivity range is consistently achieved by deliberately selecting only semiconducting CNTs, in accordance with theoretical expectations [AZL+16].

These observed trends confirm that CNTs and their composites are promising materials for thermoelectric applications, particularly at high electrical conductivities and if metallic tubes can be removed. Since no definitive maximum of $S^2\sigma$ versus $\sigma$ has been observed yet, investigating the doping of CNTs to reach even higher $\sigma$ looks particularly promising.

THERMAL CONDUCTIVITY OF CNTs Yet compared to polymers, CNTs have very high thermal conductivity. For single tubes, values as high as $\kappa = 3000\,\mathrm{W\,m^{-1}\,K^{-1}}$ have been reported [KSM+01]. For films, values range between $\kappa \approx 10\text{--}300\,\mathrm{W\,m^{-1}\,K^{-1}}$ [DTK+15] [LLL+16]. For comparison, doped polymers and polymer:CNT composites can achieve values $\kappa \lessapprox 1\,\mathrm{W\,m^{-1}\,K^{-1}}$.

[AZL+16] Azure D. Avery et al.
*Nat. Energy*, **1**, 16033 (2016)

[BDC+13] Celine Bounioux et al.
*Energy Environ. Sci.* **6**, 918 (2013)

[GCP+15] Anne M. Glaudell et al.
*Adv. Energy Mater.* **5**, 1401072 (2015)
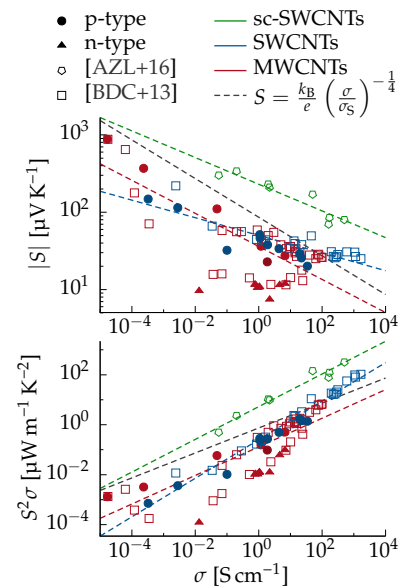
Figure 6.1: Absolute Seebeck coefficient $|S|$ and power factor $S^2\sigma$ for MWCNTs, SWCNTs, as well as semiconducting SWCNTs, plotted versus electrical conductivity $\sigma$.

[KSM+01] P Kim et al.
*Phys. Rev. Lett.* **87**, 215502 (2001)

[DTK+15] A. Duzynska et al.
*Appl. Phys. Lett.* **106**, 183108 (2015)

[LLL+16] Feifei Lian et al.
*Appl. Phys. Lett.* **108**, 103101 (2016)

Synergy  It is because of this synergistic potential, which allows conjugated polymers to lower $\kappa$, while at the same time doping the CNTs—affecting $S$ and $\sigma$—that composites are a promising thermoelectric material. On top of that, the mechanical properties of composites are better than those of the pure constituents. Polymers used for thermoelectric applications are often brittle, due to the introduction of large quantities of dopant which is required to reach the necessary levels of electrical conductivity. Pure carbon nanotubes on the other hand can easily become airborne and may pose a respiratory hazard, unlike CNT composites.

## 6.2. P3HT:N-MWCNT Composites

Idea  This section details investigations on organic composites composed of a p-type conjugated polymer and nitrogen-doped n-type MWCNTs. P3HT was chosen as the conjugated polymer, since it can show ambipolar transport [KBS+09], and because it has a favorable interaction with CNTs, wrapping around them [LYP+11]. Previous work in our group on composites of CNTs and doped P3HT has shown them to deliver power factors of $95\,\mu\mathrm{W\,m^{-1}\,K^{-2}}$ [BDC+13]. The initial objective was to extend the developed methods to n-type composites, since there is comparably little work done on materials with $S < 0$, even though both are equally important for an optimal thermoelectric generator.

Some of the results presented in the following two sections have been published in
[DRC+16] Bernhard Dörling et al.
*Adv. Mater.* **28**, 2782 (2016)

[KBS+09] Avinesh Kumar et al.
*Adv. Mater.* **21**, 4447 (2009)
[LYP+11] Hang Woo Lee et al.
*Nat. Commun.* **2**, 541 (2011)
[BDC+13] Celine Bounioux et al.
*Energy Environ. Sci.* **6**, 918 (2013)

N-MWCNT Nitrogen-doped multi-walled carbon nanotube

Sample Preparation  For this, composites of nitrogen-doped multi-walled carbon nanotubes and P3HT with different stoichiometries were prepared by sonicating the mixture in solvent and drop-casting it on PET substrates. A complete description of the preparation protocol is provided in Chapter B: Experimental Methods.

Physical Characterization  We employed transmission X-ray microscopy at the ALBA synchrotron to confirm that the N-MWCNTs are distributed homogeneously all throughout the film. Figure 6.2 shows the measurements of a sample containing $c = 30\,\mathrm{wt\%}$ of N-MWCNTs. The false-color micrograph is composed of three distinct measurements:

*399 eV* Slightly above the absorption edge $\mathrm{K}_\alpha\,(\text{nitrogen})$ in blue.
*520 eV* Used to indicate a non element-specific change in absorption, due to a variation in sample thickness in green.
*707 eV* Slightly above the absorption edge $\mathrm{L}_\alpha\,(\text{iron})$ in red.

This confirms, that N-MWCNTs are indeed dispersed throughout the sample in the form of bundles. Unexpectedly, the measurements also revealed the presence of large amounts of residual catalyst from the N-MWCNT synthesis in the sample [QAM+12] [QAJ+03]. These iron-rich clusters cause slight aggregation of the nanotubes, since some of them are still attached to each other. Prompted by this observation, an additional batch of samples was prepared from purified N-MWCNTs which had undergone an additional acid-cleaning step. The iron content was reduced from $37\,\mathrm{wt\%}$ to $20\,\mathrm{wt\%}$, as estimated by elemental analysis and confirmed by energy-dispersive X-ray spectroscopy. While an accurate quantitative analysis is complicated, these values can serve as an upper bound for iron content.

[QAM+12] Dali Qian et al.
*Nanomater. Energy*, **1**, 168 (2012)

[QAJ+03] Dali Qian et al.
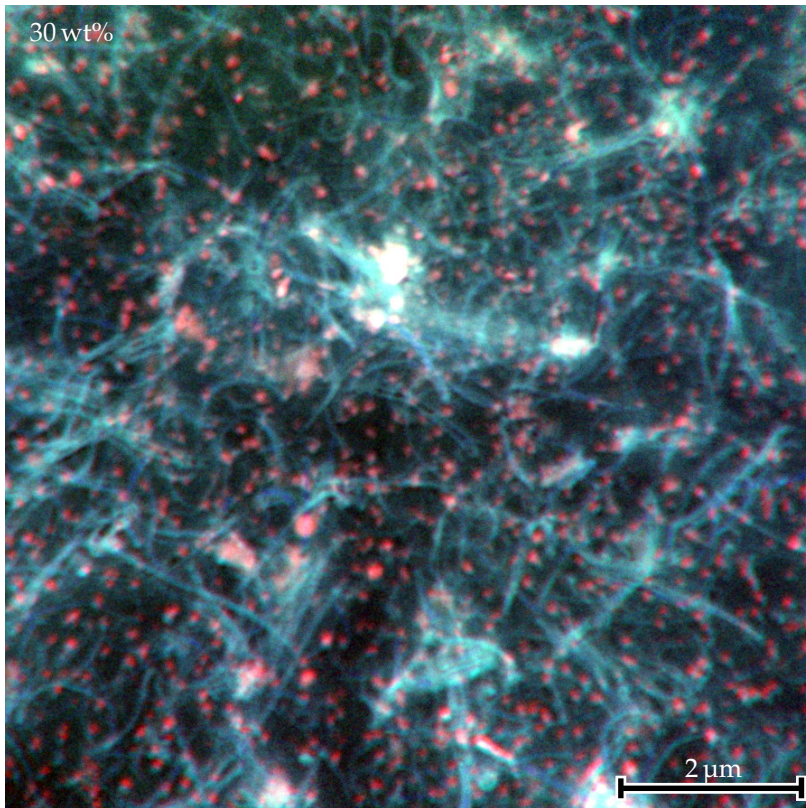*J. Nanosci. Nanotechnol.* **3**, 93 (2003)

Figure 6.2: False-color X-ray micrograph combining information on transmission measurements at three distinct energies. Increased absorption due to nitrogen is pictured in blue, while iron is represented in red. Variations due to sample thickness are shown in green.
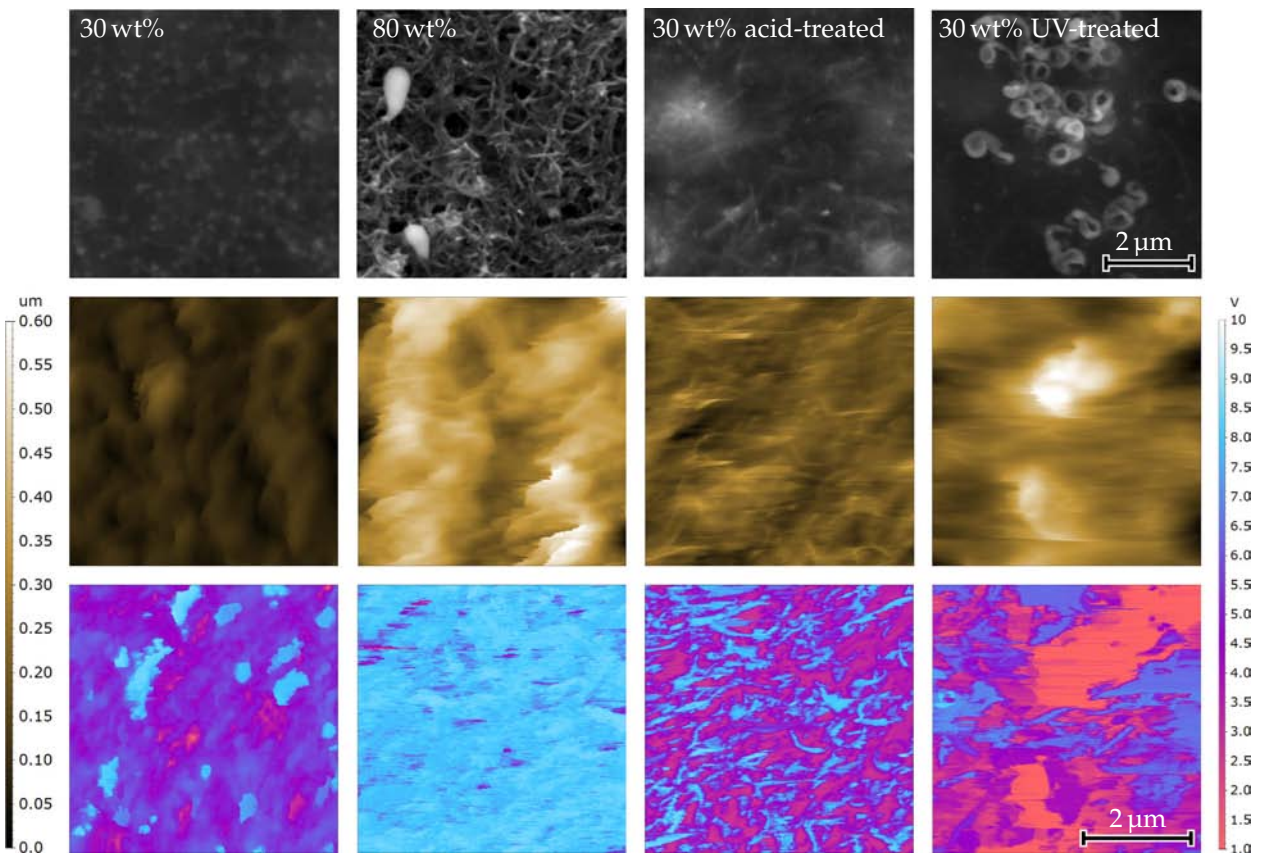
Figure 6.3: Scanning electron micrographs (top row), AFM topography (middle row) and corresponding conductivity maps (bottom row) of four representative composites. For the conductivity maps, the color scale in V is proportional to the logarithm of the measured current.

SEM Scanning electron microscopy

Scanning electron microscopy images of several representative composites are displayed in Figure 6.3. In all cases, fibrillar structures are observed, most likely P3HT-wrapped CNT bundles. Samples with low N-MWCNT content $c = 30\,\text{wt\%}$ appear well dispersed, while samples containing large fractions of N-MWCNTs $c = 80\,\text{wt\%}$ exhibit agglomeration as well as visible catalyst particles. Samples that have been exposed to UV irradiation are included for easy comparison, but will only be discussed in detail in the following section.

AFM Atomic force microscopy

Atomic force microscopy measurements of the same four samples, consistent with the SEM measurements, reveal an increase in surface roughness of the films with increasing N-MWCNT content. The low N-MWCNT content films show a fine fibrillar structure with an average bundle diameter of $(55 \pm 15)\,\text{nm}$, which is significantly smaller than for the high N-MWCNT content samples with $(90 \pm 30)\,\text{nm}$, attesting to the capability of P3HT to disperse and debundle CNTs. Electrically, the composites consist of highly conductive, N-MWCNT-rich regions surrounded by polymer-rich regions that exhibit circa four orders of magnitude lower electrical conductivity.
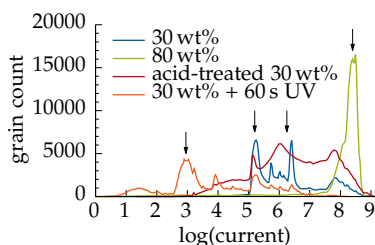
Figure 6.4: Histograms of the AFM conductivity maps in Figure 6.3.

This is further detailed in the histograms in Figure 6.4. The percentage of highly electrically conducting areas increases with increasing N-MWCNT content, suggesting an improved percolation. Acid treatment results in similar percentages but smaller domains of higher purity. We relate the four marked peaks to degraded P3HT, P3HT of increasing doping level, and N-MWCNTs.

THERMOELECTRIC CHARACTERIZATION    The prepared films were cut into samples, to measure $S$ using a custom built setup, and $\sigma$ using the van der Pauw method, as is explained in detail in Chapter A: Experimental Setups. Additionally, the values of $S$ were cross-checked using a commercial equipment from MMR Technologies by Jason D. Ryan at Chalmers University of Technology, giving good agreement.The results are plotted in Figure 6.5. Macroscopically, the electrical conductivity exhibits percolating behavior, increasing by several orders of magnitude after crossing a threshold value for the N-MWCNT content of $c > c_\text{p} \approx 3.5\,\text{wt\%}$, similar to earlier results [BDC+13]. This threshold points to relatively well dispersed carbon nanotubes, in agreement with the physical characterization. At high N-MWCNT content, a dip in $\sigma$ is observed for as-synthesized N-MWCNTs. The dashed line sketches the expected behavior for similar composites prepared from regular, undoped CNTs. The Seebeck coefficient steadily decreases with increasing $c$, spanning values from that of the neat polymer ($\approx 1000\,\mu\text{V K}^{-1}$) [BDC+13] to that of the N-MWCNTs ($\approx -10\,\mu\text{V K}^{-1}$) and correlates well with the percolation threshold observed for $\sigma$. Notably, at a value of $c_\text{s} = 40\,\text{wt\%}$ $S$

Figure 6.5: Thermoelectric properties of composites of as-synthesized and acid-treated N-MWCNTs with P3HT.
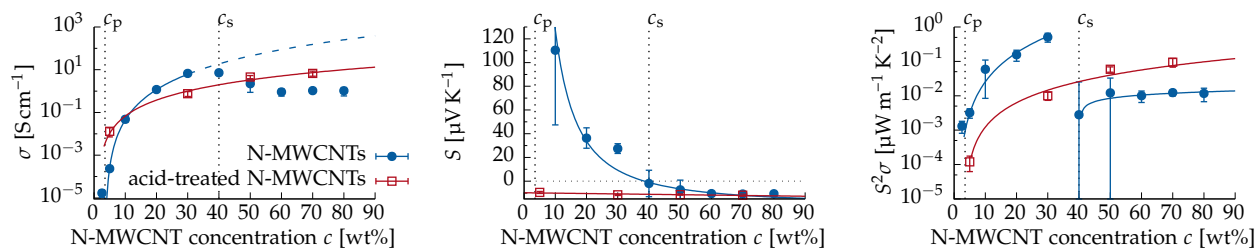
changes sign. For the acid-treated N-MWCNTs, a completely differ-
ent, simpler behavior is observed, with $S \approx -10\,\mu V\,K^{-1}$ independent
of $c$ in the investigated range. The calculated power factor stays well
below earlier reported values. Instead, two regions are apparent for
$S^2\sigma$ of as-synthesized N-MWCNTs. One below $c_s$, where the compos-
ite has p-type properties, and another above $c_s$, where the material is
n-type.

Using p-legs made from $c = 20\,wt\%$ and n-legs with $c = 80\,wt\%$, a
simple module in an in-plane geometry was manufactured from these
composites. It is comprised of five pairs of legs and shown in Fig-
ure 6.6. An example measurement of the average generated Seebeck
voltage is plotted in Figure 6.7. The device delivers a thermovoltage
of $191\,\mu V\,K^{-1}$ which is reasonably close to sum of Seebeck coefficients
of the constituting legs $5 \cdot \left[36 - (-10)\right]\,\mu V\,K^{-1} = 230\,\mu V\,K^{-1}$.

CHARGE TRANSPORT IN COMPOSITES    Since $c_p \ll c_s$, we ar-
gue that the majority carriers for $c < c_s$ are holes, even though
charges move through the N-MWCNTs, which are electrically more
conductive than P3HT by orders of magnitude. A possible expla-
nation for this observation is that P3HT is effectively doping the
CNTs [DZ11] [SJS+01]. This hypothesis is supported by photolumi-
nescence quenching experiments summarized in Figure 6.8, which
indicate that there is a strong photoinduced charge-transfer between
P3HT and N-MWCNTs [SWP+11]. Upon addition of N-MWCNTs,
the PL of P3HT is strongly quenched. Samples based on acid-treated
N-MWCNTs on the other hand , show less effective PL quenching.
This can be explained by a weaker interaction between P3HT and
N-MWCNTs, resulting in less efficient p-doping of the tubes, which
is in agreement with their unaltered n-type character, as well as with
the purer domains observed in the conductivity maps in Figure 6.4.

The observed change from p- to n-type character of the nanocompos-
ites can be explained in terms of a simple band model [BS92], which
considers the semiconducting CNTs as being co-doped. The sub-
stitutional nitrogen atoms that are incorporated during N-MWCNT
synthesis act as donor impurities, whereas the P3HT wrapped around
the nanotubes is effectively acting as an acceptor, injecting holes into
the CNT valence band, as was recently shown for CNT composites
with polyelectrolytes [MRF+15]. The actual position of the Fermi level
in the CNTs at a given temperature then simply results as a graphical
solution from the difference in effective donor- and acceptor-level
densities by invoking charge neutrality, as detailed in Figure 6.9. This
determines the type of the majority carrier in the system and the sign
of $S$.

1. The simple case, in the absence of any dopants and at a finite
   temperature T, is illustrated by the dashed lines in the first panel
   of Figure 6.9. The free charge densities are plotted in dependence
   of the location of the Fermi level in the band gap. Since the net
   number of charges has to sum to zero, the free electron density
   in the conduction band in green and the free hole density in the
   valence band in orange have to be exactly equal. In the case of an
   undoped semiconductor with an identical density of states in the
   conduction and valence band $N_C = N_V$, this can only be fulfilled
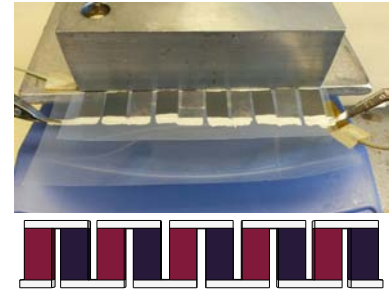   if $E_F$ lies the middle of the band gap.



Figure 6.6: Photograph and sketch
of a first in-plane proof of concept
device made from $20\,wt\%$ and $80\,wt\%$
composites on PET.
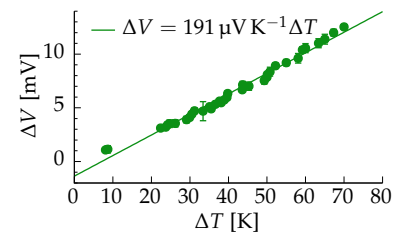


Figure 6.7: Measured Seebeck voltage
for the device in Figure 6.6.

[DZ11] D. M. Nanditha M. Dis-
sanayake et al.
*Nano Lett.* **11**, 286 (2011)

[SJS+01] Moonsub Shim et al.
*J. Am. Chem. Soc.* **123**, 11512 (2001)

PL Photoluminescence
[SWP+11] Samuel D. Stranks et al.
*Nano Lett.* **11**, 66 (2011)



Figure 6.8: Averaged PL intensity
between $675\,nm$ and $725\,nm$, for
samples excited at $514\,nm$

[BS92] Ludwig Bergmann et al.
*Lehrbuch der Experimentalphysik -
Band 6: Festkörper* (1992)

[MRF+15] Cheng-Kang Mai et al.
*Energy Environ. Sci.* **8**, 2341 (2015)

2. In the presence of both donor and acceptor impurities, charge
   neutrality holds for the sum of both the density of free charges
   plus the ionized dopant densities $N_D^+$ and $N_A^-$. These sums are
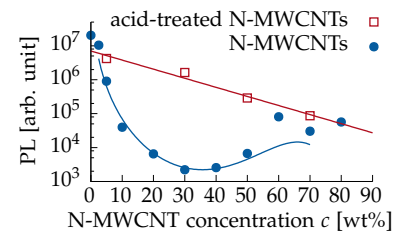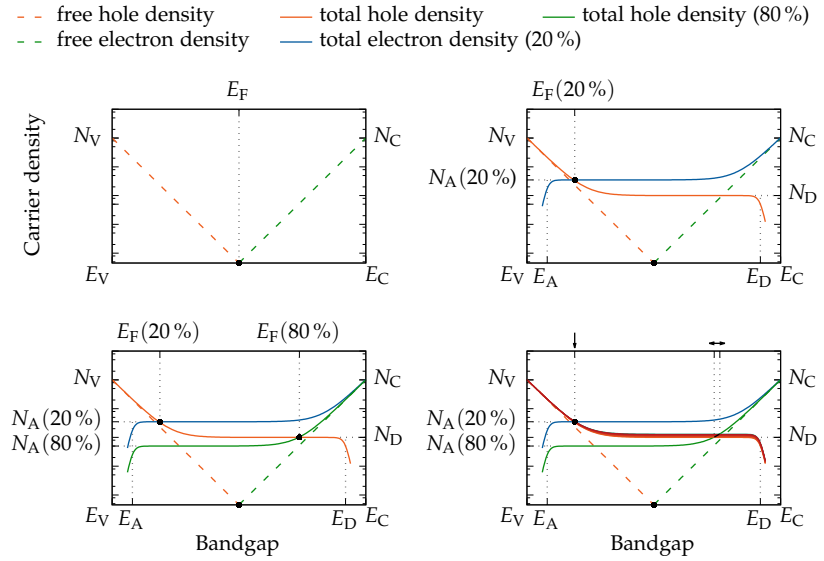   drawn as solid lines for different dopant densities. In the case of
   20 wt% p-type composites, the density of acceptors is higher than
   the density of donors, and the Fermi level is closer to the valence
   band.

3. If the density of acceptors is decreased relative to the density of
   donors, e.g. by increasing the N-MWCNT concentration, then the
   Fermi level moves toward the conduction band.

4. It is interesting to note, that these two cases differ significantly in
   their behavior for small changes of the donor or acceptor densities,
   as is the case when an additional dopant is introduced. In one
   case, a small change of for example $N_D$ shifts the Fermi level by a
   proportional amount. In the other case, doping remains ineffective,
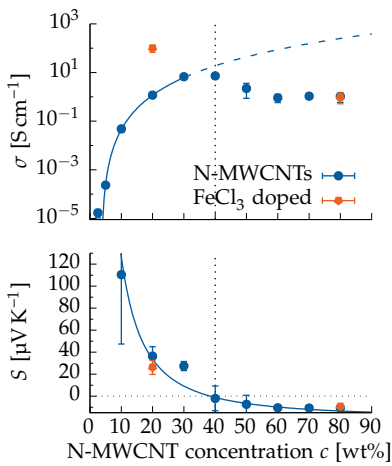   since the Fermi level remains pinned close to the valence band.

FURTHER DOPING Exactly this behavior was observed experimen-
tally by doping composites of both low and high N-MWCNT con-
centration with the additional, third dopant $FeCl_3$. As is plotted in
Figure 6.10, the p-type conductivity of 20 wt% samples increases by
more than an order of magnitude, while the n-type conductivity of
80 wt% composites is not affected, due to the aforementioned pinning
of the Fermi level.

Conversely, composites that are biased close to the transition from p-
to n-type by appropriately selecting $c$, are expected to exhibit a com-
parably large change in $S$ with just small differences in doping. This
was confirmed by $FeCl_3$-doping of n-type samples of as-synthesized
40 wt% N-MWCNTs, and 5 wt% acid-treated N-MWCNTs. As ex-
pected, after 60 s of doping, $S$ increased towards more positive values,
as given in Table 6.1.

INFLUENCE OF TEMPERATURE The comparison between com-
posites made from the two N-MWCNT batches suggests that the
thermoelectric behavior of these composites strongly depends on the
electronic properties of the matrix polymer as well as the specific



Figure 6.10: Change of $\sigma$ and $S$ upon
p-doping with $FeCl_3$.

Table 6.1: Effect of 60 s of $FeCl_3$ doping
on composites with $S \lesssim 0\,\mu V\,K^{-1}$.

| | $S[\mu V\,K^{-1}]$ | |
| | before | after |
|---|---|---|
| 40 wt% | −8 | 31 |
| 5 wt% acid-treated | −12 | −4 |

interactions between P3HT and N-MWCNTs. By influencing this interaction, it should therefore be possible to tune the thermoelectric properties. To verify this hypothesis we started simple.

By heating, one should be able to promote the partial detachment of P3HT chains from the CNT surface in solution, thereby reducing contact and concomitant doping. Indeed, these composites exhibit thermochromism in solution when heated, unlike reference P3HT solutions, which do not show any similar change. As is evidenced in Figure 6.11, upon increasing the temperature, the composite solution turns from a characteristic dark purple, indicative of $\pi$-stacked, crystalline P3HT, to the orange coloration associated with well dissolved, isolated P3HT. Unfortunately, it proved an experimental challenge to preserve this change through the transition to the dried film, and no changes of the thermoelectric properties in films prepared from heated or hot solutions were observed.



Figure 6.11: 40 wt% solution at room temperature and 120 °C.

## 6.3. UV-treated P3HT:N-MWCNT Composites

Even so, being able to influence $S$ on demand is desirable, because it could allow for the possibility to create both the p- and n- legs of thermoelectric generators from a single solution, simplifying processing.

INFLUENCE OF UV LIGHT    Another conceivable method to facilitate this, is to affect the interaction between P3HT and CNTs by irradiating solutions or dried composite films with UV-light. The required layer thicknesses for TEGs are of the order of micrometers. Due to the very short penetration depth of UV-light, it is not expected that $S$ can be changed throughout the bulk of the film, if a dry film is irradiated. Not surprisingly, no change was observed, even after hours of irradiation with $50\,\mathrm{mW\,cm^{-2}}$ of UV-light.

Things are different however, if the UV-irradiation is applied to the solution, either before deposition, or while the deposited layers are still drying. Solutions are more transparent than solid films, with a typical concentration of solid content of $1\,\mathrm{mg\,ml^{-1}}$. Coupled with the natural convection during drying, this allows to affect the characteristics of the deposited films, even though the absorption of UV-light still predominantly happens at the surface. By varying the duration of the UV-treatment, a clear trend can be observed. As plotted in Figure 6.12, $S$ continuously decreases with increasing irradiation. The Seebeck coefficient of the 30 wt% samples, turns negative after 60 s of UV-irradiation. 20 wt% composites contain comparably more P3HT and have a higher $S$. The same treatment of 60 s is therefore not enough to reach $S < 0$.
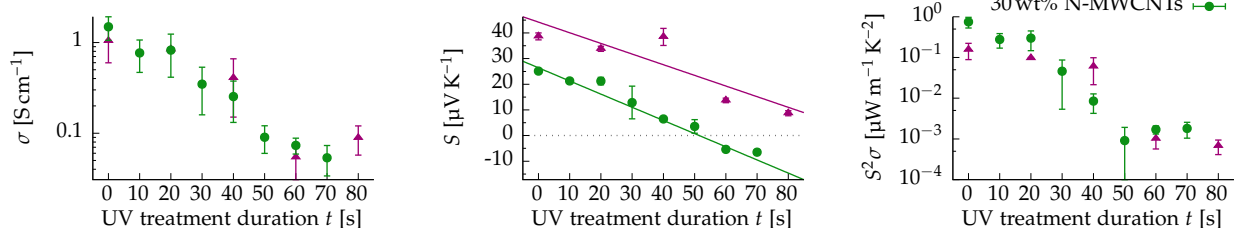
Figure 6.12: Dependence of the thermoelectric properties on the duration of the UV-treatment.

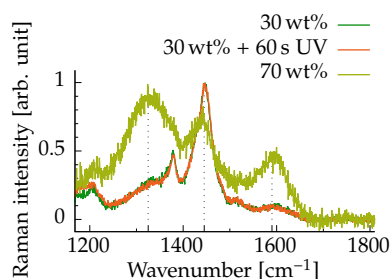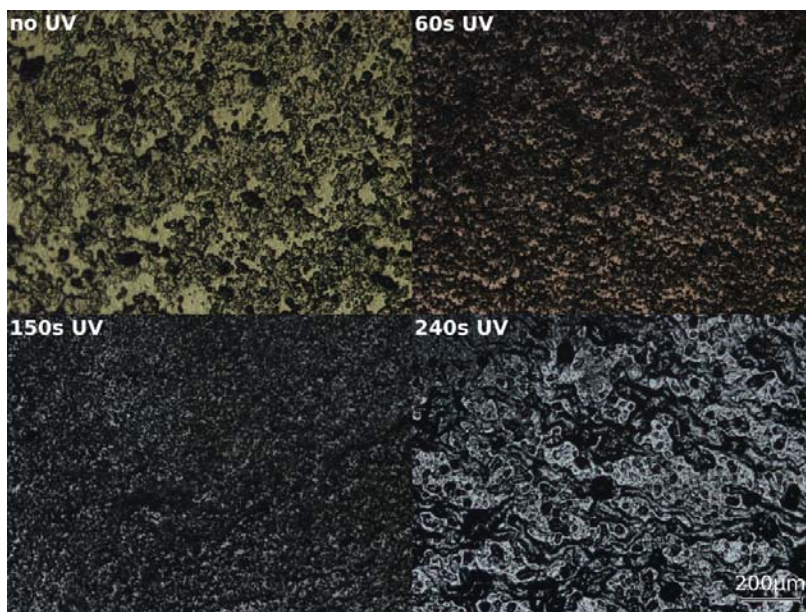Figure 6.13: Optical micrographs of UV-irradiated CNT composites.



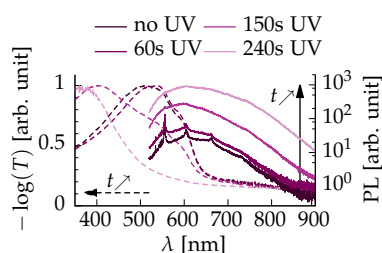Figure 6.14: Raman spectra of N-MWCNT composites.



Figure 6.15: Normalized absorbance $-\log(T)$ (dashed lines) and PL spectra (solid lines) of UV-irradiated 20 wt% composites.



$-\log(T)$ Absorbance

[MRG+09] Matthieu Manceau et al. *Polym. Degrad. Stab.* **94**, 898 (2009)

[HEL+11] Holger Hintz et al. *Chem. Mater.* **23**, 145 (2011)

Unfortunately, the electrical conductivity decreases in lockstep with the Seebeck coefficient. For the measured range of irradiations, $\sigma$ decreases by about an order of magnitude. This means, that $S^2\sigma$ decreases as well, resulting in an n-type performance that lies two orders of magnitude below that of the untreated, p-type composite. Still, using this method, one can deposit both p- and n-type legs of a TEG from the same starting solution.

PHYSICAL CHARACTERIZATION   In order to better understand the impact, the UV-light has on the thermoelectric properties, we next investigated its effect on the structural and optical properties of the composites. The optical micrographs shown in Figure 6.13 indicate that long exposure times ($\gtrsim 100$ s) yield visibly degraded samples. For samples that were irradiated for 60 s, AFM suggests an increase in surface roughness, as shown in Figure 6.3, while SEM evidences the appearance of small curled scraps, that are electrically insulating, which we ascribe to degraded polymer. Raman scattering results shown in Figure 6.14 indicate that UV-light has no negative effect on the N-MWCNTs, since the ratio of the graphene D-band at $\approx 1300$ cm$^{-1}$ and the G-band at $\approx 1600$ cm$^{-1}$ remains unaffected. We relate the peak at $\approx 1450$ cm$^{-1}$ to the symmetric C=C stretching mode of P3HT.

Overall, long exposure times clearly degrade the P3HT, as is evidenced by strong photobleaching for increasing UV treatment duration, observable even by eye. Furthermore, as is detailed in Figure 6.15, an additional blueshift of the P3HT absorbance is observed. This is interpreted as a reduction in the conjugation length due to the introduction of defects or chain scission. Concurrently, the strong PL quenching of P3HT in Figure 6.8, that was observed after addition of N-MWCNTs, is undone upon UV irradiation, demonstrating a lower degree of charge transfer between degraded polymer chains and CNTs, due to a decreased interaction.

Photodegradation of P3HT has indeed been well studied in thin films [MRG+09] [HEL+11]. Photobleaching was observed, with an

additional blueshift of the absorption, associated to an ozone mediated decrease of the average length of $\pi$-conjugation [HEP+10]. In solution on the other hand, the blueshift is not necessarily caused by ozone. Instead, simple UV irradiation in an oxygen containing atmosphere is sufficient [Hol91]. Both photobleaching in the presence of singlet oxygen, and chain scission have been observed, where the chain scission is induced by FeCl$_3$ residue in the sample [AH93].

It is this degradation of P3HT that is in close contact with CNTs, that leads to a decrease of doping, and the resultant change in $S$. Yet, if this no longer conductive material is located at the junction of two CNTs, it leads to an increase of the contact resistance and as a result, the decrease of the macroscopic electric conductivity as seen in Figure 6.12. In Figure 6.15 two clear regimes are observed. For low exposure times $t < 60\,\mathrm{s}$, there is but little degradation of the polymer, with barely any observed changes in the absorbance and PL, yet a large change in the electronic properties. Excessively long exposure times $t \gtrsim 100\,\mathrm{s}$ result in complete degradation of the polymer with destructive effects on the optical as well as electronic properties. This kind of induction period during which properties change slowly at first, is a common observation during UV-degradation of polymers [Lab76].

To further substantiate these observations, we measured the Fourier transform infrared spectra of irradiated composites. However, no conclusive results were obtained, due to a strong CNT background. Therefore we investigated the spectra of neat P3HT shown in Figure 6.16. The observed peaks are assigned to the characteristic molecular excitations of the different CH$_n$ groups and the C=C bonds of the thiophene rings as given in Table 6.2.
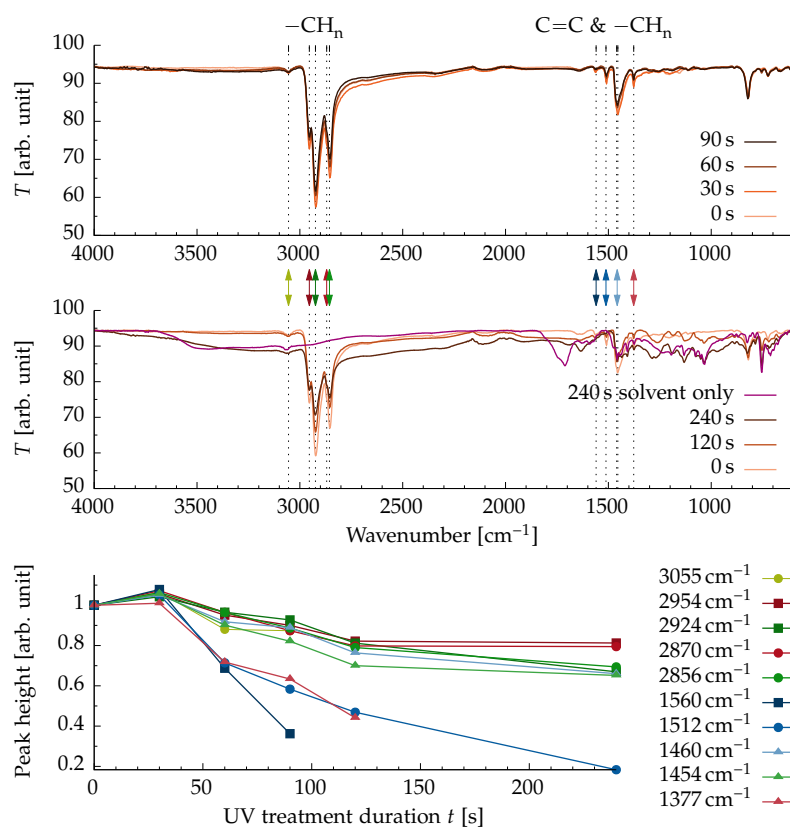
[HEP+10] Holger Hintz et al. *Polym. Degrad. Stab.* **95**, 818 (2010)

[Hol91] Steven Holdcroft. *Macromolecules*, **24**, 4834 (1991)

[AH93] Mohamed S. A. Abdou et al. *Macromolecules*, **26**, 2954 (1993)

[Lab76] *Ultraviolet Light Induced Reactions in Polymers*. ACS Symposium Series vol. 25 (1976)

FTIR Fourier transform infrared



Table 6.2: Correspondence between molecular excitations and characteristic peaks for P3HT summarized from [MRG+09] [AH93].

| | |
|---|---|
| =C−H | 3055 cm$^{-1}$ |
| −CH$_2$ | 2924 cm$^{-1}$ |
| | 2856 cm$^{-1}$ |
| | 1454 cm$^{-1}$ |
| −CH$_3$ | 2954 cm$^{-1}$ |
| | 2870 cm$^{-1}$ |
| | 1377 cm$^{-1}$ |
| C=C | 1560 cm$^{-1}$ |
| | 1512 cm$^{-1}$ |
| | 1460 cm$^{-1}$ |

Figure 6.16: FTIR spectra measured by attenuated total reflectance infrared spectroscopy of neat P3HT solutions that have been UV-treated.

With increasing duration of irradiation, the absorption of all these modes decreases, particularly those related to C=C double bonds of the thiophene ring. This provides evidence that the UV treatment affects both the carbon double bonds of the thiophene ring, as well as the alkyl side chains, influencing the doping not only by reducing conjugation, but also by impairing the interaction of P3HT with the CNTs. For excessively long durations of $\approx 240\,s$ an additional feature appeared, which was also present in the spectra of pure orthodichlorobenzene solvent exposed to the same treatment. Like the optical micrographs of Figure 6.13 and the absorbance and PL in Figure 6.15, this again gives an idea of the maximum UV-treatment, after which undesirable processes influence the result.

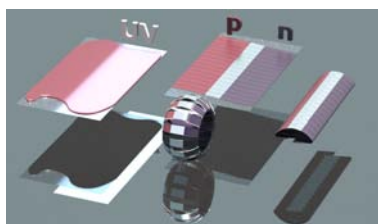oDCB Orthodichlorobenzene



Figure 6.17: Proposed fabrication of a device geometry that plays on the advantages of the presented material.

PROOF OF CONCEPT TEG    There exists a reasonable processing window to modify the thermoelectric properties of the composites by UV irradiation before unwanted degradation occurs. This allows to deposit both the p- and the n-type layer during the same step—from a single solution—potentially simplifying the whole manufacturing process. A possible implementation of the envisioned process is illustrated in Figure 6.17.

1. First, a uniform wet layer of the composite is deposited, and half of it is UV-irradiated during drying.
2. Then the individual legs are patterned simply by cutting the dry layer into ribbons.
3. Adjacent thermocouples are connected electrically in series by taking advantage of the flexible PET substrate, in effect forming a spiral of alternating p- and n-legs.
4. The ends of this spiral may then be joined to form a torus.

Two main advantages, compared to the sequential deposition of p- and n-type materials in distinct steps, are apparent.

*Large-area coating*  By depositing all of the active layer in a single step, large-area coating processes can be used, since no mechanical patterning of the active layer is required.

*Required deposition steps*  Less steps are needed to deposit a complete TEG. Not only can the active layer be deposited in one step less, but half of the metal interconnects bridging the p- and n-legs are no longer needed. Because both materials were deposited in the same step, they are forming a single layer, ensuring electrical as well as mechanical connection. In an in-plane geometry, an additional contact on top will then not provide any increase in conductance.

A proof of concept TEG, fabricated according to the proposed method is displayed in Figure 6.18. Because of experimental limitations, it was deposited by drop-casting to achieve the required layer thickness. Furthermore, contrary to what was said above, in the presented
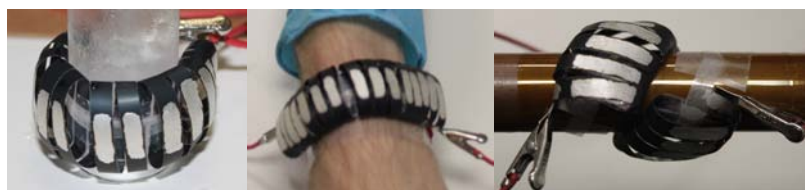
Figure 6.18: Possible application geometries as a torus, a bracelet, or a spiral. A single leg of the pictured device is 5 mm wide.

proof of concept, the p- and n-type layers are in fact bridged by an interconnect of silver paste. This proved necessary in order to traverse a region of insufficient thickness. The three presented application geometries take the form of a single torus or a wristband and an extended spiral, which could be used to harvest waste heat from pipes. The temperature difference is applied between the inner and outer radius of the torus or spiral, with the body of the device serving as a heat sink.

OUTPUT POWER   To benchmark the performance of this module comprising 15 thermocouples, it was attached to a glass of ice water, while keeping the outer side in air at room temperature without forced convection. It generated a voltage of $5\,\mathrm{mV}$ which corresponds to $14.5\,\mu\mathrm{V\,K^{-1}}$ per couple. This is only half as much as the expected value. The large difference is attributed to an actual temperature gradient $\Delta T < 23\,\mathrm{K}$, as well as to an inhomogeneous conversion from p- to n-type during the UV-treatment. The output current and power versus voltage are plotted in Figure 6.19. The module supplies $2\,\mathrm{nA}$ at $5\,\mathrm{mV}$ Seebeck voltage, which translates to an output power of $10\,\mathrm{pW}$. The reason for the low level of generated power is the large internal resistance of $\approx 2\,\mathrm{M}\Omega$, which is almost entirely due to the n-type legs. Before any usable quantities of power can be extracted from a similar device, the low electrical conductivity of the n-type legs has to be improved first.



Figure 6.19: Output current and power for the proof of concept device.

THERMAL CONDUCTIVITY   The bulk thermal conductivity of $1\,\mathrm{mm}$ thick samples of a few selected composites was measured by Jason D. Ryan at Chalmers University of Technology, using the transient plane source method, and is given in Table 6.3. Because of the large quantities of material required for these bulk measurements, we were unable to measure $\kappa$ across the whole composition range, or at all for UV-treated composites. Measurements confirm that $\kappa$ only weakly depends on the N-MWCNT content, maintaining a consistently low level across the studied samples. Even for high N-MWCNT-content samples, $\kappa$ is only about twice as high as for neat P3HT, which is about 2 orders of magnitude lower than that of neat CNT films [DTK+15] [LLL+16].

[DTK+15] A. Duzynska et al.
*Appl. Phys. Lett.* **106**, 183108 (2015)

[LLL+16] Feifei Lian et al.
*Appl. Phys. Lett.* **108**, 103101 (2016)

| N-MWCNT content | Density $\rho$ [$\mathrm{g\,cm^{-3}}$] | Specific heat $C_p$ [$\mathrm{J\,kg^{-1}\,K^{-1}}$] | Thermal diffusivity $\alpha$ [$\mathrm{mm^2\,s^{-1}}$] | Thermal conductivity $\kappa$ [$\mathrm{W\,m^{-1}\,K^{-1}}$] |
|---|---|---|---|---|
| neat P3HT | 1.05(1) | 1497(15) | 0.18(0) | 0.29(1) |
| 30 wt% | 1.13(1) | 1234(4) | 0.29(0) | 0.40(3) |
| 30 wt% acid-treated | 1.17(1) | 1194(2) | 0.35(1) | 0.49(2) |
| 80 wt% | 1.21(1) | 948(2) | 0.48(1) | 0.55(4) |

Table 6.3: Measured properties used to determine the bulk thermal conductivity $\kappa$ of $1\,\mathrm{mm}$ thick P3HT:N-MWCNT samples.

FIGURE OF MERIT   The non-optimized values for $ZT$ are then around $1 \times 10^{-3}$ and $1 \times 10^{-5}$ for the p-type and n-type composite respectively, which is not sufficient for real applications. However, the presented method is applicable to other similar material systems, and we expect that the performance can be significantly improved by using semiconducting single-wall carbon nanotubes, and appropriate dopants [WHY+15]. All the while retaining the demonstrated advantages of low processing complexity.

[WHY+15] Hong Wang et al.
*Adv. Mater.* **27**, 6855 (2015)

STABILITY   Another important aspect for possible applications is the stability of the used materials. Most reported n-type organic

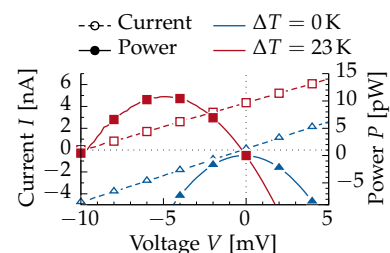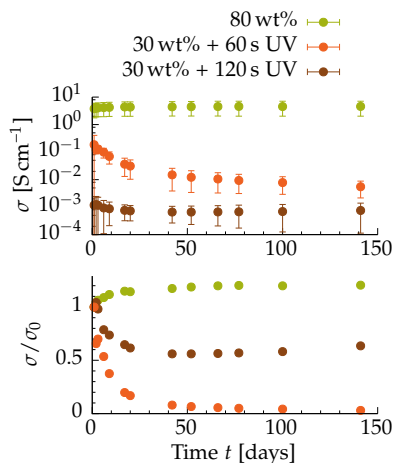Figure 6.20: Stability of $\sigma$ over time.

materials do not maintain their negative Seebeck coefficient, due to instability towards oxidation in air. To get an accurate estimate of stability, all samples were prepared, measured and stored in air. Figure 6.20 shows the results of repeated measurements of the electrical conductivity, carried out over a period of 144 days, after which the measurement setup stopped working and had to be returned for repairs. Nonetheless, the trend is clear. High N-MWCNT content composites maintain and even slightly increase their $\sigma$ during the observed duration. UV-treated, low N-MWCNT content composites have a lower initial conductivity, which also further decreases during the first 20 days. Samples that have been exposed for 60 s are least stable relative to their initial conductivity. For $S$, only little data was acquired, yet the same trend is observed . The negative Seebeck coefficient of 80 wt% composites was stable for every single measured sample, with no significant changes observed after 240 days. In the same amount of time, the Seebeck coefficient of 30 wt% p-type samples diminished to 40 % of the initial value.

These data suggest, that the n-type character of the doped nanotubes is generally stable, with no changes to $S$ and $\sigma$. On the other hand, p- and n-type composites containing P3HT are significantly less stable in both $S$ and $\sigma$.

## 6.4. UV-treated PEI:SWCNT Composites

As discovered in the previous section, it is possible to change the Seebeck coefficient of polymer:N-MWCNT composites by partially degrading the polymer component, modifying the effective doping level. In this section, we tried to investigate if this method is generally valid and extendable to other types of composites. The important detail is the ability to tune the doping level. The specific direction—from p- to n-type or in the opposite direction—is a priori not that important. Processing can be simplified either way. Another lesson learned is that SWCNTs are inherently better suited for thermoelectric applications than MWCNTs, since they contain less metallic tubes and have a higher Seebeck coefficient.

PEI:SWCNT COMPOSITES Another approach to achieve n-type thermoelectricity is then to use pristine p-type SWCNTs and a polymeric n-type dopant. One well known n-type dopant of CNTs is polyethylenimine [KCT+14][SJS+01][RFY11]. $S$ of neat CoMoCAT® SWCNTs depends on their preparation protocol. If they are dispersed in a reasonably good solvent like oDCB, $S$ has a smaller value than in water. This is because to be able to use water as a solvent, the use of a surfactant, in this case sodium dodecylbenzenesulfonate, is necessary. This surfactant remains in the sample and consequently has a considerable effect on the thermoelectric properties. Neat N-MWCNTs on the other hand have a negative Seebeck coefficient, which changes towards larger positive values with higher P3HT content, and back towards more negative values upon UV irradiation, as presented in the last section and summarized in the top part of Figure 6.21.

The same set of experiments conducted for PEI:SWCNT composites results in qualitatively similar results, though with the reversed trend. Due to its strongly electron donating character, samples containing an

The work presented in this section has been published in
[DSK+17] Bernhard Dörling et al.
*Synth. Met.* **225**, 70 (2017)

[KCT+14] Suk Lae Kim et al.
*ACS Nano*, **8**, 2377 (2014)

[SJS+01] Moonsub Shim et al.
*J. Am. Chem. Soc.* **123**, 11512 (2001)

[RFY11] Yeontack Ryu et al.
*Carbon*, **49**, 4745 (2011)
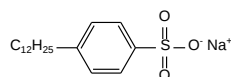


SDBS
Sodium dodecylbenzenesulfonate
Used as a surfactant.

increasing amount of PEI exhibit $S < 0$, independent of the solvent, as is pictured with the dark red bars in Figure 6.21. The required weight ratio to observe an effect are different though. As for the P3HT composites, when exposing the samples to $60\,s$ of UV-irradiation during deposition, an inverse change, towards the Seebeck coefficient of composites richer in CNTs can be observed. Again allowing both n- and p-type composites to be deposited from the same solution. This however, only works when using oDCB as a solvent. The UV-treatment is not effective when using water as a solvent, because of the large quantities of additional surfactant which are required to disperse the CNTs in this case. As shown by the light blue bar, the change of the Seebeck coefficient is then strongly suppressed.

Since the amount of SDBS required for an adequate dispersion is higher than the amount of both SWCNTs and PEI, it is expected to have a significant effect on the interaction of PEI with SWCNTs beyond the effect of the UV-treatment. This is confirmed by the fact that the Seebeck coefficients of composites prepared from a dispersion in water and SDBS are significantly different from those prepared in oDCB, attesting to the considerable interaction of SDBS and SWCNTs.

It was therefore determined that the developed method is in fact quite general, and can be used both on p-type as well as n-type composites. A patent application for the described process of tuning the majority carrier type by UV-irradiation is pending [CGD+15].



Figure 6.21: Seebeck coefficient of $60\,s$ UV-treated P3HT:N-MWCNT composites and PEI:SWCNT composites for decreasing CNT content.

[CGD+15] Mariano Campoy Quiles et al. Patent pending ES1641.1145, PCT/EP2016/078459. 2015

## 6.5. Nitrogen Doped SWCNTs

While it is possible to obtain n-type character by doping CNTs with polymer, it might still be preferable to stick with nitrogen doped CNTs. As we saw, they exhibit excellent long term stability, both for $S$ and $\sigma$. It would be desirable to replace MWCNTs with SWCNTs though, due to their generally better thermoelectric properties. [AZL+16] [BDC+13]

[AZL+16] Azure D. Avery et al. *Nat. Energy*, **1**, 16033 (2016)

[BDC+13] Celine Bounioux et al. *Energy Environ. Sci.* **6**, 918 (2013)

This section reports on results obtained from nitrogen-doped single-walled carbon nanotubes.

N-SWCNT Nitrogen-doped single-walled carbon nanotube

Nitrogen Doping by Ammonolysis   The N-SWCNTs were prepared by Stefania Sandoval at ICMAB, using a doping method that has been demonstrated to lead to a high fraction of nitrogen uptake in highly reduced graphene oxide [SKO+16]. Using this method, the degree of nitrogen doping can be varied, theoretically allowing for a detailed study. As it turns out, the particular type of doping procedure has significant impact on the obtained results, which is why it is quickly summarized here for reference. Nitrogen was introduced into the SWCNTs by ammonolysis, by annealing in a furnace in the presence of ammonia. However, to allow for any significant amount of nitrogen uptake, defects along the tubes had to be introduced first. This was done by means of treating them in nitric acid, thereby functionalizing the tubes with carboxyl and hydroxyl groups. The nitrogen content as well as the remaining oxygen content of the investigated tubes was measured by chemical analysis and is given in Table 6.4.
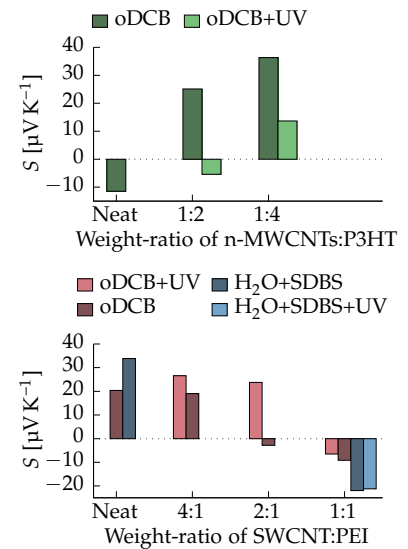
[SKO+16] Stefania Sandoval et al. *Carbon*, **96**, 594 (2016)

Table 6.4: Nitrogen and oxygen content of doped SWCNTs.

| Treatment | N [wt%] | O [wt%] |
|---|---|---|
| $NH_3$ at $500\,°C$ | 5.9 | 4.2 |
| $NH_3$ at $700\,°C$ | 3.1 | 2.4 |
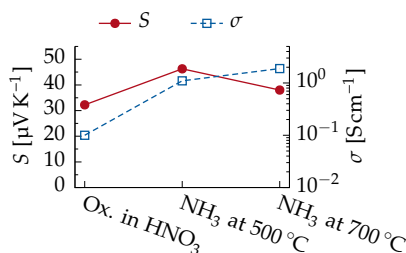
Figure 6.22: $S$ and $\sigma$ for nitrogen-doped single-walled carbon nanotubes.



P(NDI2OD-T2)
ActivInk™ N2200    High mobility
n-type polymer.

Table 6.5: Performance of 1:1 P(NDI2OD-T2):N-MWCNT composites.

| | |
|---|---|
| $S$ [μV K$^{-1}$] | −7 |
| $\sigma$ [S cm$^{-1}$] | 0.1 |
| $S^2\sigma$ [μW m$^{-1}$ K$^{-2}$] | $5 \times 10^{-4}$ |

MINT Mechanically interlocked carbon nanotube

[LP15] Alejandro López-Moreno et al. *Chem. Commun.* **51**, 5421 (2015)

[JPR+14] Alberto de Juan et al. *Angew. Chemie Int. Ed.* **53**, 5394 (2014)

THERMOELECTRIC CHARACTERIZATION    The results for $S$ and $\sigma$ of the defect-laden intermediate CNTs as well as the finished N-SWCNTs are shown in Figure 6.22. It is immediately apparent, that in all cases $S > 0$. Even though a significant amount of nitrogen was incorporated into the SWCNTs, they remain p-type. In fact, the tubes with the highest nitrogen content exhibit the largest positive $S$. This unexpected result is explained by the high amount of remaining oxygen defects in the tubes. In terms of electrical conductivity, the observed increase is mostly attributed to a decrease in oxygen content. This decreases hydrophilicity due to the decreasing amount of carboxyl and hydroxyl groups, which leads to better dispersion of the N-SWCNTs in oDCB and more homogeneous samples. At the same time, the elimination of the sp$^3$ defects restores the conjugation along the tubes, which increases $\sigma$ as well.

CONCLUSIONS    All of these observations lead us to conclude that for thermoelectric composites, a low concentration of remaining oxygen based groups—or defects in general—is more important than merely a high nitrogen uptake during substitutional nitrogen doping of SWCNTs. In other words, the type and number of functionalities have to be fine-tuned in order to obtain an appropriate compromise between nitrogen doping and remaining oxygen groups. Only then will the obtained material exhibit n-type character.

## 6.6.  P(NDI2OD-T2) Composites

Composites of the high mobility n-type polymer P(NDI2OD-T2), that is sold as ActivInk™ N2200, and N-doped MWCNTs were also prepared, with the goal of obtaining increased n-type performance. However, dispersion of CNTs was considerably worse, compared to P3HT composites. This is attributed to a less favorable interaction between components, which also resulted in visible phase separation during drop-casting. The average thermoelectric performance of composites containing 50 wt% N-MWCNTs is reported in Table 6.5. $S$ shows no significant increase over neat N-MWCNTs, while $\sigma$ and $S^2\sigma$ are lower, due to the poor dispersion. Reference values for neat P(NDI2OD-T2) could not be measured, because the electrical conductivity was too low to allow for reproducible measurements.

## 6.7.  Mechanically Interlocked CNTs

Another interesting composite material are mechanically interlocked carbon nanotubes, which were provided by Emilio M. Pérez from IMDEA Nanociencia. MINTs consist of molecules that form closed rings around SWCNTs, trapping them. The effect of different molecules, such as those based on pyrene [LP15], tetrathiafulvalene (exTTF) [JPR+14] or naphthalene bisimide (NDI) on the thermoelectric properties of SWCNTs was investigated.

Figure 6.23 shows the thermoelectric performance of these materials both for MINTs, and for simple mixtures of an identical amount of SWCNTs and the linear precursor of the respective molecules. No significant difference in $S$ was observed between composites of free

tubes and open rings, and those where a closed ring has been formed around the nanotubes. Similarly, there is little change of $S$ between the different molecules. If the molecules are indeed doping the SWCNTs, then the effect is small. The degree of functionalization is of the order of 1 molecule per 140 carbon atoms, which could explain why no larger change is observed. Compared to neat SWCNTs, $S$ increases equally for all composites, which is probably related to the concurrent decrease of $\sigma$. The only difference is exTTF, whose solubility significantly decreased upon forming MINTs. The resulting heterogeneous films contain undispersed tubes.
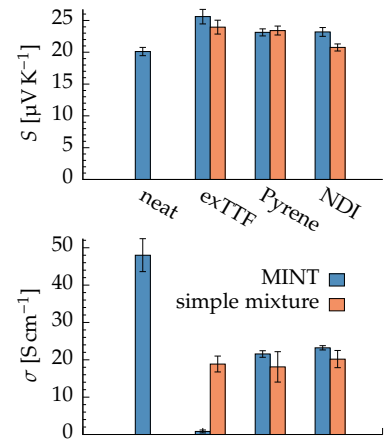


Figure 6.23: $S$ and $\sigma$ for 1:1 MINT:SWCNT composites.

# Oriented Polymer Layers

<span style="float:right">7</span>

## 7.1. Motivation

While organic photovoltaic devices show a lot of promise for electricity generation from sunlight, one should not forget one of the main advantages of organic materials over their inorganic competitors. The great variety of useful effects, that can be obtained using comparably simple processing methods, like solution deposition. While endeavors to reach record device efficiencies do have their place, it is not clear that vacuum-evaporated, glass-encapsulated complex multi-junction organic devices will be able to keep up with inorganic competitors, once they loose their advantage of low processing complexity and scalability.

As such, the central topic of this chapter is instead simplicity [TLY+17]. Not the incremental optimization of parameters to maximize a single number—the efficiency—but instead focus on how to manipulate a heretofore uncontrolled process. By using simple yet effective methods, oriented polymer layers are prepared. As we saw in Chapter 2: Conjugated Materials, orientation can be a convenient way to study fundamental material properties, as well as to obtain new functionality, such as a polarization dependent electrical response, which will be illustrated in detail in Chapter 8: Oriented Photovoltaics.

[TLY+17] Xinchun Tian et al. *Adv. Mater.* 10.1002/adma.201604681 (2017)

## 7.2. Epitaxial Crystallization

The mentioned uncontrolled process responsible for the orientation, is the crystallization during film formation. The degree of phase separation during the casting of a blend is of critical importance to the performance of bulk heterojunctions. It is no wonder then, that an array of methods, such as thermal and solvent annealing, the use of solvent mixtures, or the deposition from hot solutions has been developed that allow a precise control of the final film properties. However, these methods typically focus on crystallite size, or interconnectivity and not their large-scale orientation. Here we present a method that allows to obtain oriented polymer structures in a single step directly from solution.

From the Melt   Large-scale oriented films of conjugated polymers or small molecules can be obtained by epitaxial growth on a suitable template [WL90] [WS91]. However, unlike huge, defect-free, silicon single-crystals, organic polymers are at best semicrystalline.

An example template is the crystallizable solvent 1,3,5-trichlorobenzene, which has been shown to promote the organization of P3HT from the melt [BW06]. In this case, P3HT, and molten TCB which acts as

**Epitaxial growth**   Growth of an ordered structure with the help of a crystalline substrate that acts as a seed crystal.

[WL90] Jean Claude Wittmann et al. *Prog. Polym. Sci.* **15**, 909 (1990)

[WS91] Jean Claude Wittmann et al. *Nature*, **352**, 414 (1991)
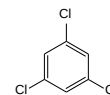
**TCB**
**1,3,5-trichlorobenzene**   Crystalline solid at room temperature. Can be used as a solvent similar to CB when liquid.

[BW06] Martin Brinkmann et al. *Adv. Mater.* **18**, 860 (2006)

a solvent, are confined between two glass slides and slowly cooled down.

1. As the temperature is lowered, TCB starts to solidify, randomly nucleating and growing numerous crystals before eventually forming a polycrystalline layer.
2. The P3HT meanwhile accumulates in the remaining liquid TCB solvent until a critical concentration is reached. Then the P3HT starts to epitaxially grow, using the TCB crystals as templates.
3. Afterwards, the TCB simply sublimates, leaving a layer of neat semicrystalline P3HT.

The morphology of the final film strongly depends on how the sample is cooled down. If all of the sample is cooled down at once, then nucleation will proceed all throughout the sample. In this case, the number of crystallites is typically so high, that no macroscopic order is observed, due to the random orientation of crystallites relative to each other. For the same reason no macroscopic order is observed when crystallizing pure P3HT. If however, the temperature is decreased starting at one side and proceeding slowly along the layer, then macroscopic fibers are observed.

FROM SOLUTION  In previous work done in our group, it was shown that the above process can be adapted to solution deposition methods such as spin coating [MAH+13]. The method still uses liquid TCB, but instead of melting it, it is itself dissolved in a second carrier solvent, for example chlorobenzene. The method is qualitatively the same, with the important difference that the solidification of TCB is no longer controlled by a decrease in temperature, but instead by the evaporation of the carrier solvent. Additionally, the material no longer has to be confined between two glass slides. Instead the method allows to make use of the large repertoire of existing solution-based deposition techniques such as spin coating and blade coating.

[MAH+13] Christian Müller et al. *Adv. Funct. Mater.* **23**, 2368 (2013)

CB Chlorobenzene

## 7.3. Uncontrolled Nucleation

SPHERULITES  Samples were prepared from a solution of $30\,\mathrm{mg\,ml^{-1}}$ of P3HT and $150\,\mathrm{mg\,ml^{-1}}$ of TCB in CB. A typical one is depicted in Figure 7.1. The visible structures are called spherulites—spherical crystallites [GPB+04] [GPT+05]. They consist of aligned fibrils of P3HT which causes the films to exhibit birefringence. Light is preferentially absorbed whenever the P3HT backbone—and with it the transition dipole moment—lies parallel to the axis of polarization. This means, that the P3HT chains in the spherulites in Figure 7.1 are oriented radially away from the points of initial nucleation. Between crossed polarizers, each spherulite exhibits the typical Maltese cross pattern, compared to an isotropic layer of unoriented P3HT fibrils, which would appear completely black.

**Spherulite**  A semicrystalline region of material with spherical, or in two dimensions circular shape.

[GPB+04] László Gránásy et al. *Nat. Mater.* **3**, 645 (2004)

[GPT+05] László Gránásy et al. *Phys. Rev. E*, **72**, 011605 (2005)
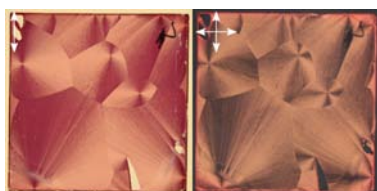


Figure 7.1: Photograph of typical randomly nucleated spherulites obtained by spin coating P3HT from a CB/TCB solution. On the left, the sample is illuminated with vertically polarized light from the back, while on the right, it is placed between crossed polarizers.

HIGH TCB CONCENTRATIONS  Compared to the original method which only used two ingredients, the crystallizable solvent and the material to orient, the solution-based methods uses a third material, the carrier solvent. While we observed little effect due to the type of carrier solvent, the concentration is an important parameter. Specif-

ically, it was observed that the ratio of TCB to P3HT determined
if the prepared samples were anisotropic or not. Figure 7.2 shows
polarized and cross-polarized micrographs of a sample deposited
from a solution of $20\,\mathrm{mg\,ml^{-1}}$ of P3HT and $360\,\mathrm{mg\,ml^{-1}}$ of TCB in CB.
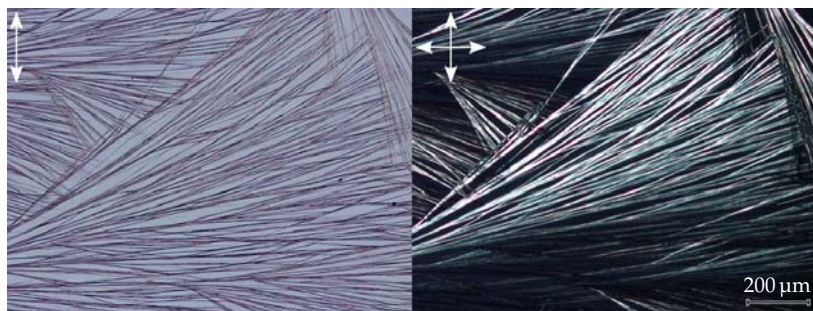Millimeter long fiber- or needle-like structures can be observed. Such
excessively high ratios, in this case 18× as much TCB as P3HT, result
in the creation of large voids, which are left upon sublimation of TCB.

LOW CONCENTRATIONS    Conversely, at very low TCB concen-
trations, no macroscopic orientation is observed. It is not without
effect however. The crystallinity of P3HT still increases, as was ob-
served by the prominent shoulder in absorption, typical of crystalline
P3HT. The increased crystallinity also results in a higher resistance
to interdiffusion of PCBM deposited from the orthogonal solvent
dichloromethane. As shown in Figure 7.3, the PL spectrum of P3HT
is strongly quenched upon deposition of PCBM under normal condi-
tions. This is explained by the well-known fact that DCM allows the
interdiffusion of PCBM into the P3HT layer, creating an intermixed
region, which is suitable for charge generation in OPV devices. When
the P3HT was deposited from a solution containing small amounts of
TCB however, then the PL quenching disappears. This is explained
by an increased crystallinity, which decreases the swelling of the
P3HT and thereby reduces interdiffusion of the PCBM. Being able
to tune the amount of interdiffusion this way, was shown to increase
the power conversion efficiency of bilayer solar cells [VDH+16]. A
similar increase in efficiency has been observed in BHJ solar cells,
where low concentrations of TCB effectively act as a high boiling
boint solvent [KPK+10].

CONTROLLING ORIENTATION    The goal of this work was then
to gain some control over the nucleation and growth of spherulites,
which are obtained at intermediate TCB concentrations, with the
hope of being able to use the resulting predictable structures in OPV
devices.

Simple approaches, like modifying the substrate topography by
scratching for example, showed no effect. On the other hand, more
complex methods, like engineering the substrate wettability, are
known to work too well. While they can be used to effectively restrict
the nucleation of spherulites, they at the same time also restrict their
growth [LTS+12]. But it is the independent control of nucleation and
growth, which is needed to achieve oriented polymer films.

By carefully examining spin coated samples, one can conceive of a
possible way to control the nucleation and subsequent growth. As
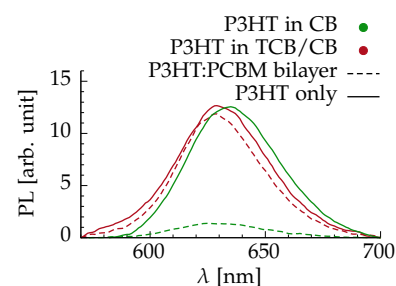
DCM Dichloromethane    Low boiling
point solvent, that dissolves PCBM but
not P3HT.

[VDH+16] Varun Vohra et al.
*Appl. Phys. Express*, **9**, 012301 (2016)

[KPK+10] Anusit Keawprajak et al.
*Sol. Energy Mater. Sol. Cells*, **94**, 531
(2010)

[LTS+12] Stephanie S. Lee et al.
*Adv. Mater.* **24**, 2692 (2012)

Contact line   Triple phase boundary between solution, substrate and atmosphere.



Figure 7.4: The drying process during regular spin coating. The three subsequent still images span 1 s.

The results presented in this section have been published in
[DVT+14] Bernhard Dörling et al. *J. Mater. Chem. C*, **2**, 3303 (2014).

Blade coating   Film forming technique by which a solution is spread across a substrate using a blade or knife.

[LCB09] Maël Le Berre et al. *Langmuir*, **25**, 2554 (2009)

[LL42] Lev D. Landau et al. *Acta Physicochim. U.R.S.S.*, **17**, 42 (1942)

can be verified by inspecting Figure 7.1, most spherulite centers are located at the sample edges—at the contact line where the sample starts drying first. Using P3HT this can be easily observed in real-time. Figure 7.4 shows still images taken during spin coating. Because P3HT is orange in solution and purple in the dried film, it is clearly visible that the solvent first evaporates at the edges, and then proceeds toward the center of the sample, which remains in a dissolved state the longest.

In the following two sections we will exploit this basic observation and present a simple method that allows to create two very different types of oriented samples.

## 7.4. Uniaxial Orientation

Blade Coating   One intuitive way to control the direction of drying is to use an inherently directional deposition method, such as blade coating. In this case, a droplet of solution is deposited on one side of a substrate, and subsequently spread across the whole sample. It is expected that for slow deposition speed—for a large asymmetry between start and end—some form of orientation should be observed.

Influence of Blade Speed   In a first series of samples, we investigated the influence of the blade speed, when coating a CB solution containing P3HT and five times as much TCB ($\frac{m_{\text{TCB}}}{m_{\text{P3HT}}} = 5$). Interestingly, depending on the deposition parameters, two distinct regimes become apparent [LCB09].

For high deposition speeds, solvent evaporation cannot keep up with the moving blade and a liquid film forms on the substrate. This liquid layer then starts drying only after the blade has passed all of the sample. This regime is usually called the Landau-Levich regime [LL42]. In this case, nucleation of TCB is uncontrolled and occurs randomly across the whole sample, resulting in a large number of spherulites, as seen on the right side of Figure 7.5.

For low deposition speed—in the evaporation regime—carrier solvent evaporation dominates the deposition behavior. The contact line can keep up with the movement of the blade and an already dried film is left behind the blade. In this case, TCB nucleation is confined along the one-dimensional blade edge, which results in cm$^2$-sized samples of uniaxially oriented polymer as shown on the left side of Figure 7.5.

The two described regimes result in distinctly different samples. However, to completely reach the evaporation regime, deposition speeds below $1 \, \text{mm s}^{-1}$ would have been required, which was not possible at the outset with the available blade coater. Instead we increased solvent evaporation with an additional flow of gas directed at the contact line. A complete description of the sample preparation is provided in Chapter B: Experimental Methods.

Figure 7.5 warrants some in-depth explanation. The second row shows vertically polarized transmission photographs of complete 25 by 25 mm$^2$ samples. The transmittance $T$ for light polarized horizon-
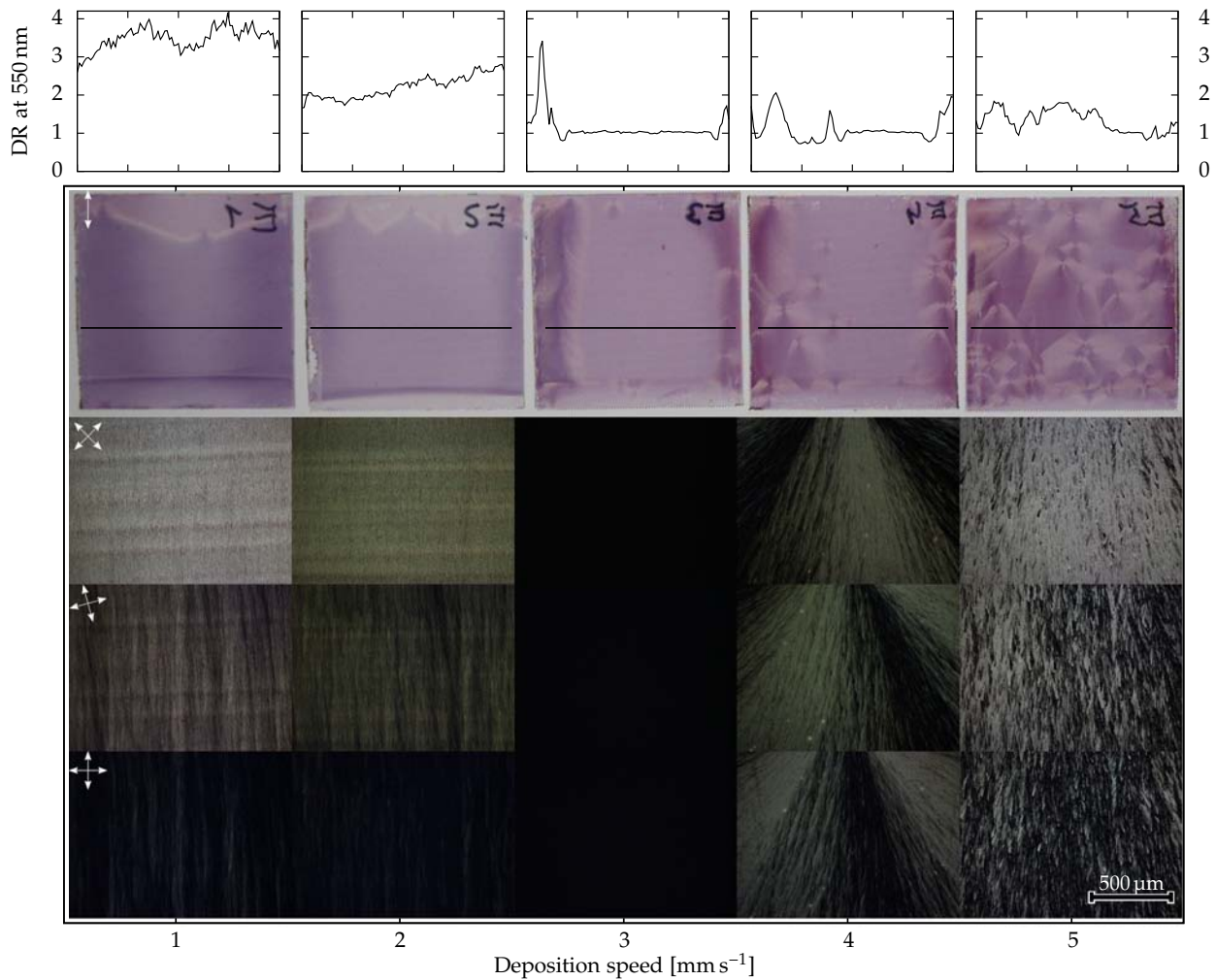
Figure 7.5: Influence of deposition speed on the orientation. Shown are the dichroic ratio at the top, polarized transmission photographs and three cross-polarized micrographs at different polarizer orientation versus deposition speed. Samples were coated from top to bottom from a solution of $20\,\mathrm{mg\,ml^{-1}}$ of P3HT and $\frac{m_{\mathrm{TCB}}}{m_{\mathrm{P3HT}}} = 5$.

DR Dichroic ratio    The ratio of absorbance for light polarized parallel to light polarized perpendicularly to some reference direction.

tally and vertically was measured at $550\,\mathrm{nm}$ along the indicated lines. From these measurements, the dichroic ratio

$$\mathrm{DR} = \frac{-\log(T_{\parallel})}{-\log(T_{\perp})}, \tag{7.1}$$

can be calculated, which is shown in the first row. The lower three rows show cross-polarized micrographs at three different angles of the polarizers, to better reveal details.

While films deposited at speeds of 1 and $2\,\mathrm{mm\,s^{-1}}$ show layers with a fibrillar texture of uniform orientation, the samples deposited at higher speed show an increasing number of spherulites embedded in an otherwise isotropic layer. There is a clear transition between both regimes at a speed of around $3\,\mathrm{mm\,s^{-1}}$, where no orientation is obtained and no light is transmitted through the crossed polarizers.

Figure 7.6 shows an example of a measurement of the dichroic ratio for a sample deposited at $2\,\mathrm{mm\,s^{-1}}$. At the maximum of absorption at $550\,\mathrm{nm}$, we observe $\mathrm{DR} = 2.6$. It should be noted that DR is expected to vanish for energies below the bandgap. The observed nonzero DR in this case is due to scattering.

We observe a reasonably homogeneous DR for layers with fibrillar



Figure 7.6: Transmittance for light polarized along and perpendicular to the fiber direction, as well as the calculated dichroic ratio.

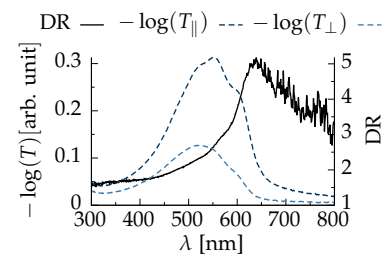texture, with an apparent increase in the degree of orientation with decreasing blade speed, going from DR $\approx$ 3.4 at $1\,\mathrm{mm\,s^{-1}}$ down to DR $\approx$ 2.3 at $2\,\mathrm{mm\,s^{-1}}$. At higher speeds, the orientation within spherulites appears smaller, with DR peaking at about 2. However, due to the angular distribution within a spherulite, DR will depend on the size of the light spot, which in this case was $250\,\mu\mathrm{m}$.

It has to be pointed out, that during blade coating, excess solvent accumulates at the edges of the sample. This leads to an elevated TCB concentration at the sides and bottom of the substrate, which in turn leads to dichroism at the edges of otherwise completely isotropic samples, as is exemplified by the middle column in Figure 7.5. These edge effects are confined to about 3 to 5 mm wide stripes and do not depend on the substrate size, provided that a large enough substrate is used. Consequently, increasing the substrate size would increase the quality of samples, allowing for a potential scale-up. Homogeneity of the whole sample could potentially be further increased by improving the control over the initial nucleation and ensuring sufficient circulation of the solution during deposition [DTG+13].

[DTG+13] Ying Diao et al. *Nat. Mater.* **12**, 665 (2013)

EFFECT OF GAS FLOW  If the rate of solvent evaporation is not increased by an additional flow of gas, the evaporation regime is not reached, and the drying does not proceed in an ordered manner along the contact line, parallel to the blade, and instead may start from the sides as seen in the first column of Figure 7.7. As soon as the drying front is pinned to the blade, any further flow does not influence the
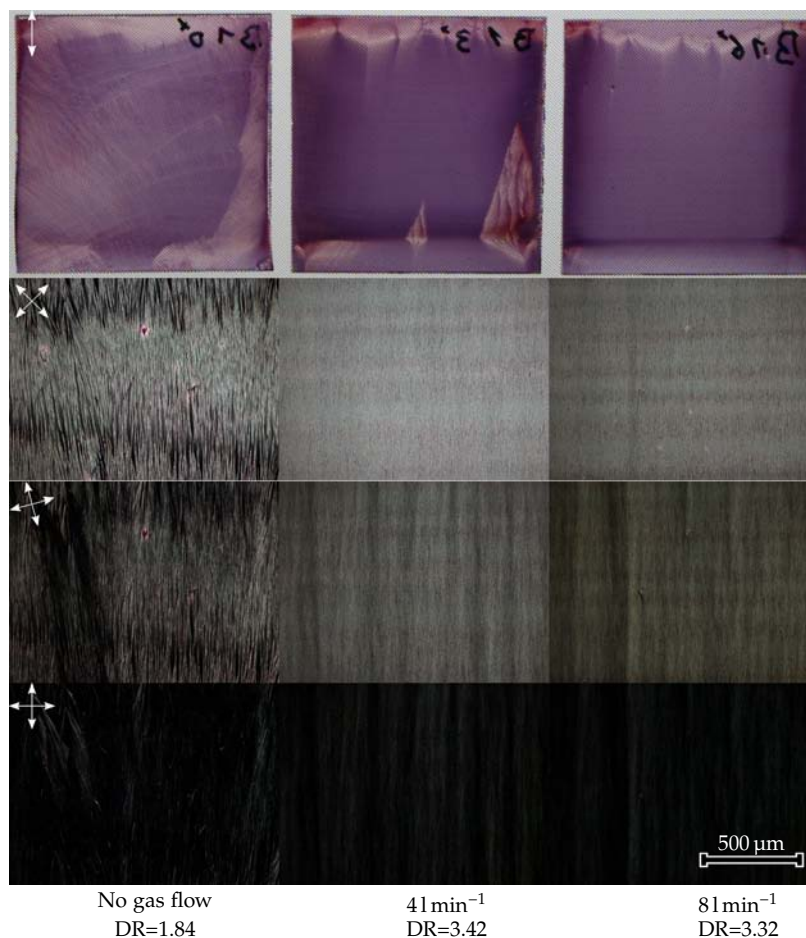


Figure 7.7: Effect of gas flow on orientation. Films were coated with $v_{\mathrm{Blade}} = 1\,\mathrm{mm\,s^{-1}}$ from a solution of $40\,\mathrm{mg\,ml^{-1}}$ P3HT and $\frac{m_{\mathrm{TCB}}}{m_{\mathrm{P3HT}}} = 5$. Dichroic ratios were measured at $550\,\mathrm{nm}$ with a 3 mm spot.

| No gas flow | $4\,\mathrm{l\,min^{-1}}$ | $8\,\mathrm{l\,min^{-1}}$ |
|---|---|---|
| DR=1.84 | DR=3.42 | DR=3.32 |

behavior significantly, as is evidenced by the very similar dichroic ratios. Two further details are worthy of note. Even though samples are oriented uniaxially all throughout, growth starts at a few distinct nucleation points, which left to their own, would form spherulites otherwise. Additionally, it is quite obvious that the process of growth is that of the growth of a spherulite—by secondary nucleation and a space-filling growth—albeit under strongly asymmetric conditions. Any present impurities can potentially influence this growth, even nucleating other spherulites with mismatched orientation, as pictured in the middle column of Figure 7.7

During blade coating, the laminar flow of gas was directed at the contact line using the 3D-printed accessory shown in Figure 7.8. This worked well for the used speeds of a few $mm\,s^{-1}$.

For significantly higher speeds, the solvent can still be evaporated very quickly over a large area, simply by increasing the gas flow. But it was observed that the number of nucleation centers then strongly increases, resulting in samples with a large number of microscopic spherulites. While the evaporation front does keep up with the blade in this case, the crystallization front cannot, because the speed of crystallization is not high enough, presenting a fundamental limitation.

During the course of this thesis, a programmable voltage source based on an Arduino microcontroller was built, which allowed to blade coat at velocities below $1\,mm\,s^{-1}$, as well as at constant acceleration, extending the functionality of the blade coater. Further details on the specifics can be found in Chapter A: Experimental Setups.

Figure 7.9 shows films deposited at speeds as low as $0.1\,mm\,s^{-1}$, without an additional flow of gas. As was seen before, at $1\,mm\,s^{-1}$ films are not uniformly oriented without increasing the evaporation of solvent. At $0.6\,mm\,s^{-1}$ orientation is restored, while at $0.1\,mm\,s^{-1}$ the fibrillar structures gain in size.



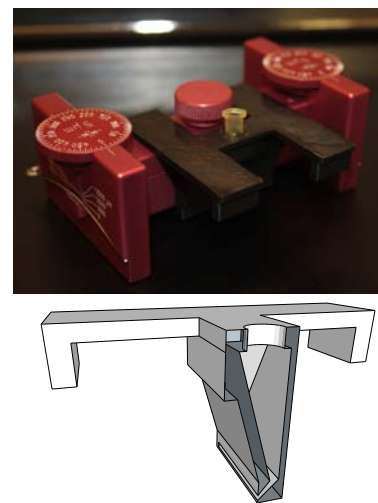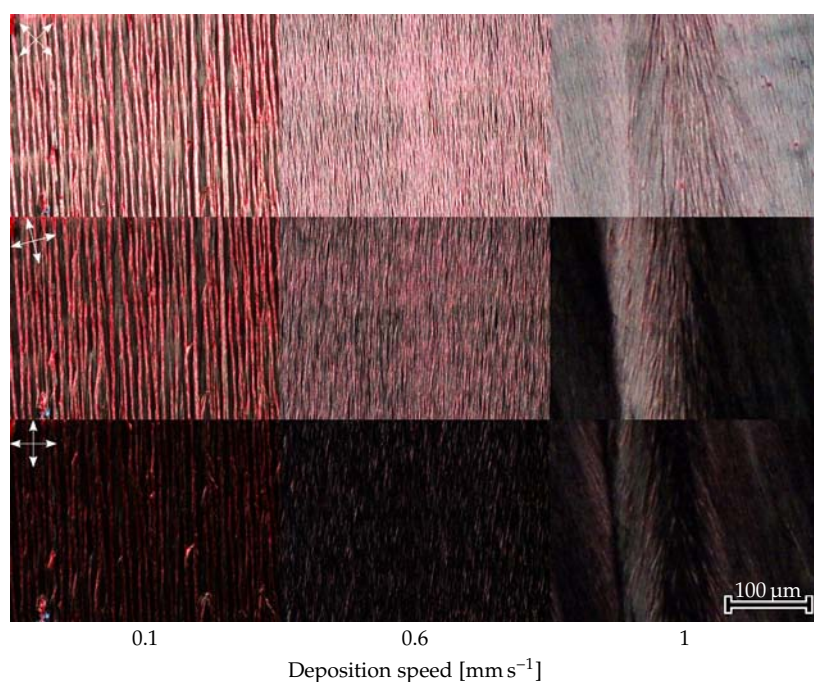Figure 7.8: Photograph of the laminar flow accessory attached to the blade, and its design.



0.1          0.6          1

Deposition speed [$mm\,s^{-1}$]

100 µm

Figure 7.9: Films blade coated without additional gas flow at speeds below $1\,mm\,s^{-1}$.

From here on in, all presented samples have been prepared using an external flow of gas, due to a better reproducibility.

EFFECT OF LAYER THICKNESS   When depositing films by blade coating, the final film thickness has a nonlinear dependence on the deposition speed, with the thinnest layers deposited at the transition from evaporation to Landau-Levich regime. For both lower and higher speeds, thicker films are obtained [LCB09].

To check if the observed behavior is not simply due to a changing layer thickness, we prepared samples with double the polymer concentration but the same ratio of TCB to P3HT, $\frac{m_{TCB}}{m_{P3HT}} = 5$. Reassuringly, the same behavior is observed. At slow deposition speeds we observe uniaxial orientation which changes to spherulitic growth at higher speeds, as depicted in Figure 7.10. Two further details are particularly apparent in these films. At higher speeds, the nucleation density seems to be correlated to the deposition speed. And last but not least, the spherulites exhibit a distinct "shooting star" morphology, which has been observed in other systems under asymmetric conditions [GRS+14].

INFLUENCE OF TCB CONCENTRATION   Next we study the effect of the ratio of TCB to P3HT. Figure 7.11 shows a combinatorial array of samples deposited at increasing blade speed on the x-axis and increasing TCB to P3HT ratio on the y-axis. The corresponding array of cross-polarized micrographs is depicted in Figure 7.12.

[LCB09] Maël Le Berre et al. *Langmuir*, **25**, 2554 (2009)

[GRS+14] László Gránásy et al. *Metall. Mater. Trans. A*, **45**, 1694 (2014)

Figure 7.10: Films deposited from a solution with increased concentration, compared to Figure 7.5.
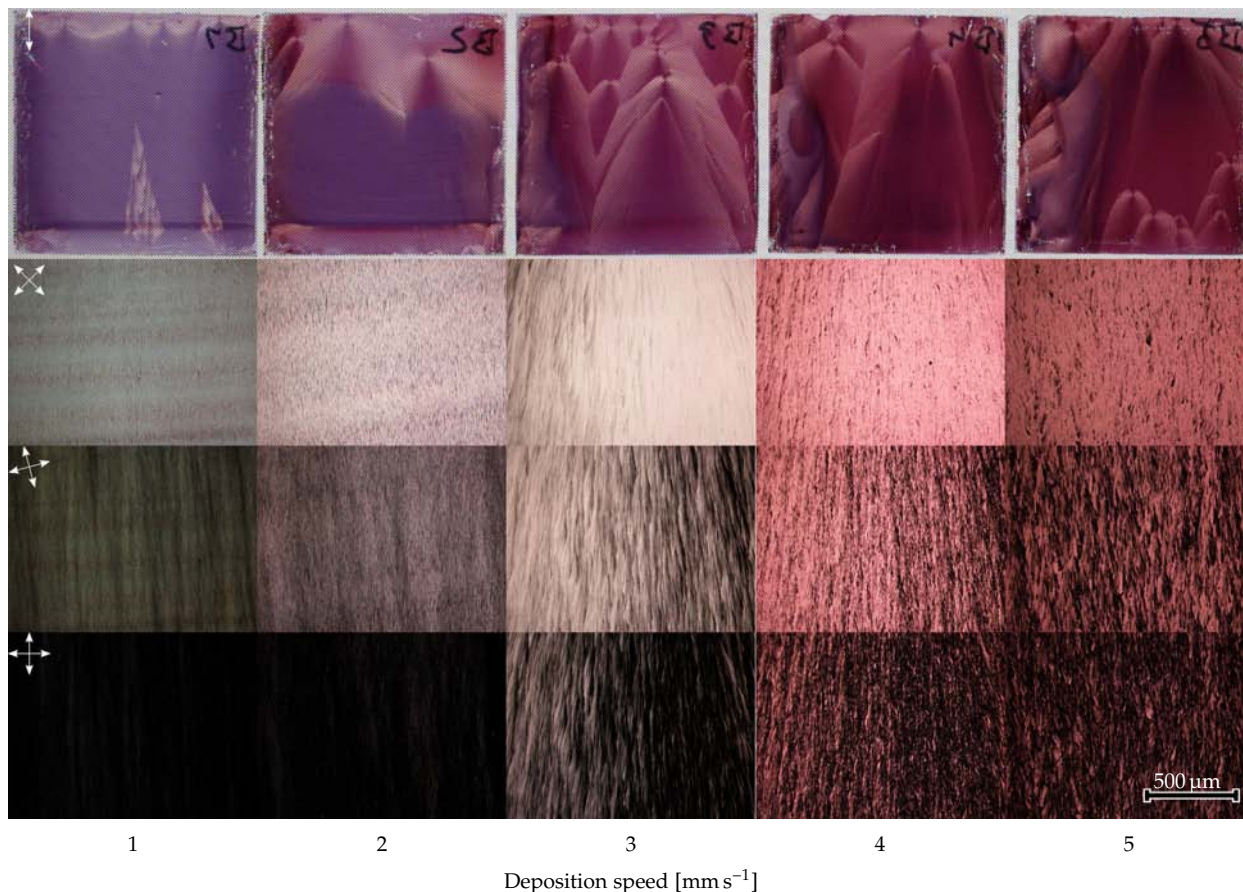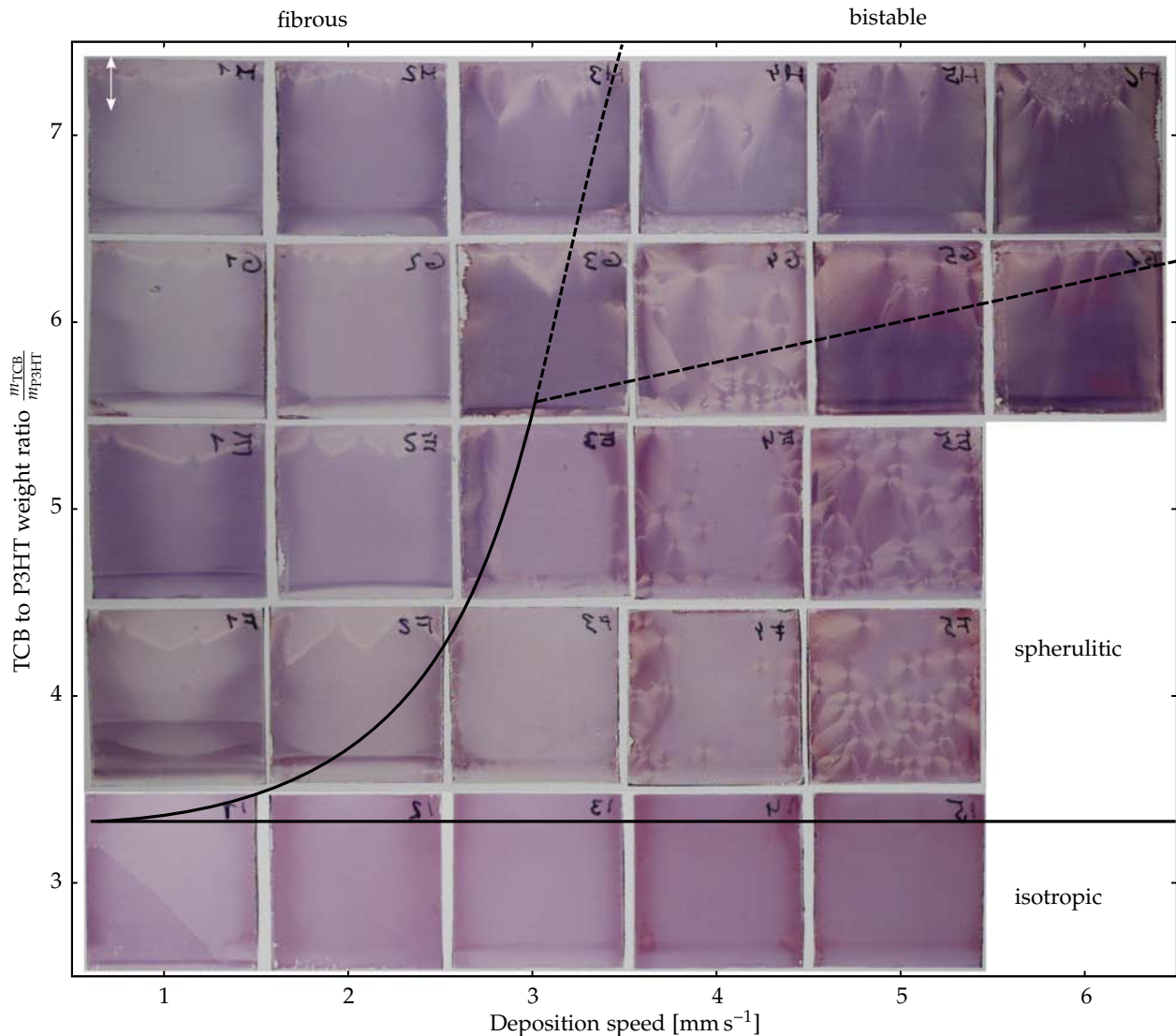


500 µm

1          2          3          4          5

Deposition speed [mm s$^{-1}$]

Samples deposited from solutions with $\frac{m_{TCB}}{m_{P3HT}} < 3$ do not exhibit dichroism. Orientation is first observed for low speeds at a ratio of 3. However, since nucleation is a stochastic process, some samples may only be partly or even not at all oriented. A clear separation between Landau-Levich and evaporation regime is observed for increasing $\frac{m_{TCB}}{m_{P3HT}}$, with a critical deposition speed of about $3\,\mathrm{mm\,s^{-1}}$. Deposition speeds below $3\,\mathrm{mm\,s^{-1}}$ consistently result in samples that have a fibrillar texture and exhibit uniaxial orientation on a macroscopic scale. Higher deposition speeds on the other hand lead to samples that are covered in spherulites. These two regimes adjoin at a deposition speed of $3\,\mathrm{mm\,s^{-1}}$, where samples are mostly isotropic, interspersed with the odd spherulite. For $\frac{m_{TCB}}{m_{P3HT}} \geq 6$, the distinction is not as clear-cut, where a fast blade speed results in bistable drying during coating, with the appearance of fibrous and spherulitic areas within the same sample.

Inspired by the useful phase diagram descriptions of mixtures, we have superimposed approximate regime frontiers on the arrays of sample pictures. Low $\frac{m_{TCB}}{m_{P3HT}}$ lead to isotropic films. Intermediate ratios result in oriented fibrous and spherulitic films for slow and fast blade
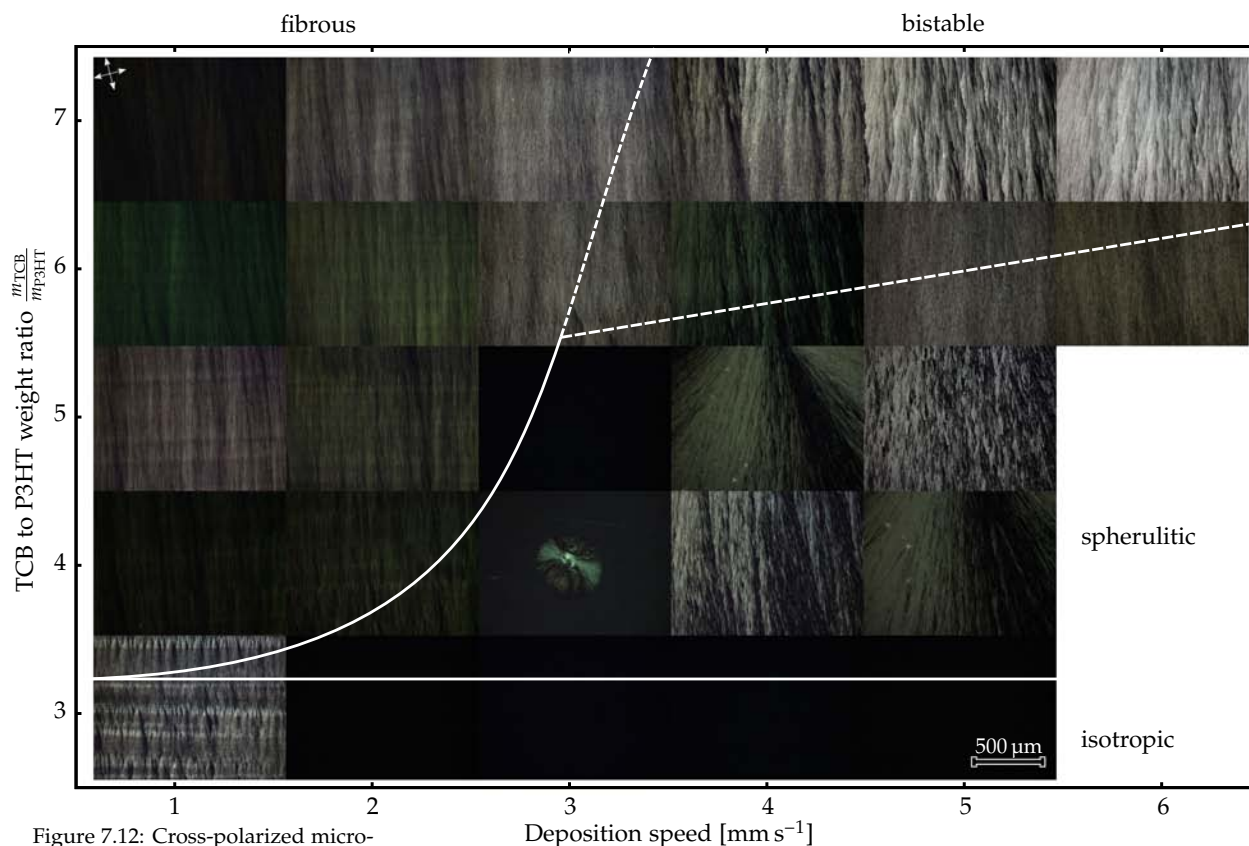
Figure 7.12: Cross-polarized micrographs corresponding to samples from Figure 7.11.

speeds, respectively. Increasing $\frac{m_{\text{TCB}}}{m_{\text{P3HT}}}$ to significantly larger values resulted in increasingly porous films with ill-defined orientation, as was shown in the beginning of this chapter in Figure 7.2.

INFLUENCE OF TEMPERATURE   As we just saw, the density of nucleation centers can be controlled by decreasing the TCB concentration. This was particularly obvious for uniaxially oriented samples, since starting from a single nucleus, the rest of the sample in deposition direction will be oriented. However, the final result proved to be quite sensitive to the exact concentration, as well as to other external factors. Because of this, controlling the nucleation was quite unpredictable when only controlling TCB concentration.

A better parameter was the substrate temperature. No anisotropy is expected for temperatures larger than the melting point $T_{\text{melt}}^{\text{TCB}} = 63\,^\circ\text{C}$. At intermediate temperatures, a gradual change can be observed as summarized in Figure 7.13. Initial nucleation occurs later during deposition, even at only slightly elevated temperatures. At temperatures as low as 40°, no orientation is observed during blade coating of a 25 mm long substrate at $1\,\text{mm}\,\text{s}^{-1}$.
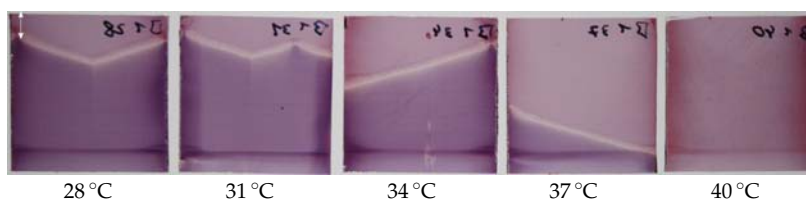


Figure 7.13: Influence of increasing substrate temperature, compared to $T_{\text{melt}}^{\text{TCB}} = 63\,^\circ\text{C}$.

DIFFERENCES BETWEEN SPHERULITES AND FIBERS  Due to the stochastic nature of the nucleation process, it is possible to obtain mutually exclusive areas of fibrillar texture and spherulites in direct contact. A photograph of a partial spherulite between uniaxial fibers was already shown in Figure 7.7, and is further detailed in Figure 7.14. Typical of spherulites, it is denser with no voids. Due to the branching, space-filling growth, the spherulite is cone-shaped. The fibers on the other hand grow in a more or less parallel direction, which seems to require large intermediate voids, possibly to allow for the variations during growth.

In order to better understand the differences resulting from the two deposition regimes, we characterized the structure of different samples by atomic force microscopy. The AFM images in Figure 7.15 depict the differences between spherulitic layers and films with a fibrillar texture. Aside from their degree and direction of orientation, their main distinguishing feature is the surface roughness. While spherulites show higher roughness than conventional layers of P3HT, the uniaxially oriented layers consist of fibrous structures that are even rougher. In fact, they are composed of stacks of largely freestanding fibrous polymer structures separated by voids that reach all the way to the substrate. After depositing PCBM on top of a fibrous layer using the orthogonal solvent DCM, the roughness strongly decreases, with the P3HT fibers rearranging, and the remaining voids being filled with PCBM.
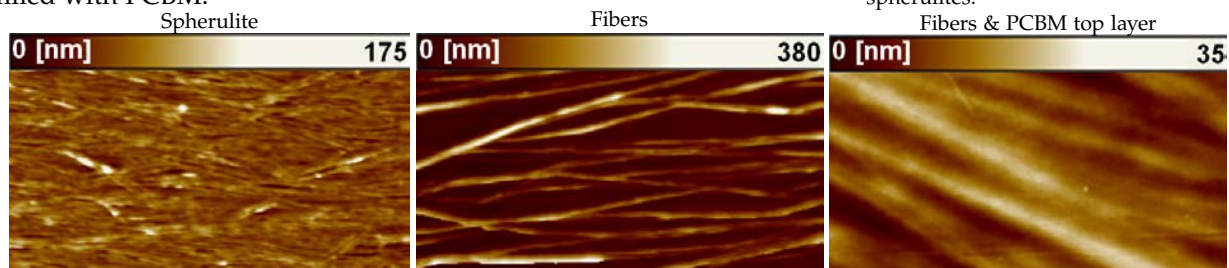


Figure 7.14: Bistability of fibers and spherulites.



Spherulite — 0 [nm] 175 | Fibers — 0 [nm] 380 | Fibers & PCBM top layer — 0 [nm] 35

Figure 7.15: AFM images of a 50 by 20 μm² area, depicting the different types of textures.

## 7.5. Pinning of Spherulites

So far, we saw that left to their own, spherulites will randomly nucleate all throughout a two-dimensional film. By confining the initial, as well as secondary nucleation to the one-dimensional contact line during blade coating, we were then able to obtain uniaxially oriented layers. In this section, we want to confine the initial nucleation at a single zero-dimensional point, without otherwise perturbing growth, thereby demonstrating the ability to position spherulites at any desired location.

NUCLEATION OF A SINGLE SPHERULITE  Like in the preceding section, to achieve this, we will selectively increase evaporation—this time at a single point only. Spin coating particularly lends itself to this undertaking, due to the radial symmetry during rotation of the substrate. However, as we saw in Figure 7.4, samples start drying from the edges inwards. This was evidenced by observing a typical spin coating process, where a change of the color of P3HT from orange to purple, within a single second all throughout the sample, was observed. Compared to the preceding 20 s with no apparent change,
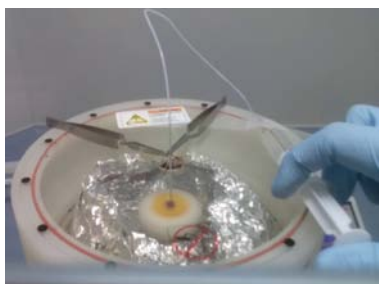
Figure 7.16: Video still of the process used to create single spherulites.



Figure 7.17: The process of accelerated drying during spin coating. The three subsequent still images span 2 s while a flow of gas is supplied through a needle visible above the substrate.



Figure 7.18: Comparison between several randomly nucleated spherulites, or a single centered one. Samples are 25 by 25 mm$^2$ in size.
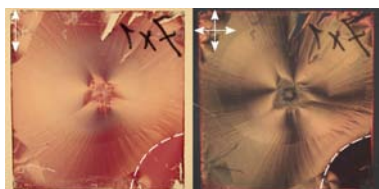


Figure 7.19: Suppression of spherulite growth. Photographs of a sample that has been heated in the bottom right corner before deposition, inhibiting solidification of TCB.

where solvent is evaporating, though P3HT is not yet solidifying. This means that samples tend to dry quite homogeneously.

By injecting gas through a needle at the central axis of rotation, as pictured in Figure 7.16, this drying process can be reversed, starting at the center. Figure 7.17 shows consecutive still images of this process, clearly demonstrating the effectiveness of this simple method. Compared to regular, random samples, the drying process now proceeds slower, since it has to be started earlier when no solvent has yet evaporated naturally—anticipating the regular drying.

The diameter of the needle, as well as the shape of the tip have an effect on the size of the initially dried center. The diameter of the needle should be as small as possible, in this case it was 0.8 mm, with the tapered tip cut off flat. Furthermore, the spin coater model also affected the results. Three different models were used, and the best results were obtained in a Laurell Technologies WS-650SZ-6NPP-LITE spin coater. The observed differences in the drying behavior are attributed to the way these models flush the spin coating chamber during deposition.

A resulting sample is presented on the right side in Figure 7.18 opposite a regular, random one. It shows a single spherulite-like structure, where the initial nucleation was restricted to an area at the center of the substrate, which is much smaller than the final spherulite size, yet not infinitesimally small, due to the finite diameter of the needle, and the extension of the flow of gas.

SUPPRESSION OF SPHERULITE GROWTH BY HEATING   Pure TCB has a melting point of 63 °C and stays liquid if sufficiently heated, acting like a regular high-boiling point solvent-additive that increases crystallinity by allowing for a longer lasting drying process. Because TCB does not solidify at elevated temperatures, it is not possible to use the local application of heat to control nucleation. Yet interestingly, combining a gas flow and heat allows to prepare samples that contain both isotropic and anisotropic regions, as depicted in Figure 7.19. Simply heating one corner of the substrate directly before deposition is enough to achieve the desired effect. As we will show in Chapter 8: Oriented Photovoltaics, this capability can be of use for detectors that measure the complete linear polarization of light.

REGULAR SPHERULITE ARRAYS   To demonstrate the general viability of the presented method, a regular array of spherulites was grown using blade coating. One major difference between the spin and blade coating deposition methods is the speed at which the solvent evaporates. For a given temperature, solvent evaporates faster during spin coating, due to the rapidly rotating sample. The additional flow of gas, that is supposed to induce controlled nucleation, must be the dominating influence, surpassing any other, undesired airflow that may be present in a laboratory fume hood or glove box. Yet at the same time, the flow cannot be increased arbitrarily, since it will disturb the wet layer, physically displacing the solution on the substrate. In order to satisfy both of these conditions during the lengthy drying process of blade coated samples, several 3D-printed arrays of nozzles, shown in Figure 7.20, were manufactured. The initial design, which used an array of micropipette tips connected
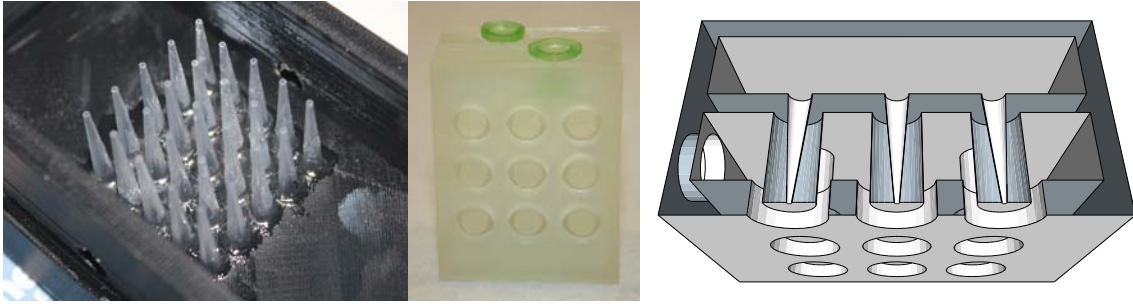
Figure 7.20: Photographs of the first nozzle array and of the improved 3D-printed version, as well as the design of the latter.

to a single interior volume, is shown on the left side of Figure 7.20. The whole assembly is placed above a wet blade coated sample, the volume is pressurized and gas injected through all tips, which are located 1 mm above the substrate. After passing over the sample, the injected gas escapes from the enclosure through holes at the top of the housing, far away from the tips. During this process, the housing covers the entire wet sample, shielding it from the strong airflows present in a typical fume hood, which will otherwise dominate the drying behavior. Using this initial design, results were not reproducible. The reasons for this were twofold. First, the tips were not all aligned perfectly, with some inaccuracies in the exact height and angle of the tips. This caused large variations of the intensity of the flow at the different tips, as is evidenced by the photograph of one such sample shown in Figure 7.21. Furthermore, individual tips were not isolated from each other, and the flow of a tip at the center was fundamentally different from that at the edges, due to a different number of neighbors.

These deficiencies were improved upon in a second design, pictured in the center of Figure 7.20. As can be seen in the sketch on the right, it features two interior volumes, one of which was pressurized as in the first design, while the second one was evacuated, confining the flow locally and providing circularly symmetric conditions. This design was 3D-printed which allowed for nozzles with only about 200 μm diameter.

Figure 7.22 shows a photograph of a blade coated sample with nine spherulites, that was prepared using this nozzle array. It is apparent that in addition to the forced drying process of the spherulites, the regular drying process, which starts at the edges of the sample, proceeds in parallel. Because of that, the growth of spherulites at the edge is disrupted by the regular drying process. However, since this process is restricted to the sample edges, it would be less of a problem when scaled up to larger samples. To further improve the results, the interior volumes have to be designed in such a way that ensures exactly identical flow at all nozzles, and the control over both the rate of injection and extraction has to be improved, ensuring truly identical conditions at all nozzles, completely isolating each one from adjacent ones.

OPTICAL CHARACTERIZATION    In order to understand the degree of orientation and crystallinity, as well as the different textures visible in the radial direction of the polarized photographs in Figure 7.18 and Figure 7.19, the samples were characterized using polarized photoluminescence spectroscopy, polarized Raman scattering and
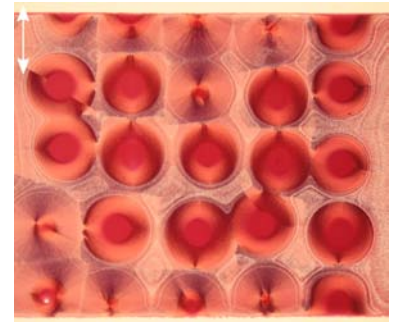


Figure 7.21: Spherulite arrays obtained using the initial design.
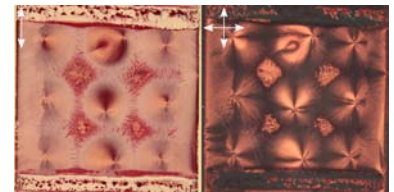


Figure 7.22: Regular array of blade coated spherulites.

Figure 7.23: Optical characterization along the radial direction of a 10 mm long section of spherulite, with the center at the right. From top to bottom are shown an optical micrograph, maps of $PL_\parallel$, $PL_\perp$ and $DR_{PL}$ as well as averaged $DR_{PL}$ and Raman peak position for both polarizations. The sample was excited at 532 nm.
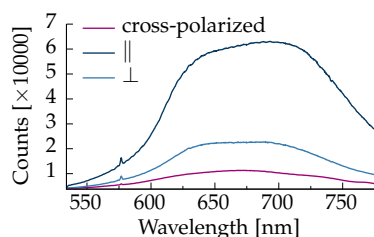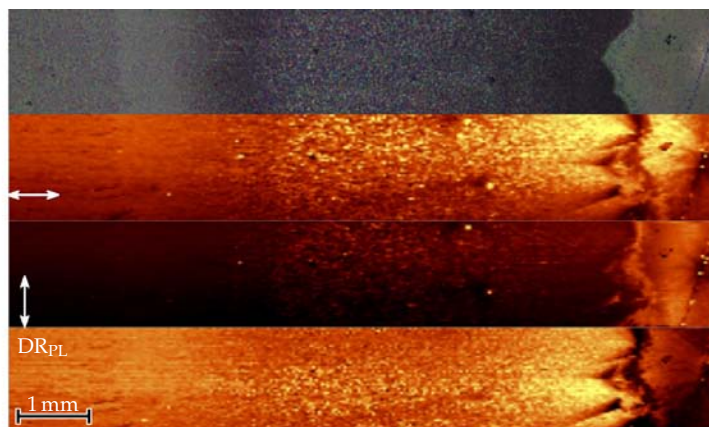


Figure 7.24: Polarized PL spectra for excitation at 532 nm.
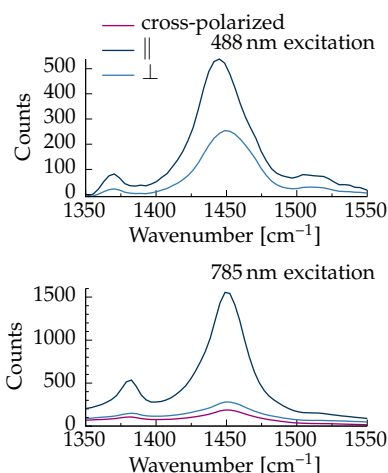


Figure 7.25: Polarized Raman spectra for excitations at 488 nm and 785 nm.

[TJK+11] Wing Chung Tsoi et al. *J. Am. Chem. Soc.* **133**, 9834 (2011)
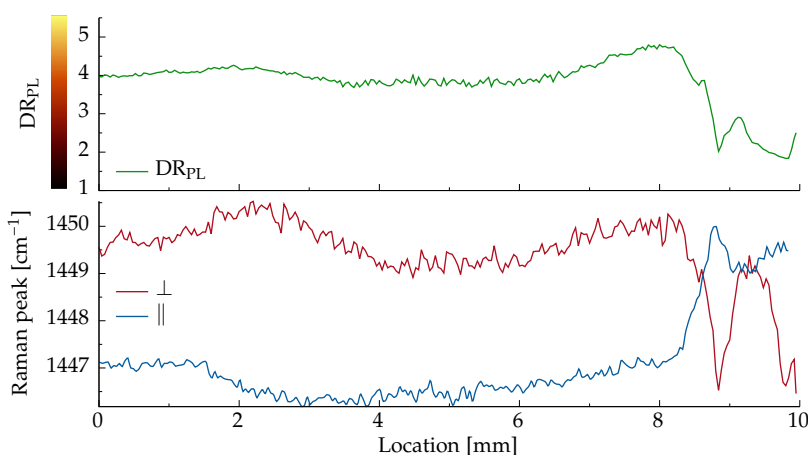
ellipsometry. The dichroic ratio of the PL, the ratio of PL for excitation parallel versus perpendicular to the orientation direction, can be used to quantify the degree of orientation. An average value of $DR_{PL} = \frac{PL_\parallel}{PL_\perp} \approx 4$ was found for a representative sample, as calculated from the PL maps shown in Figure 7.23.

Representative polarized PL spectra are shown in Figure 7.24. These values confirm a large degree of orientation for a sample with pinned nucleation center, comparable to samples deposited from solution without controlling nucleation position. At the center, crystallites are randomly oriented. Although the degree of orientation is large in the whole spherulitic structure, we observe oscillating variations of $DR_{PL}$ along the radius, which could be caused by fluctuations in solid content as the drying front progresses along the liquid film. These oscillations are correlated to the different textures observed radially, which arise from a change in the degree of misorientation of the fiber-like substructures created during the epitaxial crystallization.

Polarized Raman measurements in Figure 7.25 confirm a high degree of polymer orientation. The observed dichroic ratio is $DR_{Raman} \approx 2.5$ at 488 nm excitation. At this wavelength, the Raman signal comes from both amorphous and crystalline polymer chain segments [TJK+11]. The PL, on the other hand, arises preferentially from the crystalline segments due to an energy transfer towards the LUMO. This, together with the specific dipole orientation of PL and Raman vibration, partially explains why $DR_{PL} > DR_{Raman}$. Reassuringly, the Raman dichroic ratio increases, when exciting at a higher

wavelength of 785 nm, which preferentially excites the crystalline chain segments. It has been shown that the Raman spectra of P3HT can provide information regarding the degree of crystallinity. Specifically, the peak centered around 1450 cm$^{-1}$ consists of a superposition of an amorphous component, peaking at higher energy, and a crystalline component, peaking at lower energy [TJK+11]. Therefore, a simple analysis of the center of mass of the convoluted peak can inform us about the degree of crystallinity. As shown in Figure 7.23, the Raman peak for an excitation perpendicular to the orientation direction is shifted about 3 cm$^{-1}$ towards higher energy with respect to parallel excitation, indicating that a higher ratio of amorphous polymer chains lie in perpendicular direction.

In regions where the formation of spherulites has been suppressed by an increased substrate temperature during deposition, this shift towards higher energy disappears, as shown in Figure 7.26. This indicates that the frustrated regions have a high crystallinity, similar to that of spherulites, even though the material is not oriented. Just like the increase in crystallinity observed in P3HT films deposited from high boiling point solvents [VDH+16] [KPK+10].

Additional information regarding orientation and crystallinity can be obtained by looking at the absorption and the refractive index, or in order words, the degree of dichroism and birefringence. Spectroscopic ellipsometry has been used by Mª Isabel Alonso at ICMAB to characterize the complex refractive index $n + ik$ of a spherulitic sample, as plotted in Figure 7.27. Pinned spherulitic films exhibit a strongly anisotropic complex refractive index. Absorption features are strongly pronounced for an excitation along the radial direction. Figure 7.28 and 7.29 show false-color micrographs for the magnitude and the orientation of the linear dichroism of P3HT spherulites. The indicated orientation directly corresponds to that of the polymer chains, assuming the transition dipole moment lies along the chains. The false-color micrographs were calculated from measurements of a Mueller-matrix microscope with an excitation wavelength of 532 nm, done by Oriol Arteaga at the University of Barcelona. More details on the ellipsometric modeling and the Mueller-matrix measurements are given in Chapter B: Experimental Methods.

Figure 7.28 shows Mueller-matrix micrographs of the linear dichroism of a random spherulite, next to a region that was too hot for TCB to solidify. On the left, from the magnitude of linear dichroism, we can learn that the material is completely isotropic in the heated region, as well as at the exact center of the spherulite. On the right, from the orientation of the linear dichroism, we see that within a spherulite, the transition dipole moment is always oriented radially, while it has residual random orientation in the heated area.
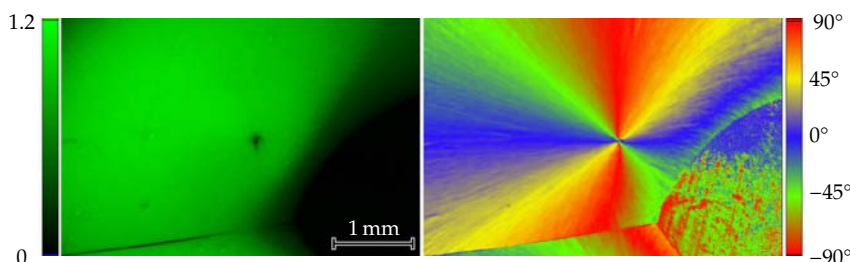
[TJK+11] Wing Chung Tsoi et al. *J. Am. Chem. Soc.* **133**, 9834 (2011)
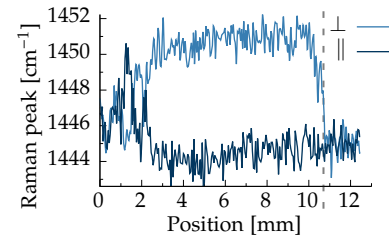


Figure 7.26: Raman peak position over a 12 mm long strip of a Raman map. The sample is optically isotropic from 10.8 mm onwards, by suppressing the orientation by heating.

[VDH+16] Varun Vohra et al. *Appl. Phys. Express*, **9**, 012301 (2016)

[KPK+10] Anusit Keawprajak et al. *Sol. Energy Mater. Sol. Cells*, **94**, 531 (2010)
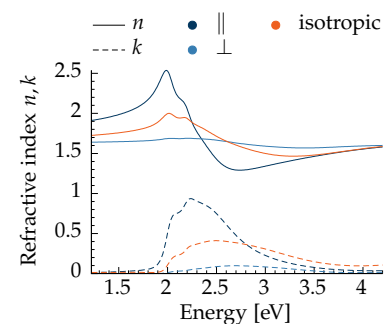


Figure 7.27: Complex refractive index of P3HT determined by ellipsometry. Measured in an isotropic region and in a spherulitic region, using an anisotropic model.



Figure 7.28: Mueller-matrix micrograph of suppressed spherulite growth. Shown are the magnitude and the orientation of the linear dichroism.

Figure 7.29: Mueller-matrix micrographs of the center of a pinned spherulite.
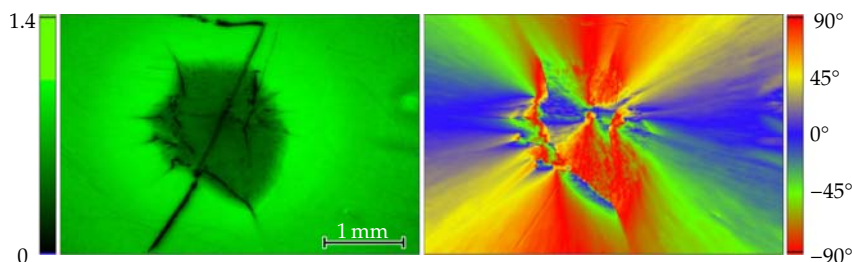
Figure 7.29 can serve to elucidate the process of spherulite formation. A comparatively isotropic region is located at the center of pinned spherulites. Here, the abrupt solvent evaporation due to the injected gas, rapidly forms a dry film, not allowing for large-scale order. Along the contact line, around the circumference of this isotropic region, numerous nucleation sites form, each of which starts to grow into a spherulite in a branching, space-filling manner. Competing with each other, they give the appearance of a single spherulite everywhere but at the center.

In the ideal case, the nucleation would be confined on a circle with infinitesimal circumference. However, mostly limited by the finite extension of the flow of gas, nucleation instead happens along a contact line that is neither a perfect circle nor infinitesimally short. In both the ideal as well as the real case, however, the nucleation itself still remains a stochastic process. Due to this remaining randomness, frontiers between neighboring spherulites can be visible in cases where the nucleation centers are distributed very irregularly along the contact line, as for example at the bottom of Figure 7.29.

## 7.6.  Extension to Other Materials

Going further, we demonstrate that the epitaxial crystallization of polymers from solution is not confined to a narrow range of materials that already show high inherent crystallinity. In Figure 7.30 we show cross-polarized microscope images of P3HT samples deposited from CB, using naphthalene as the crystallizable additive, which provides the template for epitaxial growth. The naphthalene based samples exhibit much of the same features as those deposited from solutions containing TCB. While we did not observe uniaxial orientation on a large scale, the results still mirror those of TCB samples under unoptimized conditions, specifically those that are deposited at a low TCB concentration. On the other hand, changing the polymer to one that does not crystallize easily, like PCPDTBT, still results in layers that exhibit dichroism, with strong resemblance to the asymmetric "shooting star" spherulites.

These findings suggest, that by selecting a suitable crystallizable solvent and adapting the processing conditions, a similar potential for orientation and increase in crystallinity could be obtained for a range of polymers [MAH+13].



Figure 7.30: Cross-polarized micrographs of samples fabricated using naphthalene and P3HT at the top and TCB and PCPDTBT at the bottom.



Naphthalene

[MAH+13] Christian Müller et al. *Adv. Funct. Mater.* **23**, 2368 (2013)

# 8 ORIENTED PHOTOVOLTAICS

After having developed this toolkit of processing techniques, we now will put it to use, manufacturing organic photovoltaic devices that provide new functionality, thanks to the integration of oriented P3HT layers. In particular, we will use a normal OPV geometry, with an active layer composed of a P3HT:PCBM bilayer. The P3HT layer is oriented—either uniaxial or spherulitic—and is covered by a PCBM layer, which is deposited from the orthogonal solvent dichloromethane, which does not damage the underlying P3HT layer during deposition. Instead, it slightly swells the polymer, allowing for some interdiffusion of the PCBM, creating not a simple bilayer with a very sudden interface, but instead a graded bilayer, where the composition gradually changes from pure PCBM at the top, to pure P3HT at the bottom [VAB+12]. A exhaustive description of the device manufacturing process is provided in Chapter B: Experimental Methods.

[VAB+12] Varun Vohra et al.
*J. Phys. Chem. Lett.* **3**, 1820 (2012)

## 8.1. Uniaxially Oriented Devices

Most methods to orient polymer layers rely on post-processing methods like rubbing [ZKY11], or even more complicated approaches like stretching [RAS+16], which are difficult to integrate into existing fabrication processes. Conversely, our approach does not require any additional steps, and the only additional requirement is that coating speed and solvent evaporation be adequately matched.

[ZKY11] Rui Zhu et al.
*Adv. Mater.* **23**, 4193 (2011)

[RAS+16] S. Gupta Roy et al.
*Opt. Express*, **24**, 14737 (2016)
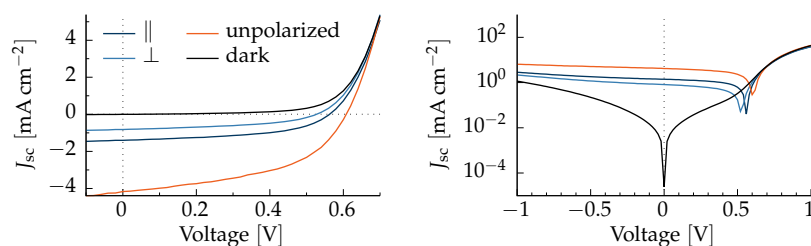


Figure 8.1: JV-characteristics of a device containing uniaxially oriented P3HT. The current densities were acquired under 0.44 Sun of polarized illumination and 0.98 Sun of unpolarized illumination.

The JV-characteristics of one of the prepared cells is plotted in Figure 8.1. The current under polarized illumination was measured by interposing a polarizer in the light path, decreasing the overall irradiance from 0.98 Sun to 0.44 Sun. By varying the angle of incident polarization, a change in current is observed, as also plotted in detail in Figure 8.2, which shows the concurrent change of the power conversion efficiency. Reassuringly, the orientation is maintained through the different processing steps and the observed photovoltaic response depends on the angle of polarization. As is expected for light passing through two consecutive polarizers, the observed behavior can be parametrized using a $\cos^2(\varphi)$ dependence—the Malus' law.

The external quantum efficiency is plotted in Figure 8.3 for light polarized parallel and perpendicular to the orientation direction. For
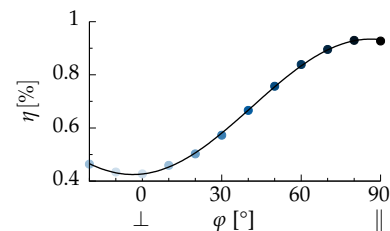


Figure 8.2: Polarization dependence of $\eta$, measured under an illumination of 0.44 Sun.
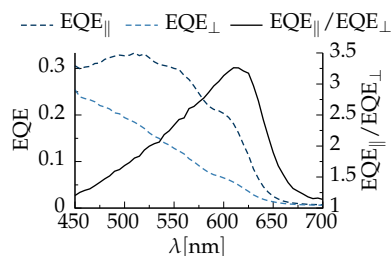
Figure 8.3: EQE of a uniaxially oriented device measured under parallel and perpendicularly polarized illumination

Table 8.1: Average performance of four uniaxially oriented bilayer devices.

incident wavelengths around the absorption maximum of 550 nm, the ratio $\frac{\text{EQE}_\parallel}{\text{EQE}_\perp} = 2.3$ agrees well with the value of the dichroic ratio DR = 2.6, which was presented in Figure 7.6. However, they do not reach the values reported for oriented devices fabricated by rubbing [ZKY11].

Table 8.1 summarizes the average performance of the four fabricated devices. The devices have a relatively low power conversion efficiency compared to values of 3 %, obtained for spin coated reference bilayer devices prepared according to an otherwise identical procedure.

| Polarization | Irradiance [mW cm$^{-2}$] | $J_{sc}$ [mA cm$^{-2}$] | $V_{oc}$ [V] | FF [%] | $\eta$ [%] |
|---|---|---|---|---|---|
| $\parallel$ | 44 | 1.1 | 0.56 | 47.2 | 0.67 |
| $\perp$ | 44 | 0.72 | 0.52 | 43.2 | 0.38 |
| Unpolarized | 98 | 3.47 | 0.61 | 45.6 | 0.97 |

In order to understand this low efficiency, we analyzed the properties of the layers at the different stages of processing. In Figure 7.15, we already showed AFM images of P3HT fibers before and after deposition of the PCBM layer. Although P3HT was not dissolved during the PCBM deposition, the fibrillar structures, which contained large voids, were compacted, leading to a total active layer thickness of 70 nm. For comparison, spin coated anisotropic reference bilayers, were composed of a 90 nm thick P3HT layer and a 30 nm thick PCBM layer, for a total active layer thickness of 120 nm.
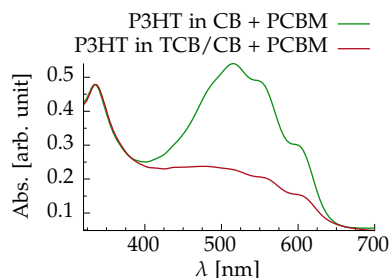


Figure 8.4: Absorption spectra of a spin coated reference bilayer and a uniaxially oriented bilayer, where the P3HT was blade coated from a solution containing TCB.

In order to better estimate the ratio between P3HT and PCBM in the uniaxially oriented bilayers, we compared their absorption to that of reference bilayers, both of which are plotted in Figure 8.4. The spectra reveal that the oriented devices contain significantly less P3HT than the reference, explaining the reduced efficiency. While the small ratio of P3HT can be explained by the low coating speeds, which result in thin layers, it was still was somewhat unexpected. Due to the large amounts of voids before PCBM deposition, equivalent thickness of the oriented P3HT layer was greatly overestimated.

The comparably large quantity of unoriented PCBM could explain the unexpectedly large efficiency under unpolarized illumination. Moreover, photoluminescence measurements already presented in Figure 7.3, determined that the PL is not effectively quenched in fibrous P3HT layers after PCBM deposition. This suggests that the interdiffusion of PCBM into the oriented P3HT is inhibited due to the increased degree of crystallinity. This is likely limiting the charge transfer efficiency, and thus together with the mismatched ratio of P3HT:PCBM, explains the relatively low overall power conversion efficiencies.

The large voids inherent to the uniaxially oriented P3HT films present a fundamental limitation of the investigated system, and a full device optimization was not performed. For a successful scale-up towards large-area polarizing solar cells, a suitable deposition method for the PCBM layer has to be found first. Dichloromethane, the solvent that we used, cannot be used during blade coating, due to its very low boiling point.

Still, the results promise to be useful for the fabrication of small area polarization dependent photodetectors. Indeed, Figure 8.5 shows the dependence of the EQE on the polarization of the incoming light and demonstrates that this type of device could be employed as a simple polarization detector. Because the photocurrent is proportional to the absorbed light, the photoresponse is proportional to $\cos^2$ of the relative orientation of polarization. The maximum and mimimum change of the EQE per degree, are $0.1880$ and $0.0017\,^{\circ-1}$ respectively. A conservative estimate of $1\,\%$ for the measurement error in the absolute EQE value, then translates to an angular resolution between $0.05$ and $5.8°$.

## 8.2. Spherulitic Devices

To increase sensitivity, polarization sensitive photodetectors are typically composed of several detectors with a relative angular offset between each other. This is because the accuracy in determining the polarization angle of incident light depends on the relative angle $\theta$ between polarizer and detector. Accuracy is poorest for angles where $\cos^2(\theta)$ has extreme values, i.e. when polarizer and detector are exactly parallel or perpendicular, since then the derivative of $\cos^2(\theta)$ is zero. This is normally circumvented by simultaneously measuring the response of several cells, for example, four detectors based on wire-grid polarizers with relative orientation of $0°$, $45°$, $-45°$ and $90°$.

This traditional setup has a remarkable similarity to a spherulite, which by definition contains all relative orientations due to the radial structure. By simply placing individual cells along the circumference of a spherulite, a favorable relative orientation between cells can be achieved in a simple manner by design, allowing for facile fabrication. Furthermore, the number of cells can be easily changed as needed, allowing for higher accuracy in an overdetermined system, if so desired.

The design has the added advantage of not requiring any moving parts, unlike conventional polarimeters composed of a rotating linear polarizer placed in front of a polarization insensitive detector. This allows for faster measurements, which are not limited by the rotation frequency of the polarizer.

Because of the ability to position a single spherulite at the center of commercial ITO covered glass substrates, we could use our regular shadow mask for the evaporation of the aluminium contacts, without any necessary further customization. Each cell will automatically have a different orientation, with an electrical response that depends on the polarization of the incident irradiation as well as the light intensity as a matter of course.

Unpolarized Characterization  The detailed results of a device containing eight cells under unpolarized illumination of 1 Sun are given in Table 8.2. Of note is the increased power conversion efficiency compared to the uniaxial devices, which is mainly due to an increased current. This is a direct result of a more optimal P3HT:PCBM ratio, as well as an unbroken P3HT layer without voids. The JV-curves under unpolarized illumination of 1 Sun are plotted
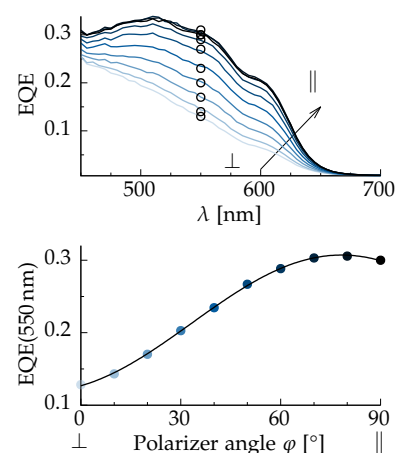


Figure 8.5: Dependence of the EQE on the polarization.

Table 8.2: Spherulite cell efficiency under unpolarized 1 Sun irradiation.

| Cell | $J_{sc}$ [mA cm$^{-2}$] | $V_{oc}$ [V] | FF [%] | $\eta$ [%] |
|---|---|---|---|---|
| 1 | 6.79 | 0.6 | 46 | 1.87 |
| 2 | 6.99 | 0.58 | 48 | 1.96 |
| 3 | 6.75 | 0.6 | 42 | 1.71 |
| 4 | 6.43 | 0.6 | 46 | 1.79 |
| 5 | 5.60 | 0.6 | 34 | 1.14 |
| 6 | 6.83 | 0.59 | 40 | 1.62 |
| 7 | 6.54 | 0.59 | 36 | 1.41 |
| 8 | 5.24 | 0.59 | 28 | 0.88 |
| Avg. | 6.40 | 0.59 | 40 | 1.55 |
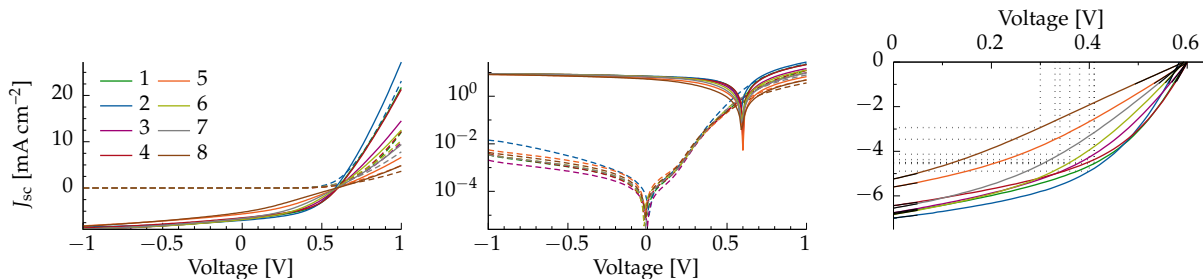
Figure 8.6: JV-characteristics of spherulite devices under 1 Sun of unpolarized light.
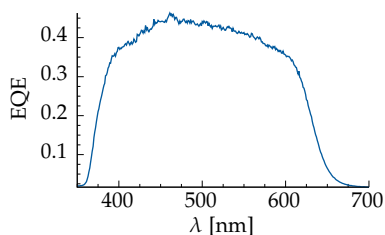


Figure 8.7: External quantum efficiency for the highest performing cell.
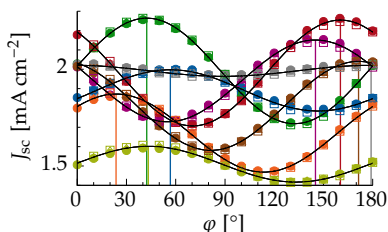


Figure 8.8: Dependence of the short circuit current $J_{sc}$ on the polarization angle $\varphi$ of the incident light. Open symbols represent measurements for angles $180° < \varphi < 540°$ to demonstrate reproducibility.

in Figure 8.6, while the external quantum efficiency of the highest performing cell is plotted in Figure 8.7.

POLARIZED CHARACTERIZATION   Next, we evaluate the performance of these devices as a polarimeter. Figure 8.8 shows $J_{sc}$ of the eight cells of one of the devices versus the angle of polarization of the incident light $\varphi$. The corresponding device is pictured in Figure 8.9. Several facts are immediately apparent and serve to demonstrate the utility of the envisaged polarization sensor. Most importantly, the electrical response of each cell does indeed depend on the polarization, following the expected behavior given by Malus' law, proportional to $\cos^2(\varphi)$. Solid lines in Figure 8.8 are fits to

$$J_{sc,n} = a_n \cos\left(\varphi - b_n\right)^2 + c_n \tag{8.1}$$

where $c_n$ is a polarization insensitive offset due to the non-oriented part of absorption of cell $n$. $b_n$ reflects the angle of preferential orientation for each cell, and $a_n$ accounts for the photoresponse of the oriented part of the absorption. The angle of maximum response $b_n$ is different for each cell, since cells are distributed around the center of the spherulite, as pictured in Figure 8.9. In particular, the grey cell exhibits a response that is essentially flat, independent of the polarization. The reason for this is that the cell's active area is entirely composed of isotropic polymer, not containing any spherulite.

Figure 8.9: Photograph of the glass-substrate side of the spherulite device corresponding to Figure 8.8. The device is illuminated by vertically polarized light from the back as well as unpolarized light from the front, to better reveal the part of spherulite shaded by the aluminium cathode. All but the outlined white 1.6 by 1.6 mm$^2$ squares were masked during measurement. The arrows represent data extracted from the fits for the corresponding colors. The length of the arrow is proportional to $\frac{a_n}{c_n}$, whereas the orientation of the arrow corresponds to $b_n$ for cells on the left side, or $b_n + 180°$ for cells on the right side, measured counterclockwise. The black line in the bottom left indicates $\varphi = 0° = 180°$
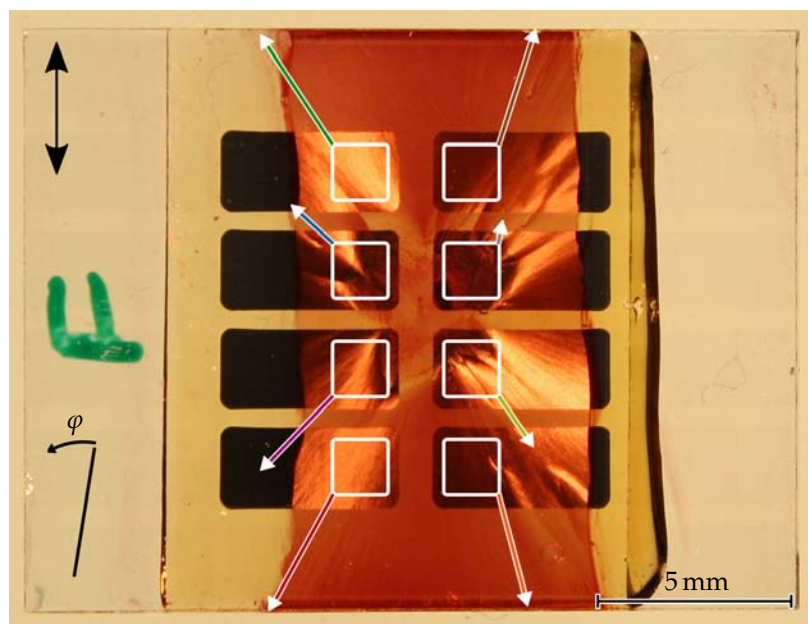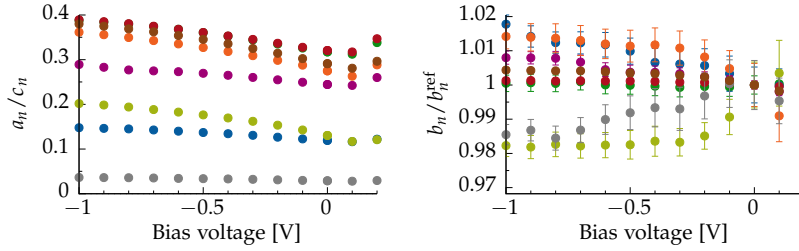
Figure 8.10 shows the parameters obtained from the fits of Figure 8.8 and their dependence on the bias voltage in more detail. The signal of interest is the ratio of the amplitude $a_n$ divided by the offset $c_n$, which is used as a proxy for the detectivity of the polarization. This ratio does only slightly increase with increasing reverse bias voltage, whereas the angle $b_n$ is not significantly influenced by the bias voltage. Because of this, the proposed polarimeter can be used under zero bias.
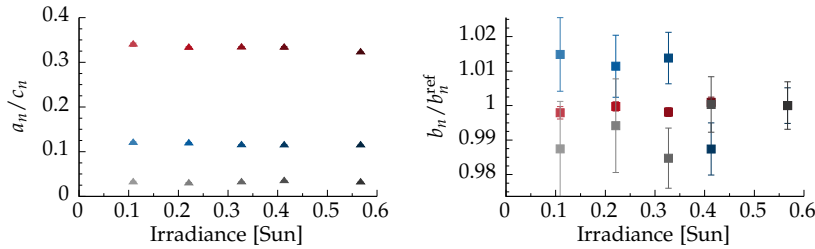
Figure 8.11 shows similar plots, this time versus the incident irradiance for three cells. Satisfyingly, $b_n$ does not depend on the incident intensity in the measured range, which allows for a simple calibration procedure of the proposed polarimeter. For reference, the complete measurements, are shown in Figure 8.12.
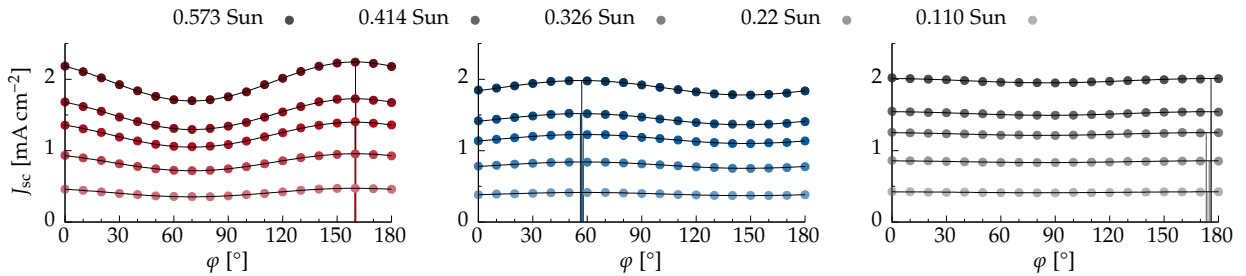
POLARIMETER OPERATION   The calibration procedure consists in determining the coefficients $a_n$, $b_n$ and $c_n$ for each of the 8 cells in one device. After calibration, the accuracy was estimated by predicting the polarization angle and irradiance of a test data set of 10 measurements, from the measured short circuit current using least squares fitting. On this data set, when using all 8 cells, the angles could be determined with a standard deviation of 2.7°, with a largest observed error of 6.4°. Similar results are obtained when using less cells, as long as cells are chosen that complement each other. Best results are obtained when selecting only a bare minimum of the best performing cells, in this particular case red, green and grey, with a standard deviation of 0.5° and a largest observed error of 1° for the test data set.

This error is of the same order than the estimated error due to the manual adjustment of the linear polarization during calibration.

Figure 8.13: Still images of a video demonstrating the real-time determination of irradiance and the angle of polarization of incident light. The three colored points represent the measured $J_{sc}$. Only a single angle exists where all three points coincide with the calibration curves. The black clock hand represents the light intensity and angle of polarization as determined by least squares fitting. Between the first and second frame, the angle of polarization was changed. Between the second and the third, the incident irradiation was decreased.

Using this device, the polarization and irradiance of incident light were determined in real-time. Figure 8.13 shows still images of a video documenting the process. A similar procedure than the one shown in the video has been used to determine the linear polarization of sunlight scattered by the sky. In this case, it is also necessary to determine the degree of depolarization, which in the experiments shown so far was constant, since the same polarizer was used for all measurements.

Since the polarization of scattered light depends on the position of the sun, this simple polarimeter can be used to determine the direction of the sun without directly observing the sun—in effect demonstrating a sundial that works in the shadow.

## 8.3. Position Sensor

Another possible application, that makes use of the polarization dependent response of the presented devices, is the determination of position along a single axis within a given spherulitic cell.

[RXL+03] Barry P. Rand et al.
*IEEE Photonics Technol. Lett.* **15**, 1279 (2003)

[CPS+11] Juan Cabanillas-Gonzalez et al.
*Appl. Phys. Lett.* **99**, 103305 (2011)

Previous organic position sensitive photodetectors are based on the resistivity of ITO [RXL+03], or on a thickness gradient of the active layer [CPS+11]. In our case, we use the continuous change of orientation of a spherulite. Specifically, we take advantage of the local change of the angle of maximum absorption within a single extended cell. A position sensitive photodetector can be achieved by locally illuminating part of a cell with a small polarized light spot, while monitoring the photocurrent. We used a 532 nm polarized laser, which was focused down to a spot size of 50 µm. As was shown in Figure 8.8, the measured local photocurrent depends on the polarization of the incoming light and is proportional to the local orientation of the spherulite. Because this local orientation changes throughout a cell, so does the photocurrent for a fixed polarization. A two-dimensional scan covering the whole purple cell from Figure 8.9, excited at four different angles of polarization, is shown in Figure 8.14. These light beam induced current maps were taken at polarization increments of 45°. Using an average profile of these photocurrent maps along the vertical direction, the location of the light spot along one dimension can be determined from the photocurrent.

Figure 8.14: Photocurrent maps excited at 532 nm overlayed on a photo of the measured cell. Incident light was polarized at 100°, 145°, 190° and 235°. Profiles were measured across the indicated vertical lines.

This simple approach can be further improved, making it independent of light intensity, by instead considering the ratio of two photocurrent measurements at orthogonal polarizations. The inverse of this ratio can be parametrized using a quadratic fit.

Because of the small size of 2 by 2 mm$^2$ of the cells used in this study, this only allows for an accurate detection of position along a relatively short distance of 0.6 mm. However, this distance can be increased by using longer electrode contacts and a suitably aligned spherulite.

# III

# Conclusions & Outlook

Scientific Progress Goes "Boink"
—Bill Watterson

This thesis detailed results of work on conjugated materials, particularly polymers and carbon nanotubes, and their applications to thermoelectricity and organic photovoltaics.

I demonstrated that ellipsometry can be used to relate film morphology to device efficiency, and that material screening can be used to gain knowledge, which in turn may lead to improved materials.

5 - Ellipsometry

Specifically, I described how ellipsometry was used to quantify the degree of vertical phase segregation in polymer:fullerene blends, observing an accumulation of acceptor at the cathode. This was found to correlate with an increased charge carrier selectivity and a higher device efficiency in organic photovoltaic cells [GDR+13].

[GDR+13] Antonio Guerrero et al. *ACS Nano*, **7**, 4637 (2013)

By determining the optical constants of new conjugated polymers, a remarkably high extinction coefficient was observed for a particular type of diketopyrrolopyrrole-thienothiophene copolymer. This could ultimately be explained by the preferred linear extension of the polymer backbone, which could lead to new design rules for high-efficiency polymers for photovoltaic applications [VFM+16].

[VFM+16] Michelle S. Vezie et al. *Nat. Mater.* **15**, 746 (2016)

This demonstrates that ellipsometry is a valuable tool for the initial characterization of new, unknown materials, as well as for the investigation of complex multi-component structures.

Going on, I presented the results on thermoelectric nanocomposites of conjugated polymers and carbon nanotubes [DRC+16]. The initial goal of finding an environmentally stable n-type thermoelectric material has not been completely reached yet. It was found that nitrogen-doped carbon nanotubes are stable in air over at least months, whereas the performance of high polymer content composites degraded faster. But these composites have other advantages, one of which is that their majority charge carrier type can be switched from p-type to n-type using UV-light. This observation could potentially pave the way for simple large-scale deposition of complementary conductors via solution coating [CGD+15].

6 - Carbon Nanotube Composites
[DRC+16] Bernhard Dörling et al. *Adv. Mater.* **28**, 2782 (2016)

[CGD+15] Mariano Campoy Quiles et al. Patent pending ES1641.1145, PCT/EP2016/078459. 2015

Speaking generally, it was found that single-walled carbon nanotubes, particularly purely semiconducting tubes are better suited for thermoelectric applications, which prompted investigations into further ways to obtain stable n-doped composites [DSK+17].

[DSK+17] Bernhard Dörling et al. *Synth. Met.* **225**, 70 (2017)

Of particular interest in the future are approaches that allow to achieve several of the following points in a simple manner at the same time.

- Disperse carbon nanotubes at high concentrations.
- Discriminate between metallic and semiconducting nanotubes, or even between distinct chiralities.
- Adjust the charge carrier concentration by doping.
- Prevent the direct contact between carbon nanotubes, limiting thermal conductivity.
- Yet at the same time not significantly increasing the electrical resistance across nanotube junctions.
- Allow working in aqueous media.

Possible candidate materials under investigation, and which could satisfy several of these prerequisites at once, are conjugated polyelectrolytes and biopolymers. All of the mentioned points are related to the surface of the carbon nanotubes, which gives a further hint. For example, it is possible to take care of some of these problems individually, by starting with pre-sorted semiconducting tubes, or by adjusting the carrier density of the nanotubes via the infiltration of dopants. In any case, the interaction between polymer and nanotubes has proven to be a crucial parameter for mechanical properties by allowing for an effective dispersion, as well as for the thermoelectric properties.

### 7 - ORIENTED POLYMER LAYERS

The last topic concerned oriented films of conjugated polymers, that can be deposited directly from solution using the crystalline solvent additive 1,3,5-trichlorobenzene. Simply by influencing solvent evaporation, the nucleation of the additive—and thereby the orientation of the epitaxially growing polymer film— can be controlled.

[DVT+14] Bernhard Dörling et al.
*J. Mater. Chem. C*, **2**, 3303 (2014)

[DSA+17] Bernhard Dörling et al.
*submitted*, (2017)

When nucleation is confined to the one-dimensional contact line during blade-coating, then uniaxially oriented layers of conjugated polymers result [DVT+14]. If it is further restricted to a single point, then circular, polycrystalline spherulites can be grown at controlled locations [DSA+17]. Using 3D-printed nozzles, a directed flow of gas allows to control the exact number and location of macroscopic spherulites. Furthermore, these spherulites can be deposited in the same step, together with isotropic regions of material, simply by heating part of the substrate.

### 8 - ORIENTED PHOTOVOLTAICS

Using these oriented films, I demonstrated organic photovoltaic bilayer devices. These devices exhibit a polarization dependent photoresponse, and could find use as polarization sensors. Samples containing both oriented and isotropic regions enabled a detector that can determine the angle and degree of polarization as well as the light intensity. This is sufficient to detect the polarization of the sky, in effect demonstrating a sundial that works in the shade.

[VDH+16] Varun Vohra et al.
*Appl. Phys. Express*, **9**, 012301 (2016)

In the context of photovoltaics, it was observed that the solvent additive allows to increase polymer crystallinity even at low concentrations, before any orientation is observed. This produced an improvement in device efficiency of organic bilayer solar cells, due to a more favorable vertical composition gradient [VDH+16].

The developed method to orient conjugated polymers works both for other polymers besides polythiophene, as well as for other crystalline solvents. It could be improved by using a less soluble additive, which would start to crystallize earlier during the drying process. This would allow to decrease the concentration of additive, and reduce the roughness of the oriented polymer layer.

Attempts to adapt the method to polymer composites are ongoing.

# IV

## APPENDIX

In theory, there is no difference between theory
and practice. But, in practice, there is.
—(mis)attributed to YOGI BERRA

# EXPERIMENTAL SETUPS

<span style="color:red">A</span>

This chapter provides a summary of the different experimental setups that were built or modified during the course of this thesis.

## A.1. Seebeck Measurement Rig

The thermoelectric samples prepared for this work were drop casts on PET substrates, which were cut into strips of 1 by $2\,cm^2$. Compared to the mm-sized samples which are typically used in commercial devices, these larger samples could be easily prepared and handled.

To accurately measure the Seebeck coefficient of a thin film sample, a suitable sample geometry has to be selected. It was shown that carelessly dimensioned contacts on an unpatterend sample can lead to large errors [RK14]. The best sample geometry is one where the contribution from active material, that is not directly between the electrodes, is minimized. For example, this is the case for thin and wide electrodes that are spaced very close to each other. In our case, these undesired contributions can easily be avoided simply by cutting the sample to shape and applying silver paste contacts across the whole width. For an overview over other sources of error during measurement of the Seebeck coefficient, see [BBL+15].

[RK14] Stephan Van Reenen et al. *Org. Electron.* **15**, 2250 (2014)

[BBL+15] Davide Beretta et al. *Rev. Sci. Instrum.* **86**, 075104 (2015)

However, using large samples only allows to determine the spatial average of the Seebeck coefficient, which may be a problem if the samples are inhomogeneous. In any case, samples should have the same dimensions as the legs of a TEG, since that way, the measured properties resemble those of the final device most closely.

MEASUREMENT METHOD When starting this work, samples were measured in a straightforward, manual manner. Using a resistive heater—in this case a Kofler bench—to heat up one end of the sample, while the other end was kept close to room temperature by connecting it to a heat sink. Temperature was measured at both contacts with a pair of fine-wire k-type thermocouples with 0.075 mm diameter, while the Seebeck voltage was acquired at the same points, using a Keithley 2400 SourceMeter, by fixing the sample with stainless steel clamps.

During measurement, the temperature of the hot side is ramped up, before the heater is turned off, and left to slowly cool back down, all the while acquiring readings for the voltage and temperatures. The average Seebeck coefficient in the applied temperature range can then be determined simply from the slope of the $V - \Delta T$ plot. While this method does not provide the full information on how the Seebeck coefficient $S(T)$ changes with temperature, it does allow to compare the average performance close to room temperature for different materials.
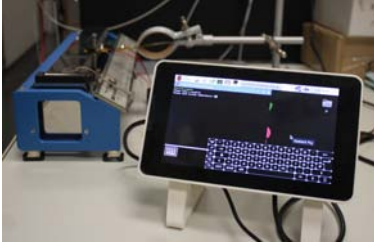
Figure A.1: Photograph of the Raspberry Pi, used to automate the measurement of the Seebeck coefficient.

SPI Serial peripheral interface Synchronous four-wire protocol that allows for two-way communication of digital components.

GPIB General purpose interface bus Legacy 8-bit parallel protocol still used to connect laboratory instruments.

VISA Virtual instrument software architecture Standardized interface used to control laboratory instruments from a PC.

AUTOMATION The same setup was continued to be used during this thesis, with only one change. It was automated using a Raspberry Pi single board computer, which controls the temperature and logs the readings acquired from the thermocouples and the multimeter.

HARDWARE The Raspberry Pi is controlled via a touchscreen and housed in a 3D-printed case, pictured in Figure A.1. The Keithley 2400 SourceMeter is connected via a National Intruments NI GPIB-USB-HS adapter to the Raspberry Pi. Each of the two k-type thermocouples is connected to a MAX31855 cold-junction compensated thermocouple-to-digital converter, with a resolution of 0.25 K. They communicate with the Raspberry Pi via the SPI bus. The Kofler bench is switched on and off automatically via a USB-controllable power socket.

SOFTWARE The Raspberry Pi runs the Raspbian operating system, which by default includes most of the necessary software packages. Additionally, to control the GPIB to USB adapter, `linux-gpib` is needed, as well as `pyvisa` and `pyvisa-py` to be able to communicate with the Keithley 2400 using only Python without the need for any other VISA installation. The power socket can be controlled from the command line using `sispmctl`.

Everything is integrated into a small Python2 script, which allows to set the desired experimental parameters, as well as perform the experiment and log the data to file.

During a typical run, the Kofler bench is turned on first. Then 100 voltage measurements and 10 temperature measurements are acquired and averaged every 10 s between 40 °C and 80 °C, while heating up the hot side. Upon reaching 80 °C, heating is turned off and measurements are paused. Due to thermal inertia, the temperature continues to rise. As soon as it falls below 80 °C, data acquisition is resumed until reaching 40 °C again. A full thermal cycle takes 40 min, corresponding to a rate of about 1 K min$^{-1}$. A single measurement is acquired over 6 s, which is the time it takes the multimeter to take 100 voltage readings. Voltage and temperature are approximated to be constant during this time and the acquired readings are averaged.

CALIBRATION The setup has been verified using a variety of reference samples, among them measurements of copper, stainless steel,
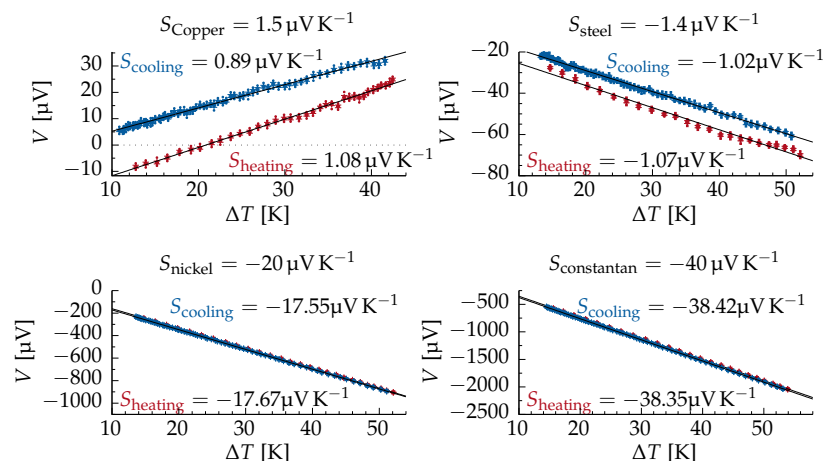


Figure A.2: Reference measurements of Seebeck coefficient of copper, steel, nickel and constantan tapes. Plotted are the mean, standard deviation, minimum and maximum value of 100 measurements per temperature.

nickel and constantan tapes with dimensions that are identical to those of CNT samples. Some example measurements are plotted in Figure A.2, showing data acquired during both heating and cooling. The observed values agree very well with the reference values for copper $S_{\text{Copper}} = 1.5\,\mu\text{V}\,\text{K}^{-1}$ and stainless steel $S_{\text{steel}} = -1.4\,\mu\text{V}\,\text{K}^{-1}$ confirming that the observable offset due to spurious voltages is only about $1\,\mu\text{V}\,\text{K}^{-1}$. The measurements for nickel and constantan show a slight deviation from their room temperature refererence values of $S_{\text{nickel}} = -20\,\mu\text{V}\,\text{K}^{-1}$ and $S_{\text{constantan}} = -40\,\mu\text{V}\,\text{K}^{-1}$, which is mostly due to the averaging nature of the experiment. Upon close inspection, it can be observed that the data does not follow an exactly linear dependence, since $S = S(T)$. The accuracy was further cross-checked by measuring CNT composites using a commercial SB1000 instrument with a K2000 temperature controller from MMR Technologies, giving good agreement. For repeated measurements of the same samples, the setup reproduces the same values to within $1\,\mu\text{V}\,\text{K}^{-1}$, giving an indication of its precision.

Code  The python script used to automate the measurement is provided in Chapter C: Scripts.

## A.2. Blade Coater Acceleration Control

During the course of this work, it became apparent to members of our group, that it would be desirable to be able to deposit films of different thicknesses in one go. A controlled linear gradient being the ideal case. That way, the effect of layer thickness on absorption and device performance could be determined quickly from a small number—or even just a single—sample. The thickness of a blade coated layer depends on the deposition velocity. However, the Zehntner ZAA 2300 blade coater used in our group, only allows for a constant velocity, so an external controller was custom-made.

In the context of this thesis, the external controller allowed to deposit at speeds below the former limit of $1\,\text{mm}\,\text{s}^{-1}$, allowing for thicker uniaxially aligned layers.

Blade Coater Modifications  The ZAA 2300 uses a Maxon Motor LSC 30/2 servo controller, which is controlled by an external voltage between $\pm 3.9\,\text{V}$, corresponding to a deposition speed of $\pm 99\,\text{mm}\,\text{s}^{-1}$. In the unmodified device, this voltage can be manually adjusted in coarse-grained steps by a mechanical potentiometer.

To allow for an arbitrary control of velocity, the potentiometer was bypassed by soldering a switch and two sockets into the circuit, such that an external voltage source could be connected between pins 6 and 8 of the connector J4. It was then possible to select between the built-in potentiometer, or an external voltage source.

Arduino-Based Voltage Source  An Arduino UNO microcontroller was chosen as the basis for the voltage source, due to its price and ease of programmability, theoretically allowing for arbitrarily shaped voltage ramps. An Analog Devices AD420 16 bit digital-to-analog converter was chosen to generate a voltage with

Figure A.3: Wiring diagram of the voltage source. LATCH, CLOCK, and DATA are connected to the Arduino digital input pins 7,8 and 9 respectively. $V_{IN}$ and GND are connected to the Arduino $V_{IN}$ and GND respectively. The voltage ramp, which is generated between $V_{OUT}$ and GND, is fed to the blade coater.
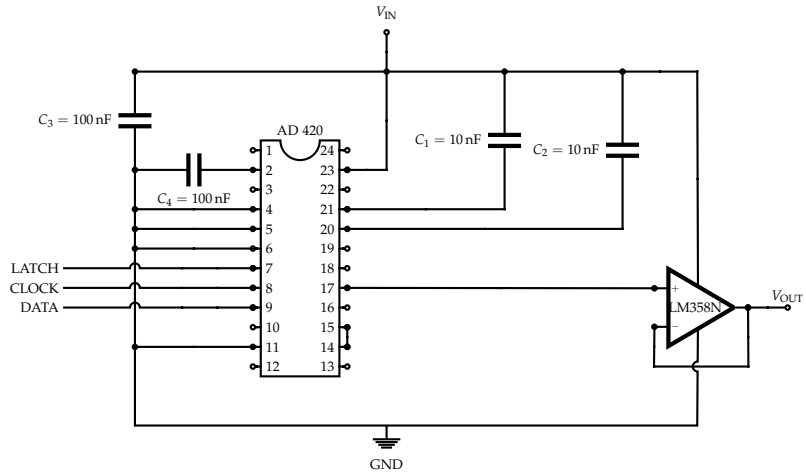


Figure A.4: Photo of the custom-made voltage source inside its case made from a repurposed box of candy.
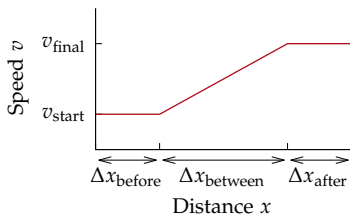


Figure A.5: Sketch of a possible velocity profile.

sufficient resolution. The circuit sketched in Figure A.3 was adapted from a similar one reported at http://www.shaduzlabs.com/blog/12/highaccuracy-16-bit-dac-for-arduino.html. The complete device also comprises an LCD screen and input buttons, such that it can be operated stand-alone. Because of the input voltage requirements of the AD420, the Arduino UNO has to be supplied with 12V DC, which is at the upper limit of its typical operating range. The finished device is shown in Figure A.4.

SOFTWARE  The Arduino runs a program loop, that allows to generate simple sequences of constant voltages, and a linear voltage ramp. Sketched in Figure A.5 are the parameters that can be directly edited. Two velocities, $v_{start}$ and $v_{final}$, as well as three distances $\Delta x_{before}$, $\Delta x_{between}$ and $\Delta x_{after}$.

CODE  The complete program is provided in Chapter C: Scripts.

# EXPERIMENTAL METHODS

This chapter summarizes all those remaining experimental details, which went unmentioned so far, and which are needed to reproduce the work described in this thesis.

## B.1. Materials

N-MWCNTs   Nitrogen-doped multi-walled carbon nanotubes were provided by Prof. Matthew C. Weisenberger and Prof. John E. Anthony at the University of Kentucky. They were synthesized from a saturated solution of acetonitrile and ferrocene feedstock by chemical vapor deposition using a continuous process [QAM+12] [QAJ+03] [KAM+09] [JA07] [JA09]. N-MWCNTs contained approximately 7 wt% nitrogen, as determined by scanning transmission electron microscopy / electron energy loss spectroscopy. The N-MWCNTs typically contained residual iron from the catalyst used in their formation. In order to minimize iron content, a sample of the nanotubes was heated at reflux first in concentrated aqueous HCl for 18 hours, followed by extensive washing with water, and then heated in refluxing acetic acid for 24 h, again followed by extensive washing with water.

[QAM+12] Dali Qian et al.
*Nanomater. Energy*, **1**, 168 (2012)

[QAJ+03] Dali Qian et al.
*J. Nanosci. Nanotechnol.* **3**, 93 (2003)

[KAM+09] Illayathambi Kunadian et al.
*Carbon*, **47**, 589 (2009)

[JA07] David N. Jacques et al. Patent US7160531. 2007

[JA09] David N. Jacques et al. Patent US7504078. 2009

N-SWCNTs   Nitrogen-doped single-walled carbon nanotubes provided by the group of Dr. Gerard Tobias at ICMAB, were synthesized by ammonolysis treatment of CVD SWCNTs (Elicarb®, supplied by Thomas Swan & Co). The as-received SWCNTs were initially purified using steam, in order to remove the amorphous carbon and graphitic nanoparticles resulting from the synthesis. A 6 M hydrochloric acid solution was then employed to remove the catalytic metal nanoparticles exposed after the steam treatment [KPS+16]. Afterwards, the purified SWCNTs were functionalized with carboxyl and hydroxyl groups by treating them in nitric acid [LCT+09]. These functionalized SWCNTs were placed into a sintered $Al_2O_3$ boat in the center of a silica furnace tube. The sample was then annealed at 500 °C and 700 °C in the presence of pure $NH_3$ gas (Carburos Metálicos 99.99 %), flowing at 300 ml min$^{-1}$ [SKO+16]. The $NH_3$ treatments lead to N-SWCNTs with N contents of 5.9 wt% (500 °C) and 3.1 wt% (700 °C), as determined by chemical analysis.

[KPS+16] Magdalena Kierkowicz et al.
*ChemNanoMat*, **2**, 108 (2016)

[LCT+09] Chin-Ching Lin et al.
*Nanotechnology*, **20**, 105703 (2009)

[SKO+16] Stefania Sandoval et al.
*Carbon*, **96**, 594 (2016)

SWCNTs   SG65i CoMoCAT® single-walled carbon nanotubes (South-West NanoTechnologies) containing ≈ 40 % (6,5) tubes were bought from Sigma-Aldrich.

P3HT   For the CNT composites and the spherulites, the used Poly(3-hexylthiophene-2,5-diyl) had $M_w ≈ 97$ kg mol$^{-1}$, Đ ≈ 2.4, RR > 90 % and was obtained from Rieke Metals. A moderate regioregularity was selected in order to not limit the solubility of the polymer. For uniaxial OPV devices, a different batch with $M_w = 40$ kg mol$^{-1}$, Đ ≈ 2.0,

RR $\geq$ 90 % was bought from Merck. Finally, for spherulitic devices, yet another batch with $M_w \approx 82\,kg\,mol^{-1}$, Đ $\approx$ 2.4, RR > 90 % was obtained from Rieke Metals.

OTHER CONJUGATED MATERIALS   PEDOT:PSS (Clevios P VP Al 4083) was bought from H.C. Starck. PCPDTBT with $M_w \approx$ $25\,kg\,mol^{-1}$, Đ $\approx$ 2.3 was purchased from 1-Material. PCBM was purchased from Luminescence Technology Corp for uniaxial OPV devices and from Solenne BV for spherulitic devices.

SOLVENTS   Orthodichlorobenzene (oDCB, 99 % ReagentPlus), chlorobenzene (CB, CHROMASOLV 99.9 %), chloroform (> 99.9 % CHROMASOLV) and dichloromethane (DCM, CHROMASOLV Plus > 99.9 %) were obtained from Sigma Aldrich.

THE REST   1,3,5-trichlorobenzene (TCB, 99 %), naphthalene ($\geq$ 99 %), branched polyethylenimine (PEI, $M_w \approx 800\,g\,mol^{-1}$, Đ $\approx$ 1.33) and sodium dodecylbenzenesulfonate (SDBS, technical grade) were obtained from Sigma Aldrich. Patterned ITO substrates, encapsulation cover slides and UV-curable epoxy were purchased from Ossila.

All materials were used as received.

## B.2. Drop Casts of CNT Composites

SOLUTION PREPARATION   For P3HT composites, CNTs were dispersed in oDCB at a concentration of $0.5–1\,g\,L^{-1}$ and sonicated in ice water for 60 min (Bransonic CPX2800H). P3HT was dissolved in chloroform at a concentration of $20\,g\,L^{-1}$ and an appropriate amount was added in three steps to the CNT dispersion, to create mixtures of a desired ratio. After each addition, the mixture was sonicated an additional 30 min in ice water. After a day, a precipitate of residual carbon and sedimented CNTs can be observed, the remaining solution was stable for months.

For PEI composites, dispersions of $1\,g\,L^{-1}$ of SWCNTs in deionized water that contained $4\,g\,L^{-1}$ of SDBS were sonicated for 60 min. An amount of PEI equal to the amount of SWCNTs by weight was added in three steps, followed each time by 30 min sonication.

SAMPLE PREPARATION   1.5 ml of the prepared solution was drop-cast onto PET substrates bent into a convex shape and left to evaporate. Some samples were irradiated with $50\,mW\,cm^{-2}$ of UV-light directly after deposition in a Jelight UVO-Cleaner 42.

ELECTRICAL CHARACTERIZATION   The drop casts were cut into $cm^2$-sized samples and contacted with silver paste.

The average Seebeck coefficient between 310 K and 350 K was measured in ambient atmosphere using a custom built setup, as described in Chapter A: Experimental Setups. Additionally, measurements were checked on a commercial SB1000 instrument equipped with a K2000 temperature controller from MMR Technologies using a thermal load of about 2 K and a constantan wire as an internal reference.

The electrical conductivity was measured on 1 by 1 cm$^2$ samples from the same drop casts with an Ecopia HMS-5000 Hall measurement system, using the van der Pauw method [Pau58]

[Pau58] Leo J. van der Pauw. *Philips Tech. Rev.* **20**, 220 (1958)

BULK THERMAL CONDUCTIVITY   Jason Ryan at Chalmers Institute of Technology measured the thermal conductivity of bulk composite samples. They were prepared by compacting drop casts at ambient temperature and a pressure of 18.5 kN cm$^{-2}$ to form two identical round pellets with a diameter of 13 mm and thickness of 1 mm. These pellets were then hot-pressed at 150 °C at a pressure of less than 7.4 kN cm$^{-2}$. The density was estimated by measuring the volume and weight of the pellets. The heat capacity and thermal diffusivity were measured at ambient temperature with a TPS 2500 S Thermal Constants Analyser from Hot Disk AB using an isotropic model.

PHYSICAL CHARACTERIZATION   Sample thickness was measured using a KLA Tencor MicroXAM-100 optical surface profilometer for samples with 50 wt% CNTs and below. Samples with higher CNT concentration were measured using a KLA Tencor P16+ profilometer. The sample thickness ranged between 15 μm and 0.8 μm, depending on the total solution concentration. For high CNT wt% composites, the samples contain a significant amount of voids, which leads to an overestimation of the total amount of material and a corresponding underestimation of $\sigma$.

Scanning electron microscopy images were acquired using a Quanta FEI 200 ESEM FEG microscope, operating between 15 and 20 kV.

AFM and current sensing AFM were measured using an Agilent 5500LS instrument with a Rocky Mountain Nanotechnology solid platinum tip. Transmission X-ray microscopy was conducted at the MISTRAL beamline at the ALBA synchrotron [PNF+09] [SNV+15]. For this, samples were drop-cast onto copper grids.

[PNF+09] Eva Pereiro et al. *J. Synchrotron Radiat.* **16**, 505 (2009)

[SNV+15] Andrea Sorrentino et al. *J. Synchrotron Radiat.* **22**, 1112 (2015)

OPTICAL CHARACTERIZATION   Transmission spectra of samples were measured using a GES5E ellipsometer from Semilab SOPRA. Raman and photoluminescence spectra were measured in backscattering configuration with a Horiba Jobin Yvon LabRAM HR800 spectrometer coupled to a confocal Olympus microscope, using 514 nm and 633 nm excitation wavelengths. FTIR spectra were measured using a Perkin-Elmer Spectrum One spectrometer coupled to a universal attenuated total reflectance accessory. Optical micrographs were taken using an Olympus BX51 optical microscope and a DP20 microscope digital camera.

## B.3. Blade Coated Uniaxial Films

PREPARATION OF SAMPLES FOR OPTICAL CHARACTERIZATION
Cleaned and cut 25 by 25 mm$^2$ glass microscope slides were used as substrates. Samples were blade coated using a Zehntner ZAA 2300 motorized stage and ZUA 2000 applicator, from solutions containing 20 and 40 mg ml$^{-1}$ P3HT in CB and $3 \leq \frac{m_{TCB}}{m_{P3HT}} \leq 7$. The blade height was set to 75 μm and the substrate temperature to 25 °C. The deposition speed varied between 1 and 6 mm s$^{-1}$. During deposition,

the evaporation of solvent was accelerated by applying a horizontal flow of nitrogen of $4 \, l \, min^{-1}$ in deposition direction across the sample. Samples were stored in a mild vacuum overnight to completely sublimate remaining TCB.

PREPARATION OF OPV DEVICES  ITO coated glass substrates were sonicated in acetone, detergent and isopropanol, before being dried in isopropanol vapor and UV-ozone treated. An approximately 40 nm thick layer of PEDOT:PSS was spin coated at 4000 rpm for 30 s and subsequently annealed at 100 °C for 10 min. The P3HT layer was blade coated at a speed of $2 \, mm \, s^{-1}$ from a CB solution containing $40 \, mg \, ml^{-1}$ P3HT and $\frac{m_{TCB}}{m_{P3HT}} = 5$. PCBM was spin coated for 10 s at 4000 rpm from a $10 \, mg \, ml^{-1}$ solution in DCM. After thermally evaporating a 100 nm aluminium cathode, samples were annealed for 10 min at 120 °C. The device active area was defined to $2 \, mm^2$.

MEASUREMENTS  Polarized photometry was carried out using a GES5E ellipsometer from Semilab SOPRA. Polarized optical micrographs were taken using an Olympus BX51 optical microscope and a DP20 microscope digital camera. AFM images were taken using a Keyence Nanoscale Hybrid Microscope VN-8000. Device characteristics were measured using a Keithley 2400 SourceMeter under simulated AMG 1.5G illumination of an 150 W Xenon Oriel Research Arc Source. In the case of polarized illumination, a polarizer was placed in the light path.

## B.4. Pinning of Spherulites

SAMPLE PREPARATION  Solutions contained $30 \, mg \, ml^{-1}$ of P3HT and $\frac{m_{TCB}}{m_{P3HT}} = 5$. PCBM was dissolved in DCM at a concentration of $10 \, mg \, ml^{-1}$. ITO-coated substrates with patterned electrodes and cut glass microscope slides were cleaned by consecutive sonications for 15 min in water with detergent, acetone, isopropanol and finally in a solution of 10 wt% of NaOH in water, rinsing them with deionized water after each step.

PEDOT:PSS was filtered using a $0.2 \, \mu m$ PVDF syringe filter, spin-coated at 3000 rpm and annealed at 120 °C for 10 min. P3HT was spin-coated at 2500 rpm in a Laurell WS-400-6NPP-LITE spin coater, or blade-coated on a Zehntner ZAA 2300 motorized stage at $20 \, mm \, s^{-1}$ with a ZUA 2000 blade, set to a height of $200 \, \mu m$. For some samples, a flow of gas of $2 \, ml \, s^{-1}$ was supplied through a flat-tipped needle with 0.8 mm diameter to induce controlled nucleation of a single spherulite.

The array of nozzles was 3D-printed with a Miicraft+ stereolithography printer with $100 \, \mu m$ feature size in z-direction and 7 s exposure per layer, using the resin BV-001 (model cream). Gas was injected and extracted using two NE 1000X syringe pumps from New Era Pump Systems.

Additionally, to inhibit the nucleation of TCB, some samples were partially placed on a hotplate at 70 °C for several seconds, directly before deposition.

PCBM solution was filtered using a 0.22 µm PTFE syringe filter and spin-coated at 4000 rpm. Samples were annealed at 120 °C for 10 min in a nitrogen filled glovebox, before thermally evaporating 100 nm of aluminium to form the cathode. Afterwards, finished samples were annealed again at 140 °C for 10 min in inert atmosphere, and subsequently encapsulated using UV curable epoxy and a glass cover slide. For optical characterization, P3HT was deposited directly onto cleaned glass substrates, and stored in a desiccator overnight to sublimate the TCB.

SAMPLE CHARACTERIZATION   Photovoltaic performance was characterized using a AAA Solar Simulator conforming to the AM1.5G spectrum (SAN-EI Electric, XES-100S1). Irradiation was calibrated to 1000 W m$^{-2}$ using an NREL certified Si reference cell (Oriel Instruments, 91150V). For polarized measurements, a linear polarizer (Thorlabs, LPVISE200-A) on a rotatable mount was interposed in the light path, lowering the irradiation to $\approx$ 575 W m$^{-2}$. Individual cells had an area of 2 by 2 mm$^2$ and were covered by a shadow mask with 1.6 by 1.6 mm$^2$ sized holes during measurement. Before the measurement, samples were exposed for 1 h to an irradiation of 1000 W m$^{-2}$, in order to burn in and stabilize subsequent performance.

EQE was measured using a custom-built setup. Light from a xenon lamp is passed through a monochromator (Horiba microHR). Using a beamsplitter (Thorlabs BPD254-G), this light then simultaneously illuminates the sample and a photodiode connected to a power meter (Thorlabs S120VC & PM100A). Current was acquired using a multimeter (Keithley 2400 SourceMeter).

Light beam induced current was measured on a custom-made system. The sample was located on a motorized x,y,z-stage, and illuminated locally by a 532 nm laser (Thorlabs, CPS532). After passing through a multi-mode optical fiber and a beamsplitter (Thorlabs, EBS1), the laser was again polarized using a linear polarizer (Thorlabs, LPVISE200-A). The incident light intensity was monitored with a photodiode power sensor (Thorlabs, S120VC) connected to a digital power meter (Thorlabs, PM100D). The short circuit current was monitored with a multimeter (Keithley 2400 SourceMeter). Data was acquired using a custom software, which allowed to keep the sample plane in focus and the diameter of the laser spot below 30 µm.

Photographs were taken, using a Canon EOS 1000D camera, by illuminating samples from the back and placing them on a single, or between two crossed polarizer sheets (Thorlabs, LPVISE2x2).

Polarized photoluminescence and Raman scattering images were acquired using a WITec alpha300 confocal Raman microscope. The samples were placed on a combined step motor/piezo stage and excited through a 10x objective using solid state lasers centered at 488 nm and 785 nm. Images were analyzed using WITec Project FOUR software.

Space-resolved Mueller-matrix measurements of spherulites were conducted by Oriol Arteaga at the University of Barcelona with a custom-made Mueller-matrix microscope that is described in detail in [ABA+14] [KAA+15]. The basic optical design of the instrument is

[ABA+14] Oriol Arteaga et al. *Appl. Opt.* **53**, 2236 (2014)

[KAA+15] E. Kuntman et al. *Opt. Pura y Apl.* **48**, 309 (2015)

based on a commercial Carl-Zeiss JENAVAL polarization microscope and it allows for measurements at different levels of magnification and wavelength. The instrument works by frequency-analyzing the intensity of light captured at every pixel of a camera detector, while two rotating film compensators, one placed before the sample and another one after it, continuously modulate the polarization of light with two distinct frequencies. The Mueller-matrix captured at each pixel of the image can then be processed to calculate, among other things, the linear birefringence and linear dichroism at that point of the sample with a simple analytic formalism [AC10a] [AC10b].

[AC10a] Oriol Arteaga et al.
*Opt. Lett.* **35**, 559 (2010)

[AC10b] Oriol Arteaga et al.
*Opt. Lett.* **35**, 3525 (2010)

The spectroscopic values of the linear birefringence and linear dichroism were measured in transmission with a Mueller-matrix polarimeter [AFW+12]. The spot size had a diameter of $\approx 0.8$ mm so that different parts of the spherulite could be selected for measurement.

[AFW+12] Oriol Arteaga et al.
*Appl. Opt.* **51**, 6805 (2012)

Spectroscopic ellipsometry was measured by Mª Isabel Alonso with a Semilab SOPRA GES5E ellipsometer. Based on the images of linear dichroism and linear birefringence, we measured at several points, with the plane of incidence of light oriented parallel or perpendicular to the directions of largest absorption or refraction, which coincide with the directions along or perpendicular to the fibers. The anisotropic optical response is uniaxial with the optic axis along the fibers [CAB+14]. Thus, the extraordinary components $n_e$ and $k_e$ are high and the ordinary ones $n_o$ and $k_o$ are low. Accordingly, we have analyzed the ellipsometric spectra by combining pairs of spectra measured in the two described configurations to evaluate the film thickness and the $n$ and $k$ parameters of the uniaxial films. The spectra vary from point to point due to changes in thickness, roughness, and crystallinity. From these, the thickness seems to be rather constant. In order to obtain a reliable description of the spectral optical anisotropy, the ellipsometric and polarimetric results have been combined.

[CAB+14] Mariano Campoy-Quiles et al.
*Adv. Funct. Mater.* **24**, 2116 (2014)

## B.5. Ellipsometry

Samples from collaborators as well as a few select other conjugated polymers were characterized by variable angle spectroscopic ellipsometry using a GES5E rotating polarizer ellipsometer from Semilab SOPRA. The software used to acquire data was WinSE, while WinElli II was used to fit the data. Typically $\approx 40$ nm thin films on glass substrates were characterized in the range of 1.22–5 eV, using 3 or 5 angles of incidence between 55–75°. The spot size was focused down to $\approx 200$ µm.

# Scripts

## C

This concluding chapter contains the code that was written to control the measurement of the Seebeck coefficient and the velocity of the blade coater. The scripts are reproduced here in their entirety for future reference.

## C.1. Seebeck Measurement Rig

```python
#!/usr/bin/env python2.7
# -*- coding: utf-8 -*-
#proper floating point division
from __future__ import division
#proper print function
from __future__ import print_function
import time
import Adafruit_GPIO.SPI as SPI
import Adafruit_MAX31855.MAX31855 as MAX31855
import visa
import numpy as np
#to exit properly
import sys
#to provide already filled prompt
import readline as rl
#In order to call external command
import subprocess as sp
#For a nice save as file dialog
import Tkinter, tkFileDialog
import os
#For cleanup if closing via 'x'
import signal
def handler(signum, frame):
    exit_script(failed+"Closing script"+normal)
    pass
signal.signal(signal.SIGHUP, handler)

# Use both RPi chip selects, and switch between reading one and the other thermocouple
# "ls /dev" lists devices as spidev0.0 and spidev0.1
SPI_PORT = 0
SPI_DEVICE0 = 0
SPI_DEVICE1 = 1
Thermocouple0 = MAX31855.MAX31855(spi=SPI.SpiDev(SPI_PORT, SPI_DEVICE0))
Thermocouple1 = MAX31855.MAX31855(spi=SPI.SpiDev(SPI_PORT, SPI_DEVICE1))
keithley = False
heating_status = False
#Use gpib0 "ls /dev" lists gpib0 to gpib20
card_address = 0
#The GPIB adress of the Keithley 2400 sourcemeter
gpib_address = 24
#Colored output text
failed = "\033[91m"
worked = "\033[92m"
normal = "\033[0m"

def keithley_connect(gpib_address=gpib_address, card_address=card_address):
```

```python
47      """Connect to Keithley 2400 at /dev/gpib"""
48      #Use pyvisa-py ('@py') instead of NI-visa ()
49      rm = visa.ResourceManager('@py')
50      global keithley
51      try:
52          connected_devices = rm.list_resources()
53          keithley = rm.open_resource(connected_devices[0])
54          #keithley = rm.open_resource('GPIB%d::%d::INSTR' % (card_address, gpib_address))
55          keithley.read_termination = '\n'
56          print(worked+"Connected successfully to "+normal+keithley.query('*IDN?'))#Basic identification
57          return True
58      except:
59          print(failed+"Connection failed"+normal+" Please check if the device is turned on and plugged in.")
60          if query_yes_no("Do you want to repeat the initialization?") == True:
61              return False
62          else:
63              sys.exit(0)
64
65  def keithley_setup_resistance_measurement(voltage_number):
66      """Transmit parameters for resistance measurement to Keithley"""
67      keithley.write('*RST')#Reset
68      time.sleep(0.1)
69      keithley.write('*CLS')#Clear error and command queue
70      time.sleep(0.1)
71      keithley.write('TRAC:FEED:CONT NEV')
72      time.sleep(0.1)
73      keithley.write('SOUR:CLE:AUTO ON')#Automatically turn ouput off after measurement
74      time.sleep(0.1)
75      keithley.write('SENS:FUNC:CONC OFF')
76      time.sleep(0.1)
77      keithley.write('FORM:ELEM RES')
78      time.sleep(0.1)
79      keithley.write('SENS:FUNC "RES"')
80      time.sleep(0.1)
81      keithley.write('SENS:RES:MODE AUTO')
82      time.sleep(0.1)
83      keithley.write('SYST:RSEN OFF')#off=2-wire-sensing
84      time.sleep(0.1)
85      keithley.write('TRAC:FEED SENS')
86      time.sleep(0.1)
87      keithley.write('TRAC:POIN {0}'.format(voltage_number))
88
89  def keithley_setup_voltage_measurement(voltage_number):
90      """Transmit parameters for voltage measurement to Keithley"""
91      keithley.write('*RST')#Reset
92      time.sleep(0.1)
93      keithley.write('*CLS')#Clear error and command queue
94      time.sleep(0.1)
95      keithley.write('TRAC:FEED:CONT NEV')
96      time.sleep(0.1)
97      keithley.write('SOUR:CLE:AUTO ON')#Automatically turn ouput off after measurement
98      time.sleep(0.1)
99      keithley.write('SENS:FUNC:CONC OFF')
100     time.sleep(0.1)
101     keithley.write('FORM:ELEM VOLT')
102     time.sleep(0.1)
103     keithley.write('SOUR:FUNC CURR')
104     time.sleep(0.1)
105     keithley.write('SOUR:CURR:MODE FIX')
106     time.sleep(0.1)
107     keithley.write('SOUR:CURR:RANG MIN')
108     time.sleep(0.1)
109     keithley.write('SOUR:CURR 0')
110     time.sleep(0.1)
111     keithley.write('SENS:FUNC "VOLT"')
112     time.sleep(0.1)
113     keithley.write('SENS:VOLT:PROT 2.1')
114     time.sleep(0.1)
115     keithley.write('SENS:VOLT:RANG MIN')
116     time.sleep(0.1)
```

```python
117     keithley.write('SENS:VOLT:NPLC 1')
118     time.sleep(0.1)
119     keithley.write('TRAC:FEED SENS')
120     time.sleep(0.1)
121     keithley.write('TRAC:POIN {0}'.format(voltage_number))
122
123 def keithley_initiate(voltage_number):
124     """Start acquisition of data at a single temperature"""
125     global keithley
126     try:
127         keithley.write('TRAC:CLE')
128         time.sleep(0.1)
129         keithley.write('TRAC:FEED:CONT NEXT')
130         time.sleep(0.1)
131         keithley.write('TRIG:COUN {0}'.format(voltage_number))
132         time.sleep(0.1)
133         keithley.write('INIT')
134     except:
135         print(failed+'Triggering Keithley measurement failed'+normal)
136         pass
137     return
138
139 def keithley_get_data(column):
140     """Get mean, sdev, min and max of measured data
141
142 columns 0 to 4 are voltage, current, resistance, timestamp, and status bytes"""
143     global keithley
144     try:
145         keithley.write('CALC3:FORM MEAN')
146         time.sleep(0.1)
147         data_mean = keithley.query_ascii_values('CALC3:DATA?')
148         time.sleep(0.1)
149         keithley.write('CALC3:FORM SDEV')
150         time.sleep(0.1)
151         data_sdev = keithley.query_ascii_values('CALC3:DATA?')
152         time.sleep(0.1)
153         keithley.write('CALC3:FORM MIN')
154         time.sleep(0.1)
155         data_min = keithley.query_ascii_values('CALC3:DATA?')
156         time.sleep(0.1)
157         keithley.write('CALC3:FORM MAX')
158         time.sleep(0.1)
159         data_max = keithley.query_ascii_values('CALC3:DATA?')
160         return (data_mean[column], data_sdev[column], data_min[column], data_max[column])
161     except:
162         print(failed+'Getting data from Keithley failed'+normal)
163         pass
164     return(float('NaN'),float('NaN'),float('NaN'),float('NaN'))
165
166 def query_yes_no(question, default_answer="yes"):
167     """Ask a yes/no question via raw_input() and return the answer."""
168     valid_answers = {"yes": True, "y": True, "no": False, "n": False}
169     if default_answer is None:
170         prompt = " [y/n] "
171     elif default_answer == "yes":
172         prompt = " [Y/n] "
173     elif default_answer == "no":
174         prompt = " [y/N] "
175     else:
176         raise ValueError("Invalid default answer: '%s'" % default_answer)
177
178     while True:
179         print(question + prompt)
180         choice = raw_input().lower()
181         if default_answer is not None and choice == '':
182             return valid_answers[default_answer]
183         elif choice in valid_answers:
184             return valid_answers[choice]
185         else:
186             print("Please answer 'yes' or 'no'")
```

```python
187
188
189   def query_click_filename(default_filename):
190       """Open a save as dialog"""
191       root = Tkinter.Tk()
192       root.withdraw()
193       print("Please input a savefile")
194       filename = tkFileDialog.asksaveasfilename(defaultextension=".txt", initialdir='/home/pi/ICMAB/Data',
                  initialfile=default_filename)
195       return filename
196
197
198   def query_text(question, default_answer):
199       """Ask a question, while also providing a default answer"""
200       rl.set_startup_hook(lambda: rl.insert_text(default_answer))
201       try:
202           return raw_input(question)
203       finally:
204           rl.set_startup_hook()
205
206
207   def toggle_heating(heating_status, sockets="all"):
208       """Turn the hotplate on or off via the USB controlled power socket
209
210   sockets can be a single number from 1 to 4, or all"""
211       if heating_status:
212           try:
213               sp.check_call(["sispmctl", "-q", "-o", sockets])
214           except sp.CalledProcessError:
215               sys.exit(failed+"USB controllable power socket not connected"+normal)
216       else:
217           try:
218               sp.check_call(["sispmctl", "-q", "-f", sockets])
219           except sp.CalledProcessError:
220               sys.exit(failed+"USB controllable power socket not connected"+normal)
221
222
223   def get_integer(question, str_default_answer, allowed_minimum, allowed_maximum):
224       still_asking = True
225       while still_asking == True:
226           try:
227               answer = int(query_text(question, str_default_answer))
228               if answer >= allowed_minimum and answer <= allowed_maximum:
229                   still_asking = False
230                   return answer
231               else:
232                   raise ValueError("Integer out of bounds")
233           except:
234               print("Please enter an integer between {0!s} and {1!s}".format(allowed_minimum, allowed_maximum))
235               pass
236
237
238   def get_temperatures(temperature_number, duration):
239       """Get the average temperatures of both thermocouples, from n measurements each, done over m seconds"""
240       temp_sensor0 = []
241       temp_internal0 = []
242       temp_sensor1 = []
243       temp_internal1 = []
244       try:
245           for x in range(temperature_number):
246               temp_sensor0.append(Thermocouple0.readTempC())
247               temp_sensor1.append(Thermocouple1.readTempC())
248               time.sleep(duration / temperature_number)
249           temp_sensor0_mean = np.mean(temp_sensor0)
250           temp_sensor1_mean = np.mean(temp_sensor1)
251           return (temp_sensor0_mean, temp_sensor1_mean)
252       except:
253           return(float('NaN'),float('NaN'))
254
255
```

```python
256  def measurement_step(voltage_number, temperature_number, duration, savefile):
257      keithley_initiate(voltage_number)
258      datapoint_temperatures = get_temperatures(temperature_number, duration)
259      try:
260          keithley.query('*OPC?')#Wait for Keithley to finish
261      except:
262          print(failed+'Waiting on Keithley failed'+normal)
263      datapoint_voltages = keithley_get_data(0)
264      datapoint_complete = datapoint_temperatures + datapoint_voltages
265      str_datapoint = ' '.join(['%g' % data for data in datapoint_complete])
266      savefile.write(str_datapoint + '\n')
267
268
269  def main():
270      print(worked+"Starting script"+normal)
271      global keithley
272      global heating_status
273      ramping_up = False
274      ramping_down = False
275      entering_filename = True
276      while keithley_connect() is False:
277          continue
278      print("Hot side temperature is {0!s}".format(Thermocouple0.readTempC()))
279      print("Cold side temperature is {0!s}".format(Thermocouple1.readTempC()))
280      while (entering_filename == True):
281          try:
282              filename = query_click_filename(time.strftime('%y%m%d-%H%M.txt'))
283              savefile = open(filename, 'w')
284              entering_filename = False
285          except TypeError:
286              exit_script(failed+"Please enter a proper filename next time"+normal)
287      savefile.write('#Input parameters:\n')
288      temperature_low = get_integer("Please input minimal temperature: ", "40", 30, 110)
289      savefile.write('#Minimum temperature: {0}C\n'.format(temperature_low))
290      temperature_high = get_integer("Please input maximal temperature: ", "80", 40, 120)
291      savefile.write('#Maximum temperature: {0}C\n'.format(temperature_high))
292      temperature_number = get_integer("Please input the number of temperature measurements to average over: ", "10", 1, 200)
293      savefile.write('#Number of temperature measurements per point: {0}\n'.format(temperature_number))
294      voltage_number = get_integer("Please input the number of voltage measurements to average over: ", "100", 2, 2500)
295      savefile.write('#Number of voltage measurements per point: {0}\n'.format(voltage_number))
296      measurement_delay = get_integer("Please input the delay between subsequent measurements: ", "10", 0, 60)
297      savefile.write('#Delay between measurements: {0}s\n'.format(measurement_delay))
298      time_for_100 = 6#seconds it takes keithley to measure 100 samples
299      duration = voltage_number / 100 * time_for_100#approximate time it takes the Keithley to measure
300      keithley_setup_resistance_measurement(voltage_number)
301      keithley_initiate(voltage_number)
302      sample_temperature = get_temperatures(temperature_number, duration)
303      keithley.query('*OPC?')
304      sample_resistance = keithley_get_data(2)
305      if (sample_resistance[0] >= 100000000):
306          exit_script("Open circuit detected")
307      print("Sample resistance is {0}Ohm".format(sample_resistance[0]))
308      savefile.write('#Sample Resistance: {0}Ohm at temperatures of {1}C and {2}C\n'.format(sample_resistance[0], sample_temperature[0], sample_temperature[1]))
309      savefile.write('#All units are C and V\n#Temp-0 Temp-1 Vmean Vsdev Vmin Vmax\n#Heating up\n')
310      keithley_setup_voltage_measurement(voltage_number)
311      savefile.flush()
312      os.fsync(savefile.fileno())
313      if query_yes_no("Do you want to start the measurement?") == True:
314          print(worked+"Start heating up at "+normal+time.strftime('%X'))
315          ramping_up = True
316          heating_status = True
317          toggle_heating(heating_status, "1")
318          current_hotside_temperature = Thermocouple0.readTempC()
319          while (ramping_up == True):
320              if (current_hotside_temperature < temperature_low):
321                  time.sleep(measurement_delay)
```

```python
322             current_hotside_temperature = Thermocouple0.readTempC()
323         elif (current_hotside_temperature >= temperature_low and current_hotside_temperature <=
                temperature_high):
324             measurement_step(voltage_number, temperature_number, duration, savefile)
325             time.sleep(measurement_delay)
326             current_hotside_temperature = Thermocouple0.readTempC()
327         elif (current_hotside_temperature > temperature_high):
328             ramping_up = False
329             ramping_down = True
330             savefile.write('\n#Cooling Down\n')
331             heating_status = False
332             toggle_heating(heating_status, "1")
333             print(worked+"Start cooling down at "+normal+time.strftime('%X'))
334             savefile.flush()
335             os.fsync(savefile.fileno())
336             time.sleep(measurement_delay)
337             current_hotside_temperature = Thermocouple0.readTempC()
338     while (ramping_down == True):
339         if (current_hotside_temperature > temperature_high):
340             time.sleep(measurement_delay)
341             current_hotside_temperature = Thermocouple0.readTempC()
342         elif (current_hotside_temperature >= temperature_low and current_hotside_temperature <=
                temperature_high):
343             measurement_step(voltage_number, temperature_number, duration, savefile)
344             time.sleep(measurement_delay)
345             current_hotside_temperature = Thermocouple0.readTempC()
346         elif (current_hotside_temperature < temperature_low):
347             ramping_down = False
348             print(worked+"Measurement finished at "+normal+time.strftime('%X'))

350     print("Exiting script")
351     savefile.close()
352     try:
353         toggle_heating(False, "all")
354     except:
355         print(failed+"Failed to turn off heating"+normal)
356     try:
357         #print("During this run, Keithley reported the following errors:\n"+keithley.query('SYST:ERR:ALL?'))
358         keithley.close()
359     except:
360         print(failed+"Failed to close connection to Keithley"+normal)
361     sys.exit(0)

363 def exit_script(message):
364     print(message)
365     toggle_heating(False)
366         sys.exit(0)

368 # Start the script if called from the command line with "python thisfilename.py" or "./thisfilename.py"
        (after having made it executable with "chmod +x thisfilename.py")
369 if __name__ == '__main__':
370     main()
```

## C.2.  Blade Coater Acceleration Control

```
1   /*
2   Zehntner Blade Coater Acceleration Control
3
4   analogWrite(pin,{0,255}) PWM possible with:
5     - 980Hz: 5,6
6     - 490Hz: 3,9,10,11
7   Used Pins:
8     - I2C: SCL,SDA
9     - Analog: 4,5
10    - Digital: 7,8,9
11  Noteworthy Commands
12  delayMicroseconds(t) (3 < t < 16383)
13
14  LCD commands
15  begin(uint8_t cols, uint8_t lines, uint8_t dotsize)
16  clear()
17  home()
18  print
19  setCursor(uint8_t col, uint8_t row)
20  cursor()        noCursor() shows underline
21  blink()         noBlink() blinks block
22  display()       noDisplay() toggles writing, not backlight
23  autoscroll(void)   noAutoscroll(void) right/left justified
24  leftToRight(void)  rightToLeft(void) text normal, or mirrored
25  scrollDisplayLeft(void) scrollDisplayRight(void)
26  createChar(uint8_t location, uint8_t charmap[])
27  setBacklight(uint8_t status)
28  */
29
30  //included libraries
31  #include <Wire.h>
32  #include <Adafruit_MCP23017.h>
33  #include <Adafruit_RGBLCDShield.h>
34
35  //Pins
36  const byte LATCH = 7;
37  const byte CLOCK = 8;
38  const byte DATA = 9;
39
40  //definitions
41  Adafruit_RGBLCDShield lcd = Adafruit_RGBLCDShield();
42
43  //color
44  #define BLACK 0
45  #define RED 1
46  #define GREEN 2
47  #define YELLOW 3
48  #define BLUE 4
49  #define VIOLET 5
50  #define TEAL 6
51  #define WHITE 7
52  uint8_t displayColor = 7;
53
54  #define ARRAY_SIZE(x) (sizeof(x) / sizeof((x)[0]))//use this to determine length of array
55
56  const uint8_t HALF_CLOCK_PERIOD=3;//should be 3 or bigger
57
58  //Menu Items that go into first line of LCD. All of these have the have the same amount of fields
59  char* menuItems[] = {
60    "Ready        ",
61    "Start Speed ",
62    "Final Speed ",
63    "Distance between",
64    "Distance before ",
65    "Distance after ",
```

```
66  };
67
68  // menu values that go into second line
69  // 6 digits of range in um [xth row][ythcolumn] 0-indexed
70  const uint8_t digitPrecision = 5;
71  uint8_t menuValues[][digitPrecision] = {
72    {0,0,0,0,0},
73    {0,1,0,0,0},
74    {0,2,0,0,0},
75    {0,3,0,0,0},
76    {0,1,0,0,0},
77    {0,1,0,0,0},
78  };
79
80  // units of the aforemention values, also second LCD line
81  char* menuUnits[] = {
82    "      ",
83    "0 um/s",
84    "0 um/s",
85    "0 um ",
86    "0 um ",
87    "0 um ",
88  };
89
90  int8_t rampDirection = 0;
91  uint16_t j=0;//counter for the ramp
92  uint8_t toggleInput = 0;//am I changing values(=1), or menus(=0)?
93  uint8_t digitCurrent = 2;//which digit of menuValue am I changing?
94  const uint8_t digitOffset = 0;//offset the bottom line by this number of digits, to rightalign
95  const uint8_t menuSize = ARRAY_SIZE(menuItems);//size of all menuXXX has to be identical
96  int8_t menuCurrent = 0;//currently visible menu
97  uint32_t speedStart = 0;//in um/s
98  uint32_t speedFinal = 0;
99  uint32_t distanceBetween = 0;//in um
100 uint32_t distanceBefore = 0;
101 uint32_t distanceAfter = 0;
102 uint32_t timeBetween = 0;//in us
103 uint32_t timeBefore = 0;
104 uint32_t timeAfter = 0;
105 uint32_t timeBetweenSingleSteps = 0;
106 uint32_t timeFudgeFactor = 412;//writing to DAC takes about this long, 348 or 356 for 2us clock,
        404-412us for 3us clock
107 uint32_t timeStart = 0;
108 uint32_t timeEnd = 0;
109 uint32_t speedStartSteps = 0;
110 uint32_t speedFinalSteps = 0;
111 uint32_t speedBetweenSteps = 0;
112 uint32_t distanceBetweenSteps = 0;
113 uint32_t distanceBeforeSteps = 0;
114 uint32_t distanceAfterSteps = 0;
115 uint16_t stepIncrement = 1;
116 uint32_t stepIncrementRest = 0;
117 uint32_t delayLong = 0;
118 uint32_t delayShort = 0;
119 //==========================================================================================
120 void setup() {
121   lcd.begin(16, 2);//display has 2 rows and 16 columns
122   lcd.setBacklight(RED);
123   pinMode(DATA, OUTPUT);
124   pinMode(CLOCK,OUTPUT);
125   pinMode(LATCH,OUTPUT);
126   digitalWrite(DATA,LOW);
127   digitalWrite(CLOCK,LOW);
128   digitalWrite(LATCH,LOW);
129   talkToDAC(0);
130   //Serial.begin(9600);//used to debug
131   lcd.clear();
132   itemUpdate();
133   valueUpdate();
134 }
```

```
135  //=====================================================================================
136  void loop() {
137    uint8_t buttons = lcd.readButtons();
138    if (buttons) {
139      if ((buttons & BUTTON_LEFT)) {
140        if (!toggleInput) {
141          menuCurrent = (((menuCurrent - 1) % menuSize) + menuSize) % menuSize;//make sure menuCurrent does
                  not go negative, due to bad C implementation of %
142          itemUpdate();
143          valueUpdate();
144        } else {
145          digitCurrent = (((digitCurrent - 1) % digitPrecision) + digitPrecision) % digitPrecision;
146          lcd.setCursor(digitOffset+digitCurrent,1);
147        }
148      }
149
150      if ((buttons & BUTTON_RIGHT)) {
151        if (!toggleInput) {
152          menuCurrent = (menuCurrent + 1) % menuSize;
153          itemUpdate();
154          valueUpdate();
155        } else {
156          digitCurrent = (digitCurrent + 1) % digitPrecision;
157          lcd.setCursor(digitOffset+digitCurrent,1);
158        }
159      }
160
161      if ((buttons & BUTTON_UP) && toggleInput) {
162        changeDigit(1);
163        valueUpdate();
164        lcd.setCursor(digitOffset+digitCurrent,1);
165        lcd.blink();
166      }
167      if (buttons & BUTTON_DOWN && toggleInput) {
168        changeDigit(-1);
169        valueUpdate();
170        lcd.setCursor(digitOffset+digitCurrent,1);
171        lcd.blink();
172      }
173
174      if (buttons & BUTTON_SELECT) {
175        if (menuCurrent != 0) {
176          if (toggleInput == 0) {
177            toggleInput = 1;
178            lcd.setCursor(digitOffset+digitCurrent,1);
179            lcd.blink();
180          } else {
181            toggleInput = 0;
182            lcd.noBlink();
183          }
184        } else {
185          calculateValues();
186          if (!checkConstraints()){
187            lcd.setCursor(0,1);
188            lcd.print("Check input");
189          } else {
190            calculateSteps();
191            calculateDelay();
192            lcd.setBacklight(GREEN);
193            talkToDAC(speedStartSteps);
194            delay(timeBefore/1000);
195            if (rampDirection == 1) {
196              timeStart = micros();
197              for(j=speedStartSteps+1;j<speedFinalSteps;j+=stepIncrement){
198                talkToDAC(j);
199                delayMicroseconds(delayShort);
200                delay(delayLong);
201              }
202              timeEnd = micros();
203              showTimeTaken();
```

```
204          } else if (rampDirection == -1) {
205            timeStart = micros();
206            for(j=speedStartSteps-1;j>speedFinalSteps;j-=stepIncrement){
207              talkToDAC(j);
208              delayMicroseconds(delayShort);
209              delay(delayLong);
210            }
211            timeEnd = micros();
212            showTimeTaken();
213          } else if (rampDirection==0) {
214            delay(timeBetween/1000);
215            lcd.clear();
216            lcd.setCursor(0,0);
217            lcd.print("Constant Speed");
218          }
219          talkToDAC(speedFinalSteps);
220          delay(timeAfter/1000);
221          talkToDAC(0);
222          lcd.setBacklight(RED);
223        }
224      }
225    }
226  }
227  delay(120);
228 }
229 //===============================================================================================
230 // Write first line of LCD
231 void itemUpdate() {
232   lcd.setCursor(0,0);
233   lcd.print(menuItems[menuCurrent]);
234 }
235
236 // Write second line of LCD
237 void valueUpdate() {
238   if(menuCurrent != 0) {
239     lcd.setCursor(digitOffset,1);
240     for (uint8_t i=0; i<digitPrecision; i++) {
241       lcd.print(menuValues[menuCurrent][i]);
242     }
243     lcd.print(menuUnits[menuCurrent]);
244   } else {
245     lcd.setCursor(0,1);
246     lcd.print("          ");
247   }
248 }
249
250 //increment or decrement current digit
251 void changeDigit(int8_t direction) {
252   menuValues[menuCurrent][digitCurrent] = (((menuValues[menuCurrent][digitCurrent] + direction) % 10) +
         10) % 10;
253 }
254
255 uint32_t calculateIntsFromArray(uint8_t row) {
256   uint32_t result = 0;
257   uint32_t significance = 10; //1 for 6 digit precision
258   for (uint8_t i=0; i<digitPrecision; i++) {
259     result = result + menuValues[row][digitPrecision - i-1]*significance;
260     significance = significance * 10;
261   }
262   return result;
263 }
264
265
266 void calculateValues(){
267   speedStart = calculateIntsFromArray(1);
268   speedFinal = calculateIntsFromArray(2);
269   distanceBetween = calculateIntsFromArray(3);
270   distanceBefore = calculateIntsFromArray(4);
271   distanceAfter = calculateIntsFromArray(5);
272 }
```

```
273
274   void calculateSteps() {
275     const unsigned int stepResolution = 65535 / 5;//13107 steps per Volt
276     const float voltageResolution = 3.9 / 100;//maximum Voltage is 3.9V= 100mm/s
277     speedStartSteps = lround(speedStart/1000.00 * voltageResolution * stepResolution);
278     speedFinalSteps = lround(speedFinal/1000.00 * voltageResolution * stepResolution);
279     timeBetween = 1000*distanceBetween/(speedStart+speedFinal)*2*1000;//Make sure there is no buffer overflow
280     timeBefore = 1000*distanceBefore/speedStart*1000;//Make sure these stay above 1
281     timeAfter = 1000*distanceAfter/speedFinal*1000;
282     if (speedStartSteps < speedFinalSteps) {
283       speedBetweenSteps = speedFinalSteps - speedStartSteps;
284       rampDirection = 1;
285     } else if (speedStartSteps > speedFinalSteps) {
286       speedBetweenSteps = speedStartSteps - speedFinalSteps;
287       rampDirection = -1;
288     } else {
289       speedBetweenSteps = speedStartSteps;
290       rampDirection = 0;
291     }
292     timeBetweenSingleSteps = timeBetween / speedBetweenSteps;
293     stepIncrement = timeFudgeFactor / timeBetweenSingleSteps + 1;
294     stepIncrementRest = timeBetweenSingleSteps - (timeFudgeFactor % timeBetweenSingleSteps);
295   }
296
297   boolean checkConstraints() {
298     uint8_t result = 0;
299     if ((speedStart > 0) && (speedStart < 100000)) {
300       if ((speedFinal > 0) && (speedFinal < 100000)) {
301         if ((distanceBetween + distanceBefore + distanceAfter) < 500000) {
302           result= 1;
303         }
304       }
305     }
306     return result;
307   }
308
309
310   // Write value to DAC
311   void talkToDAC(uint16_t value){
312     digitalWrite(LATCH,LOW);
313     digitalWrite(CLOCK,LOW);
314     //send the 16 bit sample data
315     for(int i=15;i>=0;i--){
316       digitalWrite(DATA,((value&(1<<i)))>>i);
317       delayMicroseconds(HALF_CLOCK_PERIOD);
318       digitalWrite(CLOCK,HIGH);
319       delayMicroseconds(HALF_CLOCK_PERIOD);
320       digitalWrite(CLOCK,LOW);
321     }
322     //latch enable, DAC output is set
323     digitalWrite(DATA,LOW);
324     digitalWrite(CLOCK,LOW);
325     digitalWrite(LATCH,HIGH);
326     delayMicroseconds(HALF_CLOCK_PERIOD);
327     digitalWrite(LATCH,LOW);
328   }
329
330   //Compare estimated time taken to real time taken
331   void showTimeTaken() {
332     lcd.clear();
333     lcd.setCursor(0,0);
334     lcd.print(timeBetween);
335     lcd.print(" us");
336     lcd.setCursor(0,1);
337     lcd.print(timeEnd - timeStart);
338     lcd.print(" us");
339   }
340
341   void calculateDelay() {
342     if (stepIncrementRest > 45000) {
```

```
343      delayLong = 45;
344      delayShort = stepIncrementRest - 45000;
345    } else if (stepIncrementRest > 30000) {
346      delayLong = 30;
347      delayShort = stepIncrementRest - 30000;
348    } else if (stepIncrementRest > 15000) {
349      delayLong = 15;
350      delayShort = stepIncrementRest - 15000;
351    } else {
352      delayLong = 0;
353      delayShort = stepIncrementRest;
354    }
355  }
```

# BIBLIOGRAPHY

[AB77]        R.M.A. Azzam and N.M. Bashara.
              *Ellipsometry and Polarized Light*
              (1977).
              ISBN: 9780444870162
              (See p. 45).
[ABA+14]      Oriol Arteaga, Marta Baldrís, Joan Antó, Adolf Canillas, Esther Pascual, and Enric Bertran.
              "Mueller matrix microscope with a dual continuous rotating compensator setup and digital demodulation."
              *Appl. Opt.* **53**, 2236 (2014)
              (See p. 107).
[AC10a]       Oriol Arteaga and Adolf Canillas.
              "Analytic inversion of the Mueller-Jones polarization matrices for homogeneous media."
              *Opt. Lett.* **35**, 559 (2010)
              (See p. 108).
[AC10b]       Oriol Arteaga and Adolf Canillas.
              "Analytic inversion of the Mueller–Jones polarization matrices for homogeneous media: erratum."
              *Opt. Lett.* **35**, 3525 (2010)
              (See p. 108).
[ADH+14]      Thomas R. Andersen, Henrik F. Dam, Markus Hösel, Martin Helgesen, Jon E. Carlé, Thue T. Larsen-Olsen,
              Suren A. Gevorgyan, Jens W. Andreasen, Jens Adams, Ning Li, Florian Machui, George D. Spyropoulos,
              Tayebeh Ameri, Noëlla Lemaître, Mathilde Legros, Arnulf Scheel, Detlef Gaiser, Kilian Kreul, Stephane
              Berny, Owen R. Lozman, Sirpa Nordman, Marja Välimäki, Marja Vilkman, Roar R. Søndergaard, Mikkel
              Jørgensen, Christoph J. Brabec, and Frederik C. Krebs.
              "Scalable, ambient atmosphere roll-to-roll manufacture of encapsulated large area, flexible organic tandem
              solar cell modules."
              *Energy Environ. Sci.* **7**, 2925 (2014)
              (See p. 4).
[AFW+12]      Oriol Arteaga, John Freudenthal, Baoliang Wang, and Bart Kahr.
              "Mueller matrix polarimetry with four photoelastic modulators: theory and calibration."
              *Appl. Opt.* **51**, 6805 (2012)
              (See p. 108).
[AH93]        Mohamed S. A. Abdou and Steven Holdcroft.
              "Mechanisms of photodegradation of poly(3-alkylthiophenes) in solution."
              *Macromolecules*, **26**, 2954 (1993)
              (See p. 61).
[AJW+16]      Ujwala Ail, Mohammad Javad Jafari, Hui Wang, Thomas Ederth, Magnus Berggren, and Xavier Crispin.
              "Thermoelectric Properties of Polymeric Mixed Conductors."
              *Adv. Funct. Mater.* **26**, 6288 (2016)
              (See p. 28).
[AKL+16]      Cheng Jin An, Young Hun Kang, A-Young Lee, Kwang-Suk Jang, Youngjin Jeong, and Song Yun Cho.
              "Foldable Thermoelectric Materials: Improvement of the Thermoelectric Performance of Directly Spun CNT
              Webs by Individual Control of Electrical and Thermal Conductivity."
              *ACS Appl. Mater. Interfaces*, **8**, 22142 (2016)
              (See p. 29).
[ARM+15]      Belén Alemán, Víctor Reguero, Bartolomé Mas, and Juan José Vilatela.
              "Strong Carbon Nanotube Fibers by Drawing Inspiration from Polymer Fiber Spinning."
              *ACS Nano*, **9**, 7392 (2015)
              (See p. 19).
[AVW+14]      Ardalan Armin, Marappan Velusamy, Pascal Wolfer, Yuliang Zhang, Paul L. Burn, Paul Meredith, and
              Almantas Pivrikas.
              "Quantum Efficiency of Organic Solar Cells: Electro-Optical Cavity Considerations."
              *ACS Photonics*, **1**, 173 (2014)
              (See p. 39).
[AZL+16]      Azure D. Avery, Ben H. Zhou, Jounghee Lee, Eui-Sup Lee, Elisa M. Miller, Rachelle Ihly, Devin Wesenberg,
              Kevin S. Mistry, Sarah L. Guillot, Barry L. Zink, Yong-Hyun Kim, Jeffrey L. Blackburn, and Andrew J.
              Ferguson.
              "Tailored semiconducting carbon nanotube networks with enhanced thermoelectric properties."
              *Nat. Energy*, **1**, 16033 (2016)
              (See pp. 29, 53, 65).

[BAH+16]    Derya Baran, Raja Shahid Ashraf, David A. Hanifi, Maged Abdelsamie, Nicola Gasparini, Jason A. Röhr, Sarah Holliday, Andrew Wadsworth, Sarah Lockett, Marios Neophytou, Christopher J. M. Emmott, Jenny Nelson, Christoph J. Brabec, Aram Amassian, Alberto Salleo, Thomas Kirchartz, James R. Durrant, and Iain McCulloch.
"Reducing the efficiency-stability-cost gap of organic photovoltaics with highly efficient and stable small molecule acceptor ternary solar cells."
*Nat. Mater.* **16**, 363 (2016)
(See pp. 5, 17).

[BBC12]     Olga Bubnova, Magnus Berggren, and Xavier Crispin.
"Tuning the thermoelectric properties of conducting polymers in an electrochemical transistor."
*J. Am. Chem. Soc.* **134**, 16456 (2012)
(See p. 28).

[BBL+15]    Davide Beretta, P. Bruno, Guglielmo Lanzani, and Mario Caironi.
"Reliable measurement of the Seebeck coefficient of organic and inorganic materials between 260 K and 460 K."
*Rev. Sci. Instrum.* **86**, 075104 (2015)
(See p. 99).

[BBN+13]    Kang Jun Baeg, Maddalena Binda, Dario Natali, Mario Caironi, and Yong Young Noh.
"Organic light detectors: Photodiodes and phototransistors."
*Adv. Mater.* **25**, 4267 (2013)
(See p. 11).

[BC12]      Olga Bubnova and Xavier Crispin.
"Towards polymer-based organic thermoelectric generators."
*Energy Environ. Sci.* **5**, 9345 (2012)
(See pp. 4, 10).

[BDC+13]    Celine Bounioux, Pablo Díaz-Chao, Mariano Campoy-Quiles, Marisol S. Martín-González, Alejandro R. Goñi, Rachel Yerushalmi-Rozen, and Christian Müller.
"Thermoelectric composites of poly(3-hexylthiophene) and carbon nanotubes with a large power factor."
*Energy Environ. Sci.* **6**, 918 (2013)
(See pp. 11, 53, 54, 56, 65).

[Bel08]     Lon E. Bell.
"Cooling, heating, generating power, and recovering waste heat with thermoelectric systems."
*Science*, **321**, 1457 (2008)
(See p. 32).

[BHB+14]    Martin Brinkmann, Lucia Hartmann, Laure Biniek, Kim Tremel, and Navaphun Kayunkid.
"Orienting Semi Conducting Pi-Conjugated Polymers."
*Macromol. Rapid Commun.* **35**, 9 (2014)
(See p. 18).

[BKM+11]    Olga Bubnova, Zia Ullah Khan, Abdellah Malti, Slawomir Braun, Mats Fahlman, Magnus Berggren, and Xavier Crispin.
"Optimization of the thermoelectric figure of merit in the conducting polymer poly(3,4-ethylenedioxythiophene)."
*Nat. Mater.* **10**, 429 (2011)
(See pp. 28, 31).

[BLF+17]    Yoeri van de Burgt, Ewout Lubberman, Elliot J. Fuller, Scott T. Keene, Grégorio C. Faria, Sapan Agarwal, Matthew J. Marinella, A. Alec Talin, and Alberto Salleo.
"A non-volatile organic electrochemical device as a low-voltage artificial synapse for neuromorphic computing."
*Nat. Mater.* **16**, 414 (2017)
(See p. 4).

[BLG+15]    Sadir Gabriele Bucella, Alessandro Luzio, Eliot Gann, Lars Thomsen, Christopher R. McNeill, Giuseppina Pace, Andrea Perinot, Zhihua Chen, Antonio Facchetti, and Mario Caironi.
"Macroscopic and high-throughput printing of aligned nanostructured polymer semiconductors for MHz large-area electronics."
*Nat. Commun.* **6**, 8394 (2015)
(See p. 18).

[BML+17]    Davide Beretta, Matteo Massetti, Guglielmo Lanzani, and Mario Caironi.
"Thermoelectric characterization of flexible micro-thermoelectric generators."
*Rev. Sci. Instrum.* **88**, 015103 (2017)
(See p. 30).

[BMN15]     Matt Beekman, Donald T. Morelli, and George S. Nolas.
"Better thermoelectrics through glass-like crystals."
*Nat. Mater.* **14**, 1182 (2015)
(See p. 21).

[BPL+17]    Davide Beretta, A. Perego, Guglielmo Lanzani, and Mario Caironi.
"Organic flexible thermoelectric generators: from modeling, a roadmap towards applications."
*Sustain. Energy Fuels*, **1**, 174 (2017)
(See p. 30).

[Bri11] Martin Brinkmann.
"Structure and Morphology Control in Thin Films of Regioregular Poly(3-hexylthiophene)."
*J. Polym. Sci. Part B Polym. Phys.* **49**, 1218 (2011)
(See p. 14).

[Bru35] Dirk A. G. Bruggeman.
"Berechnung verschiedener physikalischer Konstanten von heterogenen Substanzen. I. Dielektrizitätskonstanten und Leitfähigkeiten der Mischkörper aus isotropen Substanzen."
*Ann. Phys.* **416**, 636 (1935)
(See p. 50).

[BS85] Jean Luc Bredas and G. Bryan Street.
"Polarons, bipolarons, and solitons in conducting polymers."
*Acc. Chem. Res.* **18**, 309 (1985)
(See p. 10).

[BS92] Ludwig Bergmann and Clemens Schaefer.
*Lehrbuch der Experimentalphysik - Band 6: Festkörper*.
Ed. by Wilhelm Raith (1992).
ISBN: 3-11-017485-5
(See p. 57).

[BSD+16] Sadir Gabriele Bucella, Jorge Mario Salazar-Rios, Vladimir Derenskyi, Martin Fritsch, Ullrich Scherf, Maria Antonietta Loi, and Mario Caironi.
"Inkjet Printed Single-Walled Carbon Nanotube Based Ambipolar and Unipolar Transistors for High-Performance Complementary Logic Circuits."
*Adv. Electron. Mater.* **2**, 1600094 (2016)
(See p. 4).

[BSL+14] Ignasi Burgués-Ceballos, Marco Stella, Paul Lacharmoise, and Eugenia Martínez-Ferrero.
"Towards industrialization of polymer solar cells: material processing for upscaling."
*J. Mater. Chem. A*, **2**, 17711 (2014)
(See p. 4).

[BW06] Martin Brinkmann and Jean Claude Wittmann.
"Orientation of Regioregular Poly(3-hexylthiophene) by Directional Solidification: A Simple Method to Reveal the Semicrystalline Structure of a Conjugated Polymer."
*Adv. Mater.* **18**, 860 (2006)
(See pp. 19, 69).

[BYT+13] Natnael Behabtu, Colin C. Young, Dmitri E. Tsentalovich, Olga Kleinerman, Xuan Wang, Anson W. K. Ma, E. Amram Bengio, Ron F ter Waarbeek, Jorrit J. de Jong, Ron E. Hoogerwerf, Steven B. Fairchild, John B. Ferguson, Benji Maruyama, Junichiro Kono, Yeshayahu Talmon, Yachin Cohen, Marcin J. Otto, and Matteo Pasquali.
"Strong, Light, Multifunctional Fibers of Carbon Nanotubes with Ultrahigh Conductivity."
*Science*, **339**, 182 (2013)
(See p. 19).

[BZC+01] Christoph J. Brabec, Gerald Zerza, Giulio Cerullo, Sandro De Silvestri, Silvia Luzzati, Jan C. Hummelen, and Niyazi Serdar Sariciftci.
"Tracing photoinduced electron transfer process in conjugated polymer/fullerene bulk heterojunctions in real time."
*Chem. Phys. Lett.* **340**, 232 (2001)
(See p. 36).

[CAB+14] Mariano Campoy-Quiles, M. Isabel Alonso, Donal D. C. Bradley, and Lee J. Richter.
"Advanced ellipsometric characterization of conjugated polymer films."
*Adv. Funct. Mater.* **24**, 2116 (2014)
(See pp. 45, 108).

[Cam05] Mariano Campoy-Quiles.
"Exploring the potential of ellipsometry for the characterisation of thin conjugated polymer films."
PhD thesis. Imperial College London, 2005
(See p. 48).

[Cau30] Louis Cauchy.
"Sur la dispersion de la lumiere."
*Bull. des Sci. Mathématiques*, **14**, 9 (1830)
(See p. 46).

[CCY+14] Chun-Chao Chen, Wei-Hsuan Chang, Ken Yoshimura, Kenichiro Ohya, Jingbi You, Jing Gao, Zirou Hong, and Yang Yang.
"An Efficient Triple-Junction Polymer Solar Cell Having a Power Conversion Efficiency Exceeding 11%."
*Adv. Mater.* **26**, 5670 (2014)
(See p. 41).

[CD10] Tracey M. Clarke and James R. Durrant.
"Charge photogeneration in organic solar cells."
*Chem. Rev.* **110**, 6736 (2010)
(See p. 36).

[CDL+00]   B. Crone, Ananth Dodabalapur, Y.-Y. Lin, R. W. Filas, Zhenan Bao, A. LaDuca, R. Sarpeshkar, Howard E. Katz, and W. Li.
           "Large-scale complementary integrated circuits based on organic transistors."
           *Nature*, **403**, 521 (2000)
           (See p. 29).

[CEB05]    Mariano Campoy-Quiles, Pablo G. Etchegoin, and Donal D. C. Bradley.
           "Exploring the potential of ellipsometry for the characterisation of electronic, optical, morphologic and thermodynamic properties of polyfluorene thin films."
           *Synth. Met.* **155**, 279 (2005)
           (See p. 48).

[CFK+01]   Robert J. Chen, Nathan R. Franklin, Jing Kong, Jien Cao, Thomas W. Tombler, Yuegang Zhang, and Hongjie Dai.
           "Molecular photodesorption from single-walled carbon nanotubes."
           *Appl. Phys. Lett.* **79**, 2258 (2001)
           (See p. 28).

[CFL+16]   William B. Chang, Haiyu Fang, Jun Liu, Christopher M. Evans, Boris Russ, Bhooshan C. Popere, Shrayesh N. Patel, Michael L. Chabinyc, and Rachel A. Segalman.
           "Electrochemical Effects in Thermoelectric Polymers."
           *ACS Macro Lett.* **5**, 455 (2016)
           (See p. 28).

[CHT+13]   Qing Cao, Shu-jen Han, George S. Tulevski, Yu Zhu, Darsen D. Lu, and Wilfried Haensch.
           "Arrays of single-walled carbon nanotubes with full surface coverage for high-performance electronics."
           *Nat. Nanotechnol.* **8**, 180 (2013)
           (See pp. 16, 18).

[CHX+05]   Mariano Campoy-Quiles, George Heliotis, Ruidong Xia, Marilu Ariu, Martina Pintani, Pablo G. Etchegoin, and Donal D. C. Bradley.
           "Ellipsometric Characterization of the Optical Constants of Polyfluorene Gain Media."
           *Adv. Funct. Mater.* **15**, 925 (2005)
           (See p. 48).

[CM69]     Melvin Cutler and Nevill Francis Mott.
           "Observation of Anderson Localization in an Electron Gas."
           *Phys. Rev.* **181**, 1336 (1969)
           (See p. 25).

[CNB+07]   Mariano Campoy-Quiles, Jenny Nelson, Donal D. C. Bradley, and Pablo G. Etchegoin.
           "Dimensionality of electronic excitations in organic semiconductors: A dielectric function approach."
           *Phys. Rev. B*, **76**, 235206 (2007)
           (See p. 48).

[CPS+11]   Juan Cabanillas-Gonzalez, Ovidio Peña-Rodríguez, Inma Suarez Lopez, Malte Schmidt, M. Isabel Alonso, Alejandro R. Goñi, and Mariano Campoy-Quiles.
           "Organic position sensitive photodetectors based on lateral donor-acceptor concentration gradients."
           *Appl. Phys. Lett.* **99**, 103305 (2011)
           (See p. 90).

[CRR+11]   Edward Crossland, Khosrow Rahimi, Günter Reiter, Ullrich Steiner, and Sabine Ludwigs.
           "Systematic Control of Nucleation Density in Poly(3-Hexylthiophene) Thin Films."
           *Adv. Funct. Mater.* **21**, 518 (2011)
           (See p. 15).

[CSH+15]   Chungyeon Cho, Bart Stevens, Jui-Hung Hsu, Ricky Bureau, David A. Hagen, Oren Regev, Choongho Yu, and Jaime C. Grunlan.
           "Completely Organic Multilayer Thin Film with Thermoelectric Power Factor Rivaling Inorganic Tellurides."
           *Adv. Mater.* **27**, 2996 (2015)
           (See p. 29).

[CTF+12]   Edward Crossland, Kim Tremel, Florian S. U. Fischer, Khosrow Rahimi, Günter Reiter, Ullrich Steiner, and Sabine Ludwigs.
           "Anisotropic charge transport in spherulitic poly(3-hexylthiophene) films."
           *Adv. Mater.* **24**, 839 (2012)
           (See p. 15).

[DG92]     Peter Dyreklev and G Gustafsson.
           "Aligned polymer chain field effect transistors."
           *Solid State Commun.* **82**, 317 (1992)
           (See p. 18).

[DJ16]     Stephen Dongmin Kang and G. Jeffrey Snyder.
           "Charge-transport model for conducting polymers."
           *Nat. Mater.* **16**, 252 (2016)
           (See pp. 22, 27).

[DMN+12]   Arnaud Dauendorffer, Shougo Miyajima, Shuichi Nagamatsu, Wataru Takashima, Shuzi Hayase, and Keiichi Kaneto.
           "One-Step Deposition of Self-Oriented beta-Phase Polyfluorene Thin Films for Polarized Polymer Light-Emitting Diodes."
           *Appl. Phys. Express*, **5**, 092101 (2012)
           (See p. 18).

[DPG+09] Virginia A. Davis, A. Nicholas G. Parra-Vasquez, Micah J. Green, Pradeep K. Rai, Natnael Behabtu, Valentin Prieto, Richard D. Booker, Judith Schmidt, Ellina Kesselman, Wei Zhou, Hua Fan, W. Wade Adams, Robert H. Hauge, John E. Fischer, Yachin Cohen, Yeshayahu Talmon, Richard E. Smalley, and Matteo Pasquali.
"True solutions of single-walled carbon nanotubes for assembly into macroscopic materials."
*Nat. Nanotechnol.* **4**, 830 (2009)
(See p. 17).

[DTG+13] Ying Diao, Benjamin C-K. Tee, Gaurav Giri, Jie Xu, Do Hwan Kim, Hector A. Becerril, Randall M. Stoltenberg, Tae Hoon Lee, Gi Xue, Stefan C. B. Mannsfeld, and Zhenan Bao.
"Solution coating of large-area organic semiconductor thin films with aligned single-crystalline domains."
*Nat. Mater.* **12**, 665 (2013)
(See pp. 18, 74).

[DTK+15] A. Duzynska, A. Taube, K. P. Korona, J. Judek, and M. Zdrojek.
"Temperature-dependent thermal properties of single-walled carbon nanotube thin films."
*Appl. Phys. Lett.* **106**, 183108 (2015)
(See pp. 53, 63).

[DWA+13] Duc T. Duong, Chenchen Wang, Erin Antono, Michael F. Toney, and Alberto Salleo.
"The chemical and structural origin of efficient p-type doping in P3HT."
*Org. Electron.* **14**, 1330 (2013)
(See pp. 11, 27, 51).

[DZ11] D. M. Nanditha M. Dissanayake and Zhaohui Zhong.
"Unexpected hole transfer leads to high efficiency single-walled carbon nanotube hybrid photovoltaic."
*Nano Lett.* **11**, 286 (2011)
(See p. 57).

[EFP+04] Lars M. Ericson, Hua Fan, Haiqing Peng, Virginia A. Davis, Wei Zhou, Joseph Sulpizio, Yuhuang Wang, Richard Booker, Juraj Vavro, Csaba Guthy, A. Nicholas G. Parra-Vasquez, Myung Jong Kim, Sivarajan Ramesh, Rajesh K. Saini, Carter Kittrell, Gerry Lavin, Howard Schmidt, W. Wade Adams, W. E. Billups, Matteo Pasquali, Wen-Fang Hwang, Robert H. Hauge, John E. Fischer, and Richard E. Smalley.
"Macroscopic, Neat, Single-Walled Carbon Nanotube Fibers."
*Science*, **305**, 1447 (2004)
(See p. 19).

[EHA+12] Nieves Espinosa, Markus Hösel, Dechan Angmo, and Frederik C. Krebs.
"Solar cells with one-day energy payback for the factories of the future."
*Energy Environ. Sci.* **5**, 5117 (2012)
(See p. 4).

[Fal85] Gottfried Falk.
"Entropy, a resurrection of caloric—a look at the history of thermodynamics."
*Eur. J. Phys.* **6**, 108 (1985)
(See p. 26).

[Fel15] Armin Feldhoff.
"Thermoelectric Material Tensor Derived from the Onsager–de Groot–Callen Model."
*Energy Harvest. Syst.* **2**, 5 (2015)
(See p. 26).

[FFN15a] Sheridan Few, Jarvist M. Frost, and Jenny Nelson.
"Models of charge pair generation in organic solar cells."
*Phys. Chem. Chem. Phys.* **17**, 2311 (2015)
(See p. 36).

[FFN15b] Takahiro Fukumaru, Tsuyohiko Fujigaya, and Naotoshi Nakashima.
"Development of n-type cobaltocene-encapsulated carbon nanotubes with remarkable thermoelectric property."
*Sci. Rep.* **5**, 7951 (2015)
(See p. 30).

[FPT+17] Haiyu Fang, Bhooshan C. Popere, Elayne M. Thomas, Cheng-Kang Mai, William B. Chang, Guillermo C. Bazan, Michael L. Chabinyc, and Rachel A. Segalman.
"Large-scale integration of flexible materials into rolled and corrugated thermoelectric modules."
*J. Appl. Polym. Sci.* **134**, 44208 (2017)
(See p. 31).

[Fri71] Hellmut Fritzsche.
"A general expression for the thermoelectric power."
*Solid State Commun.* **9**, 1813 (1971)
(See pp. 22, 25).

[Fuc14] Hans U. Fuchs.
"A Direct Entropic Approach to Uniform and Spatially Continuous Dynamical Models of Thermoelectric Devices."
*Energy Harvest. Syst.* **1**, 1 (2014)
(See p. 26).

[Fuj07] Hiroyuki Fujiwara.
*Spectroscopic Ellipsometry: Principles and Applications*
(2007).
ISBN: 9780470016084
(See p. 46).

[Gar90]     Miquel Garriga Bacardi.
            "Ellipsometrische Untersuchungen der optischen und elektronischen Eigenschaften von AlAs, AlAs/GaAs-
            Übergittern und Hochtemperatur-Supraleitern."
            PhD thesis. Max Planck Institut für Festkörperforschung, Stuttgart, 1990
            (See p. 48).
[GB99]      Martin Grell and Donal D. C. Bradley.
            "Polarized Luminescence from Oriented Molecular Materials."
            *Adv. Mater.* **11**, 895 (1999)
            (See p. 18).
[GBI+97]    Martin Grell, Donal D. C. Bradley, Mike Inbasekaran, and Ed P. Woo.
            "A glass-forming conjugated main-chain liquid crystal polymer for polarized electroluminescence applica-
            tions."
            *Adv. Mater.* **9**, 798 (1997)
            (See p. 4).
[GCC+13]    Widianta Gomulya, Guadalupe Diaz Costanzo, Elton J Figueiredo de Carvalho, Satria Zulkarnaen Bisri,
            Vladimir Derenskyi, Martin Fritsch, Nils Fröhlich, Sybille Allard, Pavlo Gordiichuk, Andreas Herrmann,
            Siewert Jan Marrink, Maria Cristina Dos Santos, Ullrich Scherf, and Maria Antonietta Loi.
            "Semiconducting Single-Walled Carbon Nanotubes on Demand by Polymer Wrapping."
            *Adv. Mater.* **25**, 2948 (2013)
            (See p. 17).
[GCP+15]    Anne M. Glaudell, Justin E. Cochran, Shrayesh N. Patel, and Michael L. Chabinyc.
            "Impact of the Doping Method on Conductivity and Thermopower in Semiconducting Polythiophenes."
            *Adv. Energy Mater.* **5**, 1401072 (2015)
            (See pp. 27, 53).
[GH13]      Mark Geoghegan and Georges Hadziioannou.
            *Polymer Electronics*
            (2013).
            ISBN: 978-0199533831
            (See p. 8).
[GM15]      Daniel B. Gingerich and Meagan S. Mauter.
            "Quantity, Quality, and Availability of Waste Heat from United States Thermal Power Generation."
            *Environ. Sci. Technol.* **49**, 8297 (2015)
            (See p. 3).
[GMF+74]    Amal K. Ghosh, Don L. Morel, Tom Feng, Robert F. Shaw, and Charles A. Rowe.
            "Photovoltaic and rectification properties of Al/Mg phthalocyaine/Ag Schottky-barrier cells."
            *J. Appl. Phys.* **45**, 230 (1974)
            (See p. 39).
[GPB+04]    László Gránásy, Tamás Pusztai, Tamás Börzsönyi, James A. Warren, and Jack F. Douglas.
            "A general mechanism of polycrystalline growth."
            *Nat. Mater.* **3**, 645 (2004)
            (See pp. 15, 70).
[GPT+05]    László Gránásy, Tamás Pusztai, György Tegze, James A. Warren, and Jack F. Douglas.
            "Growth and form of spherulites."
            *Phys. Rev. E,* **72**, 011605 (2005)
            (See pp. 15, 70).
[GRS+14]    László Gránásy, László Rátkai, Attila Szállás, Bálint Korbuly, Gyula I. Tóth, László Környei, and Tamás
            Pusztai.
            "Phase-Field Modeling of Polycrystalline Solidification: From Needle Crystals to Spherulites—A Review."
            *Metall. Mater. Trans. A,* **45**, 1694 (2014)
            (See pp. 15, 76).
[GSD+15]    Widianta Gomulya, Jorge Mario Salazar Rios, Vladimir Derenskyi, Satria Zulkarnaen Bisri, Stefan Jung,
            Martin Fritsch, Sybille Allard, Ullrich Scherf, Maria Cristina dos Santos, and Maria Antonietta Loi.
            "Effect of temperature on the selection of semiconducting single walled carbon nanotubes using Poly(3-
            dodecylthiophene-2,5-diyl)."
            *Carbon,* **84**, 66 (2015)
            (See p. 17).
[GSN16]     Ajay Gambhir, Philip Sandwell, and Jenny Nelson.
            "The future costs of OPV – A bottom-up model of material and manufacturing costs with uncertainty
            analysis."
            *Sol. Energy Mater. Sol. Cells,* **156**, 49 (2016)
            (See p. 5).
[GSZ+11]    Christophe Goupil, Wolfgang Seifert, Knud Zabrocki, Eckhard Müller, and G. Jeffrey Snyder.
            "Thermodynamics of Thermoelectric Phenomena and Applications."
            *Entropy,* **13**, 1481 (2011)
            (See p. 26).

[GZS+14]   Suren A. Gevorgyan, Oihana Zubillaga, José María Vega de Seoane, Maider Machado, Elif Alturk Parlak, Nesrin Tore, Eszter Voroshazi, Tom Aernouts, Harald Müllejans, Giorgio Bardizza, Nigel Taylor, Wiljan J. H. Verhees, Jan M. Kroon, Pasquale Morvillo, Carla Minarini, Francesco Roca, Fernando A. Castro, Stéphane Cros, Balthazar Lechêne, Juan F. Trigo, Cecilia Guillén, Jose Herrero, Birger Zimmermann, Subarna Babu Sapkota, Clemens Veit, Uli Würfel, Pabitra S. Tuladhar, James R. Durrant, Stefan Winter, Sanna Rousu, Marja Välimäki, Volker Hinrichs, Sarah R. Cowan, Dana C. Olson, Peter Sommer-Larsen, and Frederik C. Krebs.
"Round robin performance testing of organic photovoltaic devices."
*Renew. Energy*, **63**, 376 (2014)
(See p. 39).

[GZZ+17]   Madeleine P. Gordon, Edmond W. Zaia, Preston Zhou, Boris Russ, Nelson E. Coates, Ayaskanta Sahu, and Jeffrey J. Urban.
"Soft PEDOT:PSS aerogel architectures for thermoelectric applications."
*J. Appl. Polym. Sci.* **134**, 44070 (2017)
(See p. 31).

[HD93a]   L. D. Hicks and Mildred S. Dresselhaus.
"Effect of quantum-well structures on the thermomagnetic figure of merit."
*Phys. Rev. B*, **47**, 727 (1993)
(See p. 28).

[HD93b]   L. D. Hicks and Mildred S. Dresselhaus.
"Thermoelectric figure of merit of a one-dimensional conductor."
*Phys. Rev. B*, **47**, 16631 (1993)
(See p. 28).

[Hee01]   Alan J. Heeger.
"Nobel Lecture: Semiconducting and Metallic Polymers: The Fourth Generation of Polymeric Materials."
*Rev. Mod. Phys.* **73**, 681 (2001)
(See p. 10).

[HEL+11]   Holger Hintz, Hans-Joachim Egelhaaf, Larry Lüer, Jens Hauch, Heiko Peisert, and Thomas Chassé.
"Photodegradation of P3HT - A Systematic Study of Environmental Factors."
*Chem. Mater.* **23**, 145 (2011)
(See p. 60).

[HEP+10]   Holger Hintz, Hans-Joachim Egelhaaf, Heiko Peisert, and Thomas Chassé.
"Photo-oxidation and ozonization of poly(3-hexylthiophene) thin films as studied by UV/VIS and photo-electron spectroscopy."
*Polym. Degrad. Stab.* **95**, 818 (2010)
(See p. 61).

[HGL+12]   Ming He, Jing Ge, Zhiqun Lin, Xuhui Feng, Xinwei Wang, Hongbin Lu, Yuliang Yang, and Feng Qiu.
"Thermopower enhancement in conducting polymer nanocomposites via carrier energy scattering at the organic–inorganic semiconductor interface."
*Energy Environ. Sci.* **5**, 8351 (2012)
(See p. 26).

[HHF16]   R. Haight, W. Haensch, and D. Friedman.
"Solar-powering the Internet of Things."
*Science*, **353**, 124 (2016)
(See p. 30).

[HKL+95]   Jan C. Hummelen, Brian W. Knight, F. LePeq, Fred Wudl, Jie Yao, and Charles L. Wilkins.
"Preparation and Characterization of Fulleroid and Methanofullerene Derivatives."
*J. Org. Chem.* **60**, 532 (1995)
(See p. 17).

[HMB+14]   Corey A. Hewitt, David S. Montgomery, Ryan L. Barbalace, Rowland D. Carlson, and David L. Carroll.
"Improved thermoelectric power output from multilayered polyethylenimine doped carbon nanotube based organic composites."
*J. Appl. Phys.* **115**, 184502 (2014)
(See p. 30).

[Hol91]   Steven Holdcroft.
"A photochemical study of poly(3-hexylthiophene)."
*Macromolecules*, **24**, 4834 (1991)
(See p. 61).

[HPF+96]   Jonathan J M Halls, K. Pichler, Richard H. Friend, S. C. Moratti, and A. B. Holmes.
"Exciton diffusion and dissociation in a poly(p-phenylenevinylene)/C60 heterojunction photovoltaic cell."
*Appl. Phys. Lett.* **68**, 3120 (1996)
(See p. 39).

[HWG+95]   J. J. M. Halls, C. A. Walsh, Neil C. Greenham, E. A. Marseglia, Richard H. Friend, S. C. Moratti, and A. B. Holmes.
"Efficient photodiodes from interpenetrating polymer networks."
*Nature*, **376**, 498 (1995)
(See p. 40).

[HY95]     Maki Hamaguchi and Katsumi Yoshino.
           "Polarized electroluminescence from rubbing-aligned poly(2,5-dinonyloxy-1,4-phenylenevinylene) films."
           *Appl. Phys. Lett.* **67**, 3381 (1995)
           (See p. 18).

[HZ02]     Eugene Hecht and Alfred Zajac.
           *Optics*
           (2002).
           ISBN: 0321188780
           (See p. 45).

[Int16]    International Energy Agency.
           *Key World Energy Statistics*
           (2016).
           ISBN: 9789264266520
           (See p. 3).

[JA07]     David N. Jacques and Rodney J. Andrews.
           "Process for the continuous production of aligned carbon nanotubes."
           Patent US7160531 (US).
           2007
           (See p. 103).

[JA09]     David N. Jacques and Rodney J. Andrews.
           "Continuous Production of Aligned Carbon nanotubes."
           Patent US7504078 (US).
           2009
           (See p. 103).

[JIV00]    M. P. de Jong, L. J. van Ijzendoorn, and M. J. A. de Voigt.
           "Stability of the interface between indium-tin-oxide in polymer light-emitting diodes."
           *App. Phys. Lett.* **77**, 2255 (2000)
           (See p. 41).

[JM80]     Mats Jonson and Gerald D. Mahan.
           "Mott's formula for the thermopower and the Wiedemann-Franz law."
           *Phys. Rev. B*, **21**, 4223 (1980)
           (See p. 25).

[JM96a]    Gerald E. Jellison and F. A. Modine.
           "Erratum: "Parameterization of the optical functions of amorphous materials in the interband region"
           [Appl. Phys. Lett. 69, 371 (1996)]."
           *Appl. Phys. Lett.* **69**, 2137 (1996)
           (See p. 47).

[JM96b]    Gerald E. Jellison and F. A. Modine.
           "Parameterization of the optical functions of amorphous materials in the interband region."
           *Appl. Phys. Lett.* **69**, 371 (1996)
           (See p. 47).

[JPR+14]   Alberto de Juan, Yann Pouillon, Luisa Ruiz-González, Almudena Torres-Pardo, Santiago Casado, Nazario
           Martín, Ángel Rubio, and Emilio M. Pérez.
           "Mechanically Interlocked Single-Wall Carbon Nanotubes."
           *Angew. Chemie Int. Ed.* **53**, 5394 (2014)
           (See p. 66).

[JSM+12]   Florian Jakubka, Stefan P. Schießl, Sebastian Martin, Jan M. Englert, Frank Hauke, Andreas Hirsch, and
           Jana Zaumseil.
           "Effect of Polymer Molecular Weight and Solution Parameters on Selective Dispersion of Single-Walled
           Carbon Nanotubes."
           *ACS Macro Lett.* **1**, 815 (2012)
           (See p. 17).

[JSM+15]   Nicholas E. Jackson, Brett M. Savoie, Tobin J. Marks, Lin X. Chen, and Mark A. Ratner.
           "The Next Breakthrough for Organic Photovoltaics?"
           *J. Phys. Chem. Lett.* **6**, 77 (2015)
           (See p. 39).

[JTM+09]   Leslie H. Jimison, Michael F. Toney, Iain McCulloch, Martin Heeney, and Alberto Salleo.
           "Charge-Transport Anisotropy Due to Grain Boundaries in Directionally Crystallized Thin Films of
           Regioregular Poly(3-hexylthiophene)."
           *Adv. Mater.* **21**, 1568 (2009)
           (See p. 18).

[KAA+15]   E. Kuntman, Oriol Arteaga, Joan Antó, D. Cayuela, and Enric Bertrán.
           "Conversion of a polarization microscope into a Mueller matrix microscope. Application to the measurement
           of textile fibers."
           *Opt. Pura y Apl.* **48**, 309 (2015)
           (See p. 107).

[KAB+08]   Frederik C. Krebs, Tom Aernouts, Rémi de Bettignies, Eva Bundgaard, Stéphane Cros, Muriel Firon, Mikkel Jørgensen, Eugene A. Katz, and Kion Norrman.
*Polymer Photovoltaics: A Practical Approach.*
Ed. by Frederik C. Krebs (2008).
ISBN: 9780819467812
(See p. 3).

[Kai01]   Alan B. Kaiser.
"Electronic transport properties of conducting polymers and carbon nanotubes."
*Reports Prog. Phys.* **64**, 1 (2001)
(See p. 27).

[Kai89]   Alan B. Kaiser.
"Thermoelectric power and conductivity of heterogeneous conducting polymers."
*Phys. Rev. B*, **40**, 2806 (1989)
(See p. 27).

[KAM+09]   Illayathambi Kunadian, Rodney Andrews, M. Pinar Mengüç, and Dali Qian.
"Thermoelectric power generation using doped MWCNTs."
*Carbon*, **47**, 589 (2009)
(See p. 103).

[KB15]   Anna Köhler and Heinz Bässler.
*Electronic Processes in Organic Semiconductors*
(2015).
ISBN: 9783527332922
(See p. 34).

[KBS+09]   Avinesh Kumar, Mohammed A. Baklar, Ken Scott, Theo Kreouzis, and Natalie Stingelin-Stutzmann.
"Efficient, stable bulk charge transport in crystalline/crystalline semiconductor-insulator blends."
*Adv. Mater.* **21**, 4447 (2009)
(See p. 54).

[KCT+06]   Youngkyoo Kim, Steffan Cook, Sachetan M. Tuladhar, Stelios A. Choulis, Jenny Nelson, James R. Durrant, Donal D. C. Bradley, Mark Giles, Iain McCulloch, Chang-Sik Ha, and Moonhor Ree.
"A strong regioregularity effect in self-organizing conjugated polymer films and high-efficiency polythiophene:fullerene solar cells."
*Nat. Mater.* **5**, 197 (2006)
(See p. 14).

[KCT+14]   Suk Lae Kim, Kyungwho Choi, Abdullah Tazebay, and Choongho Yu.
"Flexible power fabrics made of carbon nanotubes for harvesting thermoelectricity."
*ACS Nano*, **8**, 2377 (2014)
(See pp. 30, 64).

[KEH+14]   Frederik C. Krebs, Nieves Espinosa, Markus Hösel, Roar R. Søndergaard, and Mikkel Jørgensen.
"25th Anniversary Article: Rise to Power - OPV-Based Solar Parks."
*Adv. Mater.* **26**, 29 (2014)
(See p. 4).

[KFZ+00]   Jing Kong, Nathan R. Franklin, Chongwu Zhou, Michael G. Chapline, Shu Peng, Kyeongjae Cho, and Hongjie Dai.
"Nanotube Molecular Wires as Chemical Sensors."
*Science*, **287**, 622 (2000)
(See pp. 16, 28).

[KJP+15]   Nam-Koo Kim, Soo-young Jang, Giuseppina Pace, Mario Caironi, Won-Tae Park, Dongyoon Khim, Juhwan Kim, Dong-yu Kim, and Yong Young Noh.
"High-Performance Organic Field-Effect Transistors with Directionally Aligned Conjugated Polymer Film Deposited from Pre-Aggregated Solution."
*Chem. Mater.* **27**, 8345 (2015)
(See pp. 4, 18).

[KKL+14]   Nara Kim, Seyoung Kee, Seoung Ho Lee, Byoung Hoon Lee, Yung Ho Kahng, Yong-Ryun Jo, Bong-Joong Kim, and Kwanghee Lee.
"Highly conductive PEDOT:PSS nanofibrils induced by solution-processed crystallization."
*Adv. Mater.* **26**, 2268 (2014)
(See p. 18).

[KKM+99]   Hiromichi Kataura, Y. Kumazawa, Y. Maniwa, I. Umezu, S. Suzuki, Y. Ohtsuka, and Y. Achiba.
"Optical properties of single-wall carbon nanotubes."
*Synth. Met.* **103**, 2555 (1999)
(See p. 16).

[KKP16]   Gun-Ho Kim, Jinsang Kim, and Kevin P. Pipe.
"Humidity-dependent thermoelectric properties of poly(3,4-ethylenedioxythiophene):poly(styrene sulfonate)."
*Appl. Phys. Lett.* **108**, 093301 (2016)
(See p. 28).

[KMK+16]   Renee Kroon, Desalegn Alemu Mengistie, David Kiefer, Jonna Hynynen, Jason D. Ryan, Liyang Yu, and Christian Müller.
"Thermoelectric plastics: from design to synthesis, processing and structure–property relationships."
*Chem. Soc. Rev.* **45**, 6147 (2016)
(See p. 21).

[KP16]   *Innovative Thermoelectric Materials.*
Ed. by Howard E. Katz and Theodore O. Poehler (2016).
ISBN: 978-1-78326-605-0
(See p. 25).

[KPK+10]   Anusit Keawprajak, Phimwipha Piyakulawat, Annop Klamchuen, Phansak Iamraksa, and Udom Asawapirom.
"Influence of crystallizable solvent on the morphology and performance of P3HT:PCBM bulk-heterojunction solar cells."
*Sol. Energy Mater. Sol. Cells*, **94**, 531 (2010)
(See pp. 71, 83).

[KPS+16]   Magdalena Kierkowicz, Elzbieta Pach, Ana Santidrián, Ester Tobías-Rossell, Martin Kalbáč, Belén Ballesteros, and Gerard Tobias.
"Effect of Steam-Treatment Time on the Length and Structure of Single-Walled and Double-Walled Carbon Nanotubes."
*ChemNanoMat*, **2**, 108 (2016)
(See p. 103).

[KPT+06]   Theo Kreouzis, Dmitry Poplavskyy, Sachetan M. Tuladhar, Mariano Campoy-Quiles, Jenny Nelson, A. Campbell, and Donal D. C. Bradley.
"Temperature and field dependence of hole mobility in poly(9,9-dioctylfluorene)."
*Phys. Rev. B*, **73**, 235201 (2006)
(See p. 18).

[Kre09]   Frederik C. Krebs.
"Polymer solar cell modules prepared using roll-to-roll methods: Knife-over-edge coating, slot-die coating and screen printing."
*Sol. Energy Mater. Sol. Cells*, **93**, 465 (2009)
(See p. 4).

[KRF+13]   Felix Peter Vinzenz Koch, Jonathan Rivnay, Sam Foster, Christian Müller, Jonathan M. Downing, Ester Buchaca-Domingo, Paul Westacott, Liyang Yu, Mingjian Yuan, Mohammed Baklar, Zhuping Fei, Christine Luscombe, Martyn A. McLachlan, Martin Heeney, Garry Rumbles, Carlos Silva, Alberto Salleo, Jenny Nelson, Paul Smith, and Natalie Stingelin.
"The impact of molecular weight on microstructure and charge transport in semicrystalline polymer semiconductors–poly(3-hexylthiophene), a model study."
*Prog. Polym. Sci.* **38**, 1978 (2013)
(See p. 13).

[KSM+01]   P Kim, L Shi, A Majumdar, and P L McEuen.
"Thermal Transport Measurements of Individual Multiwalled Nanotubes."
*Phys. Rev. Lett.* **87**, 215502 (2001)
(See p. 53).

[KSM+11]   Yong Hyun Kim, Christoph Sachse, Michael L. Machala, Christian May, Lars Müller-Meskamp, and Karl Leo.
"Highly Conductive PEDOT:PSS Electrode with Optimized Solvent and Thermal Post-Treatment for ITO-Free Organic Solar Cells."
*Adv. Funct. Mater.* **21**, 1076 (2011)
(See p. 12).

[KSZ+13]   Gun-Ho Kim, Lei Shao, Kejia Zhang, and Kevin P. Pipe.
"Engineered doping of organic semiconductors for enhanced thermoelectric efficiency."
*Nat. Mater.* **12**, 719 (2013)
(See p. 28).

[KVM+07]   Krzysztof Koziol, Juan José Vilatela, Anna Moisala, Marcelo Motta, Philip Cunniff, Michael Sennett, and Alan H. Windle.
"High-Performance Carbon Nanotube Fiber."
*Science*, **318**, 1892 (2007)
(See p. 19).

[KWB+16]   Keehoon Kang, Shun Watanabe, Katharina Broch, Alessandro Sepe, Adam Brown, Iyad Nasrallah, Mark Nikolka, Zhuping Fei, Martin Heeney, Daisuke Matsumoto, Kazuhiro Marumoto, Hisaaki Tanaka, Shin-ichi Kuroda, and Henning Sirringhaus.
"2D coherent charge transport in highly ordered conducting polymers doped by solid state diffusion."
*Nat. Mater.* **15**, 896 (2016)
(See p. 27).

[Lab76]   *Ultraviolet Light Induced Reactions in Polymers.*
ACS Symposium Series vol. 25. Ed. by Santokh S. Labana (June 1976).
ISBN: 0-8412-0313-X
(See p. 61).

[LCB09]     Maël Le Berre, Yong Chen, and Damien Baigl.
            "From convective assembly to Landau-Levich deposition of multilayered phospholipid films of controlled
            thickness."
            *Langmuir*, **25**, 2554 (2009)
            (See pp. 72, 76).

[LCD+13]    Alessandro Luzio, Luigino Criante, Valerio D'Innocenzo, and Mario Caironi.
            "Control of charge transport in a semiconducting copolymer by solvent-induced long-range order."
            *Sci. Rep.* **3**, 3425 (2013)
            (See p. 18).

[LCP+16]    Ting Lei, Xiyuan Chen, Gregory Pitner, H.-S. Philip Wong, and Zhenan Bao.
            "Removable and Recyclable Conjugated Polymers for Highly Selective and High-Yield Dispersion and
            Release of Low-Cost Carbon Nanotubes."
            *J. Am. Chem. Soc.* **138**, 802 (2016)
            (See p. 17).

[LCT+09]    Chin-Ching Lin, Bryan T. T. Chu, Gerard Tobias, Serhat Sahakalkan, Siegmar Roth, Malcolm L. H. Green,
            and San-Yuan Chen.
            "Electron transport behavior of individual zinc oxide coated single-walled carbon nanotubes."
            *Nanotechnology*, **20**, 105703 (2009)
            (See p. 103).

[LFJ+04]    Mark C. Llaguno, John E. Fischer, Alan T. Johnson, and James Hone.
            "Observation of Thermopower Oscillations in the Coulomb Blockade Regime in a Semiconducting Carbon
            Nanotube."
            *Nano Lett.* **4**, 45 (2004)
            (See p. 29).

[LGV+87]    P. Lautenschlager, Miquel Garriga, L. Viña, and Manuel Cardona.
            "Temperature dependence of the dielectric function and interband critical points in silicon."
            *Phys. Rev. B*, **36**, 4821 (1987)
            (See p. 48).

[LHY+17]    Sangwook Lee, Kedar Hippalgaonkar, Fan Yang, Jiawang Hong, Changhyun Ko, Joonki Suh, Kai Liu, Kevin
            Wang, Jeffrey J. Urban, Xiang Zhang, Chris Dames, Sean A. Hartnoll, Olivier Delaire, and Junqiao Wu.
            "Anomalously low electronic thermal conductivity in metallic vanadium dioxide."
            *Science*, **355**, 371 (2017)
            (See p. 24).

[Lin13]     Bihong Lin.
            "Comment on "Optimization of power and efficiency of thermoelectric devices with asymmetric thermal
            contacts" [J. Appl. Phys. 111, 024509 (2012)]."
            *J. Appl. Phys.* **114**, 176101 (2013)
            (See p. 25).

[LKW04]     Ya-Li Li, Ian A. Kinloch, and Alan H. Windle.
            "Direct Spinning of Carbon Nanotube Fibers from Chemical Vapor Deposition Synthesis."
            *Science*, **304**, 276 (2004)
            (See p. 19).

[LL42]      Lev D. Landau and Benjamin G. Levich.
            "Dragging of a Liquid by a Moving Plate."
            *Acta Physicochim. U.R.S.S.* **17**, 42 (1942)
            (See p. 72).

[LLL+16]    Feifei Lian, Juan P Llinas, Zuanyi Li, David Estrada, and Eric Pop.
            "Thermal conductivity of chirality-sorted carbon nanotube networks."
            *Appl. Phys. Lett.* **108**, 103101 (2016)
            (See pp. 53, 63).

[LP15]      Alejandro López-Moreno and Emilio M. Pérez.
            "Pyrene-based mechanically interlocked SWNTs."
            *Chem. Commun.* **51**, 5421 (2015)
            (See p. 66).

[LPG+11]    Matthew T. Lloyd, Craig H. Peters, Andres Garcia, Isaac V. Kauvar, Joseph J. Berry, Matthew O. Reese,
            Michael D. McGehee, David S. Ginley, and Dana C. Olson.
            "Influence of the hole-transport layer on the initial behavior and lifetime of inverted organic photovoltaics."
            *Sol. Energy Mater. Sol. Cells*, **95**, 1382 (2011)
            (See p. 41).

[LTS+12]    Stephanie S. Lee, Samuel B. Tang, Detlef-M. Smilgies, Arthur R. Woll, Marsha A. Loth, Jeffrey M. Mativetsky,
            John E. Anthony, and Yueh-Lin Loo.
            "Guiding Crystallization around Bends and Sharp Corners."
            *Adv. Mater.* **24**, 2692 (2012)
            (See pp. 15, 71).

[LWG+17]    Bilu Liu, Fanqi Wu, Hui Gui, Ming Zheng, and Chongwu Zhou.
            "Chirality-Controlled Synthesis and Applications of Single-Wall Carbon Nanotubes."
            *ACS Nano*, **11**, 31 (2017)
            (See p. 16).

[LWL+15]   Jun Liu, Xiaojia Wang, Dongyao Li, Nelson E. Coates, Rachel A. Segalman, and David G. Cahill.
"Thermal Conductivity and Elastic Constants of PEDOT:PSS with High Electrical Conductivity."
*Macromolecules*, **48**, 585 (2015)
(See pp. 12, 24).

[LYP+11]   Hang Woo Lee, Yeohoon Yoon, Steve Park, Joon Hak Oh, Sanghyun Hong, Luckshitha S Liyanage, Huiliang Wang, Satoshi Morishita, Nishant Patil, Young Jun Park, Jong Jin Park, Andrew Spakowitz, Giulia Galli, Francois Gygi, Philip H Wong, Jeffrey B Tok, Jong Min Kim, and Zhenan Bao.
"Selective dispersion of high purity semiconducting single-walled carbon nanotubes with regioregular poly(3-alkylthiophene)s."
*Nat. Commun.* **2**, 541 (2011)
(See pp. 17, 54).

[LZL+14]   Yuhang Liu, Jingbo Zhao, Zhengke Li, Cheng Mu, Wei Ma, Huawei Hu, Kui Jiang, Haoran Lin, Harald Ade, and He Yan.
"Aggregation and morphology control enables multiple cases of high-efficiency polymer solar cells."
*Nat. Commun.* **5**, 5293 (2014)
(See pp. 40, 41).

[Mac01]    Alan G. MacDiarmid.
""Synthetic Metals": A Novel Role for Organic Polymers (Nobel Lecture)."
*Angew. Chemie Int. Ed.* **40**, 2581 (2001)
(See p. 10).

[MAH+13]   Christian Müller, Mahdieh Aghamohammadi, Scott Himmelberger, Prashant Sonar, Miquel Garriga, Alberto Salleo, and Mariano Campoy-Quiles.
"One-Step Macroscopic Alignment of Conjugated Polymer Systems by Epitaxial Crystallization during Spin-Coating."
*Adv. Funct. Mater.* **23**, 2368 (2013)
(See pp. 70, 84).

[MAM+13]   Iain Meager, Raja Shahid Ashraf, Sonya Mollinger, Bob C. Schroeder, Hugo Bronstein, Daniel Beatrup, Michelle S. Vezie, Thomas Kirchartz, Alberto Salleo, Jenny Nelson, and Iain McCulloch.
"Photocurrent Enhancement from Diketopyrrolopyrrole Polymer Solar Cells through Alkyl-Chain Branching Point Manipulation."
*J. Am. Chem. Soc.* **135**, 11537 (2013)
(See p. 51).

[MAN+14]   Iain Meager, Raja Shahid Ashraf, Christian B. Nielsen, Jenny E. Donaghey, Zhenggang Huang, Hugo Bronstein, James R. Durrant, and Iain McCulloch.
"Power conversion efficiency enhancement in diketopyrrolopyrrole based solar cells through polymer fractionation."
*J. Mater. Chem. C*, **2**, 8593 (2014)
(See p. 51).

[MBZ+15]   Cara J. Mulligan, Chhinder Bilen, Xiaojing Zhou, Warwick J. Belcher, and Paul C. Dastoor.
"Levelised cost of electricity for organic photovoltaics."
*Sol. Energy Mater. Sol. Cells*, **133**, 26 (2015)
(See p. 5).

[ME94]     Alan G. MacDiarmid and Arthur J. Epstein.
"The concept of secondary doping as applied to polyaniline."
*Synth. Met.* **65**, 103 (1994)
(See pp. 12, 23).

[ME95]     Alan G. MacDiarmid and Arthur J. Epstein.
"Secondary doping: A new concept in conducting polymers."
*Macromol. Symp.* **98**, 835 (1995)
(See pp. 12, 23).

[MFS+14]   Nicola Martino, Daniele Fazzi, Calogero Sciascia, Alessandro Luzio, Maria Rosa Antognazza, and Mario Caironi.
"Mapping orientational order of charge-probed domains in a semiconducting polymer."
*ACS Nano*, **8**, 5968 (2014)
(See p. 18).

[MG12]     Begoña Milián-Medina and Johannes Gierschner.
"$\pi$-Conjugation."
*Wiley Interdiscip. Rev. Comput. Mol. Sci.* **2**, 513 (2012)
(See p. 9).

[MGC12]    Christian Müller, Miquel Garriga, and Mariano Campoy-Quiles.
"Patterned optical anisotropy in woven conjugated polymer systems."
*Appl. Phys. Lett.* **101**, 171907 (2012)
(See p. 18).

[MHB+16]   David S. Montgomery, Corey A. Hewitt, Ryan Barbalace, Travis Jones, and David L. Carroll.
"Spray doping method to create a low-profile high-density carbon nanotube thermoelectric generator."
*Carbon*, **96**, 778 (2016)
(See pp. 30, 31).

[ML15]      Katherine A. Mazzio and Christine K. Luscombe.
            "The future of organic photovoltaics."
            *Chem. Soc. Rev.* **44**, 78 (2015)
            (See p. 36).

[MLE+16]    Cheng-Kang Mai, Jun Liu, Christopher M. Evans, Rachel A. Segalman, Michael L. Chabinyc, David G.
            Cahill, and Guillermo C. Bazan.
            "Anisotropic Thermal Transport in Thermoelectric Composites of Conjugated Polyelectrolytes/Single-
            Walled Carbon Nanotubes."
            *Macromolecules*, **49**, 4957 (2016)
            (See pp. 24, 29).

[MRF+15]    Cheng-Kang Mai, Boris Russ, Stephanie L. Fronk, Nan Hu, Mary B. Chan-Park, Jeffrey J. Urban, Rachel A.
            Segalman, Michael L. Chabinyc, and Guillermo C. Bazan.
            "Varying the ionic functionalities of conjugated polyelectrolytes leads to both p- and n-type carbon nanotube
            composites for flexible thermoelectrics."
            *Energy Environ. Sci.* **8**, 2341 (2015)
            (See pp. 29, 57).

[MRG+09]    Matthieu Manceau, Agnès Rivaton, Jean-Luc Gardette, Stéphane Guillerez, and Noëlla Lemaître.
            "The mechanism of photo- and thermooxidation of poly(3-hexylthiophene) (P3HT) reconsidered."
            *Polym. Degrad. Stab.* **94**, 898 (2009)
            (See pp. 60, 61).

[Nel03]     Jenny Nelson.
            *The Physics of Solar Cells*
            (2003).
            ISBN: 978-1-86094-349-2
            (See p. 33).

[NHD+07]    Adrian Nish, Jeong-Yuan Hwang, James Doig, and Robin J. Nicholas.
            "Highly selective dispersion of single-walled carbon nanotubes using aromatic polymers."
            *Nat. Nanotechnol.* **2**, 640 (2007)
            (See p. 17).

[NHY+14]    Yusuke Nakai, Kazuya Honda, Kazuhiro Yanagi, Hiromichi Kataura, Teppei Kato, Takahiro Yamamoto,
            and Yutaka Maniwa.
            "Giant Seebeck coefficient in semiconducting single-wall carbon nanotube film."
            *Appl. Phys. Express*, **7**, 025103 (2014)
            (See p. 29).

[NIG+16]    Brenna Norton-Baker, Rachelle Ihly, Isaac E. Gould, Azure D. Avery, Zbyslaw R. Owczarczyk, Andrew J.
            Ferguson, and Jeffrey L. Blackburn.
            "Polymer-Free Carbon Nanotube Thermoelectrics with Improved Charge Carrier Transport and Power
            Factor."
            *ACS Energy Lett.* **1**, 1212 (2016)
            (See p. 29).

[NNM+16]    Yoshiyuki Nonoguchi, Motohiro Nakano, Tomoko Murayama, Harutoshi Hagino, Shota Hama, Koji
            Miyazaki, Ryosuke Matsubara, Masakazu Nakamura, and Tsuyoshi Kawai.
            "Simple Salt-Coordinated n-Type Nanocarbon Materials Stable in Air."
            *Adv. Funct. Mater.* **26**, 3021 (2016)
            (See p. 30).

[NOK+13]    Yoshiyuki Nonoguchi, Kenji Ohashi, Rui Kanazawa, Koji Ashiba, Kenji Hata, Tetsuya Nakagawa, Chihaya
            Adachi, Tomoaki Tanase, and Tsuyoshi Kawai.
            "Systematic Conversion of Single Walled Carbon Nanotubes into n-type Thermoelectric Materials by
            Molecular Dopants."
            *Sci. Rep.* **3**, 3344 (2013)
            (See p. 30).

[NTI+17]    Yoshiyuki Nonoguchi, Atsushi Tani, Tomohiro Ikeda, Chigusa Goto, Naoki Tanifuji, Ryoko M. Uda, and
            Tsuyoshi Kawai.
            "Water-Processable, Air-Stable Organic Nanoparticle-Carbon Nanotube Nanocomposites Exhibiting n-Type
            Thermoelectric Properties."
            *Small*, **13**, 1603420 (2017)
            (See p. 30).

[ÖAJ+00]    Ronald Österbacka, C. P. An, X. M. Jiang, and Z. V. Vardeny.
            "Two-Dimensional Electronic Excitations in Self-Assembled Conjugated Polymer Nanocrystals."
            *Science*, **287**, 839 (2000)
            (See p. 14).

[OKC+11]    Brendan T. O'Connor, R. Joseph Kline, Brad R. Conrad, Lee J. Richter, David J. Gundlach, Michael F. Toney,
            and Dean M. DeLongchamp.
            "Anisotropic Structure and Charge Transport in Highly Strain-Aligned Regioregular Poly(3-
            hexylthiophene)."
            *Adv. Funct. Mater.* **21**, 3697 (2011)
            (See p. 18).

[OKM+15]    Yuki Oshima, Yoshimasa Kitamura, Yutaka Maniwa, and Kazuhiro Yanagi.
"Fabrication of thermoelectric devices using precisely Fermi level-tuned semiconducting single-wall carbon nanotubes."
*Appl. Phys. Lett.* **107**, 043106 (2015)
(See p. 29).

[Pau58]    Leo J. van der Pauw.
"A method of measuring the resistivity and Hall coefficent on lamellae of arbitrary shape."
*Philips Tech. Rev.* **20**, 220 (1958)
(See p. 105).

[Pei79]    Rudolf Ernst Peierls.
*Surprises in Theoretical Physics*
(1979).
ISBN: 978-0691082424
(See p. 9).

[PJN+14]    Mingxing Piao, Min-kyu Joo, Junhong Na, Yun-Jeong Kim, Mireille Mouis, Gérard Ghibaudo, Siegmar Roth, Wung-Yeon Kim, Ho-kyun Jang, Gary P. Kennedy, Urszula Dettlaff-Weglikowska, and Gyu-tae Kim.
"Effect of Intertube Junctions on the Thermoelectric Power of Monodispersed Single Walled Carbon Nanotube Networks."
*J. Phys. Chem. C*, **118**, 26454 (2014)
(See p. 29).

[PKG+16]    Albert Polman, Mark Knight, Erik C. Garnett, Bruno Ehrler, and Wim C. Sinke.
"Photovoltaic materials: Present efficiencies and future challenges."
*Science*, **352**, aad4424 (2016)
(See p. 38).

[PNF+09]    Eva Pereiro, Josep Nicolás, Salvador Ferrer, and M. R. Howells.
"A soft X-ray beamline for transmission X-ray microscopy at ALBA."
*J. Synchrotron Radiat.* **16**, 505 (2009)
(See p. 105).

[PPG+15]    Steve Park, Gregory Pitner, Gaurav Giri, Ja Hoon Koo, Joonsuk Park, Kwanpyo Kim, Huiliang Wang, Robert Sinclair, H.-S. Philip Wong, and Zhenan Bao.
"Large-Area Assembly of Densely Aligned Single-Walled Carbon Nanotubes Using Solution Shearing and Their Application to Field-Effect Transistors."
*Adv. Mater.* **27**, 2656 (2015)
(See p. 18).

[PSL+16]    Luis M. Pazos-Outón, Monika Szumilo, Robin Lamboll, Johannes M. Richter, Micaela Crespo-Quesada, Mojitaba Abdi-Jalebi, Harry J. Beeson, Milan Vrućinić, Mejd Alsari, Henry J. Snaith, Bruno Ehrler, Richard H. Friend, and Felix Deschler.
"Photon recycling in lead iodide perovskite solar cells."
*Science*, **351**, 1430 (2016)
(See p. 35).

[PWF+15]    Igor Pochorovski, Huiliang Wang, Jeremy I. Feldblyum, Xiaodong Zhang, Alexander L. Antaris, and Zhenan Bao.
"H-Bonded Supramolecular Polymer for the Selective Dispersion and Subsequent Release of Large-Diameter Semiconducting Single-Walled Carbon Nanotubes."
*J. Am. Chem. Soc.* **137**, 4328 (2015)
(See p. 17).

[QAJ+03]    Dali Qian, Rodney Andrews, David Jacques, Padmakar Kichambare, Guoda Lian, and Elizabeth C. Dickey.
"Low-Temperature Synthesis of Large-Area CNx Nanotube Arrays."
*J. Nanosci. Nanotechnol.* **3**, 93 (2003)
(See pp. 54, 103).

[QAM+12]    Dali Qian, Rodney Andrews, Mark S. Meier, and Matthew C. Weisenberger.
"Nitrogen-containing carbon nanotubes and Y junctions by floating catalytic chemical vapor deposition."
*Nanomater. Energy*, **1**, 168 (2012)
(See pp. 54, 103).

[RAM+14]    Víctor Reguero, Belén Alemán, Bartolomé Mas, and Juan José Vilatela.
"Controlling Carbon Nanotube Type in Macroscopic Fibers Synthesized by the Direct Spinning Process."
*Chem. Mater.* **26**, 3550 (2014)
(See p. 19).

[RAS+16]    S. Gupta Roy, Omar M. Awartani, P. Sen, Brendan T. O'Connor, and Michael W. Kudenov.
"Intrinsic coincident linear polarimetry using stacked organic photovoltaics."
*Opt. Express*, **24**, 14737 (2016)
(See pp. 18, 85).

[RED+04]    Sivarajan Ramesh, Lars M. Ericson, Virginia A. Davis, Rajesh K. Saini, Carter Kittrell, Matteo Pasquali, W. E. Billups, W. Wade Adams, Robert H. Hauge, and Richard E. Smalley.
"Dissolution of Pristine Single Walled Carbon Nanotubes in Superacids by Direct Protonation."
*J. Phys. Chem. B*, **108**, 8794 (2004)
(See p. 17).

[RFY11]     Yeontack Ryu, Dallas D. Freeman, and Choongho Yu.
            "High electrical conductivity and n-type thermopower from double-/single-wall carbon nanotubes by manipulating charge interactions between nanotubes and organic/inorganic nanomaterials."
            *Carbon*, **49**, 4745 (2011)
            (See p. 64).
[RGU+16]    Boris Russ, Anne M. Glaudell, Jeffrey J. Urban, Michael L. Chabinyc, and Rachel A. Segalman.
            "Organic thermoelectric materials for energy harvesting and temperature control."
            *Nat. Rev. Mater.* **1**, 16050 (2016)
            (See pp. 21, 27).
[RK14]      Stephan Van Reenen and Martijn Kemerink.
            "Correcting for contact geometry in Seebeck coefficient measurements of thin film devices."
            *Org. Electron.* **15**, 2250 (2014)
            (See pp. 28, 99).
[RRB+14]    Boris Russ, Maxwell J. Robb, Fulvio G. Brunetti, P. Levi Miller, Erin E. Perry, Shrayesh N. Patel, Victor Ho, William B. Chang, Jeffrey J. Urban, Michael L. Chabinyc, Craig J. Hawker, and Rachel A. Segalman.
            "Power factor enhancement in solution-processed organic n-type thermoelectrics through molecular design."
            *Adv. Mater.* **26**, 3473 (2014)
            (See p. 30).
[RXL+03]    Barry P. Rand, Jiangeng Xue, Michael J. Lange, and Stephen R. Forrest.
            "Thin-film organic position sensitive detectors."
            *IEEE Photonics Technol. Lett.* **15**, 1279 (2003)
            (See p. 90).
[SBG+14]    Ruth A. Schlitz, Fulvio G. Brunetti, Anne M. Glaudell, P. Levi Miller, Michael A. Brady, Christopher J. Takacs, Craig J. Hawker, and Michael L. Chabinyc.
            "Solubility-limited extrinsic n-type doping of a high electron mobility polymer for thermoelectric applications."
            *Adv. Mater.* **26**, 2825 (2014)
            (See p. 30).
[SFS+14]    Suman Kalyan Samanta, Martin Fritsch, Ullrich Scherf, Widianta Gomulya, Satria Zulkarnaen Bisri, and Maria Antonietta Loi.
            "Conjugated polymer-assisted dispersion of single-wall carbon nanotubes: the power of polymer wrapping."
            *Acc. Chem. Res.* **47**, 2446 (2014)
            (See p. 17).
[SHD+16]    Leo Shaw, Pascal Hayoz, Ying Diao, Julia Antonia Reinspach, John W. F. To, Michael F. Toney, R. Thomas Weitz, and Zhenan Bao.
            "Direct Uniaxial Alignment of a Donor–Acceptor Semiconducting Polymer Using Single-Step Solution Shearing."
            *ACS Appl. Mater. Interfaces*, **8**, 9285 (2016)
            (See p. 18).
[SHE+13]    Roar R. Søndergaard, Markus Hösel, Nieves Espinosa, Mikkel Jørgensen, and Frederik C. Krebs.
            "Practical evaluation of organic polymer thermoelectrics by large-area R2R processing on flexible substrates."
            *Energy Sci. Eng.* **1**, 81 (2013)
            (See p. 31).
[Shi01]     Hideki Shirakawa.
            "The Discovery of Polyacetylene Film: The Dawning of an Era of Conducting Polymers (Nobel Lecture)."
            *Angew. Chemie Int. Ed.* **40**, 2574 (2001)
            (See p. 10).
[SHK13]     Kouji Suemori, Satoshi Hoshino, and Toshihide Kamata.
            "Flexible and lightweight thermoelectric generators composed of carbon nanotube-polystyrene composites printed on film substrate."
            *Appl. Phys. Lett.* **103**, 2011 (2013)
            (See p. 31).
[SHT+10]    Sheng Shen, Asegun Henry, Jonathan Tong, Ruiting Zheng, and Gang Chen.
            "Polyethylene nanofibres with very high thermal conductivities."
            *Nat. Nanotechnol.* **5**, 251 (2010)
            (See pp. 18, 24).
[SJI+16]    Arno H. M. Smets, Klaus Jäger, Olindo Isabella, René A. C. M. M. van Swaaij, and Miro Zeman.
            *Solar Energy: The Physics and Engineering of Photovoltaic Conversion, Technologies and Systems*
            (2016).
            ISBN: 9781906860325
            (See p. 3).
[SJS+01]    Moonsub Shim, Ali Javey, Nadine Wong Shi Kam, and Hongjie Dai.
            "Polymer Functionalization for Air-Stable n-Type Carbon Nanotube Field-Effect Transistors."
            *J. Am. Chem. Soc.* **123**, 11512 (2001)
            (See pp. 30, 57, 64).

[SKO+16]  Stefania Sandoval, Nitesh Kumar, Judith Oro-Solé, A. Sundaresan, C.N.R. Rao, Amparo Fuertes, and Gerard Tobias.
"Tuning the nature of nitrogen atoms in N-containing reduced graphene oxide."
*Carbon*, **96**, 594 (2016)
(See pp. 65, 103).

[SL17]  Gisela L. Schulz and Sabine Ludwigs.
"Controlled Crystallization of Conjugated Polymer Films from Solution and Solvent Vapor for Polymer Electronics."
*Adv. Funct. Mater.* **27**, 1603083 (2017)
(See p. 15).

[SMK+06]  Markus C. Scharber, David Mühlbacher, Markus Koppe, Patrick Denk, Christoph Waldauf, Alan J. Heeger, and Christoph J. Brabec.
"Design rules for donors in bulk-heterojunction solar cells - Towards 10 % energy-conversion efficiency."
*Adv. Mater.* **18**, 789 (2006)
(See p. 39).

[SMO+14]  Junshi Soeda, Hiroyuki Matsui, Toshihiro Okamoto, Itaru Osaka, Kazuo Takimiya, and Jun Takeya.
"Highly oriented polymer semiconductor films compressed at the surface of ionic liquids for high-performance polymeric organic field-effect transistors."
*Adv. Mater.* **26**, 6430 (2014)
(See p. 18).

[SNV+15]  Andrea Sorrentino, Josep Nicolás, Ricardo Valcárcel, Francisco Javier Chichón, Marc Rosanes, Jose Avila, Andrei Tkachuk, Jeff Irwin, Salvador Ferrer, and Eva Pereiro.
"MISTRAL: a transmission soft X-ray microscopy beamline for cryo nano-tomography of biological samples and magnetic domains imaging."
*J. Synchrotron Radiat.* **22**, 1112 (2015)
(See p. 105).

[SPK03]  Joshua P. Small, Kerstin M. Perez, and Philip Kim.
"Modulation of Thermoelectric Power of Individual Carbon Nanotubes."
*Phys. Rev. Lett.* **91**, 256801 (2003)
(See p. 29).

[SQ61]  William Shockley and Hans J. Queisser.
"Detailed balance limit of efficiency of p-n junction solar cells."
*J. Appl. Phys.* **32**, 510 (1961)
(See p. 34).

[SRM11]  Jonathan D. Servaites, Mark A. Ratner, and Tobin J. Marks.
"Organic solar cells: A new look at traditional models."
*Energy Environ. Sci.* **4**, 4410 (2011)
(See p. 36).

[SS03]  Moonsub Shim and Giles P. Siddons.
"Photoinduced conductivity changes in carbon nanotube transistors."
*Appl. Phys. Lett.* **83**, 3564 (2003)
(See p. 28).

[SSH+12]  Robert Steyrleuthner, Marcel Schubert, Ian Howard, Bastian Klaumünzer, Kristian Schilling, Zhihua Chen, Peter Saalfrank, Frédéric Laquai, Antonio Facchetti, and Dieter Neher.
"Aggregation in a high-mobility n-type low-bandgap copolymer with implications on semicrystalline morphology."
*J. Am. Chem. Soc.* **134**, 18303 (2012)
(See p. 18).

[SSH+92]  Niyazi Serdar Sariciftci, Laura Smilowitz, Alan J. Heeger, and Fred Wudl.
"Photoinduced electron transfer from a conducting polymer to buckminsterfullerene."
*Science*, **258**, 1474 (1992)
(See p. 36).

[SSS+14]  Myungsun Sim, Jisoo Shin, Chiyeoung Shim, Min Kim, Sae Byeok Jo, Joo-Hyun Kim, and Kilwon Cho.
"Dependence of Exciton Diffusion Length on Crystalline Order in Conjugated Polymers."
*J. Phys. Chem. C*, **118**, 760 (2014)
(See p. 39).

[SWB02]  Pavel Schilinsky, Christoph Waldauf, and Christoph J. Brabec.
"Recombination and loss analysis in polythiophene based bulk heterojunction photodetectors."
*Appl. Phys. Lett.* **81**, 3885 (2002)
(See p. 40).

[SWF+00]  Henning Sirringhaus, R. J. Wilson, Richard H. Friend, M. Inbasekaran, W. Wu, E. P. Woo, Martin Grell, and Donal D. C. Bradley.
"Mobility enhancement in conjugated polymer field-effect transistors through chain alignment in a liquid-crystalline phase."
*Appl. Phys. Lett.* **77**, 406 (2000)
(See p. 18).

[SWP+11]   Samuel D. Stranks, Christian Weisspfennig, Patrick Parkinson, Michael B. Johnston, Laura M. Herz, and Robin J. Nicholas.
"Ultrafast charge separation at a polymer - Single-walled carbon nanotube molecular junction."
*Nano Lett.* **11**, 66 (2011)
(See p. 57).

[Tan86]    C. W. Tang.
"Two-layer organic photovoltaic cell."
*Appl. Phys. Lett.* **48**, 183 (1986)
(See p. 39).

[TI05]     Harland G. Tompkins and Eugene A. Irene.
*Handbook of Ellipsometry*
(2005).
ISBN: 0815514999
(See p. 46).

[TJK+11]   Wing Chung Tsoi, David T. James, Jong Soo Kim, Patrick G. Nicholson, Craig E. Murphy, Donal D. C. Bradley, Jenny Nelson, and Ji-Seon Kim.
"The nature of in-plane skeleton Raman modes of P3HT and their correlation to the degree of molecular order in P3HT:PCBM blend thin films."
*J. Am. Chem. Soc.* **133**, 9834 (2011)
(See pp. 82, 83).

[TLY+17]   Xinchun Tian, Kara R. Lind, Bin Yuan, Santosh Shaw, Oskar Siemianowski, and Ludovico Cademartiri.
"Simplicity as a Route to Impact in Materials Research."
*Adv. Mater.* 10.1002/adma.201604681 (2017)
(See p. 69).

[TMF+12]   Takumi Takano, Hiroyasu Masunaga, Akihiko Fujiwara, Hidenori Okuzaki, and Takahiko Sasaki.
"PEDOT Nanocrystal in Highly Conductive PEDOT:PSS Polymer Films."
*Macromolecules*, **45**, 3859 (2012)
(See pp. 12, 18, 28).

[TTS+03]   Taishi Takenobu, Takumi Takano, Masashi Shiraishi, Yousuke Murakami, Masafumi Ata, Hiromichi Kataura, Yohji Achiba, and Yoshihiro Iwasa.
"Stable and controlled amphoteric doping by encapsulation of organic molecules inside carbon nanotubes."
*Nat. Mater.* **2**, 683 (2003)
(See p. 30).

[VAB+12]   Varun Vohra, Gianmichele Arrighetti, Luisa Barba, Koichi Higashimine, William Porzio, and Hideyuki Murata.
"Enhanced Vertical Concentration Gradient in Rubbed P3HT:PCBM Graded Bilayer Solar Cells."
*J. Phys. Chem. Lett.* **3**, 1820 (2012)
(See pp. 18, 85).

[VPC+00]   Brigitte Vigolo, Alain Pénicaud, Claude Coulon, Cédric Sauder, René Pailler, Catherine Journet, Patrick Bernier, and Phillippe Poulin.
"Macroscopic Fibers and Ribbons of Oriented Carbon Nanotubes."
*Science*, **290**, 1331 (2000)
(See p. 19).

[VTG+09]   Koen Vandewal, Kristofer Tvingstedt, Abay Gadisa, Olle Inganäs, and Jean V. Manca.
"On the origin of the open-circuit voltage of polymer-fullerene solar cells."
*Nat. Mater.* **8**, 904 (2009)
(See p. 37).

[WAG+15]   Hui Wang, Ujwala Ail, Roger Gabrielsson, Magnus Berggren, and Xavier Crispin.
"Ionic Seebeck Effect in Conducting Polymers."
*Adv. Energy Mater.* **5**, 1500044 (2015)
(See pp. 27, 28).

[WHY+15]   Hong Wang, Jui-Hung Hsu, Su-In Yi, Suk Lae Kim, Kyungwho Choi, Gang Yang, and Choongho Yu.
"Thermally Driven Large N-Type Voltage Responses from Hybrids of Carbon Nanotubes and Poly(3,4-ethylenedioxythiophene) with Tetrakis(dimethylamino)ethylene."
*Adv. Mater.* **27**, 6855 (2015)
(See pp. 30, 63).

[WKB+15]   Annie Weathers, Zia Ullah Khan, Robert Brooke, Drew Evans, Michael T. Pettes, Jens Wenzel Andreasen, Xavier Crispin, and Li Shi.
"Significant Electronic Thermal Transport in the Conducting Polymer Poly(3,4-ethylenedioxythiophene)."
*Adv. Mater.* **27**, 2101 (2015)
(See p. 24).

[WL90]     Jean Claude Wittmann and B. Lotz.
"Epitaxial crystallization of polymers on organic and polymeric substrates."
*Prog. Polym. Sci.* **15**, 909 (1990)
(See p. 69).

[WMN+13]   Qingshuo Wei, Masakazu Mukaida, Yasuhisa Naitoh, and Takao Ishida.
"Morphological change and mobility enhancement in PEDOT:PSS by adding co-solvents."
*Adv. Mater.* **25**, 2831 (2013)
(See pp. 12, 28).

[WNC+16]    Jing Wang, Tuan Dat Nguyen, Qing Cao, Yilei Wang, Marcus Y.C. Tan, and Mary B. Chan-Park.
            "Selective Surface Charge Sign Reversal on Metallic Carbon Nanotubes for Facile Ultrahigh Purity Nanotube
            Sorting."
            *ACS Nano*, **10**, 3222 (2016)
            (See p. 17).

[WS91]      Jean Claude Wittmann and Paul Smith.
            "Highly oriented thin films of poly(tetrafluoroethylene) as a substrate for oriented growth of materials."
            *Nature*, **352**, 414 (1991)
            (See p. 69).

[WYP+15]    Hong Wang, Su-in Yi, Xiong Pu, and Choongho Yu.
            "Simultaneously Improving Electrical Conductivity and Thermopower of Polyaniline Composites by
            Utilizing Carbon Nanotubes as High Mobility Conduits."
            *ACS Appl. Mater. Interfaces*, **7**, 9589 (2015)
            (See p. 29).

[XWW+17]    Jie Xu, Sihong Wang, Ging-Ji Nathan Wang, Chenxin Zhu, Shaochuan Luo, Lihua Jin, Xiaodan Gu, Shucheng
            Chen, Vivian R. Feig, John W F. To, Simon Rondeau-Gagné, Joonsuk Park, Bob C. Schroeder, Chien Lu,
            Jin Young Oh, Yanming Wang, Yun-hi Kim, He Yan, Robert Sinclair, Dongshan Zhou, Gi Xue, Boris
            Murmann, Christian Linder, Wei Cai, Jeffery B.-H. Tok, Jong Won Chung, and Zhenan Bao.
            "Highly stretchable polymer semiconductor films through the nanoconfinement effect."
            *Science*, **355**, 59 (2017)
            (See p. 4).

[YBK+15]    Hongliu Yang, Viktor Bezugly, Jens Kunstmann, Arianna Filoramo, and Gianaurelio Cuniberti.
            "Diameter-Selective Dispersion of Carbon Nanotubes via Polymers: A Competition between Adsorption
            and Bundling."
            *ACS Nano*, **9**, 9012 (2015)
            (See p. 17).

[YDY+13]    Jingbi You, Letian Dou, Ken Yoshimura, Takehito Kato, Kenichiro Ohya, Tom Moriarty, Keith Emery,
            Chun-Chao Chen, Jing Gao, Gang Li, and Yang Yang.
            "A polymer tandem solar cell with 10.6% power conversion efficiency."
            *Nat. Commun.* **4**, 1446 (2013)
            (See p. 41).

[YGH+95]    G. Yu, J. Gao, Jan C. Hummelen, Fred Wudl, and Alan J. Heeger.
            "Polymer photovoltaic cells: enhanced efficiencies via a network of internal donor-acceptor heterojunctions."
            *Science*, **270**, 1789 (1995)
            (See p. 40).

[YH95]      G. Yu and Alan J. Heeger.
            "Charge separation and photovoltaic conversion in polymer composites with internal donor/acceptor
            heterojunctions."
            *J. Appl. Phys.* **78**, 4510 (1995)
            (See p. 40).

[YKO+14]    Kazuhiro Yanagi, Shouhei Kanda, Yuki Oshima, Yoshimasa Kitamura, Hideki Kawai, Takahiro Yamamoto,
            Taishi Takenobu, Yusuke Nakai, and Yutaka Maniwa.
            "Tuning of the Thermoelectric Properties of One-Dimensional Material Networks by Electric Double Layer
            Techniques Using Ionic Liquids."
            *Nano Lett.* **14**, 6437 (2014)
            (See p. 29).

[YMC+12]    Choongho Yu, Advaith Murali, Kyungwho Choi, and Yeontack Ryu.
            "Air-stable fabric thermoelectric modules made of N- and P-type carbon nanotubes."
            *Energy Environ. Sci.* **5**, 9481 (2012)
            (See p. 30).

[YS12]      Kazuaki Yazawa and Ali Shakouri.
            "Optimization of power and efficiency of thermoelectric devices with asymmetric thermal contacts."
            *J. Appl. Phys.* **111**, 024509 (2012)
            (See p. 25).

[YS13]      Kazuaki Yazawa and Ali Shakouri.
            "Response to "Comment on 'Optimization of power and efficiency of thermoelectric devices with asymmet-
            ric thermal contacts'" [J. Appl. Phys. 114, 176101 (2013)]."
            *J. Appl. Phys.* **114**, 176102 (2013)
            (See p. 25).

[YSY+05]    Choongho Yu, Li Shi, Zhen Yao, Deyu Li, and Arunava Majumdar.
            "Thermal Conductance and Thermopower of an Individual Single-Wall Carbon Nanotube."
            *Nano Lett.* **5**, 1842 (2005)
            (See p. 29).

[YTZ+16]    Yohei Yomogida, Takeshi Tanaka, Minfang Zhang, Masako Yudasaka, Xiaojun Wei, and Hiromichi Kataura.
            "Industrial-scale separation of high-purity single-chirality single-wall carbon nanotubes for biological
            imaging."
            *Nat. Commun.* **7**, 12056 (2016)
            (See p. 17).

[ZAB04]     Mei Zhang, Ken R. Atkinson, and Ray H. Baughman.
            "Multifunctional Carbon Nanotube Yarns by Downsizing an Ancient Technology."
            *Science*, **306**, 1358 (2004)
            (See p. 19).
[ZEP+14]    Eugen Zimmermann, Philipp Ehrenreich, Thomas Pfadler, James A. Dorman, Jonas Weickert, and Lukas Schmidt-Mende.
            "Erroneous efficiency reports harm organic solar cell research."
            *Nat. Photonics*, **8**, 669 (2014)
            (See p. 39).
[ZFB+17]    Dan Zhao, Simone Fabiano, Magnus Berggren, and Xavier Crispin.
            "Ionic thermoelectric gating organic transistors."
            *Nat. Commun.* **8**, 14214 (2017)
            (See p. 4).
[ZGH+91]    Stefan Zollner, Miquel Garriga, Josef Humlíček, Sudha Gopalan, and Manuel Cardona.
            "Temperature dependence of the dielectric function and the interband critical-point parameters of GaSb."
            *Phys. Rev. B*, **43**, 4349 (1991)
            (See p. 48).
[ZGK+93]    Stefan Zollner, Miquel Garriga, Jens Kircher, Josef Humlíček, Manuel Cardona, and Georg Neuhold.
            "Temperature dependence of the dielectric function and the interband critical-point parameters of GaP."
            *Thin Solid Films*, **233**, 185 (1993)
            (See p. 48).
[ZKY11]     Rui Zhu, Ankit Kumar, and Yang Yang.
            "Polarizing organic photovoltaics."
            *Adv. Mater.* **23**, 4193 (2011)
            (See pp. 18, 85, 86).
[ZLY+16]    Jingbo Zhao, Yunke Li, Guofang Yang, Kui Jiang, Haoran Lin, Harald Ade, Wei Ma, and He Yan.
            "Efficient organic solar cells processed from hydrocarbon solvents."
            *Nat. Energy*, **1**, 15027 (2016)
            (See p. 41).
[ZWK+16]    Dan Zhao, Hui Wang, Z. U. Khan, J. C. Chen, R. Gabrielsson, Magnus P. Jonsson, Magnus Berggren, and Xavier Crispin.
            "Ionic thermoelectric supercapacitors."
            *Energy Environ. Sci.* (2016)
            (See p. 28).

# LISTS

## List of Figures

# List of Tables

# Glossary

*absorbance* $(-\log(T))$
(*See* pp. **60**, 62)

*acceptor*
(*See* pp. 17, 35, 37, 38, 40, 49, 58)

*air mass coefficient* (AM)
The length of the path traversed within the atmosphere, relative to the length of the shortest path—that in radial direction.
(*See* p. **33**)

*angle of incidence* ($\phi$)
(*See* pp. **46**, 48)

*atomic force microscopy* (AFM)
(*See* pp. **56**, 60, 79, 86, 105, 106)

*attenuated total reflectance* (ATR)
(*See* p. 105)

*band gap*
The minimum amount of energy required to raise an electron from a localized state to a conducting state.
(*See* pp. 3, 5, **9**, 10, 16, 35, 47, 50, 51)

*bimolecular recombination*
The recombination of electrons and holes originating from different excitons.
(*See* pp. **36**, *and also* geminate recombination)

*bipolaron*
Two polarons sharing the same geometric distortion.
(*See* pp. **9**, 10)

*birefringence*
Both refraction and absorption depend on the polarization of light, $n + \mathrm{i}k = n(\varphi) + \mathrm{i}k(\varphi)$. This may lead to double refraction, a single beam of light splitting up in two, explaining the name.
(*See* pp. **46**, 70, 83, 108)

*blade coating*
Film forming technique by which a solution is spread across a substrate using a blade or knife.
(*See* pp. 18, 70, **72**, 75, 80, *and also* dr. blade)

*bulk heterojunction* (BHJ)
Heterojunction with a large interfacial area between two unbroken phases.
(*See* pp. 14, 35, **40**, 48, 49, 69, 71)

*carbon nanotube* (CNT)
(*See* pp. iii, **3**, 7, 16–19, 22, 24, 26–30, 32, 53, 54, 56, 59, 63–66, 101, 103–105)

*charge carrier density* ($n$)
The number of free charge carriers per unit volume.
(*See* pp. 11, 12, **23**, 25, 27)

*charge carrier mobility* ($\mu$)
Proportionality factor between an applied electric field, and the resulting drift velocity of a charged particle.
(*See* pp. 12, 18, **22**, 23, 28, 29, 36)

*charge transfer state*
Weakly bound, energetically favorable state across a donor–acceptor interface.
(*See* p. **35**)

*chemical vapor deposition* (CVD)
A process that uses volatile precursors in the gas phase, that react to form a product.
(*See* pp. **19**, 103)

*chlorobenzene* (CB)
(*See* pp. **70**, 72, 84, 104, 106)

*chloroform*
(*See* p. 104)

*CNT concentration* ($c$)
(*See* p. 58)

*conjugation*
Alternation of single and multiple bonds, resulting in delocalized electrons.
(*See* p. **8**)

*conjugation length*
Chain length over which transport is coherent and band-like.
(*See* pp. **9**, 60)

*contact line*
    Triple phase boundary between solution, substrate and atmosphere.
    (*See* pp. **72**, 74, 75, 79)

*degree of polymerization*     (DP)
    Number of monomers in a polymer chain.
    (*See* pp. **12**, 13, 17)

*device active area*     (*A*)
    (*See* p. **37**)

*dichloromethane*     (DCM)
    Low boiling point solvent, that dissolves PCBM but not P3HT.
    (*See* pp. **71**, 79, 85, 86, 104, 106)

*dichroic ratio*     (DR)
    The ratio of absorbance for light polarized parallel to light polarized perpendicularly to some reference
    direction.
    (*See* pp. **73**, 74, 82, 86, *and* absorbance)

*dichroism*
    Selective absorption of one polarization direction of light, $k = k(\varphi)$. When this absorption is wavelength
    dependent, this results in two colors, hence the name.
    (*See* pp. **46**, 74, 83, 84, 108, *is a special case of* birefringence)

*dimensionless figure of merit*     (*ZT*)
    The ratio between the reversible and the irreversible contributions to the flow of heat.
    (*See* pp. **25**, 26, 27, 63)

*dispersity*     (Đ)
    Measure of the spread of a molecular weight distribution.
    (*See* pp. **13**, 14, 15, 103, 104)
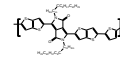
*donor*
    (*See* pp. 35, 37, 38, 40, 49, 58)

*doping*
    Increase of $\sigma$ due to a direct change of $n$.
    (*See* pp. 23, 27, 30)

*thieno[3,2-b]thiophene-diketopyrrolopyrrole*     (DPPTT-T)
    The branched side-chains may be attached to the polymer backbone across $m = 1$ or 3 intermediate carbon
    atoms, referred to as C1 and C3 respectively.
    (*See* pp. 7, **51**)

*dr. blade*
    Short for ductor blade. The misspelling "doctor blade" entered into common usage.
    (*See* p. *see* blade coating)

*easter egg*
    You sure are a thorough reader :-)
    (*See* p.  easter egg)

*electrical conductivity*     (σ)
    (*See* pp. 10, 12, 16, 18, 21, **22**, 23–29, 53, 54, 56, 60, 63–67, 105)

*electron affinity*     (EA)
    The energy gained by adding an electron to a neutral, isolated molecule or atom. Approximately the
    energy of the LUMO level relative to vacuum.
    (*See* p. *compare to* ionization energy)

*elementary charge*     (*e*)
    $\approx 1.602 \times 10^{-19}$ C.
    (*See* p. 39)

*ellipsometry*
    Coherent measurement of the change in polarization state of light reflected from materials.
    (*See* pp. **45**, 46, 82, 83, 108)

*energy payback time*     (EPBT)
    The time it takes a device to generate as much energy as is needed for its own manufacture, installation
    and disposal.
    (*See* p. **4**)

*energy return on investment*     (EROI)
    Ratio of energy produced during the lifetime of a device, relative to the energy invested during its
    fabrication.
    (*See* p. **4**)

*entropy*     (*S*$^*$)
    "Quantity of heat". Carrier of thermal energy.
    (*See* p. **26**)

*entropy conductivity*    (Λ)
   The thermal conductivity normalized by temperature $\Lambda = \frac{\kappa}{T}$.
   (*See* p. **26**)

*epitaxial growth*
   Growth of an ordered structure with the help of a crystalline substrate that acts as a seed crystal.
   (*See* p. **69**)

*exciton*
   Quasiparticle consisting of an electron–hole pair in an excited state, bound by the Coulomb interaction.
   (*See* pp. **34**, 35, 38–40, *compare* charge transfer state)

*external quantum efficiency*    (EQE)
   The number of generated charges per incoming photon.
   (*See* pp. **38**, 39, 40, 85, 87, 88, 107)

*2,3,5,6-tetrafluoro-7,7,8,8-tetracyanoquinodimethane*    ($F_4$TCNQ)
   Strong p-type dopant.
   (*See* pp. 7, 11, **27**, 50, 51)

*Fermi level*    ($E_F$)
   The energy level, that, at thermal equilibrium, has a 50 % chance of being occupied.
   (*See* pp. 25, 29, 57, 58, 152)

*fill factor*    (FF)
   A measure of the "squareness" of the JV-curve.
   (*See* p. **37**)

*Fourier transform infrared*    (FTIR)
   (*See* pp. **61**, 105)

*geminate pair*
   An electron–hole pair originating from the same exciton.
   (*See* p. **35**)

*geminate recombination*
   The recombination of a geminate pair.
   (*See* pp. 35, *and also* bimolecular recombination)

*general purpose interface bus*    (GPIB)
   Legacy 8-bit parallel protocol still used to connect laboratory instruments.
   (*See* p. **100**)

*heterojunction*
   Interface between two semiconductors with unequal band gap.
   (*See* pp. 34, **35**, *in OPV commonly a* bulk heterojunction)

*highest occupied molecular orbital*    (HOMO)
   (*See* pp. **9**, 10, 11, 35, 37, 149)

*indium tin oxide*    (ITO)
   Transparent conductor.
   (*See* pp. **40**, 41, 87, 90, 104, 106)

*internal quantum efficiency*    (IQE)
   The number of generated charges per photon absorbed in the active layer.
   (*See* pp. **39**, 40)

*ionization energy*    (IE)
   The minimum amount of energy required to remove an electron from a neutral, isolated molecule or atom.
   The energy of the HOMO relative to the vacuum.
   (*See* pp. 7, *compare to* electron affinity)

*iron chloride*    ($FeCl_3$)
   (*See* pp. 11, 50, 51)

*leg*
   A single thermoelectric element. Can be either p-type or n-type.
   (*See* pp. 31, 57, 62, 99)

*levelized cost of energy*    (LCOE)
   Total cost per Watt of produced energy.
   (*See* p. **5**)

*light beam induced current*    (LBIC)
   (*See* pp. 90, 107)

*lowest unoccupied molecular orbital*    (LUMO)
   (*See* pp. **9**, 10, 11, 34, 35, 37, 82, 148)

*mechanically interlocked carbon nanotube*     (MINT)
  (*See* p. **66**)

*morphology*
  The microscale organization and ordering of polymer chains.
  (*See* pp. **39**, 40)

*multi-walled carbon nanotube*     (MWCNT)
  (*See* pp. **16**, 53, 54, 64, 65, *see also* carbon nanotube)

*n-type*
  Material whose mobile charges are electrons in the conduction band, or LUMO.
  (*See* pp. 5, 18, 29, 30, 54, 64–66, *compare* p-type)

*ActivInk™ N2200*     (P(NDI2OD-T2))
  High mobility n-type polymer.
  (*See* pp. 7, 18, 30, **66**)

*naphthalene*
  (*See* pp. **84**, 104)

*nitrogen-doped multi-walled carbon nanotube*     (N-MWCNT)
  (*See* pp. 53, **54**, 56–60, 63–65, 103, *see also* carbon nanotube)

*nitrogen-doped single-walled carbon nanotube*     (N-SWCNT)
  (*See* pp. **65**, 103, *see also* carbon nanotube)

*number average molecular weight*     ($M_n$)
  For a given molecular weight distribution, the *number* of molecules above and below $M_n$ are equal.
  (*See* pp. **12**, 51)

*open circuit voltage*     ($V_{oc}$)
  (*See* p. **37**)

*organic field-effect transistor*     (OFET)
  An electrical switch composed of organic materials, in which an applied gate voltage tunes the electric field in the channel, which in turns changes its conductivity.
  (*See* p. 29)

*organic photovoltaic*     (OPV)
  Generation of electricity from sunlight, using carbon-based materials.
  (*See* pp. **3**, 4, 5, 14, 17, **33**, 34–36, 39, 41, 42, 45, 49, 50, 69, 71, 85, 103, 104)

*orthodichlorobenzene*     (oDCB)
  (*See* pp. **62**, 64–66, 104)

*p-type*
  Material whose mobile charge carriers are holes in the valence band or HOMO.
  (*See* pp. 11, 29, 50, 54, 64–66, *compare* n-type)

*poly(3-hexylthiophene-2,5-diyl)*     (P3HT)
  (*See* pp. **3**, 7, 11, 13–15, 40, 50, 51, 54, 56, 57, 59–65, 69–72, 76, 79, 80, 83–87, 103, 104, 106, 107)
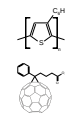
*[6,6]-phenyl C$_{61}$ butyric acid methyl ester*     (PCBM)
  A soluble fullerene, widely used as acceptor material.
  (*See* pp. 7, 14, **17**, 40, 48, 71, 79, 85–87, 104, 106, 107)

*[6,6]-phenyl C$_{71}$ butyric acid methyl ester*     (PC$_{70}$BM)
  (*See* pp. 17, 48–50)

*poly[N-9′-heptadecanyl-2,7-carbazole-alt-5,5-(4′,7′-di-2-thienyl-2′,1′,3′-benzothiadiazole)]*     (PCDTBT)
  (*See* pp. 7, **49**)
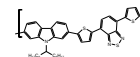
*poly[2,6-(4,4-bis-(2-ethylhexyl)-4H-cyclopenta [2,1-b;3,4-b′]dithiophene)-alt-4,7(2,1,3-benzothiadiazole)]*     (PCPDTBT)
  (*See* pp. 7, **48**, 49, 84, 104)
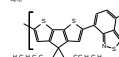
*poly(3,4-ethylenedioxythiophene)*     (PEDOT)
  Transparent conducting polymer.
  (*See* pp. 7, 12, 22, 27, 28, 30, **41**, 104, 106)

*polyethylenimine*     (PEI)
  (*See* pp. 7, **30**, 53, 64, 65, 104)

*Peltier coefficient*     (Π)
  The amount of energy, relative to the Fermi energy, that is transported per unit charge.
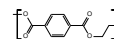  (*See* p. **22**)

*relative permittivity*     ($\varepsilon_r$)
  Factor by which the electric field between two charges is decreased compared to vacuum. Also called dielectric constant.
  (*See* p. **35**)

*persistence length*    (*P*)
  Measure of the stiffness of a polymer chain, below which a single polymer molecule can be treated as an elastic rod.
  (*See* pp. **13**, 51)

*polyethylene terephthalate*    (PET)
  (*See* pp. **40**, 62, 99, 104)

*poly(9,9-di-n-octylfluorenyl-2,7-diyl)*    (PFO)
  (*See* p. **18**)

*photoluminescence*    (PL)
  (*See* pp. **57**, 60–62, 71, 81, 82, 86, 107)

*π–π-stacking*
  Attractive interaction due to $\pi$-orbital overlap between adjacent aromatic rings.
  (*See* p. **14**)

*polaron*
  A quasiparticle composed of a charge which is screened by the surrounding atoms. Because of this, the surrounding atoms are no longer at their equilibrium positions—the polymer backbone is distorted.
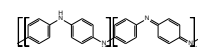  (*See* pp. **9**, 10, 14, 50, 51)

*polyacetylene*
  (*See* pp. 7, **9**, 10, 27)

*polyaniline*    (PANI)
  (*See* p. **29**)

*polyelectrolyte*
  A macromolecule with a large number of ionizable groups. Also called polysalt.
  (*See* p. **29**)

*power conversion efficiency*    ($\eta$)
  (*See* pp. **25**, 34, 37, 38, 48, 49, 71, 85–87)

*power factor*    ($S^2\sigma$)
  (*See* pp. **23**, 26, 28–30, 53, 54, 57, 60, 66)

*poly(styrenesulfonate)*    (PSS)
  Water-soluble polymer, used to disperse and dope PEDOT.
  (*See* pp. 7, 12, 27, 28, **41**, 104, 106)

*Raman*
  (*See* pp. 60, 81–83, 107)

*regioregularity*    (RR)
  Measure for the degree of order along a polymer chain that is composed of asymmetric monomers.
  (*See* pp. **13**, 103, 104)

*scanning electron microscopy*    (SEM)
  (*See* pp. **56**, 60, 105)

*secondary doping*
  Increase of $\sigma$ due to changes in morphology or crystallinity and not due to an increase in $n$. This increase remains even after the removal of the secondary dopant.
  (*See* pp. **12**, 23, 28)

*Seebeck coefficient*    (*S*)
  The average amount of entropy transported per charge carrier. Also called the thermopower $\alpha$.
  (*See* pp. **21**, 22, 23, 25–29, 53, 54, 56–61, 64–67, 99, 104, 109)

*semiconducting single-walled carbon nanotube*    (sc-SWCNT)
  (*See* pp. **17**, 22, 29, 53, *see also* carbon nanotube)

*serial peripheral interface*    (SPI)
  Synchronous four-wire protocol that allows for two-way communication of digital components.
  (*See* p. **100**)

*series resistance*    ($R_\text{series}$)
  (*See* p. **37**)

*short circuit current density*    ($J_\text{sc}$)
  (*See* pp. **37**, 38, 39, 50, 88)

*shunt resistance*    ($R_\text{shunt}$)
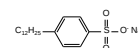  (*See* p. **37**)

*single-walled carbon nanotube*    (SWCNT)
  (*See* pp. **16**, 29, 53, 64–67, 103, 104, *see also* carbon nanotube)

*sodium dodecylbenzenesulfonate*    (SDBS)
  Used as a surfactant.
  (*See* pp. **64**, 65, 104)

*spectral irradiance*    ($F(\lambda)$)
Power arriving at a surface at a given wavelength.
(*See* p. **33**)

*speed of light*    ($c$)
Defined as $299\,792\,458\,\mathrm{m\,s^{-1}}$ in vacuum.
(*See* p. **45**)

*spherulite*
A semicrystalline region of material with spherical, or in two dimensions circular shape.
(*See* pp. **14**, 15, **70**, 71–75, 77, 79–81, 83, 84, 87, 88, 90, 91, 103, 107, 108)

*spin coating*
(*See* pp. 70, 72, 80)

*1,3,5-trichlorobenzene*    (TCB)
Crystalline solid at room temperature. Can be used as a solvent similar to CB when liquid.
(*See* pp. 7, **69**, 70–72, 74, 76, 78, 83, 84, 104, 106, 107)

*thermal conductivity*    ($\kappa$)
(*See* pp. 18, 21, **23**, 24–26, 31, 53, 54, 63, 105)

*thermal contact resistance*    ($R^{\mathrm{thermal}}$)
(*See* p. **30**)

*thermal diffusivity*    ($\alpha$)
A measure of how fast temperature spreads inside a material, comparable to an inverse inertia.
(*See* pp. **24**, 105)

*thermocouple*
The basic building block of a thermoelectric generator, composed of a p-type and an n-type leg.
(*See* pp. 31, 62, 63)

*thermoelectric generator*    (TEG)
(*See* pp. 23, 28, 29, **30**, 31, 32, 54, 59, 60, 62, 99)

*thermoelectricity*
Conversion of heat directly into electricity, and vice versa.
(*See* pp. **3**, **21**, 23, 26, 64)

*virtual instrument software architecture*    (VISA)
Standardized interface used to control laboratory instruments from a PC.
(*See* p. **100**)

*wavelength*    ($\lambda$)
(*See* pp. 11, 33, 34, 38, 46, 47)

*weight average molecular weight*    ($M_{\mathrm{w}}$)
For a given molecular weight distribution, the *weight* of molecules above and below $M_{\mathrm{w}}$ is equal.
(*See* pp. **12**, 103, 104)

*wet spinning*
Extrusion of a solution through a pinhole into a high viscosity, laminar flowing second liquid, in which the solvent is soluble, but the dissolved material is not. The dissolved material aligns itself to the flow, and coagulates due to the new environment.
(*See* p. **19**)

*work function*    ($\phi$)
The energy gained by adding an electron to the Fermi level of a material.
(*See* p. 36)

# SCIENTIFIC CONTRIBUTIONS

ORCID: 0000-0003-3171-0526     Scopus Author ID: 55750092200
ResearcherID: A-5768-2016     Google Scholar Profile: Bernhard Dörling

## Publications

[DSA+17]   Bernhard Dörling, Antonio Sánchez-Díaz, Oriol Arteaga, Andrea Veciana, M. Isabel Alonso, and Mariano Campoy-Quiles.
"Controlled Pinning of Conjugated Polymer Spherulites and its Application in Detectors."
*submitted*, (2017)
(See pp. iii, 79, 96).

[DSK+17]   Bernhard Dörling, Stefania Sandoval, Pacharapon Kankla, Amparo Fuertes, Gerard Tobias, and Mariano Campoy-Quiles.
"Exploring different doping mechanisms in thermoelectric polymer/carbon nanotube composites."
*Synth. Met.* **225**, 70 (2017)
(See pp. iii, 64, 95).

[VFM+16]   Michelle S. Vezie, Sheridan Few, Iain Meager, Galatia Pieridou, Bernhard Dörling, Raja Shahid Ashraf, Alejandro R. Goñi, Hugo Bronstein, Iain McCulloch, Sophia C. Hayes, Mariano Campoy-Quiles, and Jenny Nelson.
"Exploring the origin of high optical absorption in conjugated polymers."
*Nat. Mater.* **15**, 746 (2016)
(See pp. ii, 51, 95).

[DRC+16]   Bernhard Dörling, Jason D. Ryan, John D. Craddock, Andrea Sorrentino, Ahmed El Basaty, Andrés Gomez, Miquel Garriga, Eva Pereiro, John E. Anthony, Matthew C. Weisenberger, Alejandro R. Goñi, Christian Müller, and Mariano Campoy-Quiles.
"Photoinduced p- to n-type Switching in Thermoelectric Polymer-Carbon Nanotube Composites."
*Adv. Mater.* **28**, 2782 (2016)
(See pp. ii, 54, 95).

[VDH+16]   Varun Vohra, Bernhard Dörling, Koichi Higashimine, and Hideyuki Murata.
"Investigating the effect of solvent boiling temperature on the active layer morphology of diffusive bilayer solar cells."
*Appl. Phys. Express*, **9**, 012301 (2016)
(See pp. iii, 71, 83, 96).

[DVT+14]   Bernhard Dörling, Varun Vohra, Toan Thanh Dao, Miquel Garriga, Hideyuki Murata, and Mariano Campoy-Quiles.
"Uniaxial macroscopic alignment of conjugated polymer systems by directional crystallization during blade coating."
*J. Mater. Chem. C*, **2**, 3303 (2014)
(See pp. iii, 72, 96).

[GDR+13]   Antonio Guerrero, Bernhard Dörling, Teresa Ripolles-Sanchis, Mahdieh Aghamoham-
           madi, Esther Barrena, Mariano Campoy-Quiles, and Germà Garcia-Belmonte.
           "Interplay between Fullerene Surface Coverage and Contact Selectivity of Cathode
           Interfaces in Organic Solar Cells."
           *ACS Nano*, **7**, 4637 (2013)
           (See pp. ii, 48, 50, 95).

## Patents

[CGD+15]   Mariano Campoy Quiles, Alejandro Rodolfo Goñi Tasada, Bernhard Dörling, Christian
           Müller, and Jason Ryan.
           "A process of obtainment of an n-type organic semiconductor by UV-vis irradiation."
           Patent pending ES1641.1145, PCT/EP2016/078459 (ES, WO).
           Nov. 24, 2015
           (See pp. iii, 65, 95).

## Prizes

Bernhard Dörling, Andrés Gomez, and Mariano Campoy-Quiles
3rd prize of 3000 € for the project "TrasnoBattery", presented at
*Cleantech Camp*
Barcelona (Spain) 22. September 2016

## Presentations

Bernhard Dörling, Miquel Garriga, M. Isabel Alonso, Oriol Arteaga, and Mariano Campoy-Quiles.
"Spherulitic Bilayer Organic Photovoltaic Devices—Processing and Applications."
*MRS - Fall Meet. 2016*.
Boston (USA) 2. December, 2016.

Bernhard Dörling, Jason D. Ryan, Matthew C. Weisenberger, Andrea Sorrentino, Ahmed El Basaty,
Miquel Garriga, Eva Pereiro, John E. Anthony, Christian Müller, and Mariano Campoy-Quiles.
"Nitrogen-Doped Carbon Nanotube/Polymer Composites with p- and n-type Character for Flexible
Thermoelectrics."
*EMRS - Spring Meet. 2015*.
Lille (France) 12. May, 2015.

Bernhard Dörling, Christian Müller, Matthew C. Weisenberger, John E. Anthony, Alejandro R. Goñi,
and Mariano Campoy-Quiles.
"Tuning the Seebeck Coefficient from Positive to Negative Values in Nitrogen-Doped Carbon
Nanotube - P3HT Nanocomposites."
*ECT 2014*.
Madrid (Spain) 24. September, 2014.

Bernhard Dörling, Varun Vohra, Toan Thanh Dao, Miquel Garriga, Hideyuki Murata, and Mariano
Campoy-Quiles.
"Uniaxial Alignment of Conjugated Polymers During Deposition From Solution."
*ElecMol 2014*.
Strasbourg (France) 25. August, 2014.

## Posters

Bernhard Dörling, Jason D. Ryan, John D. Craddock, Andrea Sorrentino, Ahmed El Basaty, Andrés Gomez, Miquel Garriga, Eva Pereiro, John E. Anthony, Matthew C. Weisenberger, Alejandro R. Goñi, Christian Müller, and Mariano Campoy-Quiles.
"Photoinduced p- to n-type Switching in Thermoelectric Polymer-Carbon Nanotube Composites."
*MRS - Fall Meet. 2016.*
Boston (USA) 28. November, 2016.

Bernhard Dörling, Jason D. Ryan, John D. Craddock, Andrea Sorrentino, Ahmed El Basaty, Andrés Gomez, Miquel Garriga, Eva Pereiro, John E. Anthony, Matthew C. Weisenberger, Alejandro R. Goñi, Christian Müller, and Mariano Campoy-Quiles.
"Photoinduced p- to n-type Switching in Thermoelectric Polymer-Carbon Nanotube Composites."
*ICSM 2016.*
Guangzhou (China) 27. June, 2016.

Bernhard Dörling, Jason D. Ryan, Matthew C. Weisenberger, Andrea Sorrentino, Ahmed El Basaty, Miquel Garriga, Eva Pereiro, John E. Anthony, Christian Müller, Alejandro R. Goñi, and Mariano Campoy-Quiles.
"Nitrogen-doped CNT/P3HT composites with tunable p- and n-type character for flexible thermo-electric modules."
*ICT&ECT 2015.*
Dresden (Germany) 29. June, 2015.

Bernhard Dörling, Varun Vohra, Toan Thanh Dao, Miquel Garriga, Hideyuki Murata, and Mariano Campoy-Quiles.
"Uniaxial Alignment of Conjugated Polymers During Deposition From Solution."
*ElecMol 2014.*
Strasbourg (France) 26. August, 2014.